FIELD AND LABORATORY EXPERIMENTS TO EVALUATE THE EFFECTS OF IMPROVEMENT TECHNIQUES ON SEISMIC PERFORMANCE OF HIGHWAY EMBANKMENTS

by

Yasin Sait Toksoy

B.S., Civil Engineering, Yıldız Technical University, 2011

M.S., Earthquake Engineering, Boğaziçi University, 2014

Submitted to Kandilli Observatory and Earthquake Research Institute
in partial fulfillment of the requirements for the degree of
Doctor of Philosophy

Graduate Program in Earthquake Engineering
Boğaziçi University

2024

FIELD AND LABORATORY EXPERIMENTS TO EVALUATE THE EFFECTS OF IMPROVEMENT TECHNIQUES ON SEISMIC PERFORMANCE OF HIGHWAY EMBANKMENTS

APPROVED BY:

Prof. Ayşe Edinçliler……..
(Thesis Supervisor)

Prof. Ayfer Erken ……...
(Doğuş University)

Assoc. Prof. Gülüm Tanırcan……..

Asst. Prof. Tülay Kaya Eken ……

Prof. Musaffa Ayşen Lav ……....
(İstanbul Technical University)

DATE OF APPROVAL: 27.09.2024

ACKNOWLEDGEMENTS

Foremost, I would like to thank my thesis supervisor Prof. Dr. Ayşe Edinçliler, who has always supported, motivated, and encouraged me in any case and under any circumstances during my graduate studies and thesis stage. I appreciate her continuous support, guidance, patience, and research experience.

I would like to thank my committee members for their contributions and guidance to my thesis for years.

This study was supported by Boğaziçi University Research Fund Grant Number BAP15901, Türkiye Cumhuriyeti Cumhurbaşkanlığı Strateji ve Bütçe Başkanlığı "Geoteknik Deprem Mühendisliği Araştırma Merkezi Projesi" Fund Grant Number 2012K120500 and Scientific and Technological Research Council of Türkiye (TUBITAK) under the Grant Number 123M343. Thanks to Boğaziçi University, Türkiye Cumhuriyeti Cumhurbaşkanlığı Strateji ve Bütçe Başkanlığı and TUBITAK for their supports. I also would like to thank Istanbul Teknik company for providing the geogrid materials and EPSDER - EPS Industry Association for providing the EPS geofoam blocks and financial support.

I would like to thank the experts and technicians in KOERI Shaking Table Laboratory who helped me during my experiments.

I also would like to thank my friends Cengiz Demirtaş, Gözde Sezgin Tunçay and Esra Kalkan Ertan for supporting me during this long journey.

Finally, I would like to express my deepest gratitude to my parents, for their support, love, and encouragement throughout my academic journey. This accomplishment would not have been possible without you.

ABSTRACT

FIELD AND LABORATORY EXPERIMENTS TO EVALUATE THE EFFECTS OF IMPROVEMENT TECHNIQUES ON SEISMIC PERFORMANCE OF HIGHWAY EMBANKMENTS

Highway embankments have experienced earthquake-induced damages from minor to catastrophic scales during the past few decades despite the fact that highways are considered as major lifelines that should be in continuous operation under any circumstances. Recent advances in highway engineering suggest that geosynthetic reinforcement can be considered as a novel approach to mitigate earthquake hazards on highway embankments by reducing the effects of earthquake-induced dynamic forces successfully. The objective of this thesis is to assess the seismic performance of highway embankments as well as to evaluate the effects of improvement techniques in terms of dynamic performance of the models by performing a series of full-scale seismic performing tests and reduced scale shaking table experiments. Field experiments include the dynamic performance tests of unreinforced, geogrid reinforced and EPS geofoam highway embankments in the proposed test area using the Mobile Seismic Shaker. Local site conditions and the wave propagation properties of the test area have been investigated with the help of the geophysical and geotechnical experiments. before the full-scale seismic performance test stage. A series of shaking table tests of the 1/10 scale of the shake table models were performed. The experimental results were evaluated comparing the acceleration and displacement responses of the highway embankment models. Obtained results from full-scale experiments reveal that transmitted accelerations are up to 68.8% and 80%, and displacements are up to 95.1% and 99.3% less for the geogrid reinforced and EPS geofoam embankment models. Similar results were also obtained from shaking table experiments as geogrid reinforcement and EPS geofoam inclusions can notably enhance the structural stability and resilience of the embankment.

ÖZET

İYİLEŞTİRME TEKNİKLERİNİN KARAYOLU DOLGULARININ SİSMİK PERFORMANSINA ETKİSİNİN ARAZİ VE LABORATUVAR DENEYLERİYLE DEĞERLENDİRİLMESİ

Karayolları her şart altında hizmet vermesi beklenen temel yaşam hatlarından birisi olarak kabul edilmelerine rağmen, son yıllarda deprem etkisi altında en küçüğünden en büyük ölçeğine varacak şekilde hasar görmüşlerdir. Karayolu mühendisliğindeki güncel araştırmalar, geosentetik kullanımıyla deprem kaynaklı dinamik yüklerin başarıyla azaltılarak, deprem kaynaklı hasarların azaltılması için yeni bir yaklaşım olarak değerlendirilebileceğini önermektedir. Bu tezin amacı, karayolu dolgularının sismik performansını belirlemek ve iyileştirme tekniklerinin dinamik performans üzerindeki etkilerini incelemektir. Bu bağlamda arazi koşullarında tam ölçekli sismik performans testleri Mobil Sismik Sarsıcı kullanılarak, ölçekli sismik performans testleri ise sarsma masası testleriyle gerçekleştirilmiştir. Arazi çalışmaları güçlendirilmemiş, geogridle güçlendirilmiş ve EPS geofoam karayolu dolgularının dinamik performans testlerinin Mobil Sismik Sarsıcı kullanılarak yapılmasını içermektedir. Arazi deneylerinden bir önceki aşamada ise yerel zemin koşulları ve arazinin dalga yayılım özelliklerinin belirlenmesi amacıyla detaylı jeofizik ve geoteknik testler gerçekleştirilmiştir. Sarsma masası deneyleri ise üç farklı modelin 1/10 ölçekli olarak dinamik performans testlerine tabii tutulmasını içermektedir. Deneysel sonuçlar, karayolu dolgularının ivme ve yer değiştirme tepkileri karşılaştırılarak değerlendirilmiştir. Tam ölçekli arazi deneylerinden elde edilen sonuçlarda, ölçülen ivmelerin geogrid donatılı ve EPS geofoam karayolu dolgusu modellerinde sırasıyla %68.8'e ve %80'e, yer değiştirmelerin ise sırasıyla %95.1'e and %99.3'e varan oranda azalmaktadır. Sarsma masası deneylerinden de benzer sonuçlar elde edilmiş olup, geogrid ile güçlendirme ve EPS geofoam kullanımının karayolu dolgularının yapısal stabilitesini ve dayanıklılığını önemli ölçüde artırabileceğini ortaya koymaktadır.

TABLE OF CONTENTS

ACKNOWLEDGEMENTS iii
ABSTRACT iv
ÖZET v
LIST OF FIGURES xi
LIST OF TABLES xxxii
LIST OF SYMBOLS/ABBREVIATIONS xxxiv
1. INTRODUCTION 1
1.1. Problem Statement 1
1.2. Objective of the Study 1
1.3. Organization of the Thesis 2
2. THE STABILITY OF SLOPES AND EMBANKMENTS 3
2.1. Main Reasons of Slope Failures 3
2.2. Common Earthquake Effects and Case Studies 4
2.2.1. Surface Rupture 4
2.2.2. Liquefaction and Lateral Spreading 6
2.3. Seismic Analysis 9
2.3.1. Pseudostatic Method 9
2.3.2. Newmark's Displacement Method 11
2.3.3. Weakening Slope Stability Analysis 12
2.3.4. Finite Element Method 13
2.4. Embankment Failure Modes 14
2.4.1. Shallow Surface Sliding 14
2.4.2. Slip Surface Development within the Body of Embankment 15
2.4.3. Development of Slip Surface within the Soft Foundation Soil 18
2.4.4. Liquefaction Damage of Embankments 20
2.4.5. Settlement Damage of Embankments 21
3. STATIC AND DYNAMIC PROPERTIES OF GEOSYNTHETICS 22
3.1. Material Properties of Geosynthetics and Geosynthetic-Soil Interactions 23
3.2. Static and Dynamic Properties of EPS Geofoam 30
3.2.1. EPS Geofoam under Monotonic Loading 31

3.2.2. EPS Geofoam under Cyclic Loading 33
4. LITERATURE SURVEY 39
4.1. Experimental Studies with Full Scale Highway Embankments and Pavements 39
4.2. Experimental Studies with Mobile Seismic Shaker 59
4.3. Experimental Studies with Full Scale Railway Embankments 86
4.4. Experimental Studies with Shaking Table and Centrifuge Tests 91
4.5. EPS Geofoam Embankments 101
4.6. Embankments with Tire Chips-Sand Mixtures 106
4.7. Numerical Studies 108
5. EXPERIMENTAL STUDIES 112
5.1. Geotechnical and Geophysical Experiments 112
5.1.1. Site Investigation and Rehabilitation of the Test Area 112
5.1.2. Soil Sampling and Pressuremeter Tests 115
5.1.3. Microtremor Tests 118
5.1.4. Multichannel Analysis of Surface Waves (MASW) Tests 122
5.1.5. Electrical Resistivity Tomography (ERT) Tests 129
5.1.6. Spectral Analysis of Surface Waves (SASW) Tests 132
5.2. Highway Embankment Design and Field Scale Experiments 140
5.2.1. Materials 140
5.2.1.1. Subbase and Base Material 142
5.2.1.2. Geogrid Material 146
5.2.1.3. EPS Geofoam Material 147
5.2.2. Embankment Design Considerations 148
5.2.3. Mobile Seismic Shaker (MSS) 149
5.2.4. Construction of the Highway Embankment Models 151
5.2.5. Instrumentation Plan 161
5.2.6. Dynamic Excitations 170
5.2.7. Test Results Obtained from Field Scale Experimental Studies (E-W) ... 171
5.2.7.1. Test Results for Unreinforced Embankment Model 171
5.2.7.1.1. Test Results for Unreinforced Embankment Model under 1-100Hz 172
5.2.7.1.2. Test Results for Unreinforced Embankment Model under 1-250Hz 175

5.2.7.1.3. Test Results for Unreinforced Embankment Model under 1-250Hz 27kN 120s 178
5.2.7.2. Test Results for Geogrid Reinforced Embankment Model 181
5.2.7.2.1. Test Results for Geogrid Reinforced Embankment Model under 1-100Hz 182
5.2.7.2.2. Test Results for Geogrid Reinforced Embankment Model under 1-250Hz 185
5.2.7.2.3. Test Results for Geogrid Reinforced Embankment Model under 1-250Hz 27kN 120s 188
5.2.7.3. Test Results for EPS Geofoam Embankment Model..... 191
5.2.7.3.1. Test Results for EPS Geofoam Embankment Model under 1-100Hz 192
5.2.7.3.2. Test Results for EPS Geofoam Embankment Model under 1-250Hz 195
5.2.7.3.3. Test Results for EPS Geofoam Embankment Model under 1-250Hz 27kN 120s 198
5.3. Shaking Table Experiments 201
5.3.1. Materials 202
5.3.1.1. Sand 202
5.3.1.2. Geogrids 202
5.3.1.3. Plexiglas Soil Box 203
5.3.2. Methods 203
5.3.2.1. Soil Box Performance Check 204
5.3.2.2. Preperation of the Reduced Scale Highway Embankment Models 204
5.3.2.3. Instrumentation 207
5.3.3. Shaking Table Experiments 209
5.3.4. Shaking Table Test Results 210
5.3.4.1. Test Results for Unreinforced Case 211
5.3.4.1.1. Test Results for Unreinforced Case under 1-30Hz 211
5.3.4.1.2. Test Results for Unreinforced Case under 1-50Hz 213

5.3.4.1.3. Test Results for Unreinforced Case under 10Hz 215
5.3.4.1.4. Test Results for Unreinforced Case under 20Hz 217
5.3.4.1.5. Test Results for Unreinforced Case under 30Hz 219
5.3.4.2. Test Results for Geogrid Reinforced (T_{ult}:20kN/m) Case 221
5.3.4.2.1. Results for Geogrid Reinforced (T_{ult}:20kN/m) under 1-30Hz 221
5.3.4.2.2. Results for Geogrid Reinforced (T_{ult}:20kN/m) under 1-50Hz 223
5.3.4.2.3. Results for Geogrid Reinforced (T_{ult}:20kN/m) under 10Hz 225
5.3.4.2.4. Results for Geogrid Reinforced (T_{ult}:20kN/m) under 20Hz 227
5.3.4.2.5. Results for Geogrid Reinforced (T_{ult}:20kN/m) under 30Hz 228
5.3.4.3. Results for Geogrid Reinforced (T_{ult}:40kN/m) Case 230
5.3.4.3.1. Results for Geogrid Reinforced (T_{ult}:40kN/m) 1-30Hz 230
5.3.4.3.2. Results for Geogrid Reinforced (T_{ult}:40kN/m) 1-50Hz 232
5.3.4.3.3. Results for Geogrid Reinforced (T_{ult}:40kN/m) 10Hz 233
5.3.4.3.4. Results for Geogrid Reinforced (T_{ult}:40kN/m) 20Hz 235
5.3.4.3.5. Results for Geogrid Reinforced (T_{ult}:40kN/m) 30Hz 237
5.3.4.4. Results for EPS Geofoam Case 238
5.3.4.4.1. Results for EPS Geofoam Case 1-30Hz 239
5.3.4.4.2. Results for EPS Geofoam Case 1-50Hz 241
5.3.4.4.3. Results for EPS Geofoam Case 10Hz 243
5.3.4.4.4. Results for EPS Geofoam Case 20Hz 245

5.3.4.4.5. Results for EPS Geofoam Case 30Hz 247
6. DISCUSSIONS ON SEISMIC PERFORMANCE OF EMBANKMENT MODELS 249
6.1. Shaking Table Tests 249
6.1.1. Effects of Geogrid Reinforcement on Seismic Response of Embankment Models 249
6.1.2. Effects of EPS Geofoam on Seismic Response of Embankment Models . 255
6.1.3. Discussions on Effect of Geogrid Tensile Strength 258
6.1.4. Discussions on Normalized Accelerations and Displacements of All Embankment Models 259
6.2. Full Scale Seismic Performance Tests 263
6.2.1. Effects of Geogrid Reinforcement on Seismic Response of Embankment Models 265
6.2.2. Effects of EPS Geofoam on Seismic Response of Embankment Models 279
6.2.3. Discussions on Normalized Accelerations and Displacements of All Embankment Models 292
7. SUMMARY AND CONCLUSIONS 297

LIST OF FIGURES

Figure 2.1. Fault displacement damage in Pazarcık, Kahramanmaraş (ITU, 2023). 5

Figure 2.2. Fault displacement damage up to 340cm on a road in Türkoğlu, Kahramanmaraş (ITU, 2023). 5

Figure 2.3. Fault displacement damage up to 430cm on a road in Göksun, Kahramanmaraş (ITU, 2023). 6

Figure 2.4. Lateral spreading damage at Dörtyol, Hatay (METU/EERC Report, 2023). 7

Figure 2.5. Lateral spreading damage at İskenderun, Hatay (METU/EERC Report, 2023). 7

Figure 2.6. Road damage after Jan 2, 2024 Noto, Ishikawa, Japan Earthquake (https://edition.cnn.com/2024/01/02/asia/japan-earthquake-tsunami-warnings-tuesday-intl-hnk/index.html). 8

Figure 2.7. Road damage after Jan 2, 2024 Noto, Ishikawa, Japan Earthquake (https://www.theguardian.com/world/2024/jan/03/japan-earthquake-death-toll-emergency-warnings-landslide-aftershock-ishikawa). 8

Figure 2.8. Pseudostatic Equilibrium Method Analysis (Abramson, 2002). 10

Figure 2.9. Example diagram of Newmark's Method (Day, 2002). 12

Figure 2.10. Illustration of FEM for slope analysis (Abramson, 2002). 13

Figure 2.11. Shallow surface sliding (Towhata, 2008). 15

Figure 2.12. A sliding failure case of a road embankment (Towhata, 2008). 15

Figure 2.13. A sliding failure case (Towhata, 2008). 16

Figure 2.14. Slip surface development (Towhata, 2008). 16

Figure 2.15 Illustration of the failed embankment due to slip surface development (Towhata, 2008). 17

Figure 2.16. Damaged residential area due to the failure of the embankment subject to slip surface development (Towhata, 2008). 17

Figure 2.17. Road damage in Nanao after Jan 2, 2024 Noto, Ishikawa, Japan Earthquake (https://www3.nhk.or.jp/nhkworld/en/news/backstories/2935/). 18

Figure 2.18. Road damage in Kanazawa after Jan 2, 2024 Noto, Ishikawa, Japan Earthquake (https://www3.nhk.or.jp/nhkworld/en/news/backstories/2938/). 18

Figure 2.19. Development of the slip surface within embankment body within soft foundation soil (Towhata, 2008). 19

Figure 2.20. A failed embankment causing collapse of a river bank (Towhata, 2008). 19

Figure 2.21. A failed embankment causing the collapse of houses in Sumatra (Towhata, 2008). 19

Figure 2.22. The liquefaction damage (Towhata, 2008). 20

Figure 2.23. Road embankment with slumping damage (Towhata, 2008). 20

Figure 2.24. Settlement damage (Towhata, 2008). 21

Figure 2.25. Settlement damage of a road embankment (Towhata, 2008). 21

Figure 3.1. Compression behavior of geosynthetics (Shukla, 2016). 24

Figure 3.2. Wide-width strip tensile tests. 25

Figure 3.3. Typical Strength properties of Selected Geosynthetics (Shukla, 2016). 25

Figure 3.4. Illustration of direct shear test (Shukla, 2016). 26

Figure 3.5. The effect of strain rate on monotonic tensile load-strain behavior (Bathurst and Cai, 1994). 27

Figure 3.6. Dynamic material behavior of in-isolation HDPE type of geogrid (Cai and Bathurst, 1995). 27

Figure 3.7. Low-strain non-hysteretic behavior of geosynthetics (after Yogendrakum et al., 1991). 28

Figure 3.8. The influence of frequency on secant stiffness of HDPE and PET geogrids (Bathurst and Cai, 1994). 29

Figure 3.9. Stress-Strain relationship from monotonic loading tests on 20kN/m2 EPS specimen (Malai and Youwai, 2021). 31

Figure 3.10. Stress-Strain relationship of EPS geofoams with different densities (Malai and Youwai, 2021). 32

Figure 3.11. Effect of geofoam density on strength parameters (Koerner, 2005). 33

Figure 3.12. Obtained results for resonant column tests, a) G, b) D (Athanasopoulos et. al. (1999). 34

Figure 3.13. The effect of loading frequency on cyclic stress-strain relationship (Athanasopoulos et. al., 1999). 35

Figure 3.14. Cyclic uniaxial test results, a) Variation of (E), b) Variation of (D) with respect to cyclic axial strain amplitudes (Athanasopoulos et. al., 1999). 36

Figure 3.15. Results obtained from EPS 1 and EPS 2 (Trandafir et. al., 2010). 37

Figure 4.1. Test sections (Forsman et al., 2016). 40

Figure 4.2. Field testing. (a) Cross section of pavement, (b) Pavement itself, (c) Roughness of pavement surface (Chen et. al., 2015). 40

Figure 4.3. Typical plan view (Tutumluer et. al., 2019). 41

Figure 4.4. Test equipment and measurement of rutting (Tutumluer et. al., 2019). 42

Figure 4.5. Inclusion of geogrid layers on highway pavement (Abdessemed et. al., 2015). 43

Figure 4.6. Cross section of the pavement structure with the instrumentations (Saevarsdottir and Erlingsson, 2015). 44

Figure 4.7. Typical pavement cross-section (Correia, 2014). 45

Figure 4.8. Plan view of test site and instrumentation (Nunez et. al., 2013). 46

Figure 4.9. Cross sections of test embankments (Bergado et. al., 2002). 47

Figure 4.10. A-A and B-B section views of the test embankment Chaiyaput et. al. (2014). 48

Figure 4.11. Experimental plan (Huckert et. al., 2016). 49

Figure 4.12. Experimental test set-up (Likitlersuang et. al., 2020). 51

Figure 4.13. Laboratory loading system (Liu et. al., 2021). 51

Figure 4.14. Physical model details (Liu et. al., 2021). 52

Figure 4.15. Cross section of the embankment (Cao et. al., 2015). 53

Figure 4.16. Plan of the test embankment (Turan et. al., 2013). 54

Figure 4.17. Schematic view of the embankment (Vega-Meyer and Shao, 2005). 55

Figure 4.18. Unreinforced and reinforced embankments (Wang and Yao, 2013)..... 55

Figure 4.19. Dimensioning and instrumentation plan of embankments (Arsyad et. al., 2020). 56

Figure 4.20. PLAXIS model of the Haarajoki embankment (Rezania et. al., 2017). 57

Figure 4.21. Cross section of the column supported embankment (Huang and Han, 2019). 58

Figure 4.22. Numerical model of the case study (Huang and Han, 2019)..... 59

Figure 4.23. a) Input dynamic excitation, b) Sweep frequency range (Boaga et. al., 2021). 60

Figure 4.24. a) Instrumentation plan for the building, b) Location of sensors by floor, c) Data logger and geophones (Bertero et. al., 2022). 61

Figure 4.25. a) Measured velocities at station 1, b) Close up view for chirp excitations, c) Ground velocity spectra for each direction and technique (Bertero et. al., 2022). 62

Figure 4.26. Experimental setup (Wang et. al., 2022). 63

Figure 4.27. Road embankment cross section before and after failure (Hryciw et. al.,1990). 64

Figure 4.28. Applied static and dynamic force by the RDD system (Bay and Stokoe, II, 1998). 65

Figure 4.29. The vibroseis used during the field experiments (Chang, 2002). 66

Figure 4.30. In situ dynamic liquefaction test (Chang, 2002). 66

Figure 4.31. Field vibration test (Chang, 2002). 67

Figure 4.32. Dynamic excitation (a) and slow pull-over tests (b) on scaled bridge structure performed by large mobile shakers in the field (Wood et. al, 2004). 68

Figure 4.33. Experiments at test location C (Cox, 2006). 69

Figure 4.34. Voltage-Time Histories generated by Thumper truck at 100Hz, (a) Low amplitude, (b) High amplitude (Leblanc, 2013). 70

Figure 4.35. Obtained results at 50Hz, (a) Low amplitude, (b) High amplitude (Leblanc, 2013). 71

Figure 4.36. Instrumentation plan (Roberts, 2014). 72

Figure 4.37. Output force vs dynamic frequency of vibroseis (Roberts, 2014). 72

Figure 4.38. Shear wave velocity (Vs) profiles, a) two unimproved zones, b) between improvements at LMG, SRB, RAP and RIC zones, c) across improvements at SRB and DRB, d) across improvements at LMG, RIC and RAP zones (Stokoe et. al., 2016). 73

Figure 4.39. a) Instrumentation, b) T-Rex (Sahadewa, 2015). 74

Figure 4.40. Arrangement for deep downhole testing and example waveforms (Stokoe et. al. 2017). 75

Figure 4.41. The bridge to be tested and its instrumentation (Farrag et. al., 2019). 76

Figure 4.42. (a) Thumper truck used as an active source in SASW testing, (b) Resultant Vs profile (Stokoe et al., 2019). 77

Figure 4.43. Deep Vs profiling using Liquidator (Stokoe et al., 2019). 77

Figure 4.44. Obtained Vs profiles, (a) Softer site, (b) Stiffer site (Stokoe et al., 2019). 78

Figure 4.45. Very deep Vs profiling at Georgia (Stokoe et al., 2019). 78

Figure 4.46. Test configuration and developed Vs profile suits for Canterbury basin (Stokoe et al., 2019). 79

Figure 4.47. Instrumentation and the location of THOMAS at frame bridge (Drygala et al., 2020). 80

Figure 4.48. THOMAS vibroseis (Drygala et al., 2020). 80

Figure 4.49. a) Cross-section view of the instrumentation and site; b) Plan view, c) Plan view of the pier grids (Zalachoris et. al., 2023). 82

Figure 4.50. Railway embankment models (Li et al., 2017). 87

Figure 4.51. Instrumented railway embankment loading experiment (Lehtonen et al., 2015). 88

Figure 4.52. Experimental model (Chen et al., 2016). 88

Figure 4.53. Experimental set-up (Feng et. al., 2021). 89

Figure 4.54. Instrumented railway sections and its details (Wu et. al.,2019). 90

Figure 4.55. Centrifuge experiments (Ling et al., 2009). 91

Figure 4.56. Test set-up (Tamate et al., 2012). 92

Figure 4.57. Shake Table Studies (Lin and Wang, 2006). 92

Figure 4.58. Instrumentation plan (Toksoy, 2014). 95

Figure 4.59. Amplification factors (Edinçliler and Toksoy, 2016). 95

Figure 4.60. Comparison of crest level TA and SA values (Edincliler and Toksoy, 2017). 96

Figure 4.61. Embankment model and instrumentation plan (Lin et. al., 2015). 97

Figure 4.62. Acceleration-Time History and Fourier Amplitude Spectrum of Wenchuan Earthquake (Lin et. al., 2015). 97

Figure 4.63. Shaking table model and dimensioning (Wang et. al., 2018). 98

Figure 4.64. Responses in Time and Frequency Domain, (a) Artificial motion, (b) El Centro Earthquake, (c) Kobe Earthquake (Wang et. al., 2018). 98

Figure 4.65. Method of using soil bags for embankments (Nakazawa et.al., 2020). 99

Figure 4.66. Outline of the experimental models (Nakazawa et.al., 2020). 100

Figure 4.67. Experimental set-up (Han et. al., 2021). 100

Figure 4.68. Experimental set-up and instrumentations (Akay et al., 2013). 102

Figure 4.69. Cross section of the geofoam roadway (Ozer and Akinay, 2018). 103

Figure 4.70. Cross section view of the embankment (Sloan, 2011). 104

Figure 4.71. Rehabilitated highway embankment with EPS geofoam blocks (Puppala et. al., 2019). 105

Figure 4.72. Instrumented Embankment Model (Yoon et al., 2005). 106

Figure 4.73. Two test section of highway embankments (Bosscher et. al., 1997). 108

Figure 4.74. Highway Embankment Models (Toksoy and Edinçliler, 2023). 109

Figure 4.75. Dimensioning of the model (Edinçliler and Toksoy, 2022). 110

Figure 4.76. Total displacements in EPS Geofoam model (Toksoy and Edincliler, 2024). 111

Figure 5.1. Construction and Seismic Performance Test Area at KOERI. 113

Figure 5.2. Locations of Boreholes for the Site Investigation (Safir Jeoteknik, 2012). 113

Figure 5.3. Geologic Horizontal Cross-Section (Safir Jeoteknik, 2012). 114

Figure 5.4. Rehabilitation of the Test Area. 115

Figure 5.5. Pressuremeter Probe for Pressuremeter Tests. 116

Figure 5.6. Elastic Modulus Profile of the Test Area (Rumeli Zemin, 2019). 117

Figure 5.7. Locations of Microtremors. 119

Figure 5.8. Microtremor Set-up (a) and Coordinate Readings (b). 119

Figure 5.9. Obtained H/V Spectra from M-1 data (Geometrik Mühendislik, 2021). 120

Figure 5.10. Obtained H/V Spectra from M-2 data (Geometrik Mühendislik, 2021). 121

Figure 5.11. Obtained H/V Spectra from M-3 data (Geometrik Mühendislik, 2021). 122

Figure 5.12. A view from MASW experiments. 123

Figure 5.13. MASW Profiles across the test area. 124

Figure 5.14. Shear wave profile along S1 (Geometrik Mühendislik, 2021). 125

Figure 5.15. Shear wave profile along S2 (Geometrik Mühendislik, 2021). 126

Figure 5.16. Shear wave profile along S3 (Geometrik Mühendislik, 2021). 127

Figure 5.17. Shear wave profile along S4 (Geometrik Mühendislik, 2021). 128

Figure 5.18. Distribution of the electrodes in the test area (Geometrik Mühendislik, 2021). 130

Figure 5.19. Stages of ERT Testing, a) Driving the electrodes, b) Watering the electrodes for increased conductivity, c) Setting up connections, d) A view from the test area, e) Data acquisition system. 131

Figure 5.20. Generated 3-D resistivity map of the test area (Geometrik Mühendislik, 2021). 132

Figure 5.21. Wave propagation for dynamically loading circular footing on elastic half space (Chang, 2002). 133

Figure 5.22. Instrumentation plan for the SASW tests. 134

Figure 5.23. Field vibration test set-up. 135

Figure 5.24. Acceleration Responses from Test 1 (E-W), a) Sensor 1, b) Sensor 2, c) Sensor 3, d) Sensor 4. 137

Figure 5.25. Measured Peak Accelerations (U-D) versus Applied Force by MSS. 138

Figure 5.26. Measured Peak Accelerations (U-D) versus Frequency Content applied by MSS. 139

Figure 5.27. Typical layers of a flexible highway embankment (FHWA NHI-05-037). .. 141

Figure 5.28. Subbase material obtained from Ergenekon Ocak. 144

Figure 5.29. Base material obtained from Ergenekon Ocak. 144

Figure 5.30. Particle size distribution of subbase material. 145

Figure 5.31. Particle size distribution of base material. 146

Figure 5.32. The mobile seismic shaker (MSS). 151

Figure 5.33. Dimensions of the Unreinforced Embankment Model (not to scale). 152

Figure 5.34. Construction steps of the unreinforced embankment, a) Preperation of the site, b) Excavation, c) Preperation of the foundation, d) Construction of the subbase, e) Construction of the base, f) Asphalt paving. 153

Figure 5.35. Dimensions of the Geogrid Reinforced Embankment Model (not to scale). 155

Figure 5.36. Construction steps of the geogrid reinforced embankment, a) Rolling the first geogrid layer, b) Construction of the subbase, c) Rolling the second geogrid layer, d) Construction of the base, e) Asphalt paving. 156

Figure 5.37. Dimensions of the EPS Geofoam Embankment Model (not to scale). 158

Figure 5.38. Construction steps of the EPS geofoam embankment, a) Levelling the EPS geofoam blocks, b) EPS geofoam blocks as subbase, c) Construction of the base, d) Asphalt concrete paving, e) Protection layer. 159

Figure 5.39. The completed highway embankment models after construction. 161

Figure 5.40. Fixing the accelerometers on asphalt concrete layer. 162

Figure 5.41. Instrumentation Plan along the Road Direction. 163

Figure 5.42. Instrumentation Plan Perpendicular to the Road Direction. 164

Figure 5.43. Unreinforced Embankment Model prior to seismic performance tests, a) along the road direction, b) perpendicular to the road direction. 164

Figure 5.44. Geogrid reinforced Embankment Model prior to seismic performance tests, a) along the road direction, b) perpendicular to the road direction. 165

Figure 5.45. EPS Geofoam Embankment Model prior to seismic performance tests, a) along the road direction, b) perpendicular to the road direction. 166

Figure 5.46. Conducting the seismic performance tests. 167

Figure 5.47. Shear wave velocity conditions under embankments by MASW Tests (Geometrik Mühendislik, 2021). 168

Figure 5.48. Sub-Surface conditions under embankments (Geometrik Mühendislik, 2021). 170

Figure 5.49. Acceleration Response of A1, a) 1-100Hz 15kN 30s, b) 1-100Hz 27kN 30s. 172

Figure 5.50. Acceleration Response of A3, a) 1-100Hz 15kN 30s, b) 1-100Hz 27kN 30s. 173

Figure 5.51. Acceleration Response of A7, a) 1-100Hz 15kN 30s, b) 1-100Hz 27kN 30s. 173

Figure 5.52. Acceleration Response of A11, a) 1-100Hz 15kN 30s, b) 1-100Hz 27kN 30s. 174

Figure 5.53. Displacement Response of D3, a) 1-100Hz 15kN 30s, b) 1-100Hz 27kN 30s. 174

Figure 5.54. Displacement Response of D4, a) 1-100Hz 15kN 30s, b) 1-100Hz 27kN 30s. 175

Figure 5.55. Acceleration Response of A1, a) 1-250Hz 15kN 30s, b) 1-250Hz 27kN 30s. 175

Figure 5.56. Acceleration Response of A3, a) 1-250Hz 15kN 30s, b) 1-250Hz 27kN 30s. 176

Figure 5.57. Acceleration Response of A7, a) 1-250Hz 15kN 30s, b) 1-250Hz 27kN 30s. 177

Figure 5.58. Acceleration Response of A11, a) 1-250Hz 15kN 30s, b) 1-250Hz 27kN 30s. 177

Figure 5.59. Displacement Response of D3, a) 1-250Hz 15kN 30s, b) 1-250Hz 27kN 30s. 178

Figure 5.60. Displacement Response of D4, a) 1-250Hz 15kN 30s, b) 1-250Hz 27kN 30s. 178

Figure 5.61. Acceleration Response of A1. 179

Figure 5.62. Acceleration Response of A3. 179

Figure 5.63. Acceleration Response of A7. 180

Figure 5.64. Acceleration Response of A11. 180

Figure 5.65. Displacement Response of D3. 181

Figure 5.66. Displacement Response of D4. 181

Figure 5.67. Acceleration Response of A1, a) 1-100Hz 15kN 30s, b) 1-100Hz 27kN 30s. 182

Figure 5.68. Acceleration Response of A3, a) 1-100Hz 15kN 30s, b) 1-100Hz 27kN 30s. 183

Figure 5.69. Acceleration Response of A7, a) 1-100Hz 15kN 30s, b) 1-100Hz 27kN 30s. 183

Figure 5.70. Acceleration Response of A11, a) 1-100Hz 15kN 30s, b) 1-100Hz 27kN 30s. 184

Figure 5.71. Displacement Response of D3, a) 1-100Hz 15kN 30s, b) 1-100Hz 27kN 30s. 184

Figure 5.72. Displacement Response of D4, a) 1-100Hz 15kN 30s, b) 1-100Hz 27kN 30s. 185

Figure 5.73. Acceleration Response of A1, a) 1-250Hz 15kN 30s, b) 1-250Hz 27kN 30s. 185

Figure 5.74. Acceleration Response of A3, a) 1-250Hz 15kN 30s, b) 1-250Hz 27kN 30s. 186

Figure 5.75. Acceleration Response of A7, a) 1-250Hz 15kN 30s, b) 1-250Hz 27kN 30s. 187

Figure 5.76. Acceleration Response of A11, a) 1-250Hz 15kN 30s, b) 1-250Hz 27kN 30s. 187

Figure 5.77. Displacement Response of D3, a) 1-250Hz 15kN 30s, b) 1-250Hz 27kN 30s. 188

Figure 5.78. Displacement Response of D4, a) 1-250Hz 15kN 30s, b) 1-250Hz 27kN 30s. 188

Figure 5.79. Acceleration Response of A1. 189

Figure 5.80. Acceleration Response of A3. 189

Figure 5.81. Acceleration Response of A7. 190

Figure 5.82. Acceleration Response of A11. 190

Figure 5.83. Displacement Response of D3. 191

Figure 5.84. Displacement Response of D4. 191

Figure 5.85. Acceleration Response of A1, a) 1-100Hz 15kN 30s, b) 1-100Hz 27kN 30s. 192

Figure 5.86. Acceleration Response of A3, a) 1-100Hz 15kN 30s, b) 1-100Hz 27kN 30s. 193

Figure 5.87. Acceleration Response of A7, a) 1-100Hz 15kN 30s, b) 1-100Hz 27kN 30s. 193

Figure 5.88. Acceleration Response of A11, a) 1-100Hz 15kN 30s, b) 1-100Hz 27kN 30s. 194

Figure 5.89. Displacement Response of D3, a) 1-100Hz 15kN 30s, b) 1-100Hz 27kN 30s. 194

Figure 5.90. Displacement Response of D4, a) 1-100Hz 15kN 30s, b) 1-100Hz 27kN 30s. 195

Figure 5.91. Acceleration Response of A1, a) 1-250Hz 15kN 30s, b) 1-250Hz 27kN 30s. 195

Figure 5.92. Acceleration Response of A3, a) 1-250Hz 15kN 30s, b) 1-250Hz 27kN 30s. 196

Figure 5.93. Acceleration Response of A7, a) 1-250Hz 15kN 30s, b) 1-250Hz 27kN 30s. 196

Figure 5.94. Acceleration Response of A11, a) 1-250Hz 15kN 30s, b) 1-250Hz 27kN 30s. 197

Figure 5.95. Displacement Response of D3, a) 1-250Hz 15kN 30s, b) 1-250Hz 27kN 30s. 197

Figure 5.96. Displacement Response of D4, a) 1-250Hz 15kN 30s, b) 1-250Hz 27kN 30s. 198

Figure 5.97. Acceleration Response of A1. 198

Figure 5.98. Acceleration Response of A3. 199

Figure 5.99. Acceleration Response of A7. 199

Figure 5.100. Acceleration Response of A11. 200

Figure 5.101. Displacement Response of D3. 200

Figure 5.102. Displacement Response of D4. 201

Figure 5.103. Particle size distribution of Silivri Sand. 202

Figure 5.104. The plexiglass soil box (Toksoy, 2014). 203

Figure 5.105. Physical appearance of unreinforced embankment model. 205

Figure 5.106. Placement of a geogrid layer. 205

Figure 5.107. Physical appearance of geogrid reinforced embankment model. 206

Figure 5.108. EPS Geofoam embankment model. 207

Figure 5.109. Instrumentation plan for shaking table experiments. 208

Figure 5.110. Input motions used in shaking table experiments, a) 1-30Hz 9.5s incremental sine wave, b) 1-30Hz 38s incremental sine wave, c) 1-50Hz 9.5s incremental sine wave, d)

1-50Hz 38s incremental sine wave, e) 10Hz 9.5s sine wave, f) 10Hz 38s sine wave, g) 20Hz 9.5s sine wave, h) 20Hz 38s sine wave, i) 30Hz 9.5s sine wave, j) 30Hz 38s sine wave. 210

Figure 5.111. Acceleration Response of A9, a) 1-30 Hz 9.5s, b) 1-30 Hz 38s. 212

Figure 5.112. Displacement Response of D12, a) 1-30 Hz 9.5s, b) 1-30 Hz 38s. 212

Figure 5.113. Displacement Response of D13, a) 1-30 Hz 9.5s, b) 1-30 Hz 38s. 212

Figure 5.114. Deformed shape of the unreinforced embankment model under 1-30Hz-9.5s. 213

Figure 5.115. Acceleration Response of A9, a) 1-50 Hz 9.5s, b) 1-50 Hz 38s. 214

Figure 5.116. Displacement Response of D12, a) 1-50 Hz 9.5s, b) 1-50 Hz 38s. 214

Figure 5.117. Displacement Response of D13, a) 1-50 Hz 9.5s, b) 1-50 Hz 38s. 215

Figure 5.118. Deformed shape of the unreinforced embankment model under 1-50Hz-38s. 215

Figure 5.119. Acceleration Response of A9, a) 10Hz 9.5s, b) 10Hz 38s. 216

Figure 5.120. Displacement Response of D12, a) 10Hz 9.5s, b) 10Hz 38s..... 216

Figure 5.121. Displacement Response of D13, a) 10Hz 9.5s, b) 10Hz 38s..... 217

Figure 5.122. Acceleration Response of A9, a) 20Hz 9.5s, b) 20Hz 38s. 218

Figure 5.123. Displacement Response of D12, a) 20Hz 9.5s, b) 20Hz 38s..... 218

Figure 5.124. Displacement Response of D13, a) 20Hz 9.5s, b) 20Hz 38s..... 218

Figure 5.125. Acceleration Response of A9, a) 30Hz 9.5s, b) 30Hz 38s. 219

Figure 5.126. Displacement Response of D12, a) 30Hz 9.5s, b) 30Hz 38s..... 220

Figure 5.127. Displacement Response of D13, a) 30Hz 9.5s, b) 30Hz 38s..... 220

Figure 5.128. Deformed shape of the unreinforced embankment model subjected to 30Hz-9.5s. 220

Figure 5.129. Acceleration Response of A9, a)1-30Hz 9.5s, b) 1-30Hz 38s. 222

Figure 5.130. Displacement Response of D12, a)1-30Hz 9.5s, b) 1-30Hz 38s. 222

Figure 5.131. Displacement Response of D13, a)1-30Hz 9.5s, b) 1-30Hz 38s. 222

Figure 5.132. Deformed shape of the geogrid reinforced embankment model (Tult:20kN/m) under 1-30Hz-9.5s. 223

Figure 5.133. Acceleration Response of A9, a)1-50Hz 9.5s, b) 1-50Hz 38s. 224

Figure 5.134. Displacement Response of D12, a)1-50Hz 9.5s, b) 1-50Hz 38s. 224

Figure 5.135. Displacement Response of D13, a)1-50Hz 9.5s, b) 1-50Hz 38s. 224

Figure 5.136. Acceleration Response of A9, a) 10Hz 9.5s, b) 10Hz 38s. 225

Figure 5.137. Displacement Response of D12, a) 10Hz 9.5s, b) 10Hz 38s..... 226

Figure 5.138. Displacement Response of D13, a) 10Hz 9.5s, b) 10Hz 38s..... 226

Figure 5.139. Deformed shape of the geogrid reinforced embankment model (Tult:20kN/m) under 10Hz 9.5s. 226

Figure 5.140. Acceleration Response of A9, a) 20Hz 9.5s, b) 20Hz 38s. 227

Figure 5.141. Displacement Response of D12, a) 20Hz 9.5s, b) 20Hz 38s..... 228

Figure 5.142. Displacement Response of D13, a) 20Hz 9.5s, b) 20Hz 38s..... 228

Figure 5.143. Acceleration Response of A9, a) 30Hz 9.5s, b) 30Hz 38s. 229

Figure 5.144. Displacement Response of D12, a) 30Hz 9.5s, b) 30Hz 38s..... 229

Figure 5.145. Displacement Response of D13, a) 30Hz 9.5s, b) 30Hz 38s..... 230

Figure 5.146. Acceleration Response of A9, a) 1-30Hz 9.5s, b) 1-30Hz 38s. 231

Figure 5.147. Displacement Response of D12, a) 1-30Hz 9.5s, b) 1-30Hz 38s. 231

Figure 5.148. Displacement Response of D13, a) 1-30Hz 9.5s, b) 1-30Hz 38s. 231

Figure 5.149. Acceleration Response of A9, a) 1-50Hz 9.5s, b) 1-50Hz 38s. 232

Figure 5.150. Displacement Response of D12, a) 1-50Hz 9.5s, b) 1-50Hz 38s. 233

Figure 5.151. Displacement Response of D13, a) 1-50Hz 9.5s, b) 1-50Hz 38s. 233

Figure 5.152. Acceleration Response of A9, a) 10Hz 9.5s, b) 10Hz 38s. 234

Figure 5.153. Displacement Response of D12, a) 10Hz 9.5s, b) 10Hz 38s..... 234

Figure 5.154. Displacement Response of D13, a) 10Hz 9.5s, b) 10Hz 38s..... 235

Figure 5.155. Acceleration Response of A9, a) 20Hz 9.5s, b) 20Hz 38s. 236

Figure 5.156. Displacement Response of D12, a) 20Hz 9.5s, b) 20Hz 38s..... 236

Figure 5.157. Displacement Response of D13, a) 20Hz 9.5s, b) 20Hz 38s..... 236

Figure 5.158. Acceleration Response of A9, a) 30Hz 9.5s, b) 30Hz 38s. 237

Figure 5.159. Displacement Response of D12, a) 30Hz 9.5s, b) 30Hz 38s..... 238

Figure 5.160. Displacement Response of D13, a) 30Hz 9.5s, b) 30Hz 38s..... 238

Figure 5.161. Acceleration Response of A9, a) 1-30Hz 9.5s, b) 1-30Hz 38s. 239

Figure 5.162. Displacement Response of D12, a) 1-30Hz 9.5s, b) 1-30Hz 38s. 240

Figure 5.163. Displacement Response of D13, a) 1-30Hz 9.5s, b) 1-30Hz 38s. 240

Figure 5.164. Deformed shape of the EPS geofoam embankment model subjected to 1-30Hz 9.5s. 241

Figure 5.165. Acceleration Response of A9, a) 1-50Hz 9.5s, b) 1-50Hz 38s. 242

Figure 5.166. Displacement Response of D12, a) 1-50Hz 9.5s, b) 1-50Hz 38s. 242

Figure 5.167. Displacement Response of D13, a) 1-50Hz 9.5s, b) 1-50Hz 38s. 242

Figure 5.168. Deformed shape of the EPS geofoam embankment model subjected to 1-30Hz 9.5s. 243

Figure 5.169. Acceleration Response of A9, a) 10Hz 9.5s, b) 10Hz 38s. 244

Figure 5.170. Displacement Response of D12, a) 10Hz 9.5s, b) 10Hz 38s..... 244

Figure 5.171. Displacement Response of D13, a) 10Hz 9.5s, b) 10Hz 38s..... 245

Figure 5.172. Acceleration Response of A9, a) 20Hz 9.5s, b) 20Hz 38s. 246

Figure 5.173. Displacement Response of D12, a) 20Hz 9.5s, b) 20Hz 38s..... 246

Figure 5.174. Displacement Response of D13, a) 20Hz 9.5s, b) 20Hz 38s..... 246

Figure 5.175. Acceleration Response of A9, a) 30Hz 9.5s, b) 30Hz 38s. 247

Figure 5.176. Displacement Response D12, a) 30Hz 9.5s, b) 30Hz 38s. 248

Figure 5.177. Displacement Response of D13, a) 30Hz 9.5s, b) 30Hz 38s..... 248

Figure 6.1. a) Initial conditions of URE, b) Deformed shape of the URE subjected to 1-50Hz 38s of motion. 250

Figure 6.2. a) Initial conditions of GRE, b) Deformed shape of the geogrid reinforced embankment model (Tult:20kN/m) under 10Hz 9.5s of motion. 251

Figure 6.3. Comparison of the Transmitted Accelerations at toe (A8) for Unreinforced and Tult:20kN/m Geogrid Reinforced Models under 1-50Hz 38s of motion. 252

Figure 6.4. Comparison of the Horizontal Displacements at D12 for Unreinforced and Tult:20kN/m Geogrid Reinforced Models under 10Hz-38s of motion. 252

Figure 6.5. Comparison of the Transmitted Accelerations at toe (A8) for Unreinforced and Tult:40kN/m Geogrid Reinforced Models under 1-50Hz-38s of motion. 254

Figure 6.6. Seismic Demand Reduction on Tult:40kN/m Geogrid Reinforced Model Compared to Unreinforced Model at toe (A8) under 1-50Hz-38s of motion. 255

Figure 6.7. a) Initial conditions of EGE, b) Deformed shape of the EGE subjected to 1-30Hz 9.5s of motion. 256

Figure 6.8. Comparison of the Transmitted Accelerations at Crest for Unreinforced and EPS Geofoam Models under 1-50Hz-38s of motion. 257

Figure 6.9. Variation of Amplification Factors with Respect to Relative Height under 1-50Hz 38s of motion for URE, GRE (Tult :20kN/m) and GRE (Tult :40kN/m). 258

Figure 6.10. The variation of normalized acceleration at crest (A9) and toe (A8) under 1-50Hz 38s of motion 260

Figure 6.11. The variation of normalized horizontal displacement at crest (D12) under 10Hz 38s of motion. 261

Figure 6.12. The variation of normalized vertical displacement at crest (D13) under 10Hz 38s of motion. 262

Figure 6.13. Comparison of the transmitted accelerations on slope from A3, a) 1-100Hz 15kN 30s, b) 1-100Hz 27kN 30s. 266

Figure 6.14. Comparison of the transmitted accelerations on slope from A3, a) 1-250Hz 15kN 30s, b) 1-250Hz 27kN 30s. 267

Figure 6.15. Comparison of the transmitted accelerations on slope from A3 under 1-250Hz 27kN 120s. 268

Figure 6.16. Comparison of the transmitted accelerations at crest (A11), a) 1-100Hz 15kN 30s, b) 1-100Hz 27kN 30s. 269

Figure 6.17. Comparison of the transmitted accelerations at crest (A11), a) 1-250Hz 15kN 30s, b) 1-250Hz 27kN 30s. 270

Figure 6.18. Comparison of the transmitted accelerations at crest (A11) under 1-250Hz 27kN 120s. 271

Figure 6.19. Comparison of Response Spectra from slope (A3), a) 1-100Hz 15kN 30s, b) 1-100Hz 27kN 30s, c) 1-250Hz 15kN 30s, d) 1-250Hz 27kN 30s, e) 1-250Hz 27kN 120s. 273

Figure 6.20. Comparison of Response Spectra from crest (A11), a) 1-100Hz 15kN 30s, b) 1-100Hz 27kN 30s, c) 1-250Hz 15kN 30s, d) 1-250Hz 27kN 30s, e) 1-250Hz 27kN 120s. 275

Figure 6.21. Comparison of Horizontal Displacement Responses from slope (D2), a) 1-100Hz 15kN 30s, b) 1-100Hz 27kN 30s, c) 1-250Hz 15kN 30s, d) 1-250Hz 27kN 30s, e) 1-250Hz 27kN 120s. 277

Figure 6.22. Comparison of Vertical Displacement Responses from crest (D4), a) 1-100Hz 15kN 30s, b) 1-100Hz 27kN 30s, c) 1-250Hz 15kN 30s, d) 1-250Hz 27kN 30s, e) 1-250Hz 27kN 120s. 278

Figure 6.23. Comparison of the transmitted accelerations at slope (A3), a) 1-100Hz 15kN 30s, b) 1-100Hz 27kN 30s. 280

Figure 6.24. Comparison of the transmitted accelerations at slope (A3), a) 1-250Hz 15kN 30s, b) 1-250Hz 27kN 30s. 281

Figure 6.25. Comparison of the transmitted accelerations at slope (A3) under 1-250Hz 27kN 120s. 282

Figure 6.26. Comparison of the transmitted accelerations at crest (A11), a) 1-100Hz 15kN 30s, b) 1-100Hz 27kN 30s. 283

Figure 6.27. Comparison of the transmitted accelerations at crest (A11), a) 1-250Hz 15kN 30s, b) 1-250Hz 27kN 30s. 284

Figure 6.28. Comparison of the transmitted accelerations at crest (A11) under 1-250Hz 27kN 120s. 285

Figure 6.29. Comparison of Response Spectra at slope (A3), a) 1-100Hz 15kN 30s, b) 1-100Hz 27kN 30s, c) 1-250Hz 15kN 30s, d) 1-250Hz 27kN 30s, e) 1-250Hz 27kN 120s. 286

Figure 6.30. Comparison of Response Spectra at crest (A11), a) 1-100Hz 15kN 30s, b) 1-100Hz 27kN 30s, c) 1-250Hz 15kN 30s, d) 1-250Hz 27kN 30s, e) 1-250Hz 27kN 120s. 288

Figure 6.31. Comparison of Horizontal Displacement Responses at slope (D2), a) 1-100Hz 15kN 30s, b) 1-100Hz 27kN 30s, c) 1-250Hz 15kN 30s, d) 1-250Hz 27kN 30s, e) 1-250Hz 27kN 120s. 290

Figure 6.32. Comparison of Vertical Displacement Responses at crest (D4), a) 1-100Hz 15kN 30s, b) 1-100Hz 27kN 30s, c) 1-250Hz 15kN 30s, d) 1-250Hz 27kN 30s, e) 1-250Hz 27kN 120s. 291

Figure 6.33. Normalized accelerations for URE, GRE and EGE at crest (A11) for all dynamic motions..... 293

Figure 6.34. Horizontal Normalized Displacements at Crest (D3) for URE, GRE and EGE for all dynamic motions. 294

Figure 6.35. Normalized Settlements at crest (D4) for URE, GRE and EGE for all dynamic motions..... 295

LIST OF TABLES

Table 2.1. The coefficients used in Pseudostatic Equilibrium Method Analysis (Abramson, 2002). 11

Table 3.1. Geogrid material requirements in FHWA NHI-07-092. 30

Table 3.2. Requirements of EPS and XPS geofoams (ASTM D6817). 31

Table 4.1. Properties of geotextile reinforcements (Bergado et. al., 2002). 47

Table 4.2. Shear wave velocities for different force levels. 60

Table 4.3. Literature summary of the studies with Mobile Seismic Shakers. 83

Table 4.4. Experimental program (Toksoy, 2014). 94

Table 5.1. Calculated Elastic Modulus Values for different boreholes and depths (Rumeli Zemin, 2019). 116

Table 5.2. Net Limit Pressures from Experiments (Rumeli Zemin, 2019). 117

Table 5.3. Coordinates of Microtremor Measurements. 120

Table 5.4. Site characteristics for M-1 location. 120

Table 5.5. Site characteristics for M-2 location. 121

Table 5.6. Site characteristics for M-3 location. 122

Table 5.7. Site Classification according to NEHRP (1994). 129

Table 5.8. Site Classification according to Turkish Earthquake Code (2018). 129

Table 5.9. Details of field vibration tests. 136

Table 5.10. Subbase Classifications of 2013 KGM Technical Regulation. 142

Table 5.11. Base Layer Classifications of 2013 KGM Technical Regulation. 142

Table 5.12. Subgrade Classifications of 1999 AASHTO. 143

Table 5.13. Geogrid material requirements of FHWA NHI-07-092. 147

Table 5.14. Engineering parameters of EPS geofoam blocks in NCHRP (2004). 148

Table 5.15. The effect of temperature and stress on expected strains for 20kg/m3 density EPS geofoam NCHRP (2004)..... 148

Table 5.16. Embankment Location Coordinates. 169

Table 5.17. Vs30 Variation under Embankments. 169

Table 5.18. Inverted Resistivity to Vs30 Conversion. 170

Table 5.19. Input motions to be applied by MSS for the full scale experiments. 171

Table 5.20. Adopted Scaling Laws (Iai and Sugano, 1999). 206

Table 5.21. Input motions for the shaking table experiments. 209

Table 7.1. Summary of the performed experimental studies. 297

LIST OF SYMBOLS / ABBREVIATIONS

a	Acceleration
A	Accelerometer
AF	Amplification factor
a_{max}	Maximum horizontal acceleration
ASTM	American society for testing and materials
a_y	Yielding acceleration
CA	California
C_c	Coefficient of curvature
C_u	Coefficient of uniformity
D	Displacement sensor
Dr	Relative density
EGE	EPS geofoam embankment
EPS	Expanded polystyrene
f	Frequency
F_h	Horizontal pseudostatic force
FOS	Factor of safety
ft	Feet
g	Acceleration of gravity
GCL	Geosynthetic clay liner
GRE	Geosynthetic reinforced embankment
Hz	Hertz
k_h	Seismic coefficient
M	Magnitude
m	Total mass of the sliding mass
MSE	Mechanically stabilized earth
MSS	Mobile seismic shaker
M_w	Moment magnitude
PGA	Peak ground acceleration
PIV	Particle image velocimetry

SA	Spectral acceleration
SP	Poorly graded sand
T	Natural period of vibration
TDA	Tire derived aggregate
T_{ult}	Ultimate tensile strength
URE	Unreinforced embankment
USCS	Unified soil classification system
W	Total weight of the sliding mass

1. INTRODUCTION

1.1. Problem Statement

Earthquakes are among the most devastating natural disasters due to the primary and subsequent secondary effects they cause. Highways are crucial lifelines that must remain operational even in the aftermath of such events to ensure required safety and emergency services. However, highway embankments can experience various types of damages during earthquakes including settlement and differential settlement, cracking, slope failure, liquefaction and bearing capacity failure of the underlying soil. To mitigate earthquake-induced damages to highway embankments, improvement methods can be employed such as using geosynthetics and lightweight materials like EPS geofoam.

Reduced scale shaking table testing is an efficient way to determine the seismic performance but due to the assumptions and limitations in the nature of the laboratory testing, full-scale testing is a superior technique. Thus, it is important to study with full-scale highway embankments, assess their seismic performance in field conditions and to differentiate the effect of reinforcement techniqes without any limitations.

1.2. Objective of the Study

The objective of this thesis is to evaluate the seismic performance of highway embankments and to assess the impact of improvement techniques on dynamic performance of embankments in the field through a series of full-scale seismic performance tests using a mobile seismic shaker. In addition, a series of the reduced-scale shaking table experiments was performed. The proposed improvement techniques are the use of geogrid reinforcement and EPS geofoam inclusions on highway embankments. Experimental studies cover the determination of local site conditions and wave propagation properties of the proposed test area through geophysical and geotechnical experiments (MASW tests, ERT tests, microtremour

tests, pressuremeter tests, SASW tests), construction of full-scale unreinforced, geogrid reinforced and EPS geofoam embankments. Laboratory tests cover 1/10 scaled shaking table tests of the highway embankment models. This thesis aims to be the first study in literature to determine the dynamic performance of embankment models with different improvement techniques in field conditions and to assess the impact of improvement techniques.

1.3. Organization of the Thesis

This experimental study presents the details of full-scale seismic performance tests on field and reduced scale shaking table experiments to assess the improvement techniques by using geogrid reinforcement and EPS Geofoam fill on the dynamic performance of highway embankments Second chapter of the thesis gives detailed information about the stabilty of slopes and embankments. Static and dynamic properties of geosynthetics are presented in the third chapter and followed by the detailed literature review in the forth chapter. Fifth chapter consists of the experimental studies including the geotechnical and geophysical experiments, full-scale seismic performance tests on Unreinforced, Geogrid Reinforced and EPS Geofoam highway embankment models and 1/10 scaled shaking table tests of the same embankment models. In the sixth chapter, obtained experimental results from full-scale field tests and reduced scale shaking table tests are discussed in detail and followed by the conclusions part.

2. THE STABILITY OF SLOPES AND EMBANKMENTS

Failure of slopes, embankments, landslides etc., can be attributed to various many different factors and often considered as very complex. The main reasons behind a slope failure is internal and external stability problems. Earthquakes also have an underestimated role on the instability problems of such structures.

2.1. Main Reasons of Slope Failures

Slope stability analysis aims to ensure that the forces acting on a slope are balanced. When the shear strength of soil exceeds the shear stresses, a slope or embankment will remain stable. However, various external factors can disrupt this equilibrium, causing a decrease or increase in shear strength, which can directly impact slope stability. Following reasons are the common causes of the failure of slopes and embankments due to decreasing shear strength (Duncan, 2005):

- Increase of Pore Pressure
- Cracking
- Swelling
- Development of Slickensides
- The disintegration of rock fills
- Creep
- Leaching
- Strain Softening
- Weathering
- Cyclic Loading

2.2. Common Earthquake Effects and Case Studies

The term earthquake refers to the vibration or tremor of the earth caused by the abrupt discharge of stored energy in faults. This energy is released in all directions and travels as seismic waves, which can result in significant damage due to their impact on soil layers. The effects of earthquakes are explained in the following sections.

2.2.1. Surface Rupture

Surface rupture refers to the phenomenon where movement along fault lines causes it to break and leave surface trace. It should be noted that ground surface rupture is not common, especially for lower magnitudes, earthquakes that take place at subduction zones, and earthquakes that occur on blind faults. Conversely, large earthquakes typically lead to surface rupture, particularly on strike-slip faults. The movement that occurs between the two sides of a fault is explained as fault displacement. This movement can span several meters in distance. When a fault experiences surface rupture, it is anticipated that engineering structures, particularly highway or railway embankments, will probably get considerable damage.

Catastrophic earthquakes (Mw:7.7 and Mw:7.6) occured February 2023 in Kahramanmaraş region of Turkey caused many examples of surface rupture damages on highway and railway embankments and roads. Figure 2.1 shows resultant fault displacement on a railway in Pazarcık, Kahramanmaraş.



Figure 2.1. Fault displacement damage in Pazarcık, Kahramanmaraş (ITU, 2023).

Figure 2.2 represents the road damage due to the fault displacement (340cm) in Türkoğlu, Kahramanmaraş.



Figure 2.2. Fault displacement damage up to 340cm on a road in Türkoğlu, Kahramanmaraş (ITU, 2023).

Figure 2.3 shows the fault displacement damage up to 430cm on a road in Göksun, Kahramanmaraş.



Figure 2.3. Fault displacement damage up to 430cm on a road in Göksun, Kahramanmaraş (ITU, 2023).

2.2.2. Liquefaction and Lateral Spreading

Liquefaction occurs when the soil undergoes a liquefied state due to the upward flow of water as a result of the rapid shaking of earth, which makes an increase in pore water pressures. There are certain critera of site conditions and soil types for the liquefaction to develop. The ideal site conditions for a destructive earthquake or fault rupture zone are those that are located near the epicenter. These sites typically have soil types that are prone to liquefaction, such as loose or very loose sand soils with uniform gradation and round particles. Additionally, it is important that there is no cementation between the soil particles and no previous seismic activity in the area.

Lateral spreading is characterized by incrimental displacements during seismic events where the driving forces exceed the strength of the soil but not the resisting forces. Lateral spreading is responsible to large displacements and usually observed around river, sea or lake sides (Kramer, 1996). The lateral spreading related damages due to the destructive earthquakes of Mw:7.7 and Mw:7.6 Kahramanmaraş Earthquakes given in Figure 2.4 and 2.5.



Figure 2.4. Lateral spreading damage at Dörtyol, Hatay (METU/EERC Report, 2023).



Figure 2.5. Lateral spreading damage at İskenderun, Hatay (METU/EERC Report, 2023).

The 2024 Noto Earthquake (Mw: 7.5) in Japan caused many lateral spreading related damage to highway embankments as shown in Figure 2.6 and Figure 2.7.



Figure 2.6. Road damage after Jan 2, 2024 Noto, Ishikawa, Japan Earthquake (https://edition.cnn.com/2024/01/02/asia/japan-earthquake-tsunami-warnings-tuesday-intl-hnk/index.html).



Figure 2.7. Road damage after Jan 2, 2024 Noto, Ishikawa, Japan Earthquake (https://www.theguardian.com/world/2024/jan/03/japan-earthquake-death-toll-emergency-warnings-landslide-aftershock-ishikawa).

2.3. Seismic Analysis

Major earthquakes usually produce seismic waves that have the potential to cause destructive forces for slopes and embankments. Strong ground motions resulting from such earthquakes can lead to instability issues. Seismic waves can affect the shear strength of embankments and slopes, including the changes in pore water pressure that lead to an overall decrease in slope stability. Moreover, seismic activity can induce cyclic loads that result in elevated pore water pressure. This, in turn, can trigger a change in the physical state of loose, unsolidified, and water-saturated materials such as sand and silt, causing them to liquefy. As a consequence, shear strength is effectively reduced to zero.

The most common approaches to evaluate the stability of slopes under dynamic loads are given as follows (Abramson, 2002):

- Pseudostatic Method
- Newmark's Displacement Method
- Post-Earthquake Stability (Weakening Slope Stability)
- Dynamic Finite Element Analysis

2.3.1. Pseudostatic Method

Seismic events can generate harmful forces in slopes, which can lead to their collapse. To ensure stability of slopes and embankments in the long term, it is crucial to conduct seismic analysis. The pseudostatic method is the most commonly used and straightforward approach for assessing the dynamic stability of slopes. This approach involves treating the inertial forces generated by seismic events as a static horizontal and vertical force in limit equilibrium analysis.

The Pseudostatic Method involves incorporating the earthquake forces into a limit equilibrium analysis by adding static vertical and horizontal forces. This method is widely used

and easily comprehensible and applicable. Rather than considering the cyclic nature of ground motions, dynamic loads are taken as static force.

$$F_h = m.a = Wa/g = Wa_{max}/g = kh.W \quad (2.1)$$

where; F_h is the horizontal pseudostatic force acting through the center of the sliding mass, **M** is total mass of the sliding mass, **W** is total weight of the sliding mass, **g** is acceleration of gravity, **A** is acceleration, a_{max} is maximum horizontal acceleration and k_h is seismic coefficient, respectively.

Earthquake induced motions are assumed to affect horizontally on the slope (Figure 2.8).

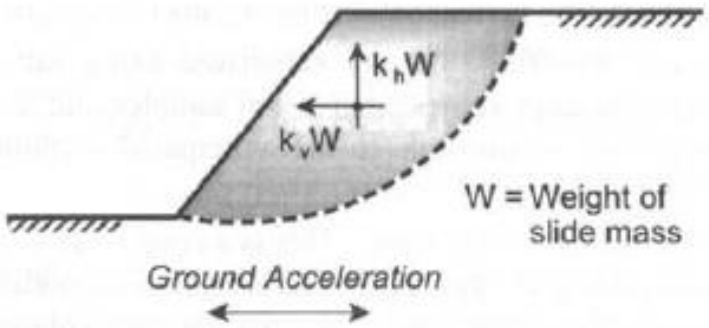

Figure 2.8. Pseudostatic Equilibrium Method Analysis (Abramson, 2002).

The seismic coefficients depend on earthquake intensity, duration of the event and the frequency content of the record and affect the desired Factor of Safety (FOS) values. A range of used seismic coefficients in this method is given in Table 2.1.

Table 2.1. The coefficients used in Pseudostatic Equilibrium Method Analysis (Abramson, 2002).

Seismic Coefficient	Remarks
0.10	Major earthquake, FOS > 1.0 (Corps of Engineers, 1982)
0.15	Great earthquake, FOS > 1.0 (Corps of Engineers, 1982)
0.15–0.25	Japan, FOS > 1.0
0.05–0.15	State of California
0.15	Seed (1979), with FOS > 1.15 and a 20 percent strength reduction
$\frac{1}{3}$–$\frac{1}{2}$ PGA[a]	Marcuson and Franklin (1983), FOS > 1.0
$\frac{1}{2}$ PGA	Hynes-Griffin and Franklin (1984), FOS > 1.0 and a 20 percent strength reduction

2.3.2. Newmark's Displacement Method

It is considered to be an improved version of the pseudostatic method and was proposed by Newmark in 1965. This method is based on comparing the yield accelerations and an acceleration-time history of the slope of interest in order to calculate displacements which indicate the movement of the sliding mass (Figure 2.9).

This approach considers that slopes experience deformation when factor of safety (FOS) falls below one. Moreover, Newmark's method relies on the presence of a well-defined slip surface. It considers the sliding material as plastic and assumes that the reduction in shear strength during seismic shaking is insignificant.

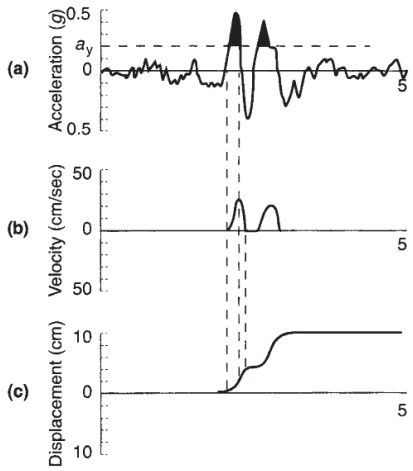

Figure 2.9. Example diagram of Newmark's Method (Day, 2002).

Four key parameters in this method influence the displacement of the slopes. These are yielding acceleration (a_y), PGA (a_{max}), duration and number of pulses. (Day, 2002). The general equation is:

$$\log d = 0.90 + \log \left[\left(1 - \frac{a_y}{a_{max}} \right)^{2.53} \cdot \left(\frac{a_y}{a_{max}} \right)^{-1.09} \right] \qquad (2.2)$$

2.3.3. Weakening Slope Stability Analysis

This approach is usually preffered when the earthquake movements cause a significant reduction in terms of shear strength. Examples of such materials and scenarios are provided below. (Day, 2002):

- Clays that have low resistance to seismic activity and can easily lose their strength
- Soft clays that are prone to slow plastic deformation and earth flows

- Loose soils below the groundwater level which can liquefy, flow slide, and lateral spread.

2.3.4. Finite Element Method

Clough and Woodward (1967) introduced a numerical technique to geotechnical engineering. Over time, this technique has become widely used, particularly for analyzing intricate earth structures. This method easily overcomes the inherent limitations found in limit equilibrium analysis (Abramson 2002).

Finite Element Method is a technique that divides a continuous soil medium into smaller, discrete elements known as finite elements. These elements are linked together at specific points called nodes, as illustrated in Figure 2.10. The method relies on fundamental physical principles and numerical techniques to obtain the necessary solutions, which are then computed using a computer.

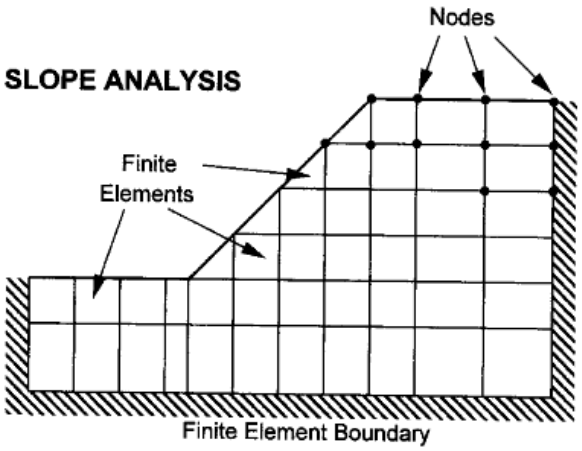

Figure 2.10. Illustration of FEM for slope analysis (Abramson, 2002).

2.4. Embankment Failure Modes

Static and dynamic stability are critical aspects of engineering structures including embankments, ensuring safety and structural integrity under different conditions. Static conditions are related to the embankment's ability to withstand constant loads such as its own weight, additional structures, and permanent forces like water pressure. It is influenced by material properties, geometry and water conditions. However, dynamic conditions deals with the embankment's response to transient, time-varying loads such as earthquakes, traffic vibrations, or other dynamic forces. Dynamic stability of embankments are influenced by the characteristics of the dynamic motion (frequency content, duration), dynamic soil parameters, use of geosynthetics and lightweight materials.

Major earthquakes have had a significant impact on road and highway embankments, causing substantial damage in near history. While earth structures are generally easier to repair compared to structures made of concrete or similar materials, it is crucial to limit the extent of damage within acceptable limits. Latest research and recent advances in geotechnical earthquake engineering suggest that geogrid reinforcement and the use of light-weight EPS geofoam blocks in highway embankments can successfully and effectively increase the seismic performance of highway embankments by limiting the extent of damage and preventing the failure. There are five primary failure modes associated with embankments.

2.4.1. Shallow Surface Sliding

This is the most commonly observed failure mode in embankments and it is typically triggered by dynamic loads including seismicity, water or additional load conditions. This phenomenon is illustrated in Figure 2.11.

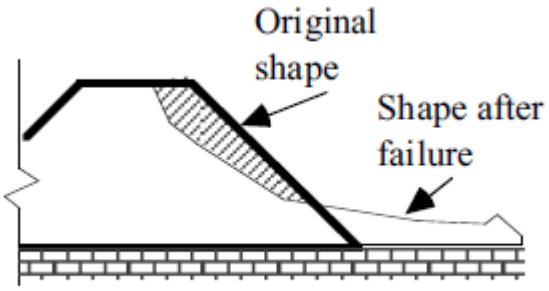

Figure 2.11. Shallow surface sliding (Towhata, 2008).

As shown in Figure 2.12, a road embankment experienced a sliding failure under the 2004 Niigata-Chuetsu Earthquake. This displacement was so severe that it caused the destruction of the buried pipelines within the embankment structure. A similar example to shallow surface sliding in embankments is represented in Figure 2.13.



Figure 2.12. A sliding failure case of a road embankment (Towhata, 2008).



Figure 2.13. A sliding failure case (Towhata, 2008).

2.4.2. Slip Surface Development within the Body of Embankment

This phenomenon is quite similar to sliding. However, in this type of failures a deeper slip plane generates and causes more damage. Slip surface development is illustrated in Figure 2.14.

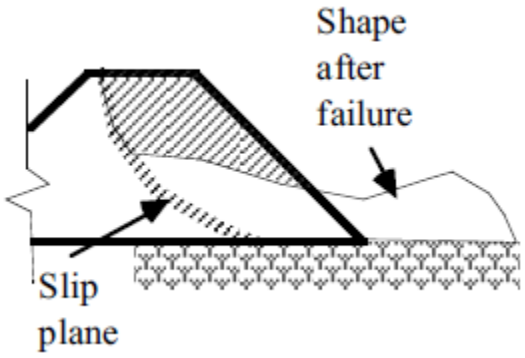

Figure 2.14. Slip surface development (Towhata, 2008).

Slip surface development within the body of the embankment may cause serious damage. A case study of an heavily damaged residential area after the failure of an embankment fill due to slip surface development is illustrated in Figure 2.15. The embankment fill was not

supported by the peat level during the earthquake, causing it to collapse. Figure 2.16. shows the residential area that was situated on the failed embankment.

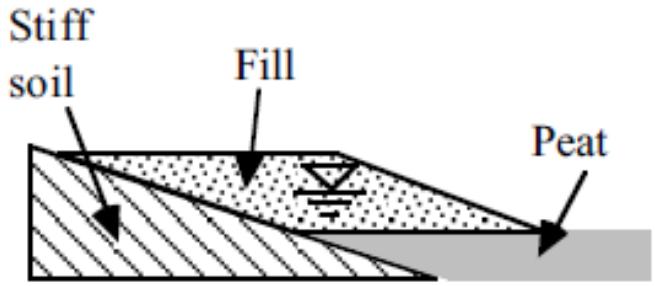

Figure 2.15 Illustration of the failed embankment due to slip surface development (Towhata, 2008).



Figure 2.16. Damaged residential area due to the failure of the embankment subject to slip surface development (Towhata, 2008).

The 2024 Noto Earthquake (Mw: 7.5) in Japan damaged many highway embankments in the region due to the earthquake-induced slip surface development within the body of the embankment. Case studies related to this type of damage are shown in Figure 2.17 and Figure 2.18.



Figure 2.17. Road damage in Nanao after Jan 2, 2024 Noto, Ishikawa, Japan Earthquake (https://www3.nhk.or.jp/nhkworld/en/news/backstories/2935/).



Figure 2.18. Road damage in Kanazawa after Jan 2, 2024 Noto, Ishikawa, Japan Earthquake (https://www3.nhk.or.jp/nhkworld/en/news/backstories/2938/).

2.4.3. Development of Slip Surface within the Soft Foundation Soil

This kind of failures occur in case the slip surface within the embankment body reaches weak soil due to a combination of change in groundwater levels and seismic loading (Figure

2.19). This phenomenon was observed in the 2007 Sumatra Earthquake and the 1998 Adana Earthquake. In Figure 2.20, the failure of river bank on the failed embankment in Adana is given, while Figure 2.21 shows the Sumatra neighbourhood case.

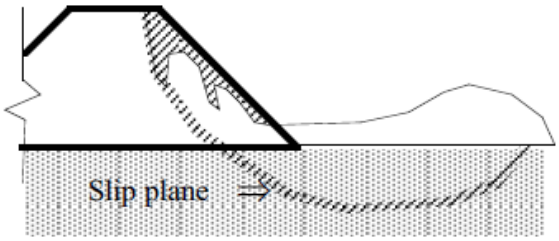

Figure 2.19. Development of the slip surface within embankment body within soft foundation soil (Towhata, 2008).

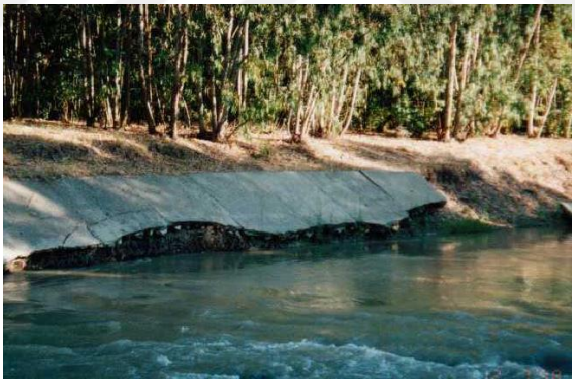

Figure 2.20. A failed embankment causing collapse of a river bank (Towhata, 2008).



Figure 2.21. A failed embankment causing the collapse of houses in Sumatra (Towhata, 2008).

2.4.4. Liquefaction Damage on Embankments

In general, embankments experience damage when the soft soil deposits beneath them liquefy and spread laterally during major earthquakes. This type of failure has the potential to cause significant damage. Liquefaction damage is shown in Figure 2.22.

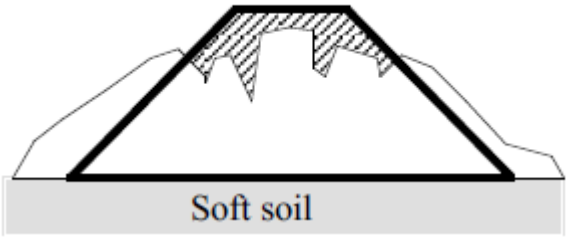

Figure 2.22. The liquefaction damage (Towhata, 2008).

Earthquake induced liquefaction lead to slumping damage during the 1983 Nihonkai-Chubu Earthquake as a road embankment that was connecting to a bridge crossing the lake failed as given in Figure 2.23.



Figure 2.23. Road embankment with slumping damage (Towhata, 2008).

2.4.5. Settlement Damage on Embankments

Settlement damage can occur during earthquakes when subsidence is observed. This type of damage can affect roads and highway embankments, causing them to be temporarily out of operation due to the damage caused by the subsidence (Figure 2.24).

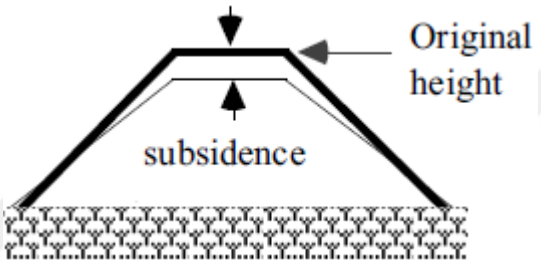

Figure 2.24. Settlement damage (Towhata, 2008).

Figure 2.25 represents a road embankment that experienced settlement damage and was situated in a subsidence zone, which is one of the various geotechnical issues that arose in the region after the 2004 Niigata-Chuetsu Earthquake.



Figure 2.25. Settlement damage of a road embankment (Towhata, 2008).

3. STATIC AND DYNAMIC PROPERTIES OF GEOSYNTHETICS

The destructive effects of earthquakes on engineering structures should be considered more seriously as many populated and well developed cities are located in highly seismic zones. Earthquake-induced strong ground motions have historically cost billions of dollars to global and local economies. To mitigate these hazards, seismic performance of engineering structures should be improved.

Highways are one of the crucial infrastructures that must remain operational at all times. To ensure the safety and integrity of highway embankments during earthquakes, it is essential to enhance their static and dynamic performance. Geosynthetics can be used to increase the tensile strength and durability of highway embankments, resulting in more stable and earthquake-resistant roads (Toksoy and Edincliler, 2024).

Geosynthetics are synthetic products made from polymeric materials that are used in conjunction with soil, rock, earth, or other geotechnical materials as an essential component of engineering projects, structures, or systems. (Koerner, 2005).

Geosynthetics have become increasingly popular worldwide in recent decades due to their numerous beneficial characteristics. (Shukla, 2016):

- corrosive-free
- high resistance to chemical and biological degradation
- durability up to 120 years
- high flexible
- low volume
- light-weight

- easy storage and transportation
- easy installment
- accelerates the construction processes
- makes environment-friendly solutions for less

Geosynthetics serve five key purposes, including separation, reinforcement, filtration, drainage, and containment. These functions are crucial in engineering projects, as they help to improve design and performance while reducing costs and time. Ultimately, the goal of using geosynthetics is to achieve better outcomes in a more efficient and cost-effective manner.

3.1. Material Properties of Geosynthetics and Geosynthetic-Soil Interactions

Geosynthetics are synthetic materials used in geotechnical engineering to enhance soil properties and to improve performance static and dynamic performance. These materials, which include geotextiles, geomembranes, geogrids, and geocells, are characterized by their high tensile strength, durability, and resistance to environmental degradation.

The most important physical properties of geosynthetics are unit weight, specific gravity, stiffness and thickness. However, there are a few more properties that are only important to geogrids and geonets. These are aperture size and shape, junction type, rib dimensions etc. (Shukla, 2016).

The material property of specific gravity is basicly the ratio of a geosynthetic material's unit weight to that of a pure 4°C water (Shukla, 2016). Unit weight is defined as the weight per unit area. For geosynthetics, mass per unit area is a good indicator of its strength parameters and cost. For most geosynthetics, the mass unit weight varies from 100g/m^2 to 1000g/m^2. The thickness of a geosynthetic material refers to the distance between its upper and lower surfaces. To measure this, a specialized instrument applies a predetermined compressible stress for a

duration of 5 seconds. Thickness is considered a fundamental characteristic that helps ensure the quality of various types of geosynthetics. On the other hand, the stiffness, also known as flexural rigidity, of a geosynthetic material describes its capacity to withstand bending or flexure caused by its own weight.

Geosynthetics possess various mechanical properties, such as their ability to compress, their tensile strength, their ability to withstand external forces, and their interaction with soil at the interface. (Shukla, 2016).

Compressibility in geosynthetics refers to how much the material's thickness decreases when subjected to increasing normal pressure. This characteristic is particularly significant for nonwoven geotextiles. The compression behavior of geosynthetics is shown in Figure 3.1.

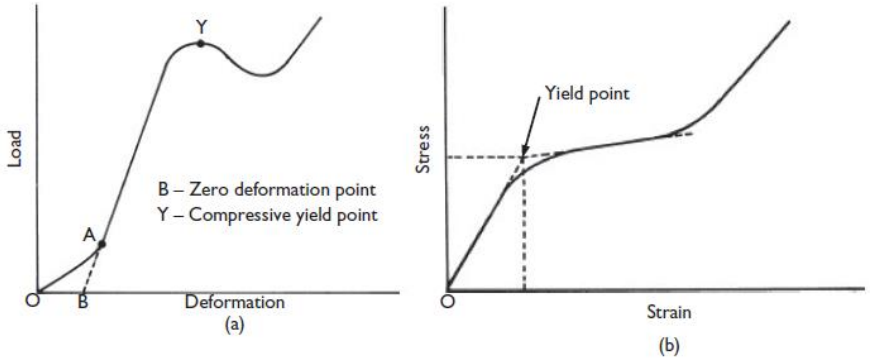

Figure 3.1. Compression behavior of geosynthetics (Shukla, 2016).

Tensile properties of geosynthetics include tensile strength and tensile modulus. Tensile strength of a geosynthetic refers to the highest level of resistance against deformation under an external force.Tensile properties are at utmost importance when the geosynthetic material is used in soil, embankment, slope and retaining wall etc. reinforcement. Wide-width strip tensile tests are performed to determine the tensile strength due to ASTM D4595-11 as shown in Figure 3.2. Strength properties of selected geosynthetics are provided in Figure 3.3.

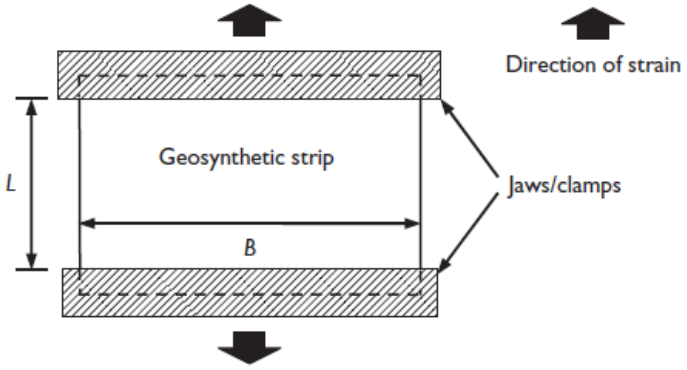

Figure 2.3 Wide-width strip tensile test. (Note $B = 200$ mm, $L = 100$ mm).

Figure 3.2. Wide-width strip tensile tests.

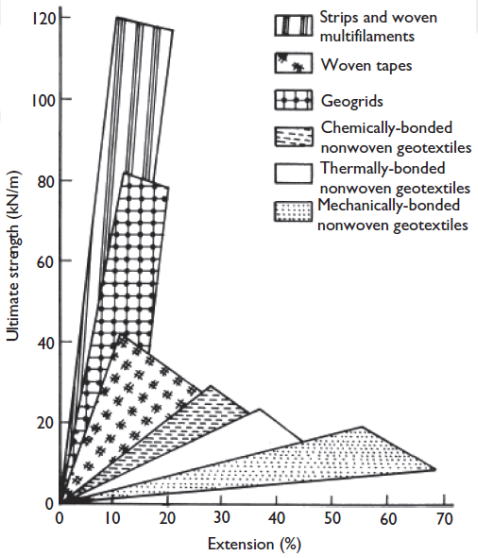

Figure 3.3. Typical Strength properties of Selected Geosynthetics (Shukla, 2016).

Survavibilty properties of geosynthetics include the tearing, puncture, bursting and fatigue strength and these mechanical properties are related to geosynthetics' survivability, constructability and seperation functions.

When geosynthetics are used in earth structures, it is essential to ensure that the connection of the soil and the geosynthetic material is strong enough for the prevention of the

soil from slipping over the geosynthetic layer or the geosynthetic from being pulled out of the soil when subjected to tensile forces. The bond strength between the geosynthetic and the soil is directly influenced by the interaction occurring at their contact surfaces. Thus, the performance of embankments, slopes, retaining walls or any other engineering structures where the geosynthetic reinforcement is used, is based on the soil-geosynthetic interface properties such as interface friction and interlocking characteristics. This mechanism is basically responsible to transfer related stresses from soil to geosynthetics. Soil-geosynthetic interface properties are determined by performing direct shear and pullout tests. In direct shear tests, the geosynthetic specimen and the soil is placed inside a direct shear box to determine the shear resistance in between (Figure 3.4). Obtained results are typically represented by comparing the shear stress and normal stress.

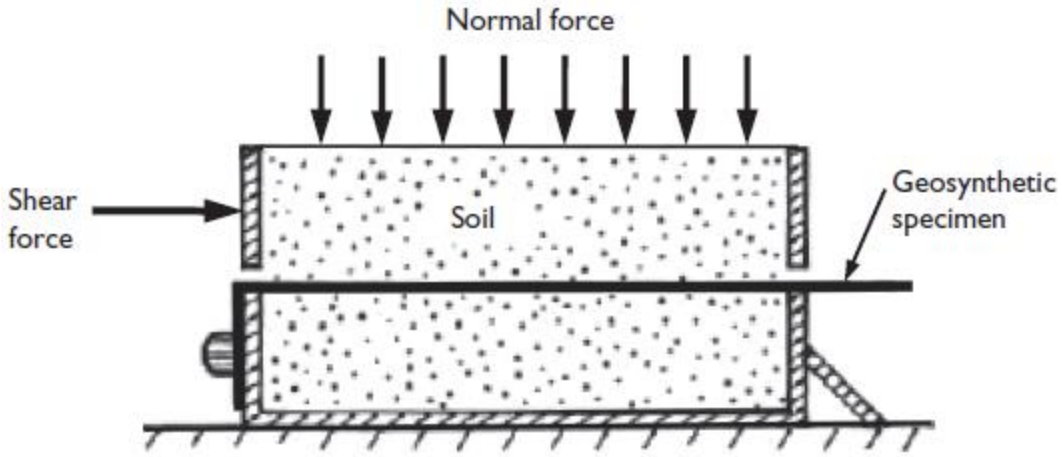

Figure 3.4. Illustration of direct shear test (Shukla, 2016).

Bathurst and Cai (1994) studied the stress-strain relationship of HDPE and PET geogrids under in-isolation monotonic load tests. Obtained results from the constant rate of loading showed that HDPE type of geogrids are more sensitive to the rate of loading than PET type geogrids (Figure 3.5).

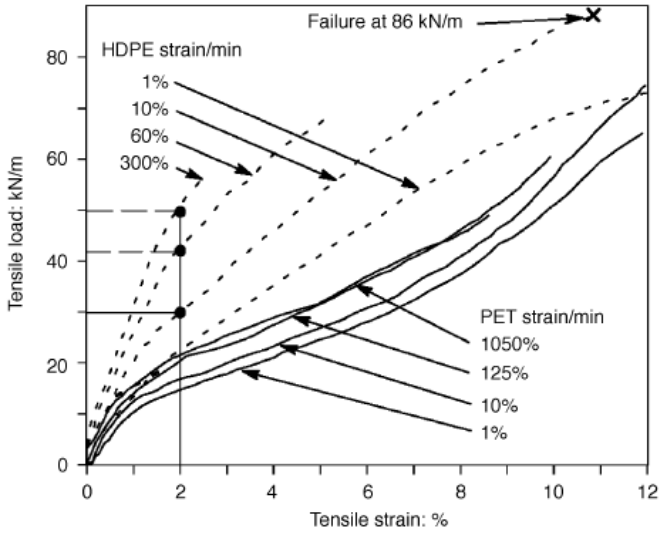

Figure 3.5. The effect of strain rate on monotonic tensile load-strain behavior (Bathurst and Cai, 1994).

In-isolation cyclic loading tests on typical geogrid samples to determine their dynamic material properties (Bathurst and Cai, 1994; Cai and Bathurst, 1995). Experimental results revealed that cyclic load-strain behavior of HDPE type geogrid exhibited non-linear hysteresis loops and a hyperbolic load-strain cap that is tangent to all loops (Figure 3.6).

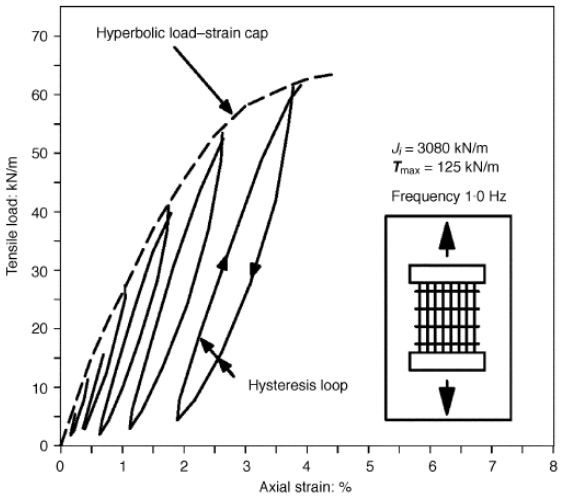

Figure 3.6. Dynamic material behavior of in-isolation HDPE type of geogrid (Cai and Bathurst, 1995).

Previous studies by Yogendrakumar et al. (1991) and Chalaturnyk et al. (1988) highlight that, at low strain levels, the hysteretic behavior of geosynthetics may be ignored. Instead, it may be assumed to be in a non-linear quadratic form (Figure 3.7).

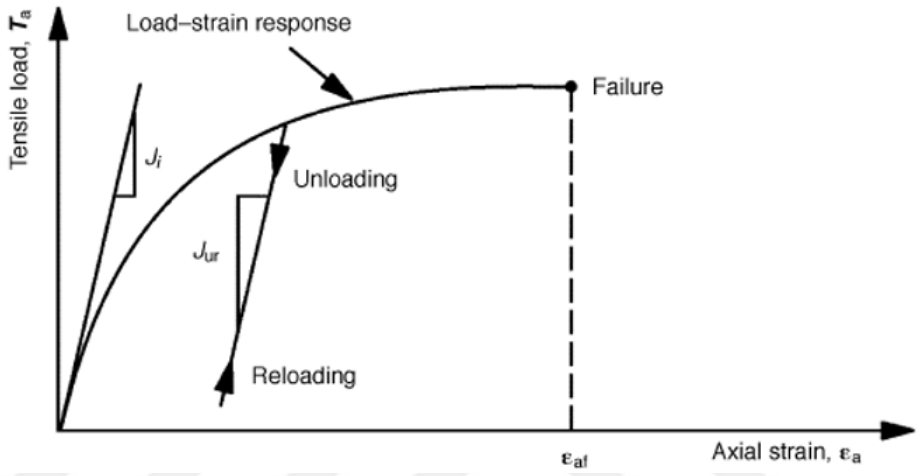

Figure 3.7. Low-strain non-hysteretic behavior of geosynthetics (after Yogendrakum et al., 1991).

As reported by Bathurst and Cai (1994), initial stiffness and the shape of load-strain cap is sensitive to the frequency of loading for HDPE type geogrids and insensitive to PET type geogrids as represented in Figure 3.8.

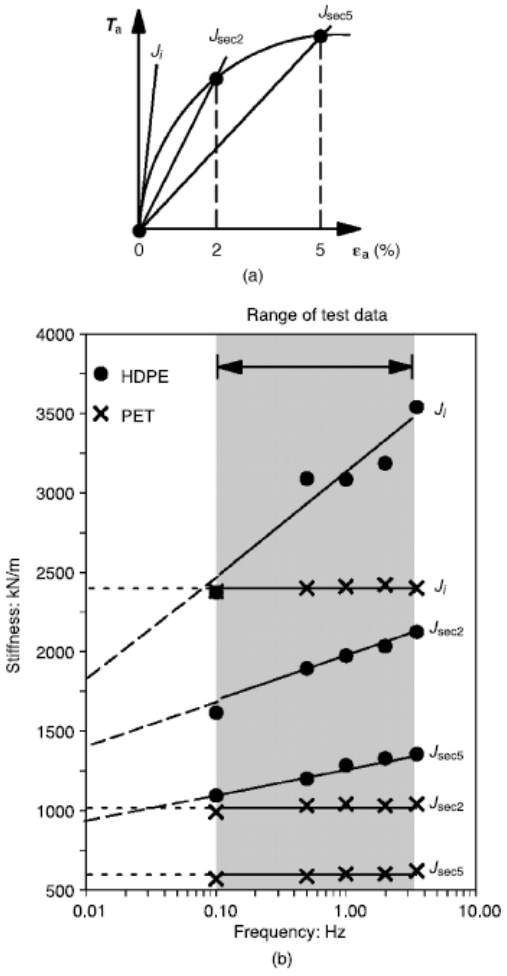

Figure 3.8. The influence of frequency on secant stiffness of HDPE and PET geogrids (Bathurst and Cai, 1994).

In addition, the proposed energy dissipation along structures and geosynthetic interfaces is directly linked to the dynamic interface shear properties of geosynthetic materials and geosynthetic reinforced soils. (Yegian et al.,1995, Kavazanjian et al.,1991, Yegian and Lahlaf, 1992).

Geogrid material properties should comply with FHWA NHI-07-092 as represented in Table 3.1.

Table 3.1. Geogrid material requirements in FHWA NHI-07-092.

Property	Test Method	Units	Requirement		
SURVIVABILITY			Geogrid Class		
			CLASS 1[4]	CLASS 2	CLASS 3
Ultimate Multi-Rib Tensile Strength	ASTM D 6637	lb/ft (kN/m)	1230 (18)	820 (12)	820 (12)
Junction Strength[5]	GSI GRI GG2	lb (N)	25[5] (110[5])	25 (110)	8 (35)
Ultraviolet Stability (Retained Strength)	ASTM D 4355	%	50% after 500 hours of exposure		
OPENING CHARACTERISTICS					
Aperture Size	Direct measure	in. (mm)	0.5 to 3 in. (12.5 to 75 mm) and Aperture Size ≥ D50 of aggregate above geogrid Aperture Size ≤ 2·D85 of aggregate above geogrid		
Separation	ASTM D 422	mm	D85 of aggregate above geogrid < 5·D85 subgrade Other wise use separation geotextile with geogrid		

As Given in Table 3.1, the ultimate tensile strength of the geogrids should be minimum 18kN/m. Aperture size is an important opening characteristics of geogrids and it is supposed to be in the range of 12.5mm to 75mm. In addition, the aperture size of the geogrid should be larger than the D50 of the aggregate and less than the 2.D85 of the aggregate above the geogrid.

3.2. Static and Dynamic Properties of EPS Geofoam

Geofoam refers to a type of cellular foam-polymeric material that is rigid and comes in block or planar form, commonly utilized in geotechnical engineering applications (ASTM D4439). In 1972, Norway first utilized Geofoam as a lightweight fill material. Geofoam is a material with a high void content and is commonly used for lightweight fills, thermal insulation, and drainage channels. This material is available in two forms: expanded polystyrene (EPS) and extruded polystyrene (XPS).Physical property requirements of EPS and XPS geofoams are given in Table 3.2.

Table 3.2. Requirements of EPS and XPS geofoams (ASTM D6817).

Type	EPS12	EPS15	EPS19	EPS22	EPS29	EPS39	EPS46	XPS20	XPS21	XPS26	XPS29	XPS36	XPS48
Density, min., kg/m^3 [lb/ft^3]	11.2 [0.70]	14.4 [0.90]	18.4 [1.15]	21.6 [1.35]	28.8 [1.80]	38.4 [2.40]	45.7 [2.85]	19.2 [1.20]	20.8 [1.30]	25.6 [1.60]	28.8 [1.80]	35.2 [2.20]	48.0 [3.00]
Compressive Resistance, min., kPa [psi] at 1 % strain	15 [2.2]	25 [3.6]	40 [5.8]	50 [7.3]	75 [10.9]	103 [15.0]	128 [18.6]	20 [2.9]	35 [5.1]	75 [10.9]	105 [15.2]	160 [23.2]	280 [40.6]
Flexural Strength, min., kPa [psi]	69 [10.0]	172 [25.0]	207 [30.0]	240 [35]	345 [50.0]	414 [60.0]	517 [75.0]	276 [40.0]	276 [40.0]	345 [50.0]	414 [60.0]	517 [75.0]	689 [100.0]
Oxygen Index, min., volume %	24.0	24.0	24.0	24.0	24.0	24.0	24.0	24.0	24.0	24.0	24.0	24.0	24.0

3.2.1. EPS Geofoam under Monotonic Loading

Literature suggests that Geofoam material is mechanically considered as elasto-viscoplastic material. Monotonic loading tests for geofoam specimens shall be performed in correlation with ASTM D1621. Malai and Youwai (2021) performed monotonic loading tests on EPS geofoam samples with a density of 20kN/m^2. Obtained stress-strain relationship consists of three zones (Figure 3.9).

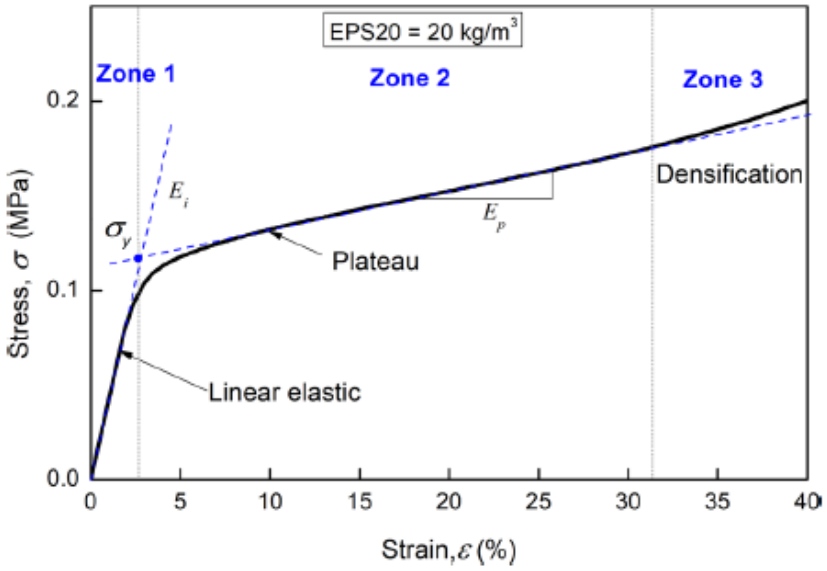

Figure 3.9. Stress-Strain relationship from monotonic loading tests on 20kN/m^2 EPS specimen (Malai and Youwai, 2021).

Geofoam material exhibits linear elastic behavior in Zone 1, which is a strain level between 1 and 2%. No deformation but buckling or bending of closed cell walls within geofoam specimen is expected. Material behavior evolves from elastic to plastic in Zone 2 where the closed cells start to deform, buckle and lose the air inside. Geofoam speciment start to densify in Zone 3 due the deformation of the internal structure and the change in shape under high strain levels. Volume of the specimen decreases as the air inside the closed cells are lost. Strain-stress relationships for different EPS geofoam densities under monotonic loading are represented in Figure 3.10.

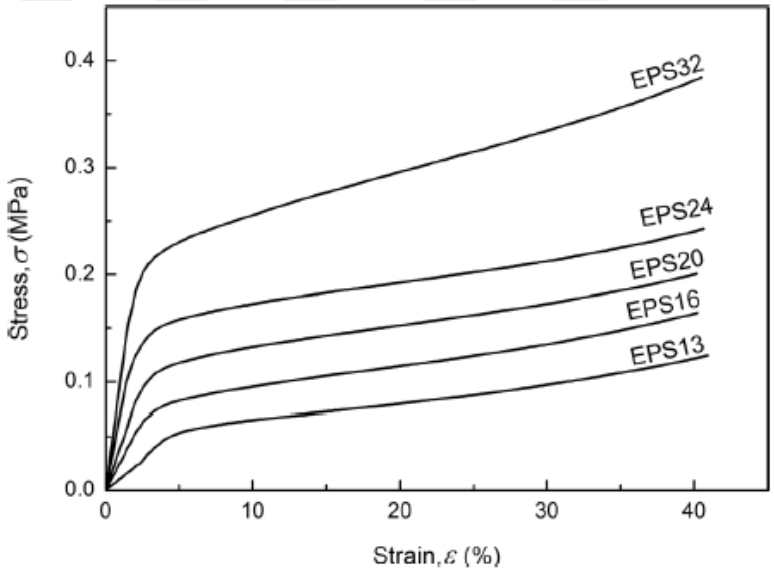

Figure 3.10. Stress-Strain relationship of EPS geofoams with different densities (Malai and Youwai, 2021).

As represented in Figure 3.10, initial elastic modulus of geofoam specimens increase with respect to the increased density. Elastic zone is in the strain range of 2 to 4% and beyond this yield strength point, EPS stiffness decreases almost linearly. Increasing EPS density leads to increased engineering properties. The effect of density on other strength properties of geofoams are represented in Figure 3.11.

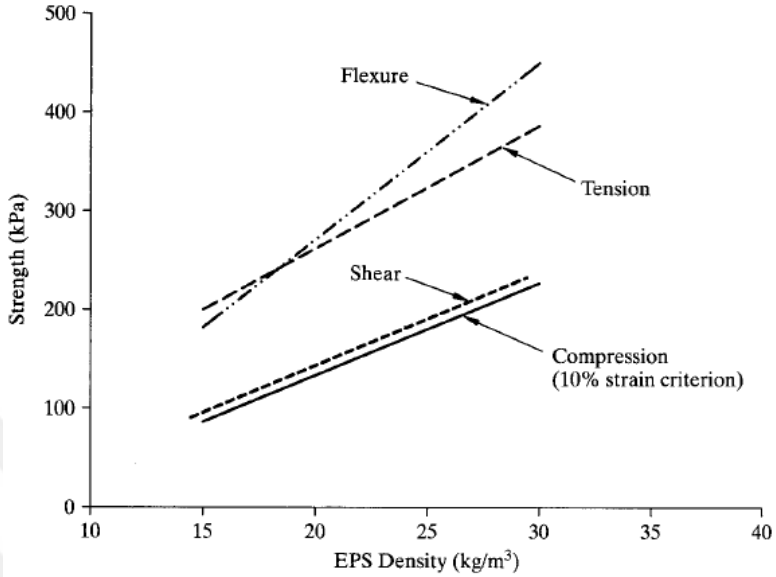

Figure 3.11. Effect of geofoam density on strength parameters (Koerner, 2005).

3.2.2. EPS Geofoam under Cyclic Loading

Athanasopoulos et. al. (1999) performed torsional resonant column and cyclic uniaxial tests to investigate the dynamic material properties of EPS geofoam. During the experiments, two EPS geofoam specimens with densities of 12.4 and 17.1 kg/m^3 were used. The resonant column tests were conducted on cylindrical specimens with 36mm dimameter and 80mm height. The resonant frequencies of geofoam specimens were found to be between 30 to 40Hz. Test results are represented in Figure 3.12.

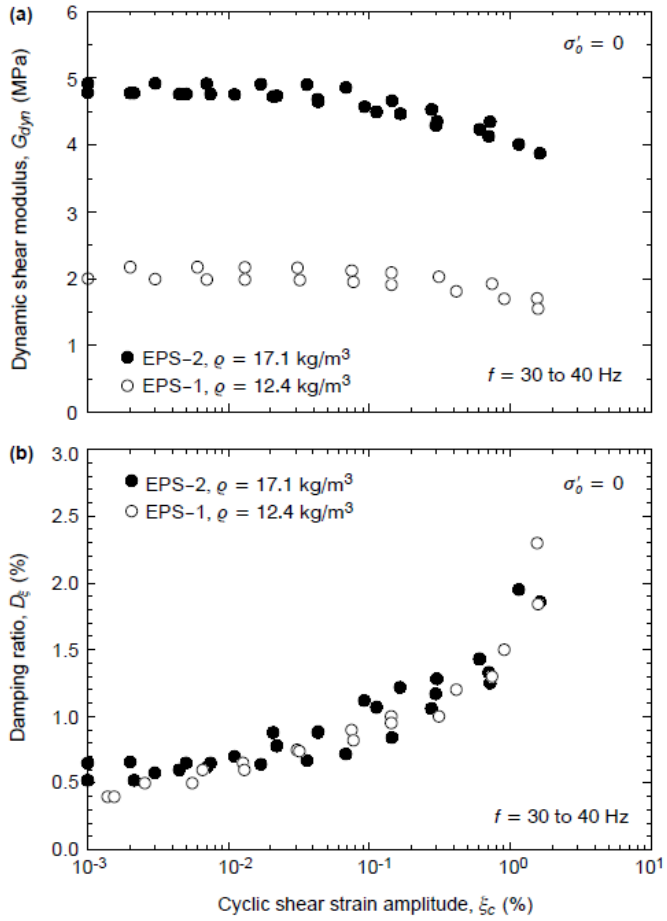

Figure 3.12. Obtained results for resonant column tests, a) G, b) D (Athanasopoulos et. al. (1999).

Obtained results reveal that linear material behavior is observed for strains up to 0.1% instead of the commonly pronounced 1% in the literature due to the fact that resonant column tests can accuretely measure low strain levels. In addition damping ratios were found to be very low for strains less than 1% with no significant difference between different geofoam specimens.

The cyclic uniaxial tests of geofoam specimens were performed using a cyclic triaxal test device using geofoam specimens with diameter of 36mm and height of 80mm. Tests were performed under zero confining pressure with applied axial deformations from 0.15 to 3mm and loading frequency from 0.01 to 2Hz. Loading cycles were restricted to 5 to 8 cycles. ASTM

D3999 procedures were followed during the experiments. As shown in Figure 3.13, dynamic modulus of elasticity didn't seem to be seriously influenced by the changes in frequency.

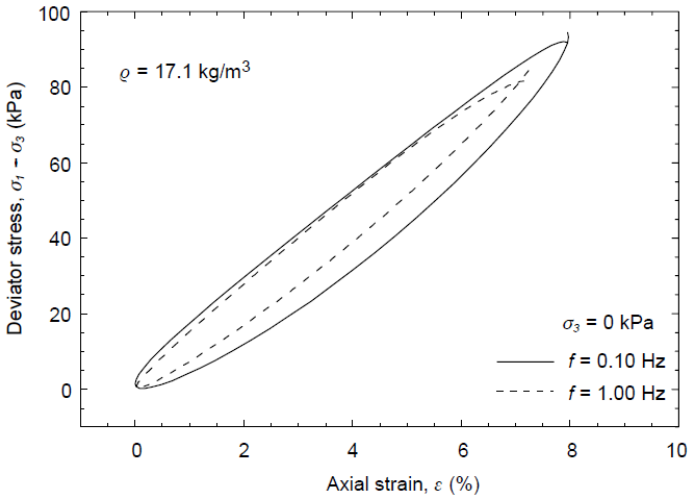

Figure 3.13. The effect of loading frequency on cyclic stress-strain relationship (Athanasopoulos et. al., 1999).

Figure 3.14 represents the modulus of elasticity (E) and damping ratio (D) variation of different EPS geofoam specimens for different loading frequencies with respect to cyclic axial strain.

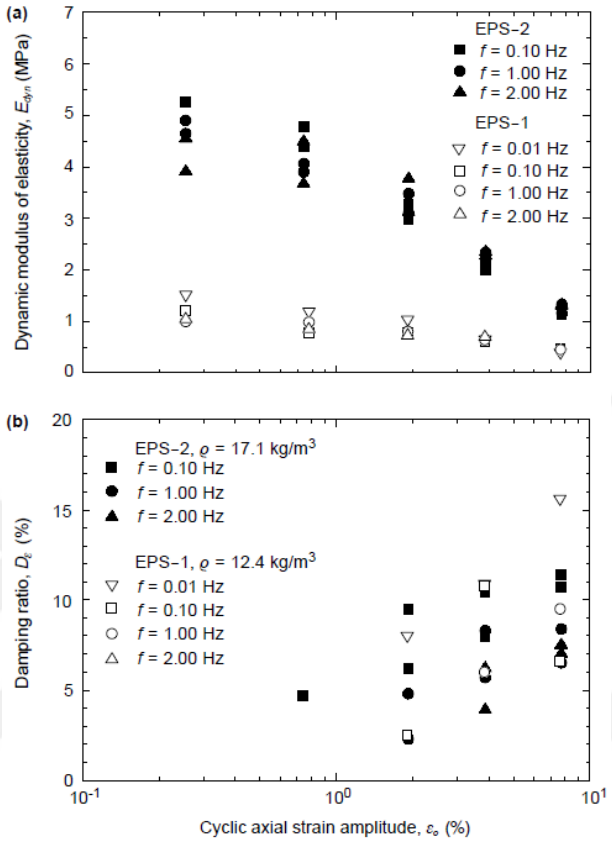

Figure 3.14. Cyclic uniaxial test results, a) Variation of (E), b) Variation of (D) with respect to cyclic axial strain amplitudes (Athanasopoulos et. al., 1999).

Test results reveal that linear dynamic behavior takes place for strain levels up to 0.1% and non-linear dynamic behavior becomes apparent for obtained strain levels higher than 1%. Damping ratios are as low as 1.5% for strain measurements up to 1%. However damping ratio increases with respect to increased strain levels and reaches to D=10% for 10% strain levels. This finding suggests that energy absorption properties of EPS geofoam become apparent for higher ranges of strain levels. Dissipation of low-strain vibrations in EPS geofoam is related to its low stiffness properties. EPS density affects the dynamic modulus but it doesn't affect the damping ratio.

Cyclic uniaxial tests under stress controlled conditions were performed by Trandafir et. al. (2010) in an attempt to investigate the dynamic material behavior of EPS geofoam. Three

EPS geofoam samples with 15 kg/m^3 (EPS 1), 25 kg/m^3 (EPS 1) and 32 kg/m^3 (EPS 3) of density were used. The EPS geofoam materials behave linear elastic for strain levels up to 1% under monotonic loading and the cylindrical specimens had a dimater of 50mm with 2:1 height to diameter ratio. Cyclic uniaxial tests were performed at 0.5Hz with up to 20 cycles for all specimens. Experimental results for EPS 1 and EPS 2 for different Static Stress Ratio (SSR) and Cyclic Deviator Stress Ratio (CDSR) values are represented in Figure 3.15.

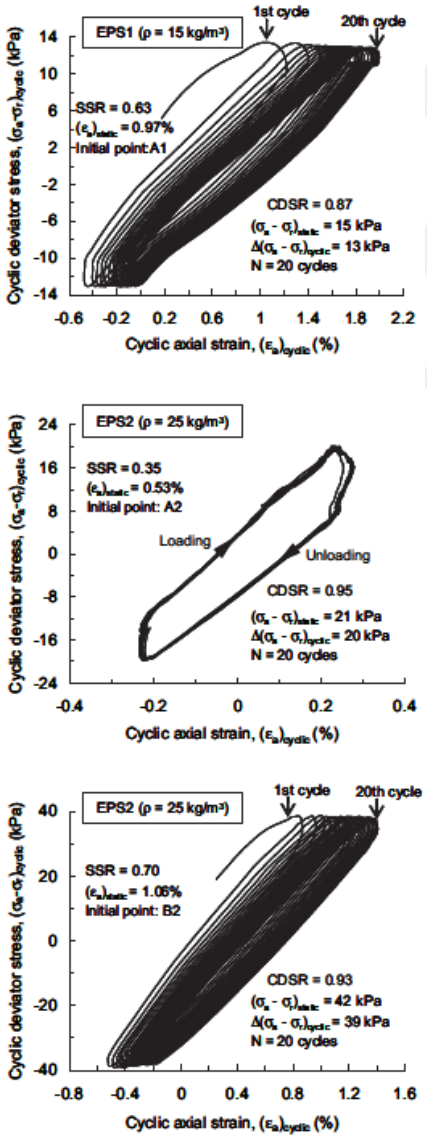

Figure 3.15. Results obtained from EPS 1 and EPS 2 (Trandafir et. al., 2010).

Given in Figure 3.15, EPS 1 and EPS 2 with SSR: 0.70 exhibits visco-elasto-plastic response and the EPS 2 with SSR: 0.35 represents non-linear viscoelastic material behavior. Obtained experimental results indicate that viscoelastic material behavior is observed on specimens for the cyclic axial strain amplitude ranges between 0.87 to 1%. Higher strain amplitude ranges are reported to be responsible of visco-elasto-plastic material behavior where permenant plastic strains may observed.

4. LITERATURE SURVEY

This section of the study covers compherensive and up to date literature review about slopes, embankments, roads and highways and their seismic performances. Firstly, experiments related with the use of Mobile Seismic Shakers (MSS) are given. Next, studies related with full scale pavements and highway embankments are reviewed and followed by the full scale railway embankments. Performed experiments with EPS geofoam embankments and embankments with tire derived aggregates are summarized later on.

4.1. Experimental Studies with Full Scale Highway Embankments and Pavements

To evalute the practical and financial viability of various reinforcement techniques for a planned road layout, Forsman et al. (2016) constructed a highway embankment with five different sections and each section was reinforced with a different reinforcement technique namely single layer of geotextile, two layer of geotextiles, geocell mattress, lightweight aggregate and EPS lightweight material. The length and width of each section was 30m and 23m, respectively (Figure 4.1). The construction process was performed over a peaty zone and in order to accelerate the consolidation process, test sections were surcharged. Highway embankment was instrumented with 98 settlement plate along the structure. Settlement plates were used to accurately measure the settlements in each test section, and high-resolution laser scanning was conducted to map the surface treatment layers of each section both before and after the surcharge. The conclusions of the study include that all the methods described can successfully be applied for the construction of highway embankments on peaty zones. Also no failure was observed in any section. The study revealed that using only one reinforcement layer during construction is simpler than using two, and there were no noticeable technical benefits to using two layers for the structure's static behavior. However, the installation of a geocell mattress was found to be very time-consuming, and there was no evidence to suggest that it was technically superior to using one or two reinforcements.



Figure 4.1. Test sections (Forsman et al., 2016).

In a full scale experiment by Chen et. al. (2015); the dynamic response of composite pavements under heavy traffic load was obtained. The objective of the paper is to comprehend how the mechanistic responses of pavement are impacted by the pressure of tire contact and the speed at which the vehicle is traveling.A four-lane highway in Hunan province of China was used for the field testing (Figure 4.2).

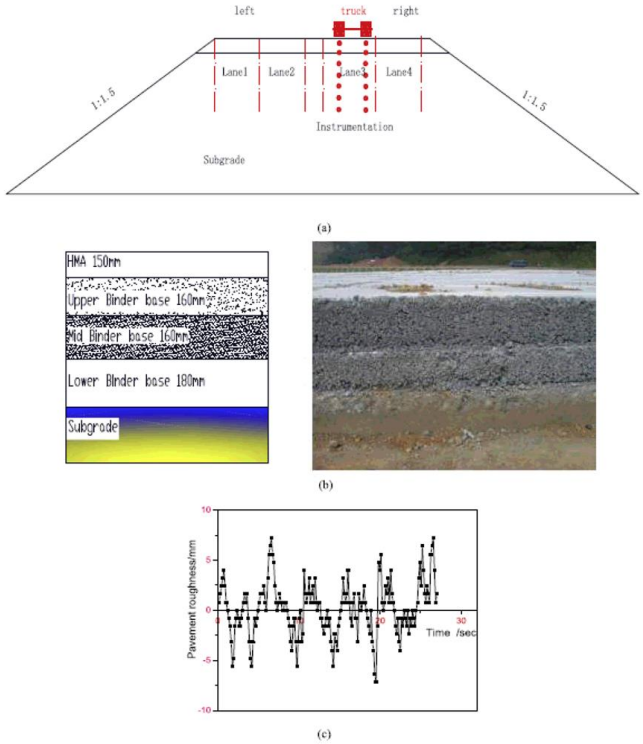

Figure 4.2. Field testing. (a) Cross section of pavement, (b) Pavement itself, (c) Roughness of pavement surface (Chen et. al., 2015).

The experiments conducted indicate that tire contact pressure has a positive impact on the dynamic strains and stress in composite pavement, as well as the dynamic soil stresses in the subgrade. Additionally, the study found that the speed of a truck and the pavement response are inversely proportional due to the viscoelastic property of the asphalt layer.

Field performance of sustainable aggregate by-products have been performed by Tutumluer et. al. (2019). The study constructed 16 test sections to evaluate the use of quarry by-products in base, subbase, and aggregate subgrade applications (Figure 4.3). The chemically stabilized test sections were stabilized with 3% cement or 10% fly ash by dry weight. Rutting and fatigue evaluations were performed on all test sections using a single wheel in accelerated pavement testing (Figure 4.4). The results showed that the proposed quarry by-products applications can be successfully implemented in standard pavement construction and rehabilitation practices as the resultant permenant deformations were obtained to be less than 5mm after 10000 wheel load cycles.

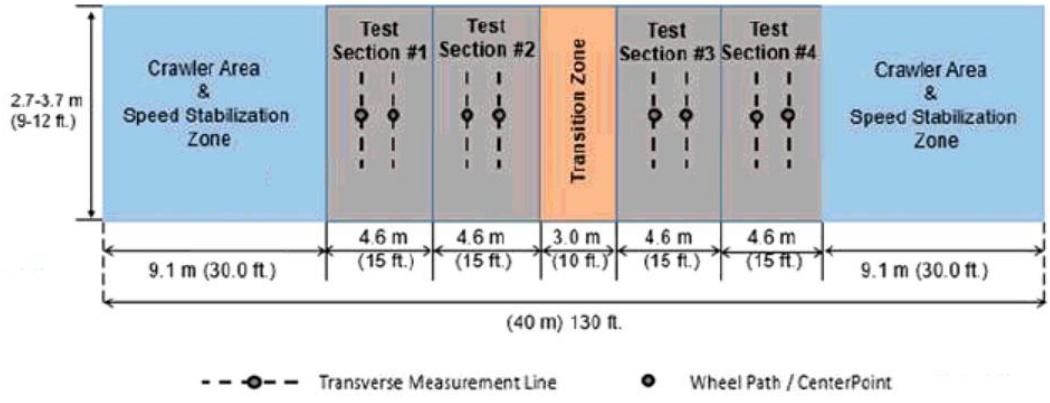

Figure 4.3. Typical plan view (Tutumluer et. al., 2019).



Figure 4.4. Test equipment and measurement of rutting (Tutumluer et. al., 2019).

The behavior of the geogrid reinforced airport pavement was experimentally and numerically assessed by Abdessemed et. al. (2015). Airport flexible pavements are constantly subjected to dynamic aircraft loads, harsh weather conditions, and the risk of fatigue and deterioration. Geosynthetics, such as geogrids, are known to enhance pavement performance by increasing its bearing capacity and extending its lifespan while reducing cracking and damage. In a study conducted at Tiksa Airport runway in Algeria, critical sections of the runway were reinforced with geogrids, and the behavior of the runway was compared before and after the reinforcement (Figure 4.5). The static behavior of the runway was evaluated using non-destructive testing with a heavy weight deflectometer, which identified the stresses and strains before and after reinforcement. The obtained results were further validated through three-dimensional numerical modeling using the finite element method with ABAQUS software. The study concluded that the implementation of geogrids improved the stresses and strains on the runway as the propagation of cracks were reduced. The results from the finite element modeling closely matched those obtained from the experimental tests.



Figure 4.5. Inclusion of geogrid layers on highway pavement (Abdessemed et. al., 2015).

Graziani et. al. (2014) conducted tests on the structural behavior of grid-reinforced pavements. Grid reinforcement is a common construction and rehabilitation technique used to enhance the structural performance of bituminous pavements. It is aimed to improve existing design and testing methods by obtaining the actual response of grid-reinforced systems under vehicular loads. An instrumented pavement section was constructed on an in-service road by installing a glass fiber polymer grid (FP) and a carbon fiber/glass fiber grid (CF) within a double-layered asphalt surfacing. Pressure cells and asphalt strain gauges were installed inside the pavement to measure the pavement's response to falling weight deflectometer and real-scale truck loads. The results showed that the average peak strains measured under the falling weight deflectometer load revealed a 65% reduction of the strains inside the CF-reinforced double-layered surfacing compared to the unreinforced case. However, no strain reduction was observed in the FP grid reinforced section. These findings suggest that CF grid reinforcement is more effective than FP grid reinforcement in improving the structural performance of bituminous pavements.

Saevarsdottir and Erlingsson (2015) conducted experiments using a heavy vehicle simulator to simulate the behavior and rutting patterns of flexible pavement structures. The

pavement was built using standard road construction equipment in a concrete test pit that measured 3 meters deep, 5 meters wide, and 15 meters long. The researchers monitored a 6-meter section of the pavement during the experiments. (Figure 4.6). Observations indicated that the increased water level had a notable impact on reducing the resilient modulus and accelerating the accumulation of permanent deformations. To confirm the experimental findings, numerical simulations were also conducted. The obtained results from two methods are in good agreement, and overall, both methods aligned closely with the experimental measurements.

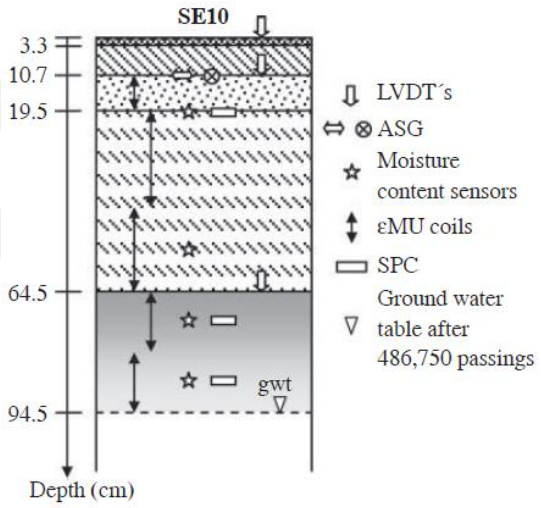

Figure 4.6. Cross section of the pavement structure with the instrumentations (Saevarsdottir and Erlingsson, 2015).

The study by Correia (2014) aimed to evaluate the effectiveness of using geogrid-reinforced asphalt overlays on the structural performance of flexible pavements against fatigue and reflection cracks. The researchers used an accelerated pavement testing method to measure the tensile-strain response of geogrids under traffic load. They applied a cyclic wheel load pressure of 700kPa to the pavement surface to measure asphalt surface deflection, stress and strains on the asphalt layer, stress in the base course and subgrade layers (Figure 4.7). The study found that geogrid-reinforced asphalt overlays improved the structural performance of flexible

pavements compared to unreinforced sections as measured strains were notably reduced at the bottom of asphalt layers and vertical stresses in lower layers were considerably reduced.

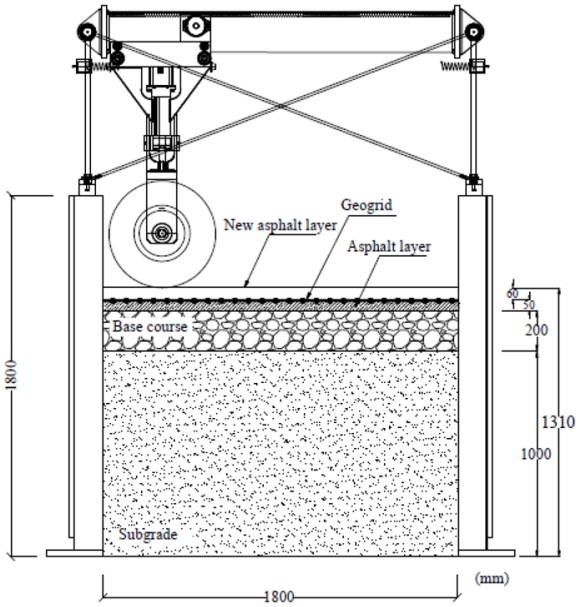

Figure 4.7. Typical pavement cross-section (Correia, 2014).

A study by Nunez et. al. (2013) examines the construction of a 5-meter-high embankment over soft alluvial ground improved by rigid vertical piles at the Chelles test site in France. The embankment is divided into four zones, with zones 3R and 4R reinforced by a geotextile layer and two geogrids, respectively. The study monitored total stresses, horizontal and vertical displacements, and assessed the arching effect using analytical methods and numerical models. The results showed that settlement efficacy, which refers to the effectiveness of a method to minimise settlement, is a reliable parameter to assess the overall performance of the rigid inclusion technique, while stress efficacy was overestimated by the methods tested. Figure 4.8 provides a plan view of the test site and instrumentation.

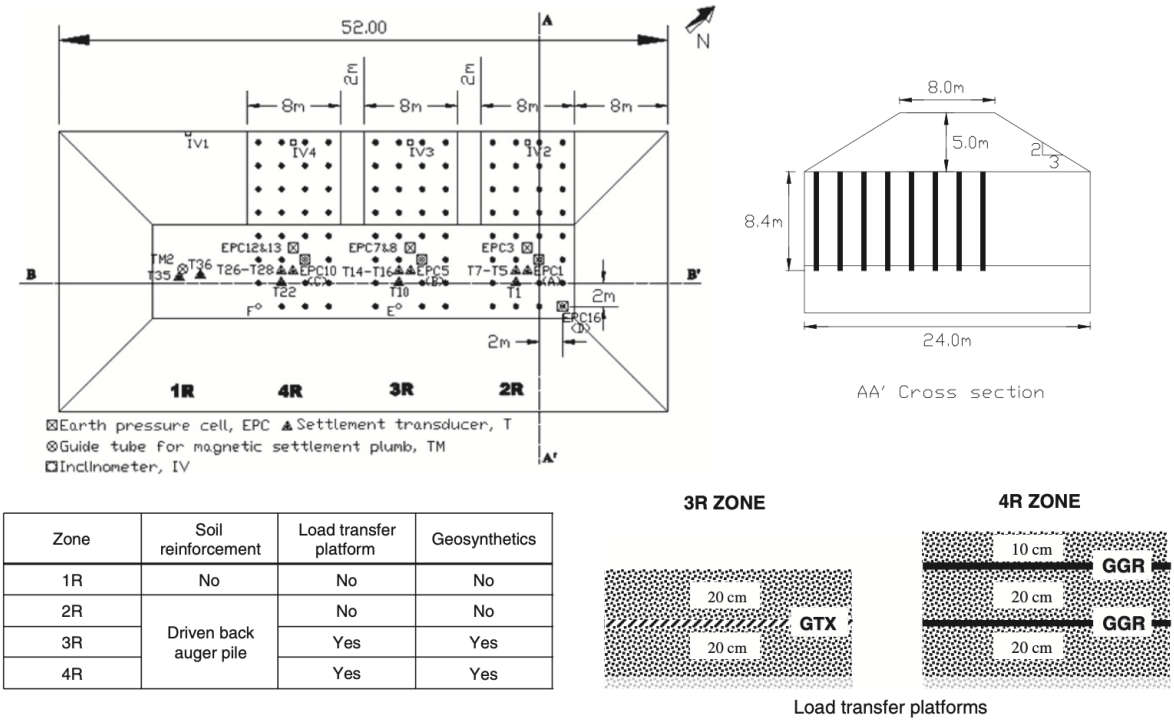

Zone	Soil reinforcement	Load transfer platform	Geosynthetics
1R	No	No	No
2R	Driven back auger pile	No	No
3R		Yes	Yes
4R		Yes	Yes

Figure 4.8. Plan view of test site and instrumentation (Nunez et. al., 2013).

Bergado et al. (2002) conducted a study on full-scale test embankments constructed on soft Bangkok clay, with and without geotextile reinforcement. The study evaluated the performance of the embankments using field measurements and FEM analysis, and investigated the failure mechanisms and embankment stability under undrained conditions. The study found that the use of high-strength geotextile can reduce plastic deformation in the foundation soil, increase the collapse height of the embankment on soft ground, and produce a two-step failure mechanism. Three full-scale test embankments were constructed, one reinforced by multiple layers of low-strength geotextile (MGE embankment), one reinforced by a single layer of high-strength geotextile (HGE embankment), and one unreinforced embankment as a control (CE

embankment). Failures were achieved, and the study compared the performance of the embankments using Table 4.1 and Figure 4.9.

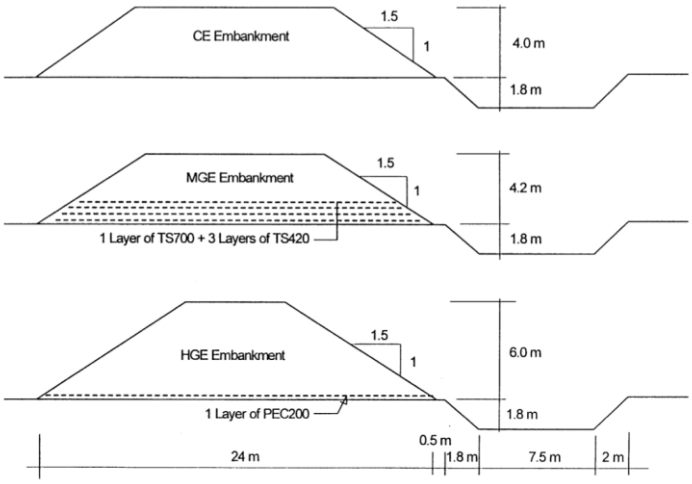

Figure 4.9. Cross sections of test embankments (Bergado et. al., 2002).

Table 4.1. Properties of geotextile reinforcements (Bergado et. al., 2002).

Properties of the geotextile reinforcements

Item	Types of geotextile	Nominal mass (g/m^2)	Secant stiffness at 5.0% strain (kN/m)	Ultimate strength (kN/m)	Remarks
1	Polyfelt TS 700	280	140	19	MGE
2	Polyfelt TS 420	130	70	9	MGE
3	Polyfelt PEC 200	700	1700	200	HGE

The findings from both experimental and numerical data indicate that using a high-strength geotextile can greatly decrease plastic deformations in the foundation soils below. Furthermore, the stiffness of the geotextile reinforcement can impact the height at which an embankment on soft ground collapses. In this particular study, the addition of a single layer of high-strength geotextile increased the collapse height by up to 1.5 times compared to the scenario where no reinforcement was used.

The study by Chaiyaput et al. (2014) investigated the use of woven Kenaf Limited Life Geosynthetics (LLGs) for short-term reinforcement of a full-scale embankment constructed on soft clay. The behavior of the LLGs was studied by comparing measured data from test embankments with simulated data using 2D and 3D finite element software. Two types of LLGs were used, coated and not coated with polyurethane, and their performance was compared (Figure 4.10). The results showed that surface settlements were higher than subsurface settlements, and both increased rapidly until 250 days after construction. Higher deformations or stresses were observed in the middle of the embankment for both coated and non-coated LLGs, and the deformation increased with time until the rate of settlement stabilized at 250 days after construction. The 3D numerical results were found to be in better agreement with field observations than the 2D analysis.

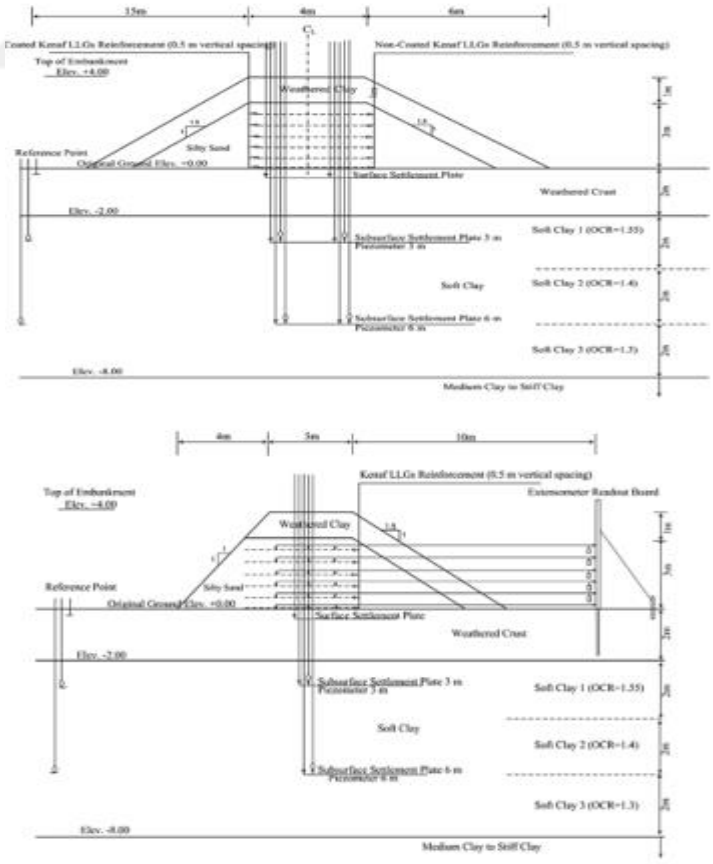

Figure 4.10. A-A and B-B section views of the test embankment Chaiyaput et. al. (2014).

Huckert et. al. (2016) conducted experimental and numerical studies on the load transfer mechanisms of geotextile reinforced embankments situated above sinkholes. The objective of these experiments was to simulate the occurrence of a circular sinkhole beneath a reinforced embankment and analyze the behavior of the fill material over the cavity. To achieve this, six full-scale experimental sections were constructed, which successfully replicated the opening of a sinkhole under geosynthetic reinforced granular embankments and treated soil layers. The instrumentation used in the experiments allowed for the monitoring of displacements, strains, and vertical pressure within the structure. The embankment used in phase 1 (sections 1, 2, 3) was 1 m high and consisted of cleaned, rounded gravel with particle sizes ranging from 20 to 40 mm. In phase 2 (sections 4, 5, 6), a 0.4 m thick layer of treated soil was used, which could be described as an as-dug material with 2% of lime as a hydraulic binder (Figure 4.11).

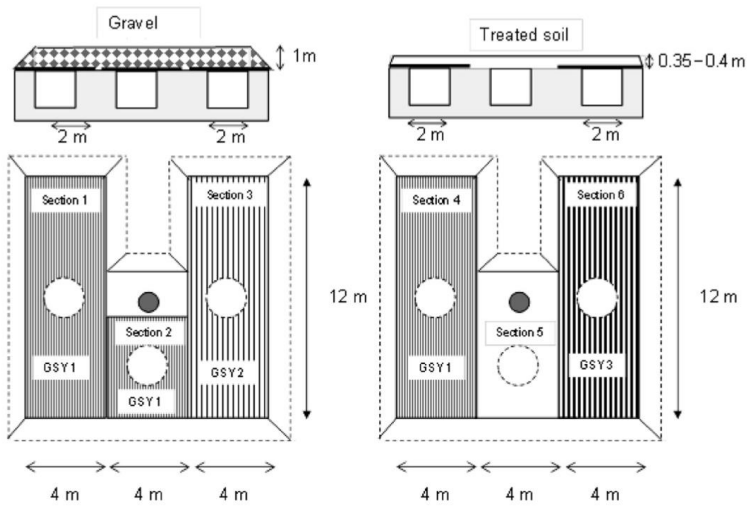

Figure 4.11. Experimental plan (Huckert et. al., 2016).

The experiments conducted indicate that the collapse mechanisms for granular materials and treated soil layers are distinct. For granular materials, the embankment's deformation is gradual during the cavity's opening, resulting in tensile force in the geosynthetic located over and around the cavity in the anchorage areas. The geosynthetic's shape is parabolic. In contrast,

for treated soil layers, the structure's deformation is minimal until collapse is achieved by applying an extra force.

Geosynthetic-reinforced and pile-supported (GRPS) embankments are gaining popularity due to their successful performance in practical applications. To analyze these structures, several design methods have been introduced. Pham and Dias (2021) conducted a study that compared the results of 25 full-scale embankments and six scaled models, evaluating the analytical models used. The study found that the existing analytical model is more effective for cohesionless fills than cohesive soils.

The issue of soil erosion can lead to disastrous landslides, especially in tropical countries. Likitlersuang et. al. (2020) conducted a field experiment to address this problem. An embankment with lateric soil, measuring 8 meters wide, 21 meters long, and 3 meters high, with a slope angle of 45 degrees was built. The soil was compacted to 70% relative compaction to simulate a natural soil slope. Two sides of the embankment were divided into six land cover areas, including three areas of bare soil, one area of geosynthetic cementitious composite mat (GCCM), one area of vetiver grass, and one area of a combination of GCCM and vegetation (Figure 4.12). The study monitored soil erosion and moisture levels for each land cover area during six natural rainfall events over the experimental period. The field results were compared with a numerical simulation and empirical soil loss equation. The study found that the different soil covers were effective in reducing soil loss during rainstorms. Additionally, the study established a link between soil moisture and erosion risk as the results showed that soil loss increased with the amount of cumulative water runoff, the area of contact between the soil surface and raindrop, and the moisture content of soils underneath the land cover.

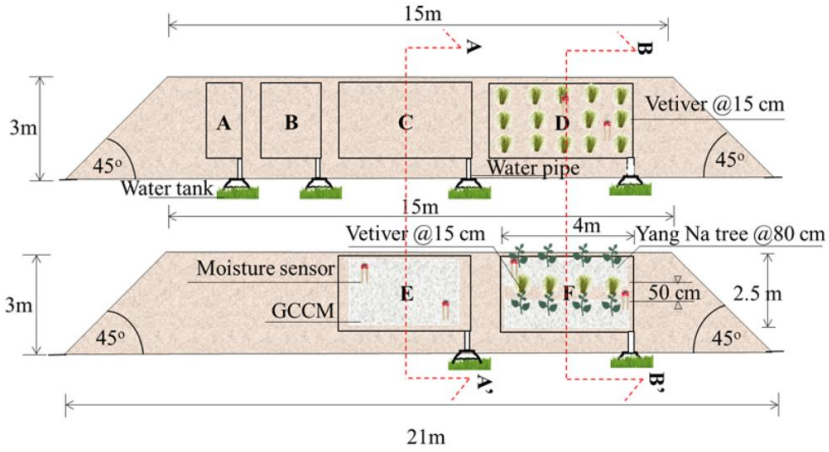

Figure 4.12. Experimental test set-up (Likitlersuang et. al., 2020).

Liu et. al. (2021) performed dynamic response tests on full scale low embankment model in laboratory conditions (Figure 4.13). Low embankments are commonly preffered in low volume roads and in rural areas. A full scale gravel soil embankment was experienced peak 50kN and dynamic loading of 1000 cycles under different moisture levels. The model has dimentions of 3x1.5x1.5m (Figure 4.14). The test findings indicate that the dynamic stress in the low embankment made of gravel soil nonlinearly decreases with depth. The lowest dynamic stresses were observed when the water content value in the foundation was 28%. Additionally, the rate of stress reduction was found to be inversely proportional to the loading cycles and directly proportional to the water content of the foundation. The dynamic stress and dynamic strain in the low embankment made of gravel soil exhibit cumulative effects as the loading cycles increase.

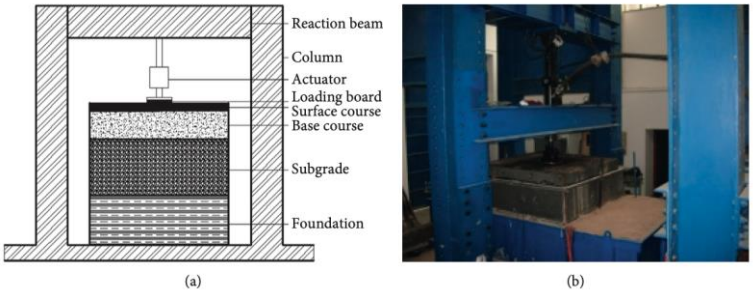

Figure 4.13. Laboratory loading system (Liu et. al., 2021).

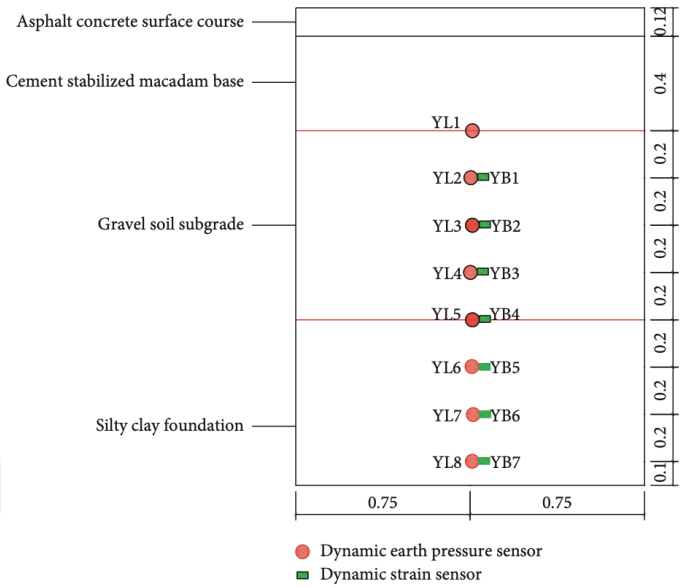

Figure 4.14. Physical model details (Liu et. al., 2021).

Cao et al. (2015) conducted a field test on a geogrid reinforced and floating pile supported embankment that was built on soft alluvial soil. The study took place at the construction site of a high-speed railway from Nanjing to Anqing in Anhui Province, China. The embankment had a height of 2.4 meters and a crown width of 13.2 meters, with a side slope of 1V:1.5H (Figure 4.15).

For the field monitoring, two test sections were selected, both using the same reinforcement solutions and fill load. The monitoring period lasted approximately 32 months. Various measurements were taken during and after the embankment is subjected to fill load, including pore water pressure, settlement, soil stress, strain in the geogrid, and lateral displacement. The performance of the geogrid reinforced and floating pile supported (GRFPS) embankment was thoroughly examined based on these measurements. The geogrid used for reinforcement had a tensile strength of Tult: 300 kN/m. The study found that the existing design procedures for GRFPS embankments constructed on alluvial soil were expected to be overly conservative because these design procedures take into account the contribution of the subsoil

whereas this leads to the over-estimation of the results when the embankment is designed on floating piles.

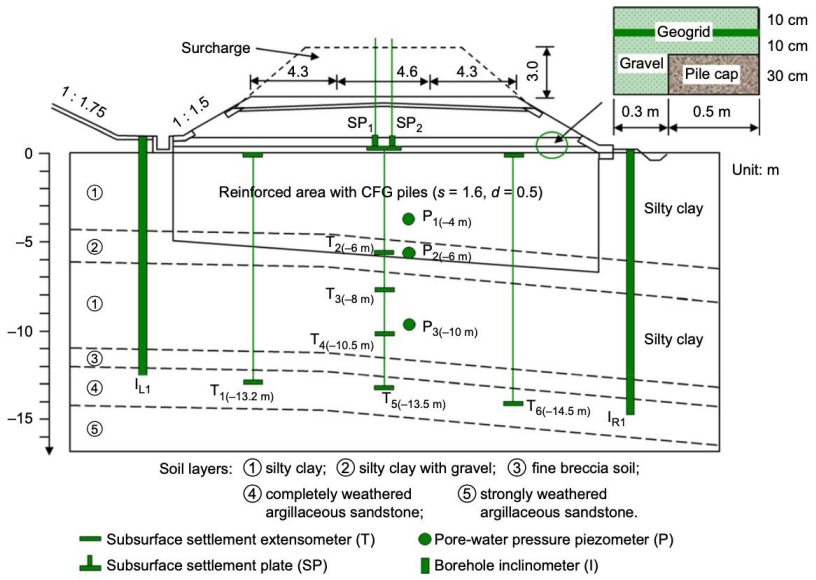

Figure 4.15. Cross section of the embankment (Cao et. al., 2015).

Highway embankments constructed in urban areas often disrupt pre-existing underground facilities, such as sewer lines and other buried structures. This can lead to severe consequences, including damage and service interruptions for both the utility and the highway. Turan et al. (2013) conducted a study on a full-scale embankment (Figure 4.16) to investigate the induced trench method (ITM). The test embankment was divided into four sections, allowing for the evaluation of four configurations, including conventional backfill, induced trenching, and two geogrid reinforcing bridging configurations with different spans. Each configuration consisted of a 3m deep trench overlain by a 10m wide, 10m long, and 6m high embankment section (Figure 4.16). The study found that vertical and horizontal stresses increased with increasing embankment height. However, when the full embankment depth was reached, the use of ITM resulted in a 47% reduction in vertical stresses at a depth of 1.5m.

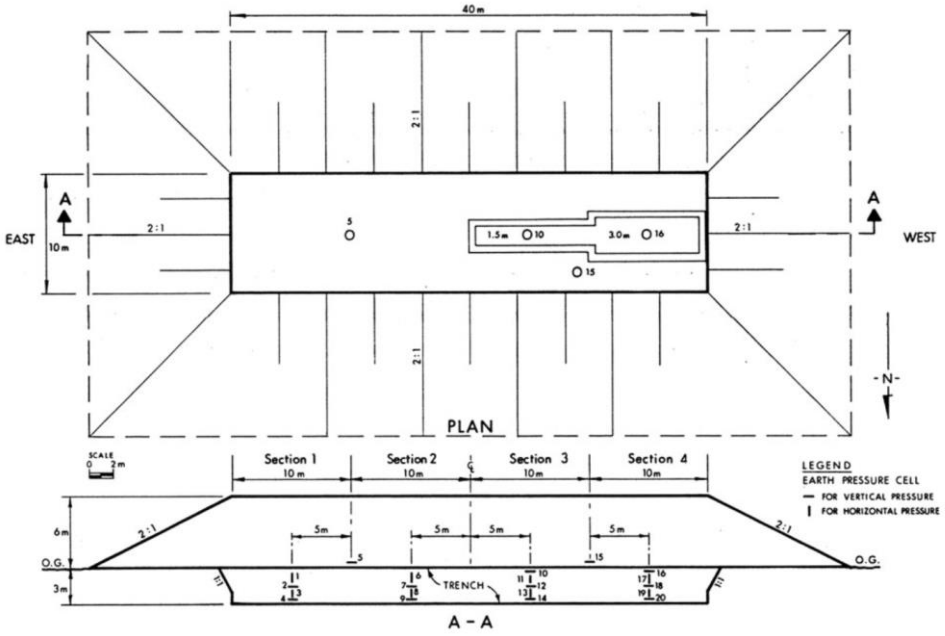

Figure 4.16. Plan of the test embankment (Turan et. al., 2013).

The construction of roadway embankments in areas with soft soil deposits is a major concern due to settlement issues. To minimize total settlement, a pile foundation system can be used to support the embankment. In recent years, geosynthetic reinforcement has been combined with pile foundations to improve settlement performance. A case study by Vega-Meyer and Shao (2005) examined a highway embankment in Panama that was built on a geogrid-reinforced crushed stone load transfer platform supported by precast piles (Figure 4.17). The embankment's behavior was monitored using various instruments, and the study found that the reinforced LTP system created a relatively stiff platform that allowed for maximizing the span between piles on weak soils and distributing loads more efficiently to the top of the pile caps.

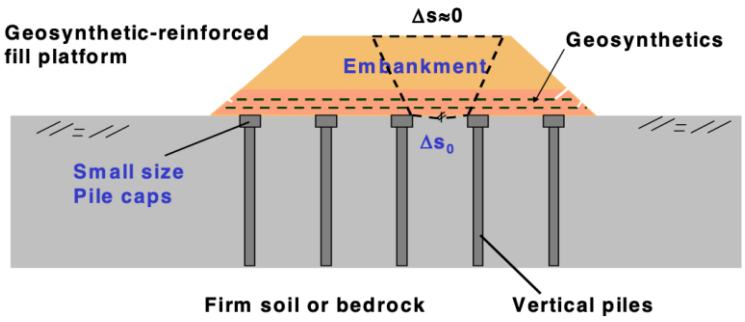

Figure 4.17. Schematic view of the embankment (Vega-Meyer and Shao, 2005).

Wang and Yao (2013) conducted experiments using full-scale models to investigate how to control the stability and deformation of sloped embankments reinforced on mountain slope foundations. They conducted two experiments in a laboratory, based on practical experience in constructing expressways in mountainous areas. One model was reinforced with geogrid, while the other was not. Both models had the same geometry and loading arrangement, with dimensions of 160cm x 160cm x 200cm (Figure 4.18). The slope gradient and foundation shape were the same as the original, and the model's embankment height and width were scaled down to 1/20th of the original size. Four layers of geotextile with a Tult of 10kN/m were used. The results showed that the reinforced embankment had a higher bearing capacity and experienced less lateral displacement compared to the unreinforced embankment.

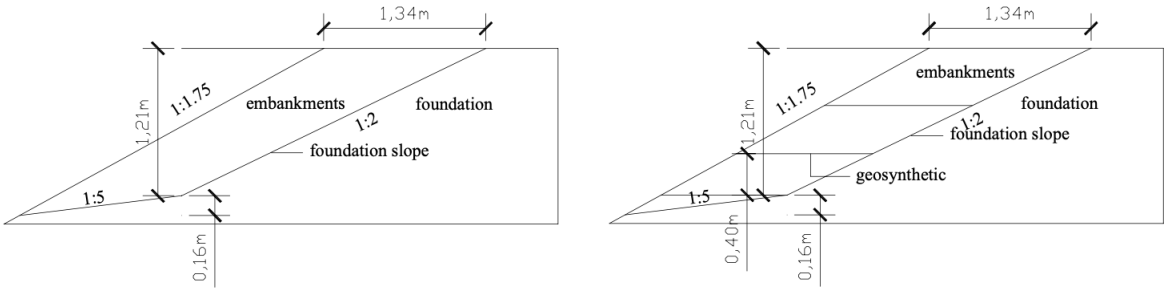

Figure 4.18. Unreinforced and reinforced embankments (Wang and Yao, 2013).

In the study of Arsyad et. al. (2020) the performance of road embankments on soft soil conditions were studied. Two full scale road embankments were constructed in Indonesia. The first embankment model was constructed using the ordinary fill material and the other one was constructed with natural soil. Dimensioning and instrumentation plan of embankments are shown in Figure 4.19. The first embankment model includes single layer of non-woven type geotextile at bottom whereas the second model includes geotextile layers in 30cm spacings. Geotextile's tensile strength is 45kN/m. Numerical experiments using PLAXIS 2D were also performed to validate the experimental observations. Obtained results reveal that Embankment 1, which includes less reinforcement experienced more settlement but the lateral movements were observed to be similar.

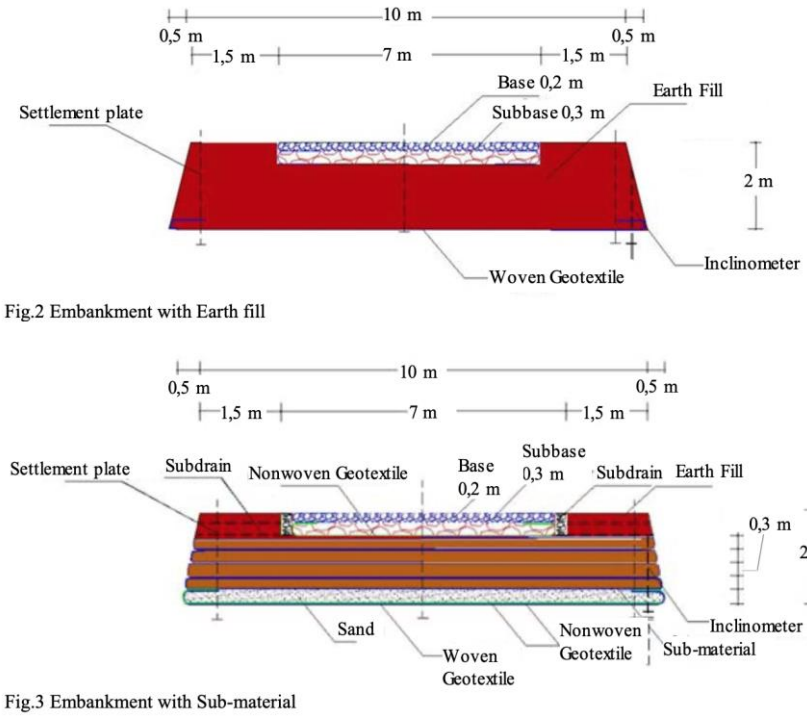

Figure 4.19. Dimensioning and instrumentation plan of embankments (Arsyad et. al., 2020).

Rezania et al. (2017) studied the impact of prefabricated vertical drains (PVDs) on the Haarajoki embankment in Finland, which was built on natural soft soil with PVDs installed under half of it to improve drainage. Using the Creep-SCLAY1S model, which incorporates

fabric anisotropy, structure, and time, they analyzed the installation effects. It was found that the model accurately predicted field settlements and excess pore pressure changes. The embankment is 2.9 m high, 100 m long, with an 8 m wide crest and a 1:2 slope angle, built on a soft clay deposit (Figure 4.20). The comparison of experimental and numerical data confirmed the model's effectiveness in predicting soft soil response.

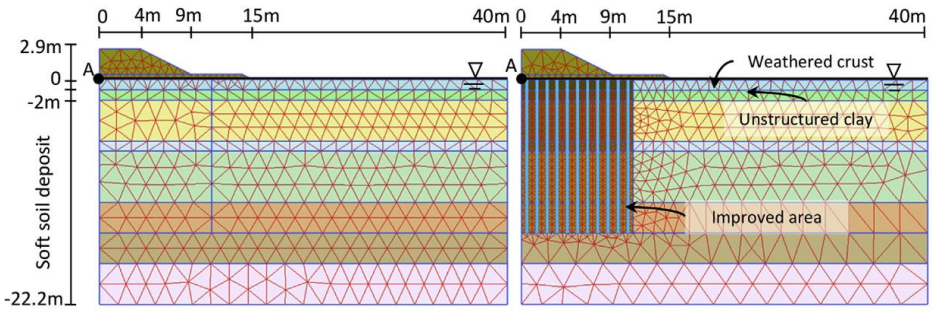

Figure 4.20. PLAXIS model of the Haarajoki embankment (Rezania et. al., 2017).

.

Huang and Han (2009) conducted numerical studies to enhance the understanding of the behavior of geosynthetic reinforced column-supported embankments. Their analysis focused on a bridge approach embankment with 2H:1V side slopes, constructed on deep mixed (DM) columns by the Sipoo River in Hertsby, approximately 30 km northeast of Helsinki, Finland. The cross-section of the column-supported embankment is illustrated in Figure 4.21.

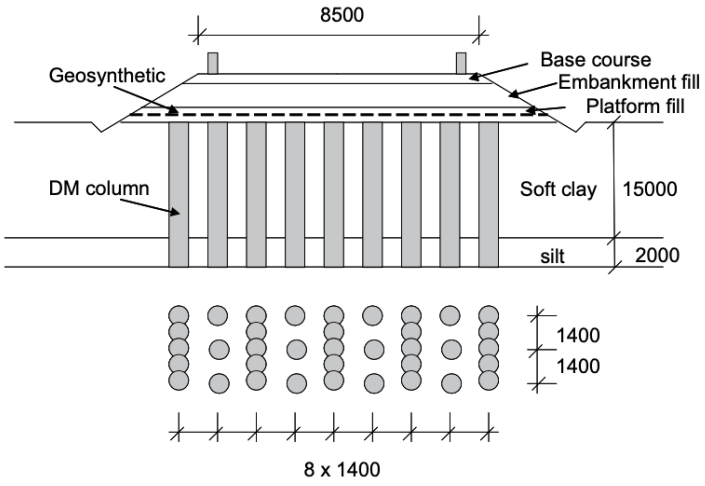

Figure 4.21. Cross section of the column supported embankment (Huang and Han, 2019).

Numerical studies were carried out to enhance the understanding of the behavior of geosynthetic reinforced column-supported embankments. The foundation soils, including soft clay and silt, the embankment fill, and the deep mixed columns, were modeled as linearly elastic-perfectly plastic materials using Mohr-Coulomb failure criteria. The geotextile reinforcement was represented by geogrid elements within the FLAC3D software. The geotextile has an ultimate strength of 200 kN/m in both longitudinal and transverse directions, with secant stiffness values of 1790 kN/m and 2120 kN/m at 2% and 6% strain, respectively. Figure 4.22, provides further details of the numerical model.

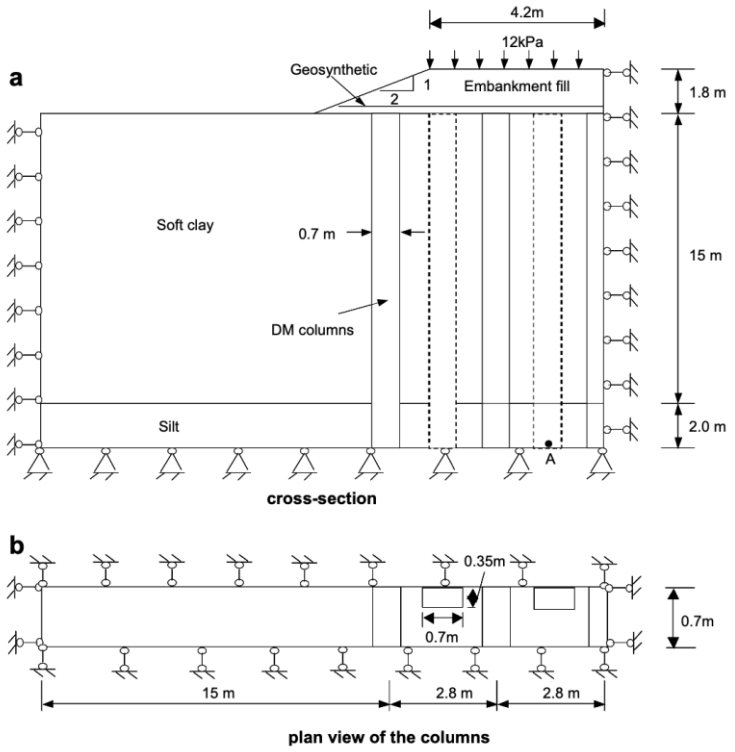

Figure 4.22. Numerical model of the case study (Huang and Han, 2019).

The numerical results indicate that settlements at the crest of the embankment are significantly smaller than those at the toe. Post-construction settlement at the crest is more critical and meaningful for the design of geosynthetic reinforced column-supported (GRCS) embankments than at the toe. The numerical results also reveal that strains in the geosynthetic reinforcement are higher in the transverse direction than in the longitudinal direction, with greater strains developing over the columns in both directions. Additionally, it was found that GRCS foundations experience a rapid reduction in excess pore water pressure due to the combined effects of drainage and stress transfer.

4.2. Experimental Studies with Mobile Seismic Shakers

A study by Boaga et. al. (2021) presents the results obtained from different force levels of vibroseis in order to assess the non-linear behavior of soft soils. During the standard seismic

reflection survey, vibroseis was used as an active source in the test area located in France. A total number of 61, 3 components, 5Hz geophones were placed in 2m spacing. Total record length was between 16-20s. The vibroseis used during the experiments is a sweep type IVI Mark Vibroseis truck. The input dynamic motion was selected as 10-80Hz sine sweep (Figure 4.23). However, many different drive force levels were used throughout the study to observe the non-linearity in soil.

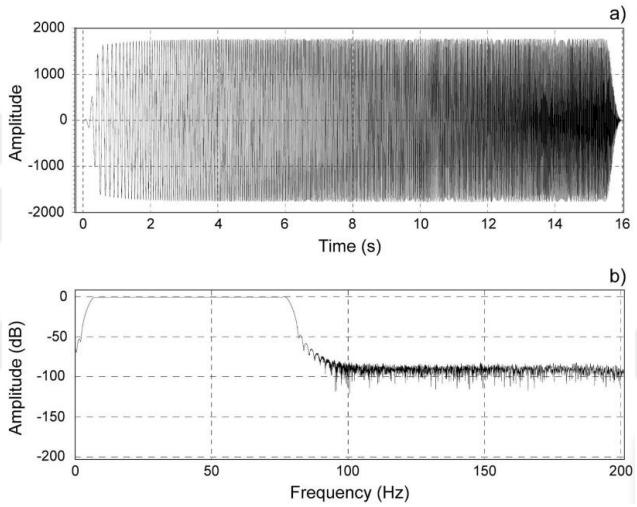

Figure 4.23. a) Input dynamic excitation, b) Sweep frequency range (Boaga et. al., 2021).

During the experiments, the non-linear behavior was clearly observed. Surface wave velocity changed around 8% when the applied for increase from 13.6kN to 217.1kN (Table 4.2). Strain estimations and active H/V ratio measurements also reflect the same outcome.

Table 4.2. Shear wave velocities for different force levels.

Drive level Layer	80% V_S(m/s)	50% V_S (m/s)	40% V_S (m/s)	10% V_S (m/s)	5% V_S (m/s)
1	210.2	214.4	216.5	220.7	224.9
2	287.3	293.0	295.9	301.7	307.4
3	282.7	288–4	291.2	296.8	302.5
4	380.1	387.6	391.2	399.0	406.6
Soft soil average	290.1	295.8	298.7	304.5	310.3

A series of in situ seismic tests were performed by Bertero et. al. (2022) for experimental modal analysis (EMA) of civil structures. Using a mobile shaker, an eleven-story instrumented building in Austin, Texas was subjected to 5 minute sets of 20s chirp excitations from 5 to 50Hz in both directions. Obtained results from EMA was compared to those obtained from ambient vibration analysis, in other words operational modal analysis (OMA). High-sensitivity wireless geophones and data loggers were used throughout the tests. As shown in Figure 4.24, horizontal and vertical geophones were deployed to the 2nd, 5th, 7th, 9th and 11th floors. Measured velocities from both techniques at station 1 is represented in Figure 4.25. It was revealed that the yield modes obtained from EMA technique was not identified in OMA especially above 11Hz. However, ambient vibration technique was found to be more consistent for the modal estimates that obtained from processing 20min long records.

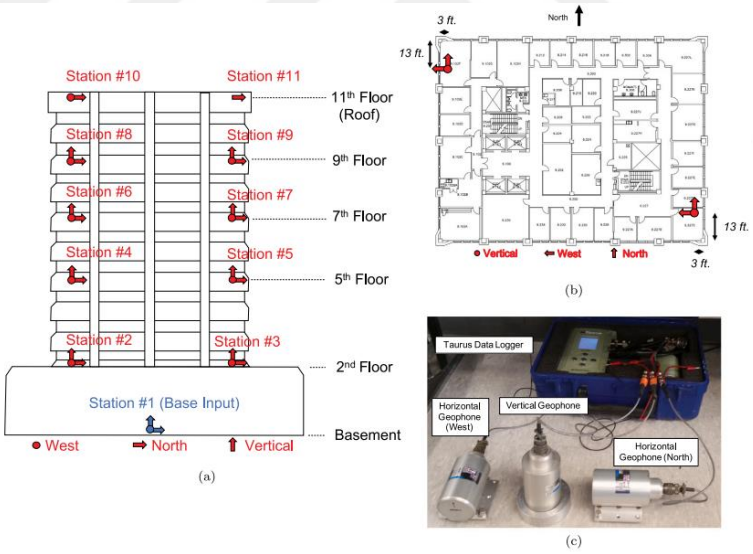

Figure 4.24. a) Instrumentation plan for the building, b) Location of sensors by floor, c) Data logger and geophones (Bertero et. al., 2022).

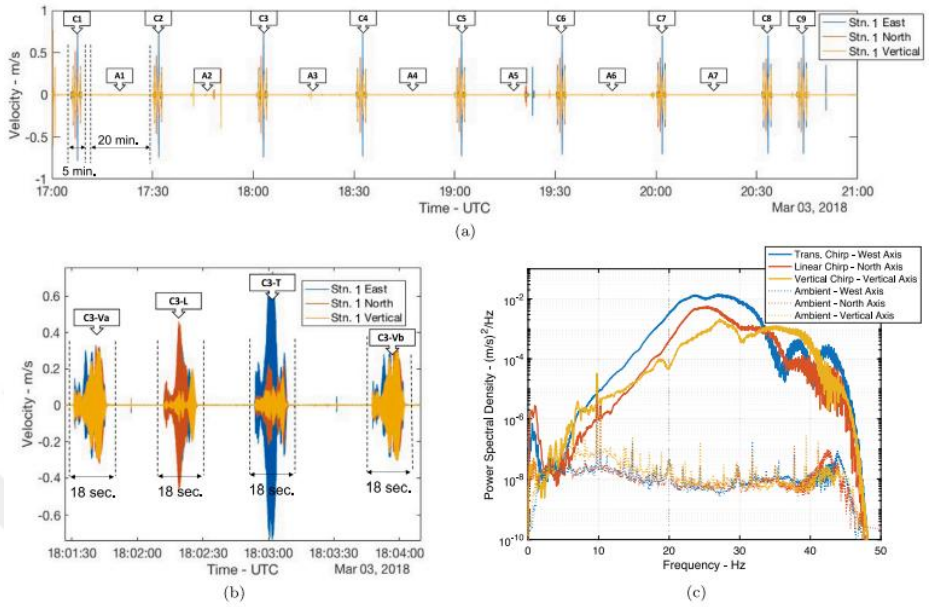

Figure 4.25. a) Measured velocities at station 1, b) Close up view for chirp excitations, c) Ground velocity spectra for each direction and technique (Bertero et. al., 2022).

In a study by Wang et. al. (2022), active isolation experiments were carried out to examine the effectiveness of metamaterial-based barriers by using a mobile shaker. A trench containing a mixture of polyurethane and reinforced concrete serves as a test barrier. An active source, a mobile shaker, was utilized on top of the barrier. Variables of the experimental study were selected as the foundation type of the steel frame, existence of a trench, number of barriers and length of barriers as represented in Figure 4.26.

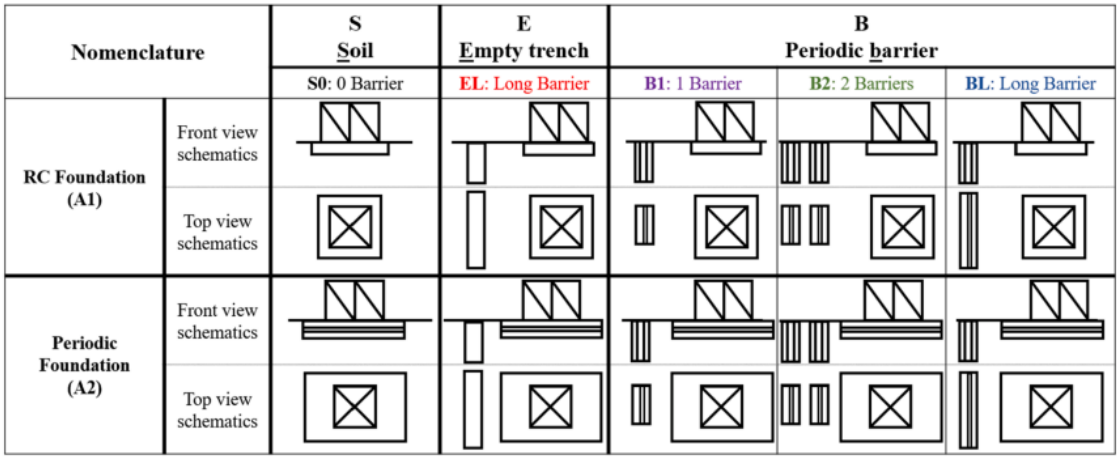

Figure 4.26. Experimental setup (Wang et. al., 2022).

The 3D geophones used to obtain the ground surface response, while the 3D accelerometers placed on the steel frame and foundation recorded the structural response. Applied dynamic motions include 15-100Hz incremental sine wave in 12s and nine scaled earthquake records. The efficiency of proposed technique was evaluated by comparing the ground surface and structural responses with respect to the barrier location. Outcomes of the study reveal that the proposed material filled in trenches can successfully restrain the vibrations generated from the seismic shaker due to the built-in active isolation barrier system. Periodic barriers performed much better than empty trench cases and the increasing barrier length enhanced the isolation performance.

A similar study performed by Zhang et. al. (2022) performed field experiments to investigate the effectiveness of periodic barriers and foundations as a passive isolation system. The mobile shaker was used as a source from a distance to the barriers. A number of 15, 3D geophones and a number of 2, 3D accelerometers were used for the instrumentation. The evaluation of the effect of periodic foundation and barriers by means of seismic performance was obtained by comparing the responses in time and frequency domain with respect to the barrier location. It was revealed from the results that the use of periodic foundations and barriers together as a passive isolation system is useful for the mitigation of the dynamic motions reaching the structure of interest. This is because the proposed system has a unique frequency

selective property, which can keep the dynamic waves within certain frequency ranges, and the rest of the frequency ranges are prohibited to propagate through the periodic material.

Hryciw et. al.,1990; triggered the failure of a road embankment while conducting a deep seismic reflection survey by six seismic shaker trucks . Due to shaking, embankment soil liquefied and caused flow slide and the embankment collapsed (Figure 4.27). After experiencing a failure, investigations were conducted which involved examining the site, conducting standard penetration tests, performing flat plate dilatometer tests, and carrying out laboratory tests. Vibratory tamping trucks simultaneously applied an incremental 8Hz-58Hz sinusoidal wave for 8 seconds until the embankment soil liquefied and the road embankment collapsed. Collected data showed that the shear strain was 5.5 x 10^{-2} %, which surpassed the upper limit for generating excess pore pressures due to the combined effect of the six seismic shaker trucks vibrating at 12.4 kPa of force.

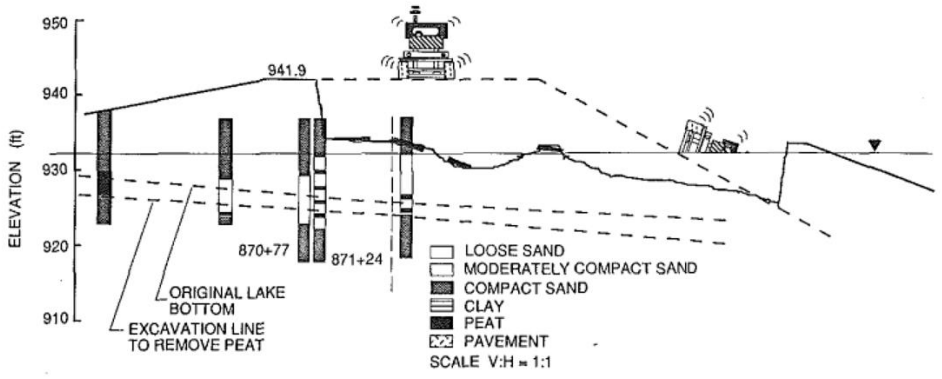

Figure 4.27. Road embankment cross section before and after failure (Hryciw et. al.,1990).

Bay and Stokoe, II, 1998; developed a rolling dynamic deflectometer (RDD) to perform deflection tests of pavements. Unlike other methods, RDD is a quick, effective, continuous and nondestructive method to characterize pavement condition. The proposed RDD system was developed by modifying a Vibroseis truck which can apply sinusoidal dynamic forces to the pavement. The RDD was used to gather data on the condition of pavement at two sites on

Interstate Highway 10 for 21 miles. The results were used to assess the pavement's condition and design an overlay. The RDD system was also used to test airport pavements at Dallas-Fort Worth International Airport to predict their remaining life. RDD testing was conducted at speeds of up to 1.5 mph.

The RDD system is a powerful tool that can generate dynamic forces up to 154 kN peak at frequencies ranging from 5 to 100 Hz. In a highway runway pavement experiment, a combination of static and dynamic forces was applied, resulting in a total force cycling between 35.6 kN and 89.0 kN (Figure 4.28). The system's testing speed was adjustable, and the operating frequency was selected based on subgrade conditions, pavement roughness, and sensor contact considerations. The force levels were chosen based on the estimated strength of the pavement being tested, with a possible range of 13−300 kN peak-to-peak. At the end of the RDD experiments, the stiffness, cracks, joints and weak regions was successfully determined at two sites on Interstate Highway 10 for 33.5km.

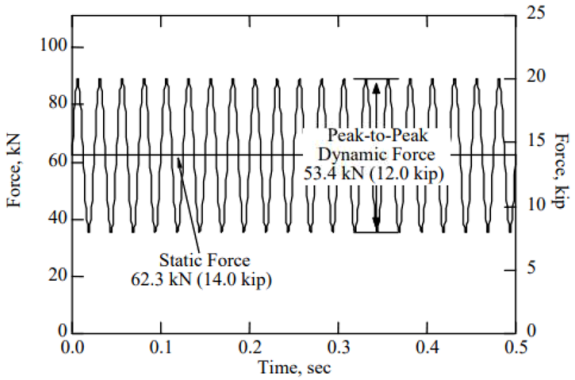

Figure 4.28. Applied static and dynamic force by the RDD system (Bay and Stokoe, II, 1998).

Chang (2002) conducted the first in-situ dynamic liquefaction test at the University of Texas at Austin. The study aimed to develop a procedure for this type of test, using a vibroseis truck as a dynamic source to apply loads to the ground surface and generate waves that propagate through the instrumented test area. The response to dynamic loading was measured to evaluate the soil's pore pressure generation characteristics, including induced shear strains and excess

pore pressures. This allowed for monitoring of excess pore pressure, shear strain amplitude, and number of cycles during the test. The vibroseis truck used in the experiments could generate sinusoidal waves within a frequency range of 15 Hz to 100 Hz, with a maximum applied force of 178 kN controlled by the truck's weight and the output of the hydraulic ram (Figure 4.29). The in-situ dynamic liquefaction test is represented in Figure 4.30.

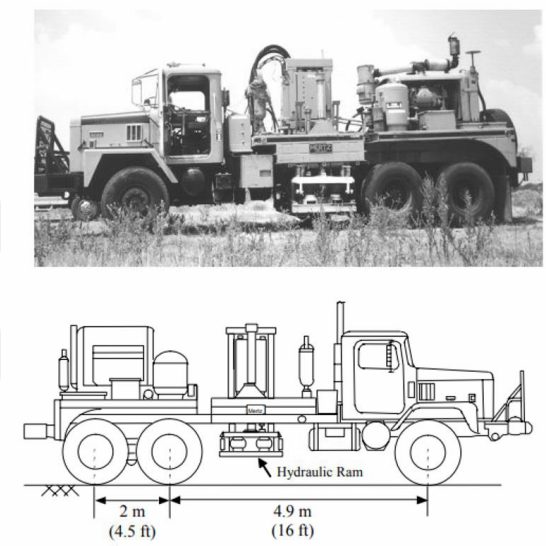

Figure 4.29. The vibroseis used during the field experiments (Chang, 2002).

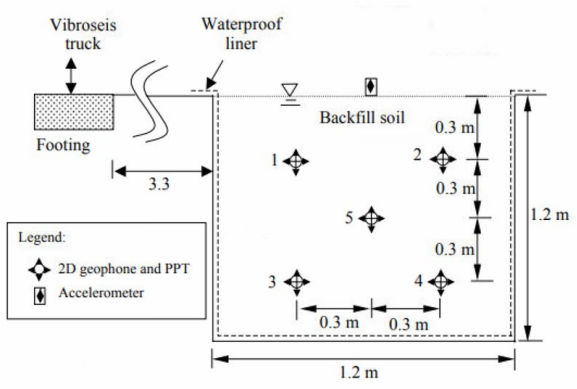

Figure 4.30. In situ dynamic liquefaction test (Chang, 2002).

Before the liquefaction experiments, field vibration tests were conducted to assess the performance of the loading system and understand the wave propagation characteristics in the test area. Four vertical accelerometers were utilized to measure the vertical accelerations caused by the vibroseis, as shown in Figure 4.31. During these tests, a linear swept sine wave with a frequency range of 10 to 100 Hz and a constant input amplitude was applied to a hydraulic ram. It was seen that the resonant frequency of the system was approximately 50 Hz. Although selected frequency range of 20Hz is usually higher than the typical frequency range of seismic events, it was selected because it is the optimum frequency range at which the vibroseis is able to generate clear sinusoidal waves during the liquefaction experiments.

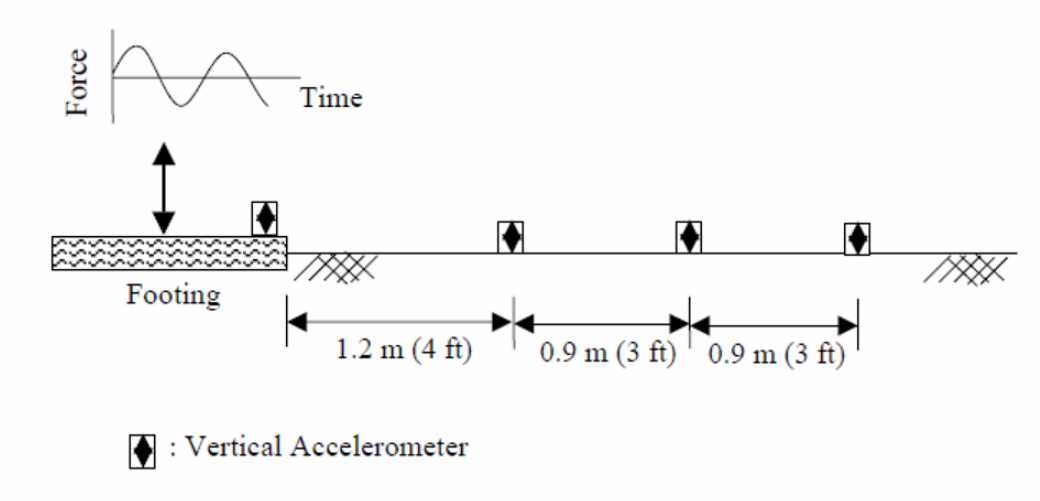

Figure 4.31. Field vibration test (Chang, 2002).

In another study, large mobile shakers were used to investigate the dynamic response of scaled structural systems (Wood et. al, 2004). Three mobile shakers of T-Rex, Liquidator and Thumper were all used to excite the scaled bridge bents in field conditions. T-Rex operated both in vertical and horizontal modes and applied sinusoidal motions. In another set of trials, shaker of the thumper was placed over the mid-span of the bridge beam and excited (Figure 4.32). Frequency and amplitude of shaking was increased until the resonant phenomenon occurs. No cracks or collapse were observed during the experiments except the pull-over tests took place with the help of the T-Rex and Liquidator pulling together the structure.



Figure 4.32. Dynamic excitation (a) and slow pull-over tests (b) on scaled bridge structure performed by large mobile shakers in the field (Wood et. al, 2004).

Cox (2006) conducted a study with the objective of creating and utilizing a novel in-situ liquefaction testing approach. This technique involves an active method that can directly assess the liquefaction resistance of soils in their natural location. The method employs a large hydraulic shaker, mounted on a truck, known as vibroseis, to vibrate the ground surface and generate stress waves of different amplitudes within a monitored section of the soil mass. Figure 4.33 illustrates this process. The instrumentation measured the generation of excess pore water pressure and nonlinear shear modulus behavior in the natural silty-sand deposits under dynamic excitations produced by vibroseis. The results obtained from these tests were then compared to those obtained from laboratory experiments. A number of 20 liquefaction sensor were used during the experiments. During the field experiments, the typical dynamic excitation was 10Hz and 20Hz fixed sine wave for 100 cycles. Test results were found to be compatible at generating pore pressure generation curves and cyclic shear strains that were previously found in laboratory tests.

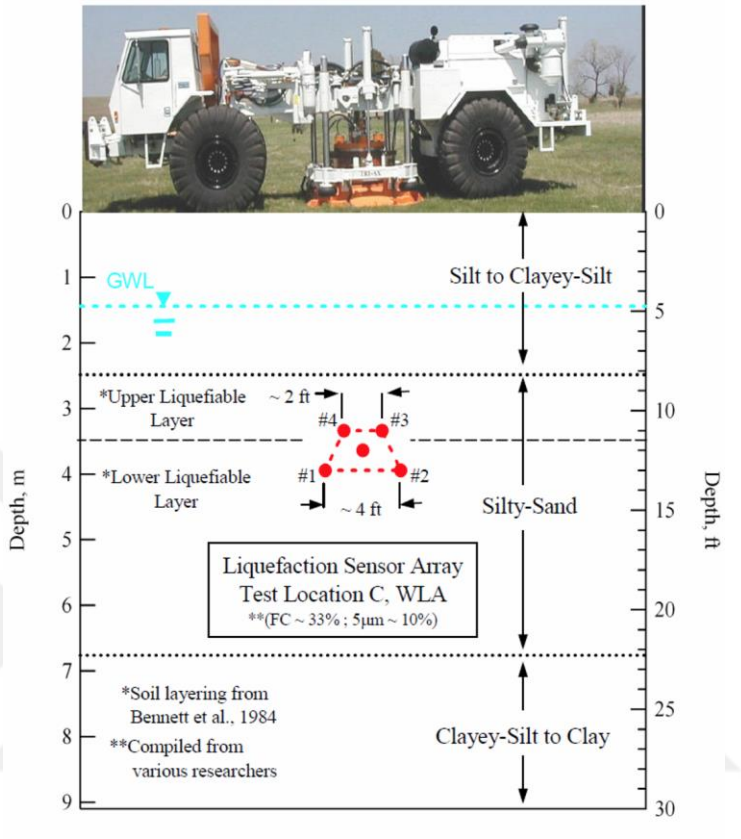

Figure 4.33. Experiments at test location C (Cox, 2006).

Frary (2012) performed high-resolution seismic reflection surveys in order to image the existing and undiscovered faults in populated Reno-Sparks metropolitan area in Nevada, where is located in a basin. Using the "Thumper truck", 11km of 2D reflection data was collected with a series of geophones spaced at every 5m. During the study 12-second sine wave was applied between 15-120Hz and the reflection data was saved via 144-channel geophones with 8Hz of resonance frequency. Experimental results indicate the existance of many undiscovered faults around the region, their location and orientation, precisely.

Leblanc (2013) introduced a technique for measuring the linear and nonlinear constrained moduli of granular soil. This method involves using large mobile shakers to create vertical sinusoidal vibrations directly above an embedded sensor array. The site is equipped with geophones to monitor wave propagation and particle movement in the soil, load cells to measure applied static loads, and a data acquisition system to record the data. Two vibroseis trucks were

used throughout the study. Applied dynamic loads by two shakers are represented in Figure 4.34 and 4.35. It was concluded that at lower confining pressures, the constrained modulus increases slightly with respect to axial strain, but it subsequently decreases as the axial strain continues to increase. It was also noted that the proposed field method can successfully be used to obtain the constrained modulus.

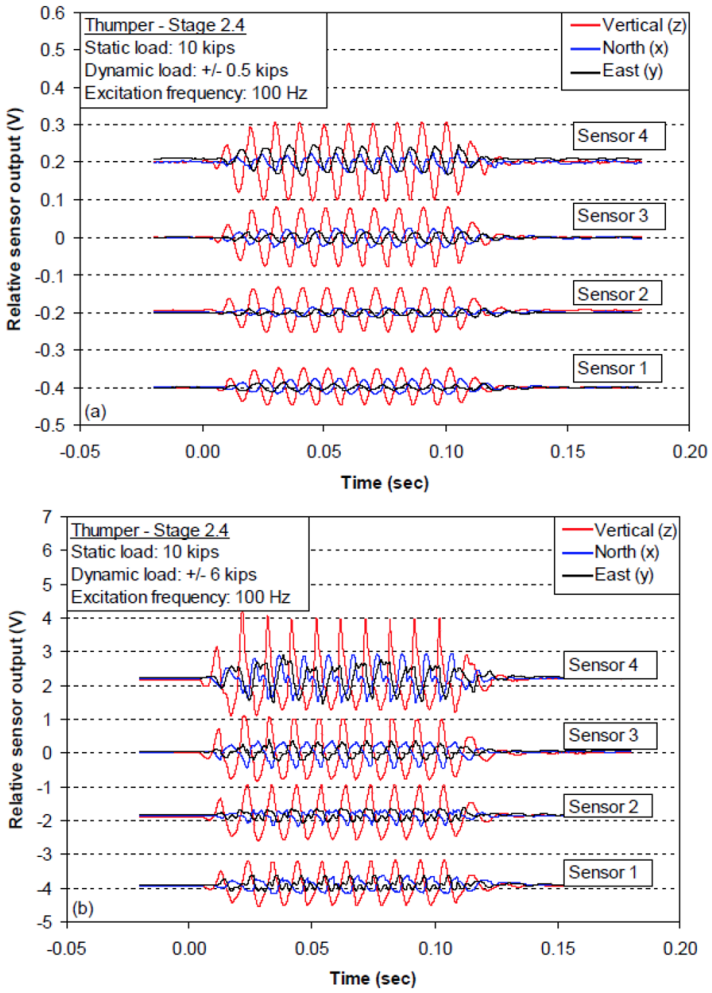

Figure 4.34. Voltage-Time Histories generated by Thumper truck at 100Hz, (a) Low amplitude, (b) High amplitude (Leblanc, 2013).

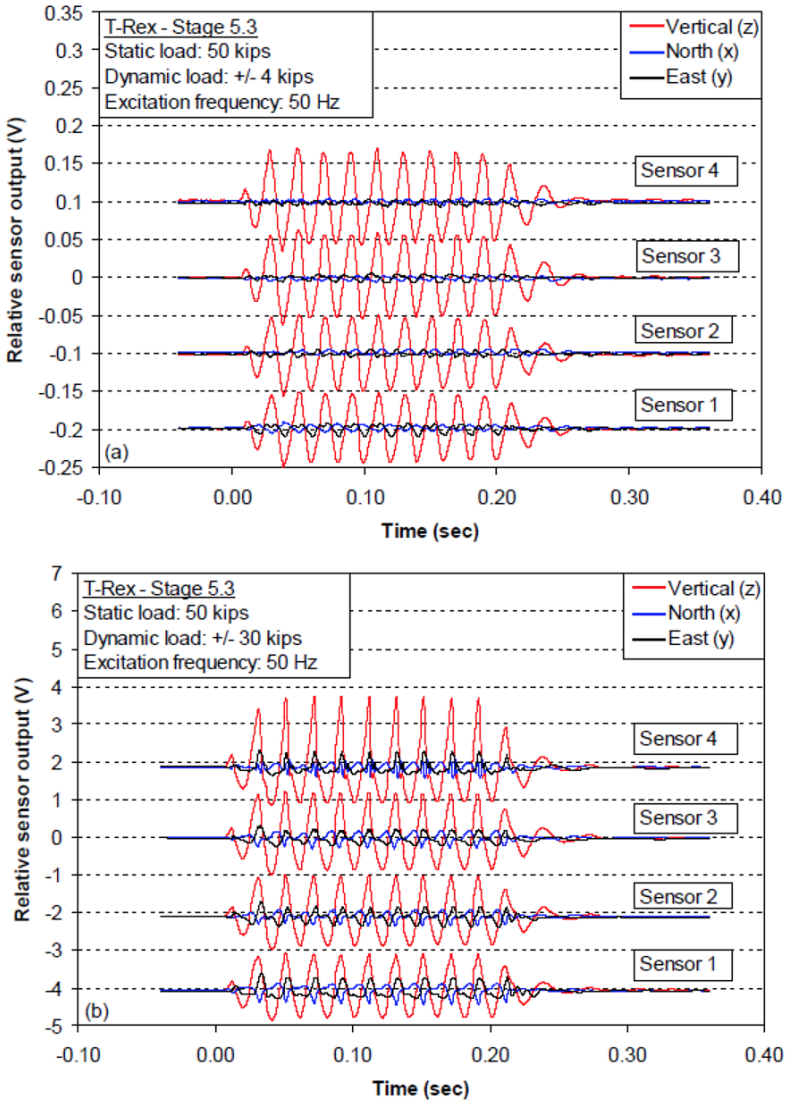

Figure 4.35. Obtained results at 50Hz, (a) Low amplitude, (b) High amplitude (Leblanc, 2013).

Roberts (2014) conducted a study in Imperial Valley, CA, where they directly evaluated the susceptibility of liquefaction in the area. The main goal of this testing method was to examine how the shear strain in the soil relates to the excess pore water pressure generation. They utilized a mobile seismic shaker to observe the effects. Pore pressure and velocity transducers were used throughout the experiments (Figure 4.36).

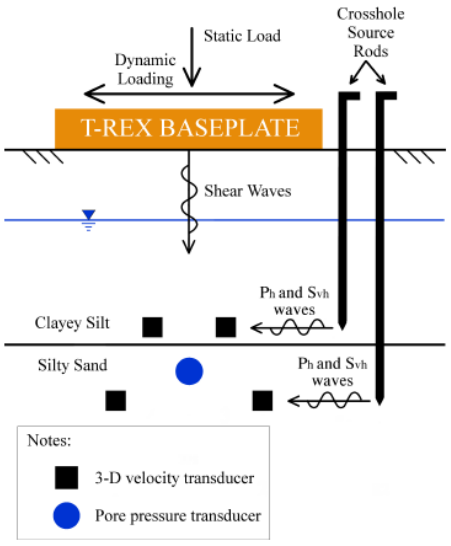

Figure 4.36. Instrumentation plan (Roberts, 2014).

It has been determined that the T-Rex's force output remains consistent within the range of 5 to 180 Hz, as shown in Figure 4.37. However, the force output significantly decreases for frequencies below 5 Hz. To account for this, the study only used shaking frequencies between 10 Hz (the minimum) and 30 Hz (the maximum), which is still within the range where force output remains relatively constant and avoids the exponential drop-off in force output occurs

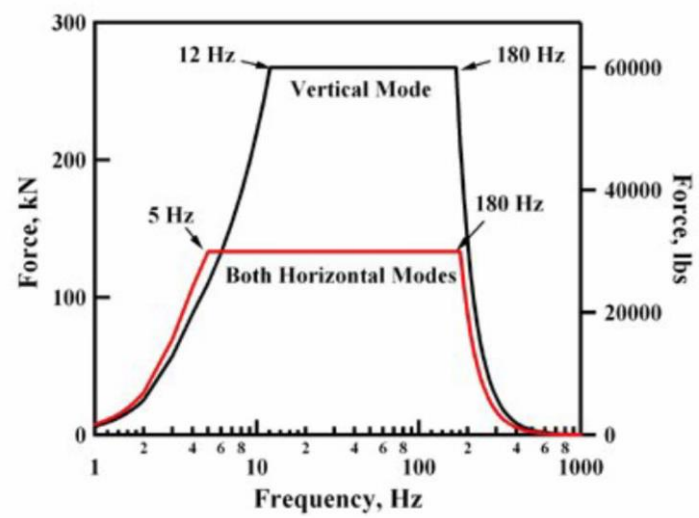

Figure 4.37. Output force vs dynamic frequency of vibroseis (Roberts, 2014).

After the 2010 Canterbury and 2011 Christchurch Earthquakes, the suburbs of Christchurch suffered severe liquefaction. Therefore, cost-effective ground improvement methods against liquefaction were implemented around the city (Stokoe et. al., 2016). Liquefaction tests were conducted by T-Rex at four improved and two unimproved zones to measure the strain and developed pore pressures under cyclic loading by large mobile shaker. Ground improvement methods evaluated during the field trials are Rapid Impact Compaction (RIC), Rammed Aggregate Piers (RAP), Low Mobility Grouts (LMG) and Single and Double Row of Horizontal Beams (SRB or DRB). T-Rex was used to generate 5-stage loading sequence 10Hz for 10 seconds each time. Obtained results show that ground improvement methods have a direct influence on the liquefaction susceptibility of soils. It was found that the ground improvement methods of RIC, RAB and DRB are quite successful at inhibiting the liquefaction susceptibility of the test site whereas LMG and SRB performed poorly (Figure 4.38).

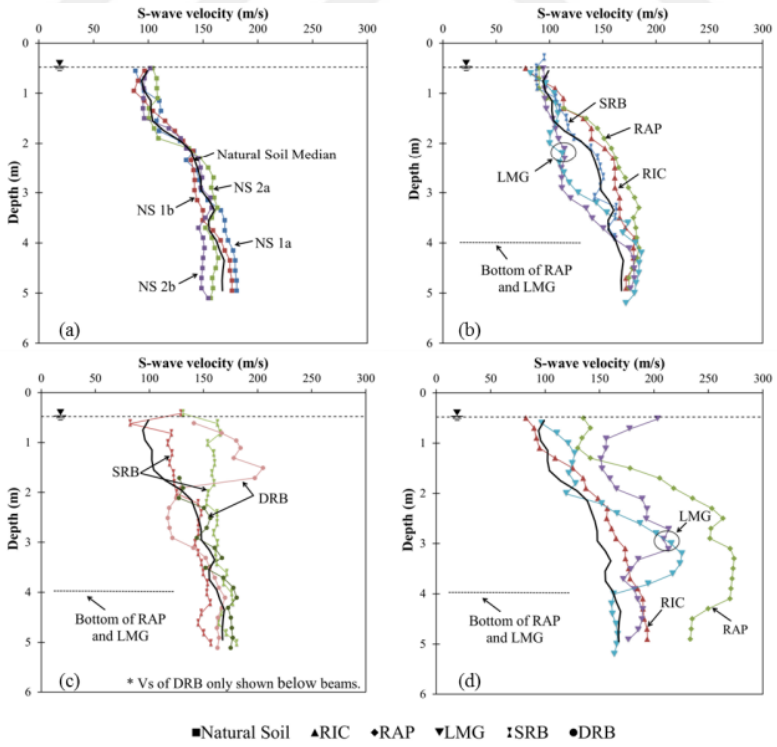

Figure 4.38. Shear wave velocity (Vs) profiles, a) two unimproved zones, b) between improvements at LMG, SRB, RAP and RIC zones, c) across improvements at SRB and DRB, d) across improvements at LMG, RIC and RAP zones (Stokoe et. al., 2016).

The stability of landfills is a significant issue for both the environment and public health. To assess the seismic response of these landfills, it is crucial to understand the dynamic properties of the solid waste they contain. Sahadewa et. al. (2015) investigated the dynamic properties of different landfills with the help of the instrumented vertical arrays and mobile shakers (Figure 4.39). 3D geophones, which were used for the experiments have a diameter of 7.62cm and are made of 3.81cm-thick acrylic. Geophones were preferred to accelerometers in many ways including the relatively low costs, no required additional power supplies and external cables. Dynamic tests were performed in 30-50 Hz for 8-10 cycles. During the experimental study, the nonlinearity in shear modulus was successfully evaluated for the shear strains in the range of 0.0004% to 0.2%. Load-settlement and unit weight measurements for varying waste materials were also made in-situ.



Figure 4.39. a) Instrumentation, b) T-Rex (Sahadewa, 2015).

To generate the P and S wave profiles of two pre-existing boreholes at Los Alamos National Laboratory in New Mexico, a deep downhole seismic examination was conducted by

Stokoe et. al. (2017). Previously developed profiles for the site were created using hand operated impulsive sources and they were able to create the P and S wave profiles up to 183m. However, T-Rex was used to reach the depths up to 415m in this project. Vibroseis was used as an active source and the frequency of 20-50Hz fixed frequency signal was selected throughout the tests (Figure 4.40). Obtained results using the T-Rex were compared to that of hand operated impulsive sources. Up to 183m of depth, obtained P and S wave profiles from both methods are in a good aggrement with less than 0.5% difference. Unlike the hand operated impulsive sources, dynamic waves generated by T-Rex can could successfully reach up to 415m of depth to obtained the desired waveforms.

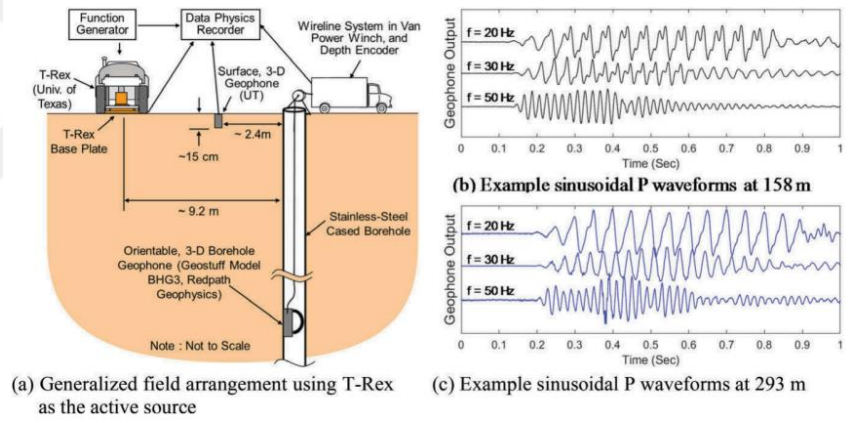

Figure 4.40. Arrangement for deep downhole testing and example waveforms (Stokoe et. al. 2017).

Dynamic response of bridges is an important aspect. Mobile seismic shakers give the ability to studys on full scale structures in the field. An experimental study proposed by Farrag et. al., 2019 demonstrates how mobile seismic shakers are a useful tool for measuring the behavior of bridges and improving our understanding of how bridge systems respond dynamically. During the study, a 67.4m bridge in Hamilton Township, New Jersey was subjected to large-amplitude shaking with the help of the mobile shaker T-Rex. The bridge system was instrumented using geophones, and accelerometers, at various locations (Figure 4.41). T-Rex applied dynamic excitations in a range of 1-15Hz during 32 seconds at 94kN of force. In addition, 2D and 3D finite element analyses using COMSOL software were performed

to compare the experimental results. Major findings of the study indicate that mobile shakers are very useful to assess the dynamic response of bridges. When the slenderness ratio (H/W) is increased while maintaining the same rigidity, there is a notable rise in the response of a structure and a decrease in its natural frequencies. Additionally, field experiments conducted on a bridge revealed the presence of two distinct modes of transverse vibration, occurring at frequencies of 4.36 and 4.61 Hz.

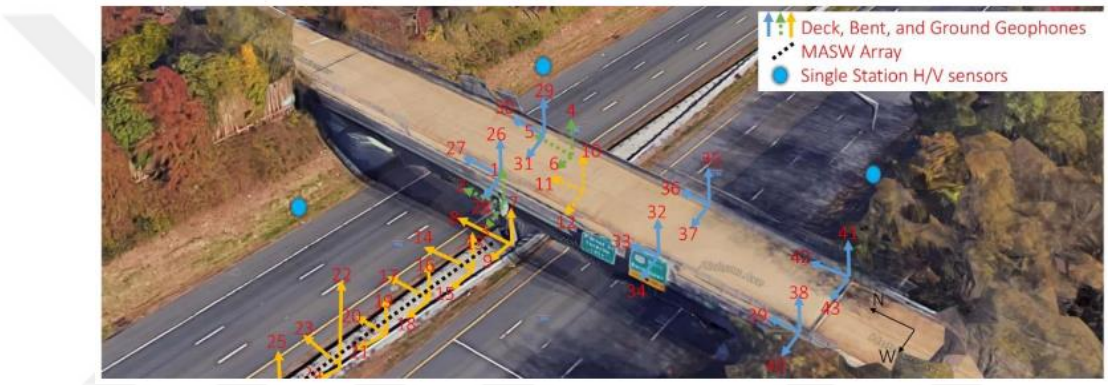

Figure 4.41. The bridge to be tested and its instrumentation (Farrag et. al., 2019).

Large mobile shakers and field support vehicles have enabled new types of field studies to be conducted, according to Stokoe et al. (2019). These studies include noninvasive shear wave velocity profiling using surface wave methods, deep downhole testing using P and S waves, parametric studies to evaluate the effects of stress state on wave velocities and strain amplitude on shear modulus nonlinearity, in-situ liquefaction testing and affecting parameters, and soil-structure interaction under dynamic loading on scaled structural systems in the field. In a shallow Vs profiling project, thumper truck was used to assess if there was a weak zone under a dam spillway within the first 8m from the surface. Using the SASW method, thumper truck was used as an active source and generated sinusoidal waves from 400Hz to 20Hz in order to obtain the Vs profile (Figure 4.42). No weak zone was determined after the tests.

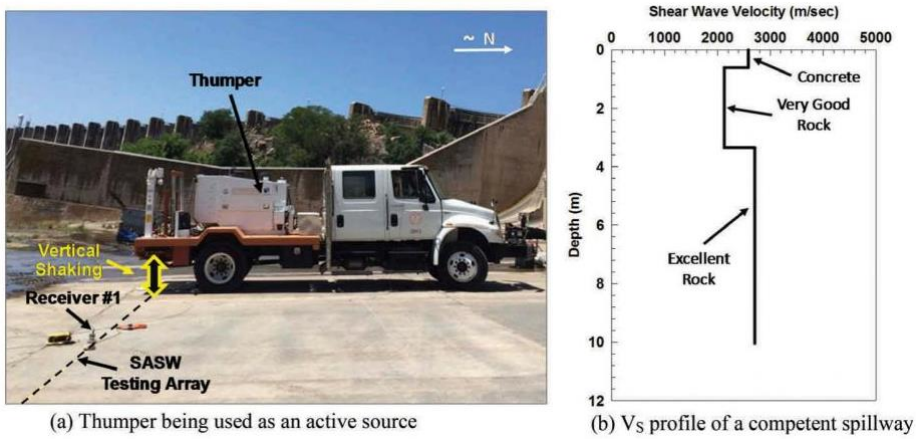

(a) Thumper being used as an active source

(b) V_S profile of a competent spillway

Figure 4.42. (a) Thumper truck used as an active source in SASW testing, (b) Resultant Vs profile (Stokoe et al., 2019).

In a deep Vs profiling project, to describe a possible geological storage site for spent nuclear fuel and high-level radioactive waste, Liquidator was employed as an active source. in Yucca Mountain, Nevada (Figure 4.43). The SASW method was implemented to profile over 300m of depth and a number of 17 Vs profiles were obtained (Figure 4.44).



Figure 4.43. Deep Vs profiling using Liquidator (Stokoe et al., 2019).

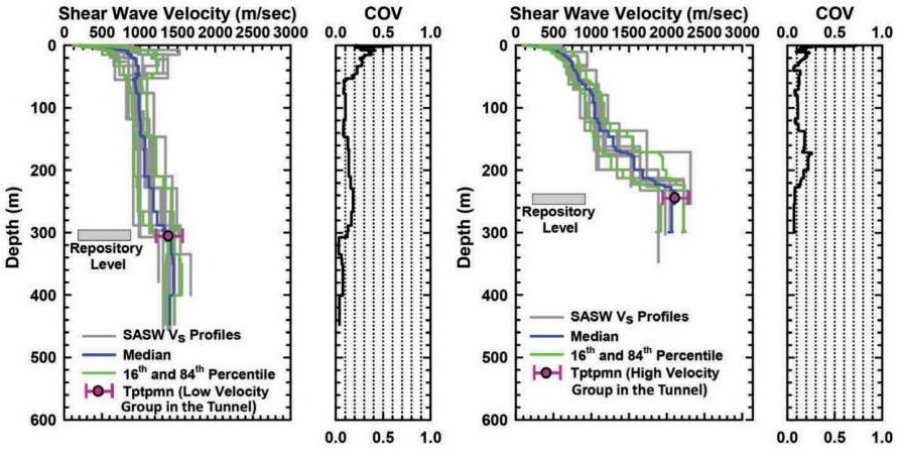

Figure 4.44. Obtained Vs profiles, (a) Softer site, (b) Stiffer site (Stokoe et al., 2019).

For a very deep Vs profiling (over 500m) project at a site in Georgia where a new nuclear power plant may be constructed, Liquidator was modified to create higher force levels at frequencies between 0.65Hz to 1.3Hz. Before the modification, Liquidator was operated in the normal mode and it was obtained that the engineering bed rock level is at 340m depth. However, the trials repeated in the modified mode revealed that the actual bed rock level actually extended up to 910m (Figure 4.45.)

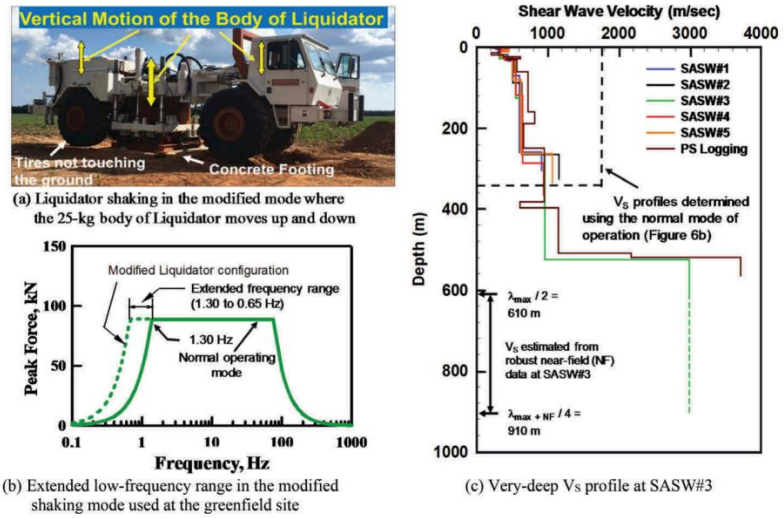

Figure 4.45. Very deep Vs profiling at Georgia (Stokoe et al., 2019).

After the 2010 Canterbury Earthquake in New Zealand, long period ground motions caused an unexpected damage due to the existence of a deep basin in Canterbury. In order to develop a 3D velocity profile of Canterbury basin up to 1000m of depth, circular receiver arrays and MASW arrays as long as 230m were used to record the waves generated by mobile shaker (Figure 4.46).

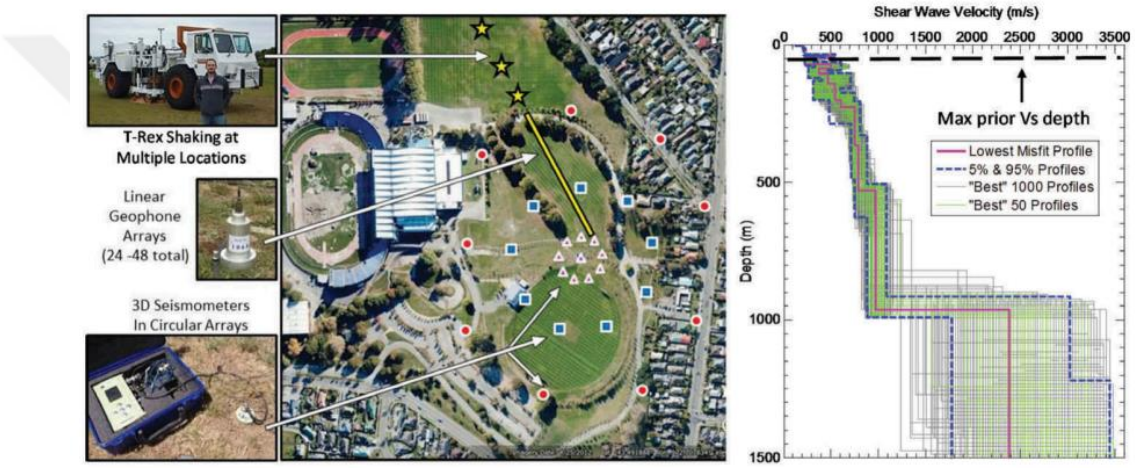

Figure 4.46. Test configuration and developed Vs profile suits for Canterbury basin (Stokoe et al., 2019).

Seismic performances of two footbridges were studied experimentally and numerically by Drygala et al., 2020. For the field experiments, high sensitivity accelerometers were used for the instrumentation (Figure 4.47). Dynamic excitations were generated by the THOMAS vibroseis (Figure 4.48). THOMAS is capable of generating vibrations of frequency linearly or exponentially fluctuating with time. Bridges were excited in an incremental frequency range of 2-60Hz for 85 seconds. Obtained experimental results were validated by numerical finite element model models using ABAQUS. Evaluation of the results revealed that the difference between experimental and numerical natural frequencies of bridges were less than 10%. It was stated that the overall agreement was satisfactory and thus, the numerical performance of structures reflected the real dynamic performance under known excitation.

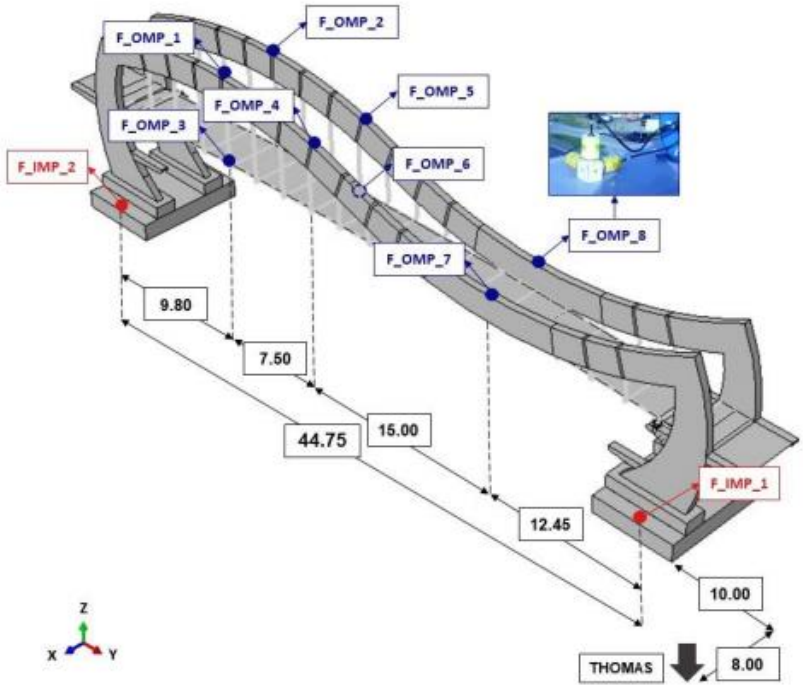

Figure 4.47. Instrumentation and the location of THOMAS at frame bridge (Drygala et al., 2020).



Figure 4.48. THOMAS vibroseis (Drygala et al., 2020).

Dadashiserej et al. (2023) conducted a full-scale, in-situ study on the 3D dynamic response of a low-plasticity silt soil deposit. Throughout the study, a multidirectional vibroseis known as T-Rex along with controlled blasting were used to generate the necessary dynamic forces. T-Rex produced horizontal shaking at a frequency of 10 Hz. To measure the particle velocity and both static and dynamic in-situ pore pressure responses of the soil deposit an array of 14 triaxial geophones and pore pressure transducers were employed.

Due to the shaking induced by T-Rex, the maximum in-situ equivalent direct simple shear strains reached 0.15%, and the excess pore pressure ratios were 14.1%. Controlled blasting generated shear waves with predominant frequencies ranging from 9.6 Hz to 14.6 Hz, resulting in maximum in-situ equivalent direct simple shear strains of 1.14% and excess pore pressure ratios of 61%.

Zalachoris et al. (2023) performed 3D numerical analyses to evaluate the effectiveness of a proposed soil improvement method against liquefaction and to assess the dynamic performance of rammed aggregate piers (Figure 4.49). As part of the Ground Improvement Testing programme in New Zealand, several sites were reinforced against liquefaction hazards using various techniques including the Rammed Aggregate Pier. The dynamic response of both unreinforced and reinforced ground was assessed through a series of dynamic response tests using the vibroseis named T-Rex, which applied 10 Hz of motion for 100 cycles with force levels ranging from 1.5 kPa to 25 kPa. The field data obtained from these tests were used to calibrate the soil profiles in numerical models, successfully capturing the hydromechanical response of the unreinforced and reinforced soil profiles. The 3D numerical results indicated that excess pore pressures and shear strains were reduced in the reinforced soil model, and these results correlated well with the field observations.

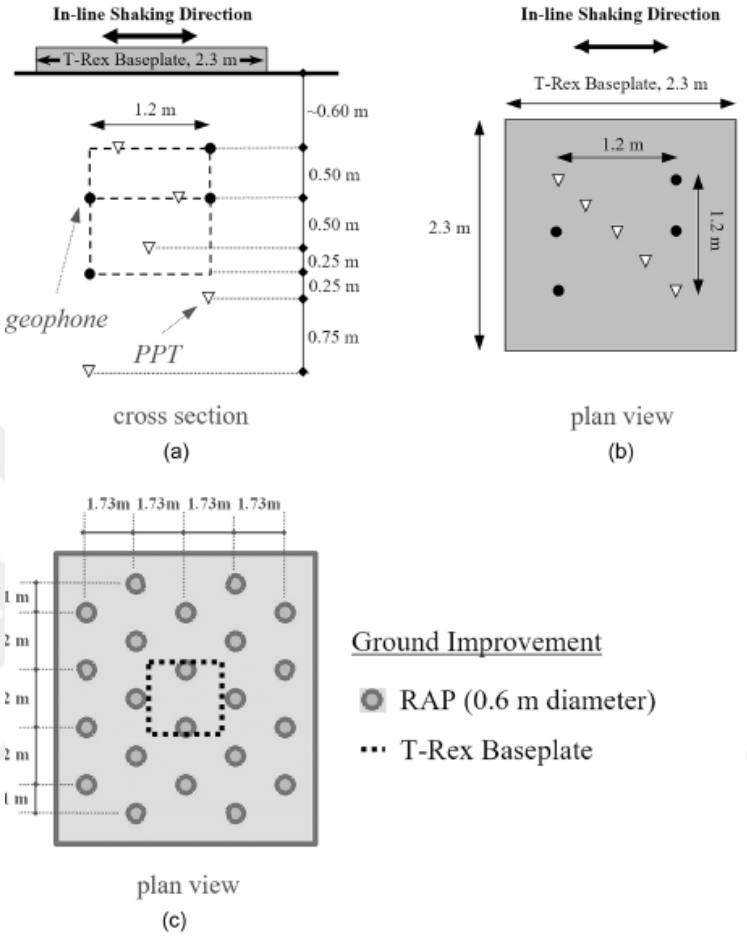

Figure 4.49. a) Cross-section view of the instrumentation and site; b) Plan view, c) Plan view of the pier grids (Zalachoris et. al., 2023).

All MSS literature are summarized in detail by means of the applied frequency range, type of MSS, shaking direction, aim of the study and further comments of the study in Table 4.3.

Table 4.3. Literature summary of the studies with Mobile Seismic Shakers.

#	*Publication*	*Frequency Range applied by MSS*	*Type of MSS*	*Shaking Direction*	*Aim of the Study*	*Comments on Results*
1	***Hryciw et. al., 1990 (journal)***	8-58Hz incremental sinusoidal (8 seconds)	Six, 22-ton (196kN) trucks with servo hydraulic vibrators	V, H, Transverse	Liquefaction of a road embankment during deep seismic reflection survey	Embankment fill was loose, cohesionless, hydraulic fill susceptible to liquefaction
2	***Bay and Stokoe,II; 1998 (project report)***	20-80Hz (20 cycles)	A modified vibroseis truck (310kN)	V	Continuous deflection testing of pavements	The RDD method is useful to observe displacements in pavements.
3	***Chang, 2002 (thesis)***	20Hz (up to 60 cycles)	Vibroseis truck (222kN)	H	Liquefaction of a test pit	Approach has the ability to effectively capture the shear strains caused by external forces and the generation of excess pore pressure, both during and after dynamic loading.
4	***Cox, 2006 (thesis)***	10-20Hz fixed sine wave (100 cycle)	T-Rex	H	Liquefaction of a test pit	Test results were found to be compatible at generating pore pressure generation curves and cyclic shear strains that were previously found in laboratory tests
5	***Frary, 2012 (thesis)***	15-120Hz sine wave (12 seconds)	Thumper	V	To discover the unknown faults	High resolution seismic refection surveys discovered the unknown faults in Reno, Nevada.

6	***Leblanc, 2013 (thesis)***	30-100Hz (10 cycles)	T-Rex and Thumper	V	To determine the stiffness properties of soil under both linear and nonlinear conditions	The behavior of the constrained modulus in response to stress and strain is complex and non-linear. It is affected by various factors, including the degree of over-consolidation and cementation in the soil, as well as the positioning of sensors within the array.
7	***Roberts, 2014 (thesis)***	10-30Hz (up to 500 cycles)	T-Rex	H	Evaluation of the liquefaction susceptibility	Obtained dynamic soil parameters of WLA sand are consistent with the literature.
8	***Sahadewa, 2015 (journal)***	30-50Hz (8-10 cycles)	T-Rex	H	In order to determine the dynamic material properties of waste material in landfills	Shear modulus reduction curves suggested for Municipal Solid Waste are similar to the previous ones, but not exactly the same.
9	***Stokoe et. al., 2016 (workshop paper)***	10Hz 100 cycle (10 seconds)	T-Rex	H	Evaluation of the effectiveness of the improvement methods to mitigate liquefaction	Obtained results from staged loading tests successfully identifies the effects of ground improvement methods.
10	***Stokoe et. al., 2017 (conference paper)***	20-50Hz fixed sine wave (10 full amplitude, 3 tapered amplitude)	T-Rex	V	To obtain the P and S wave profiles in boreholes	The set of VP and VS profiles was deemed reasonable because the calculated and measured total travel times for both P and S waves showed a good level of agreement.
11	***Stokoe et. al., 2019 (conference paper)***	20-400Hz	Thumper	V	Shallow Vs profiling a site	Thumper could generate the required lower frequencies much better than a hammer or drop-weight impacts which is essential for shallow profiling.

12	***Stokoe et. al., 2019 (conference paper)***	0.65-1.3Hz	Liquidator (using modified mode)	V	Very deep Vs profiling a site	Proposed technique enables high resolution deep profiling up to 1000m
13	***Farrag et. al., 2019 (conference paper)***	1-15Hz (32 seconds)	T-Rex	V	To assess the seismic performance of a full scale bridge	T-Rex experiments reveal that DSSI incorporated numerical results are more realistic than fixed foundation solutions.
14	***Drygala et. al., 2020 (journal)***	2-60Hz incremental sine wave (85 seconds)	Thomas	V	To determine the dynamic performance of full scale footbridges	The difference between obtained natural frequencies between experimental and numerical results are less than 10%
15	***Boaga et. al., 2021 (journal)***	10-80Hz sine wave (16-20s)	IVI Mark	V	To assess the soil's non-linear behavior while conducting a seismic reflection study.	Non-linear soil response was clearly observed on surface wave velocities, strains and H/V ratios measurements,
16	***Bertero et. al. 2022 (journal)***	5-50Hz chirp (20s, 5min sets)	T-Rex	H, V	To compare the pros and cons of experimental modal analysis to ambient vibration analysis	Experimental modal analysis could reveal more yield mode shapes especially above 11Hz but ambient vibration analysis was found to be more consistent for modal estimates
17	***Wang et. al., 2022 (journal)***	15-100Hz incremental sine wave in 12s and nine scaled earthquake records	T-Rex	H,V	To evaluate the effectiveness of meta-material based barriers and foundations in active isolation tests	Periodic barriers can successfully restrain the vibrations and perform much better than empty trenches. Increasing barrier length enhances the isolation performance.

18	***Zhang et. al., 2022 (journal)***	15-100Hz incremental sine wave in 12s and nine scaled earthquake records	T-Rex	H,V	To evaluate the effectiveness of meta-material based barriers and foundations in passive isolation tests	The use of periodic foundations and barriers together as a passive isolation system is useful for the mitigation of the dynamic motions reaching the structure of interest
19	***Dadashiserej et. al., 2023***	10Hz sine wave for 4s and blasting	T-Rex	H	To assess the dynamic response of low-plasticity silt soil deposit	Comparison of the dynamic responses and soil properties obtained from two different field-testing techniques confirms the effectiveness of controlled blasting.
20	***Zalachoris et. al., 2023***	10Hz 100 cycle sine wave with varying force levels from 1.5kPa to 25kPa	T-Rex	H	To assess the rammed aggregate pier performance under dynamic loading in liquefiable soils	Improved soil profiles experienced reduced excess pore pressures and lower shear strains compared to unreinforced profiles.

4.3. Experimental Studies with Full Scale Railway Embankments

Li et al. (2017) conducted a study on the impact of heavy haul trains on railway embankments by performing field tests and analyzing vibrations. The study involved three embankments of varying heights (6.6m, 8.1m, and 11.9m) that were equipped with accelerometers (as shown in Figure 4.50). The accelerometers were anchored vertically to the flat ground during the test, and the acceleration signals of the rail, sleeper, and embankment surface were recorded. The researchers then analyzed the propagation characteristics of ground vibration with distance from the track center. The results of the study showed that horizontal vibration was dominant near the track but decreased rapidly and became comparable to vertical levels as the distance from the track center increased. Additionally, the embankment surface

exhibited another dominant frequency zone between 30 and 80 Hz, which was attributed to dynamic excitation.

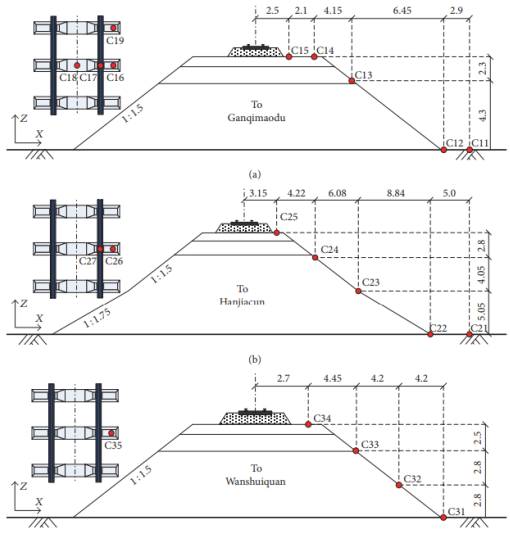

Figure 4.50. Railway embankment models (Li et al., 2017).

A study by Lehtonen et al. (2015) presents the results of a full-scale embankment failure experiment was conducted in Perniö, Finland. The experiment involved loading an instrumented railway embankment constructed on a soft clay foundation over a period of 30 hours with the help of a heavy train coming to a standstill on the embankment (Figure 4.51). The purpose of the experiment was to gather field data of a failure caused by a rapidly applied load, with a focus on the pore pressure response in the clay foundation layer. The embankment failed at T=29:57 under a surcharge load of 87kPa. The failure was triggered by an undrained creep rupture, and the observed shear geometry indicated an asymmetric bearing capacity mechanism of failure. The instrumentation included 37 piezometers and nine automatically monitored inclinometer tubes.



Figure 4.51. Instrumented railway embankment loading experiment (Lehtonen et al., 2015).

Chen et al. (2016) conducted an experimental study on the tensile strength of geogrids embedded in railway embankments. They used water bags to create a model of the subsoil and measured the settlement of the subsoil by the vertical deformation of the water bags. Optical fiber sensors were used to separately measure the tensile force of the. The geogrid reinforcement used in the experiment had a tensile strength value of Tult:130kN/m. The embankment was 2.7 m high and 5.5 m long with a crown width of 5 m and a side slope of 1.5H to 1V (Figure 4.52). After the construction of the embankment, the measured tensile force of the geogrid caused by the spreading force was about 12% of that calculated by using the Chinese railway standard.

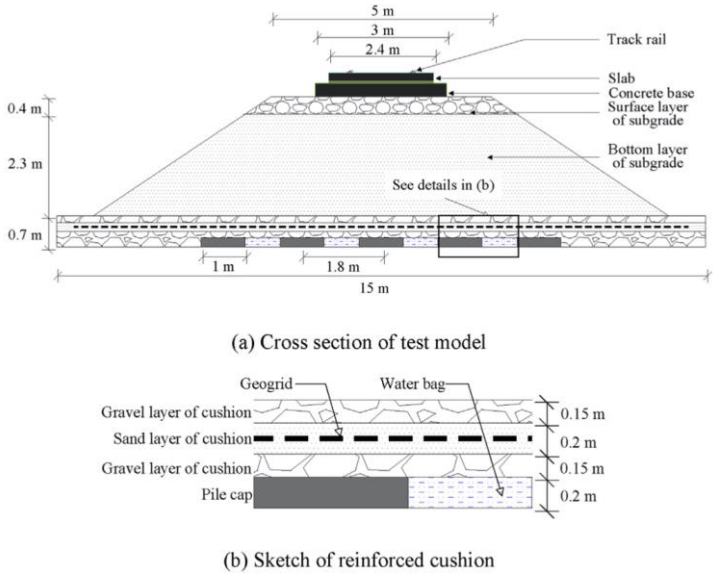

Figure 4.52. Experimental model (Chen et al., 2016).

The study by Feng et. al. (2021) conducted full-scale laboratory experiments to estimate dynamic load responses on a ballasted track using multiple sensors and validated computer models. The laboratory model consisted of a full-scale track with eight ties, ballast, subballast, and embankment (Figure 4.53). Three different speeds and axle load configurations were applied sequentially onto the track using eight actuators, capturing both slow-moving freight and high-speed passenger train loads. Vibration velocities and dynamic soil stresses were recorded at different locations on ballast surfaces and ties, and transient and permanent deformations were measured in the track substructure layers and for all eight ties. The study found that train speed significantly affects vibration velocity, and dynamic soil stresses increase with increasing axle load.

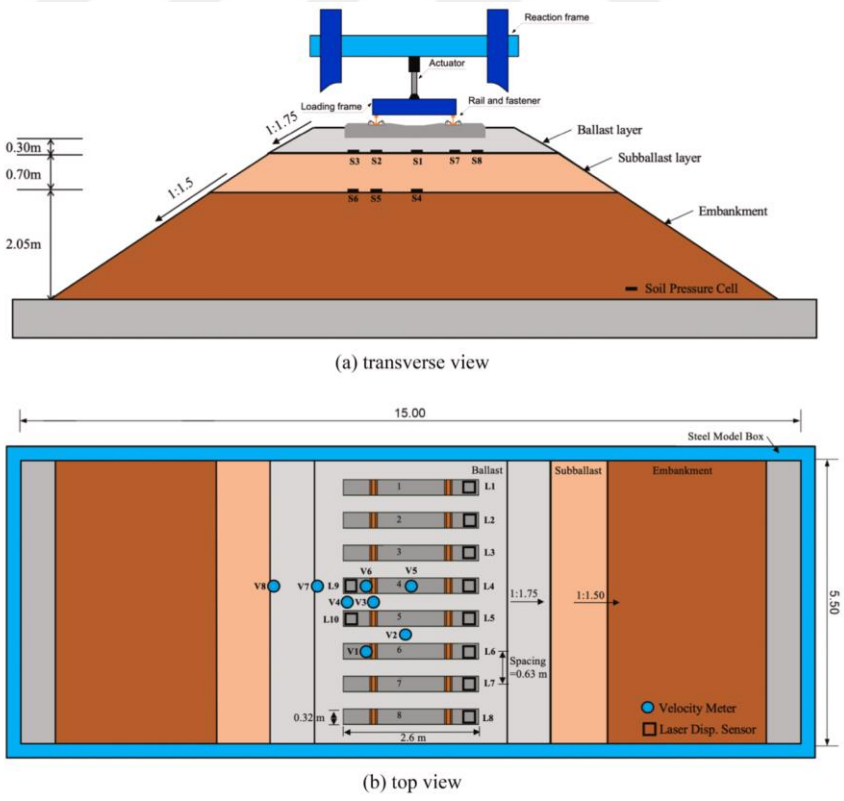

Figure 4.53. Experimental set-up (Feng et. al., 2021).

The study by Wu et al. (2019) investigated the performance of cement-fly ash-gravel (CFG) pile-supported embankments over completely decomposed granite (CDG) soil foundations in a full-scale test of high-speed railway embankments (Figure 4.54). The study conducted a numerical analysis using the finite-element software PLAXIS 2D to compare the applicability of different numerical models in terms of settlements, horizontal displacements, and load transfer from soils to piles. The instrumented embankment is located in South China and is used for 250km/h speed trains. The study compared two sections of the embankment, one reinforced with geogrid and CFG piles (G1) and the other only reinforced with geogrid (G2) for reference. Both sections had a height of 7.7 and 4.05 m, respectively, a crest width of 13.4 m, and a side slope of 1V:1.5H. The geogrid layer in both sections consisted of double geogrids with a tensile strength of 1400 kN/m in both longitudinal and transverse directions, sandwiching well-graded ballast of 0.6 m in thickness. The study found that ground surface settlements can be effectively reduced using longer piles with larger surface area and experimental and numerical results were in good agreement.

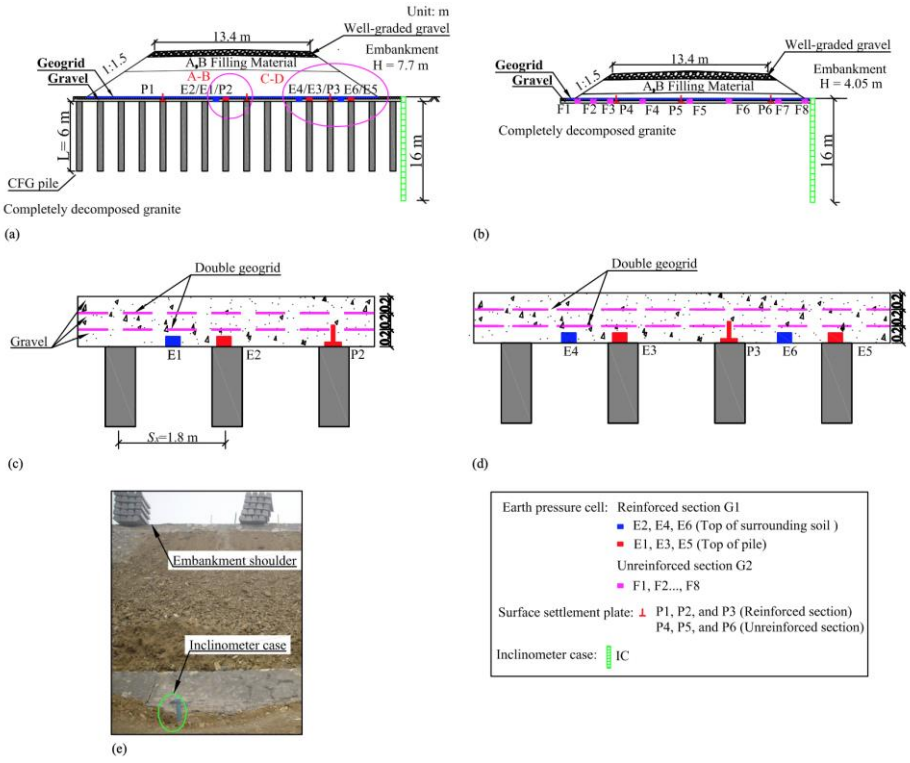

Figure 4.54. Instrumented railway sections and its details (Wu et. al.,2019).

4.4. Experimental Studies with Shaking Table and Centrifuge Tests

Ling et al. (2009) conducted a study where they modeled and tested slope instability using a centrifuge (Figure 4.55). The researchers utilized sand mixed with fines as the material and created slopes with varying angles and heights within a sturdy aluminum container. The sand's relative density (Dr) was 89%, and the researchers simulated rainfall by using a nozzle system during the tests. The findings of the experiment demonstrated that the centrifuge tests were successful in mimicking slope instability as the modeling technique was validated using centrifuge models with different heights, geometries, and properties. The study also revealed that instability in slopes caused by rainfall could be interpreted as a decrease in apparent cohesion.

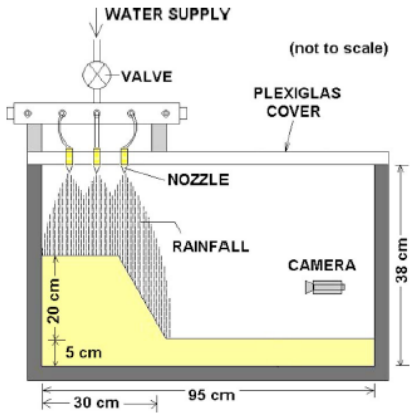

Figure 4.55. Centrifuge experiments (Ling *et al*., 2009).

Tamate et al. (2012) conducted a study to examine how heavy rainfall affects the dynamic response of slopes. Silica sand material was used in centrifuge tests to create a slope model with a 30° angle, which was placed in a rigid box measuring 50x20x40cm. Figure 4.56 shows the experimental setup. The study primarily aimed to investigate the failure mode of the slope in the shallow section under undrained conditions. It was found that heavy precipitation increases the saturation of the soil which leads to multiple flow failures in the shallow section of the slope.

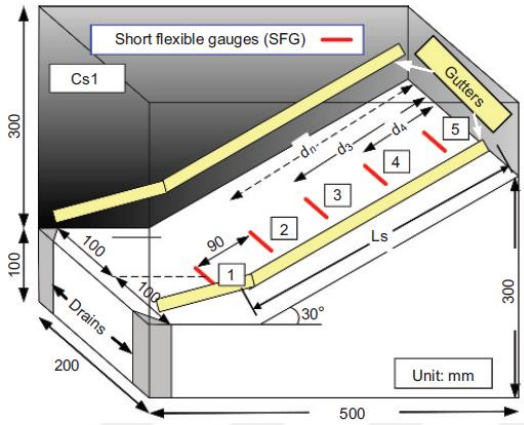

Figure 4.56. Test set-up (Tamate et al., 2012).

Lin and Wang conducted a study in 2006 to investigate the seismic behavior of a slope. They created a model slope with dimensions of 0.5x1.3m and a slope angle of 30° using uniform medium sand. To determine the seismic performance of the slope model, they conducted shaking table tests using a large plexiglas sided box measuring 4.4x1.3x1.2m. The experiments were conducted at a scaling factor of 1/20. Figure 4.57 shows the model that was tested.

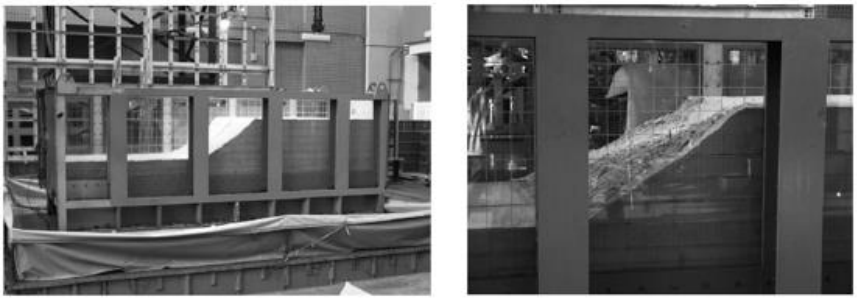

Figure 4.57. Shake Table Studies (Lin and Wang, 2006).

Results show that the slope model exhibited elastic behavior when subjected to accelerations up to 0.4g. The numerical results indicated that there were minimal boundary effects based on the FLAC modeling, but significant soil amplification was observed,

particularly when non-linear behavior occurred, which could potentially impact the slope's failure.

Srilatha *et al*. (2013) conducted a study to examine how the frequency content affects the dynamic response of slopes. Clayey soil material was used for their experiments and tested both reinforced and unreinforced slopes on a shake table in a laminar box. To reinforce the slopes, biaxial geogrids with tensile strength of 26kN/m were utilized. During the experiments, slope models with angles of 45° and 60° were exposed to 0.3g of acceleration with various predominant frequency values of 2, 5, and 7 Hz. The study's conclusion suggests that as the frequency increases, the displacement measurements also increase.

A series of shaking table experiments were performed by Toksoy (2014) in order to investigate the effect of geotextile reinforcement on the seismic performance of highway embankment models as well as to evaluate the dynamic motion characteristics on the seismic behavior of geosynthetic reinforced highway embankments. Reduced scale (1/50) shake table experiments were conducted for unreinforced and geotextile reinforced highway embankment models with the same dimensions and obtained results were compared by means of selected performance indicators. Experimental program can be seen in Table 4.4.

Table 4.4. Experimental program (Toksoy, 2014).

Test No:	PGA	Frequency	Reinforcement Type	Number of Cycles	Slope Inclination
1	0.30	2	Unreinforced	40	45°
2	0.30	5	Unreinforced	40	45°
3	0.30	7	Unreinforced	40	45°
4	0.30	14	Unreinforced	40	45°
5	0.30	2	Geotextile	40	45°
6	0.30	5	Geotextile	40	45°
7	0.30	7	Geotextile	40	45°
8	0.30	14	Geotextile	40	45°
9	0.50	2	Unreinforced	40	45°
10	0.50	5	Unreinforced	40	45°
11	0.50	7	Unreinforced	40	45°
12	0.50	14	Unreinforced	40	45°
13	0.50	2	Geotextile	40	45°
14	0.50	5	Geotextile	40	45°
15	0.50	7	Geotextile	40	45°
16	0.50	14	Geotextile	40	45°
17	0.35	-	Unreinforced	-	45°
18	0.35	-	Geotextile	-	45°
19	0.30	2	Unreinforced	40	30°
20	0.30	5	Unreinforced	40	30°
21	0.30	7	Unreinforced	40	30°
22	0.30	14	Unreinforced	40	30°
23	0.30	2	Geotextile	40	30°
24	0.30	5	Geotextile	40	30°
25	0.30	7	Geotextile	40	30°
26	0.30	14	Geotextile	40	30°
27	0.50	2	Unreinforced	40	30°
28	0.50	5	Unreinforced	40	30°
29	0.50	7	Unreinforced	40	30°
30	0.50	14	Unreinforced	40	30°
31	0.50	2	Geotextile	40	30°
32	0.50	5	Geotextile	40	30°
33	0.50	7	Geotextile	40	30°
34	0.50	14	Geotextile	40	30°
35	0.35	-	Unreinforced	-	30°
36	0.35	-	Geotextile	-	30°

Silivri sand was used for the experimental studies. The geotextile material was a woven type with reduced reinforcement stiffness with respect to the Iai (1989). Instrumentation plan includes 9 accelerometers and 3 LVDT's as represented in Figure 4.58.

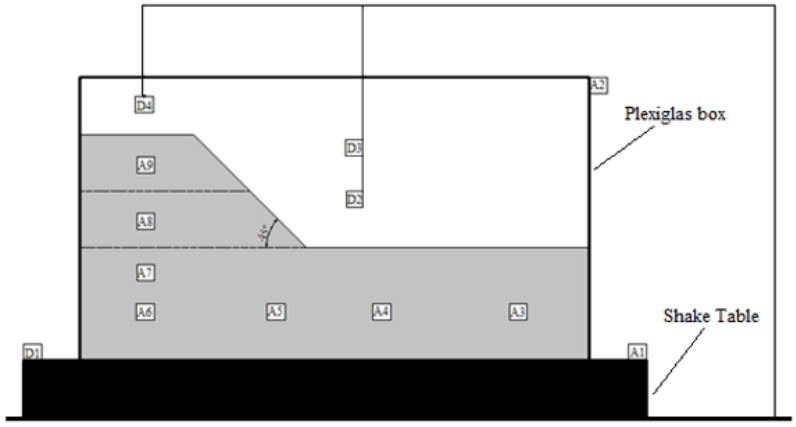

Figure 4.58. Instrumentation plan (Toksoy, 2014).

The results obtained indicate that using geosynthetic reinforcement was successful in decreasing the transmitted acceleration measurements in embankment models that have slope angles of 45° and 30°. The reduction ratio was up to 56% for the 45° slope angle and up to 55% for the 30° slope angle, with higher reduction ratios near the crest of the embankments.

Edinçliler and Toksoy (2017a) focused on the efficiency of geotextile reinforcement on the energy absorption capacity under several different dynamic motions. As represented in Figure 4.59, Amplification Factors are clearly less in reinforced models than unreinforced cases. Also, lower frequency ranges tend to de-amplify more than higher frequency ranges of this study.

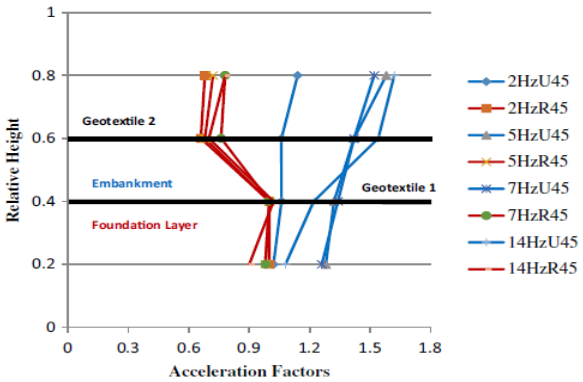

Figure 4.59. Amplification factors (Edinçliler and Toksoy, 2016).

Edinçliler and Toksoy (2017b) revealed how the use of geosynthetics can enhance the dynamic response of highway embankments and to mitigate earthquake induced damages. As can be seen in Figure 4.60, Transmitted Accelerations (TA) and Spectral Accelerations (SA) at crest level are 55% and 50% less in reinforced model subjected to 0.5g of acceleration and 5Hz of predominant frequency, respectively.

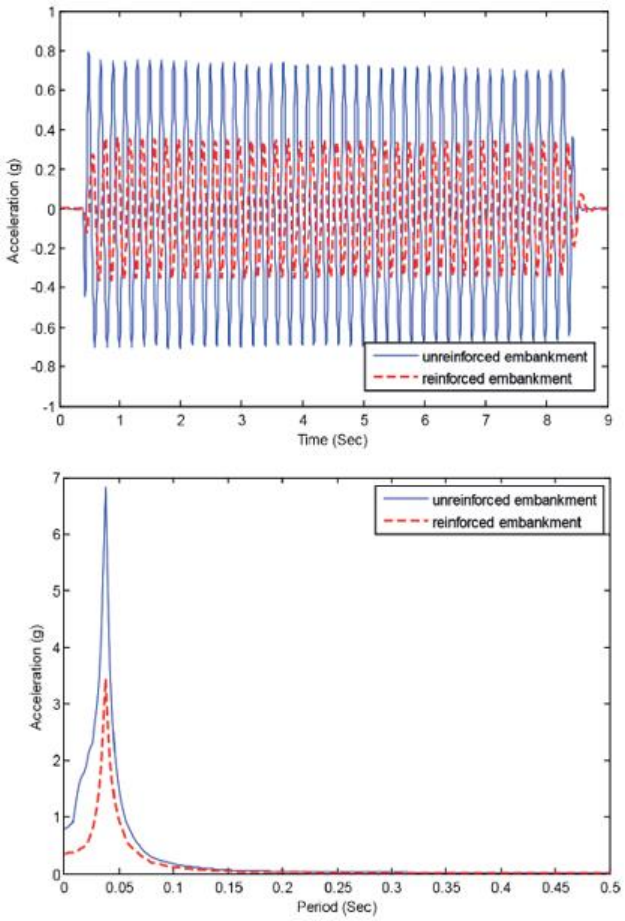

Figure 4.60. Comparison of crest level TA and SA values (Edincliler and Toksoy, 2017).

In a study conducted by Lin et al. (2015), the seismic behavior of embankment slopes using various reinforcement techniques were assessed through a series of experiments on a shaking table. Seismic performance tests were performed on unreinforced, 2-layer geogrid reinforced and 4-layer geogrid reinforced embankment models which were 1:8 times scaled

(Figure 4.61). A real earthquake record (Figure 4.62) and white noise was used for the shake table experiments. The test findings indicate that the reinforced embankment slope has a higher natural frequency compared to the unreinforced embankment slope. The study also revealed that the reinforced embankment slope is less susceptible to seismic activity. Furthermore, the horizontal acceleration magnification decreases as the peak value of horizontal acceleration increases, and the reduction ratio is greater for the reinforced case.

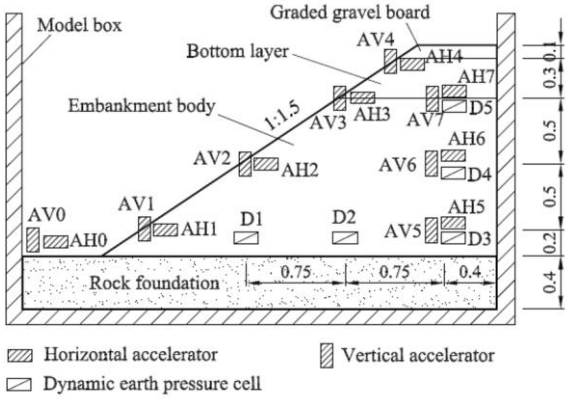

Figure 4.61. Embankment model and instrumentation plan (Lin et. al., 2015).

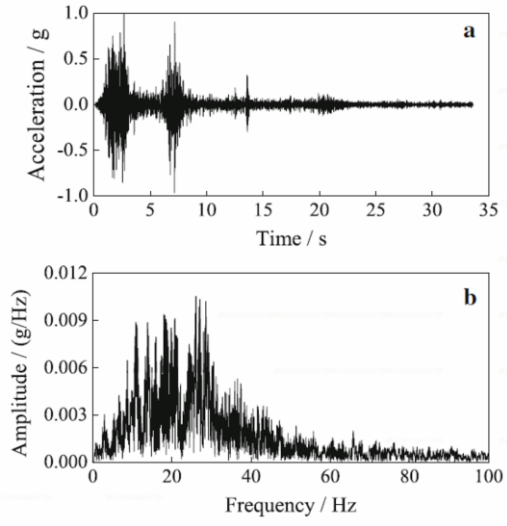

Figure 4.62. Acceleration-Time History and Fourier Amplitude Spectrum of Wenchuan Earthquake (Lin et. al., 2015).

Dynamic response and damage characteristics of a road embankment were evaluated by site investigations, a series of scaled shaking table experiments and numerical simulations by Wang et. al., 2018. Findings from the field investigation indicate that the upper section of the road embankment is susceptible to developing cracks under tension, whereas the lower section is more prone to deformation caused by compression and shearing forces.Two real earthquake records and an artificial motion were used for the dynamic response analyses (Figure 4.63). Laboratory experiments and numerical simulations have demonstrated that the way accelerations are transmitted depends on both the strength of the initial ground motion and the height of the road embankment. These studies have revealed that when the peak ground acceleration of the initial ground motion is low, the amplification of peak ground acceleration increases linearly with the height of the embankment. However, once a certain threshold is reached, non-linear amplification occurs, and eventually, when the peak ground acceleration of the initial ground motion is sufficiently high, the response shifts from amplification to attenuation. Responses in time and frequeny domain are given in Figure 4.64.

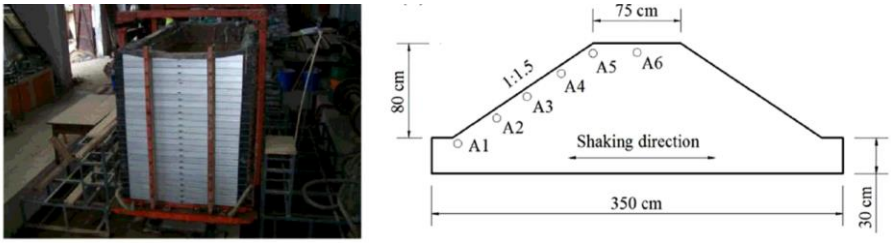

Figure 4.63. Shaking table model and dimensioning (Wang et. al., 2018).

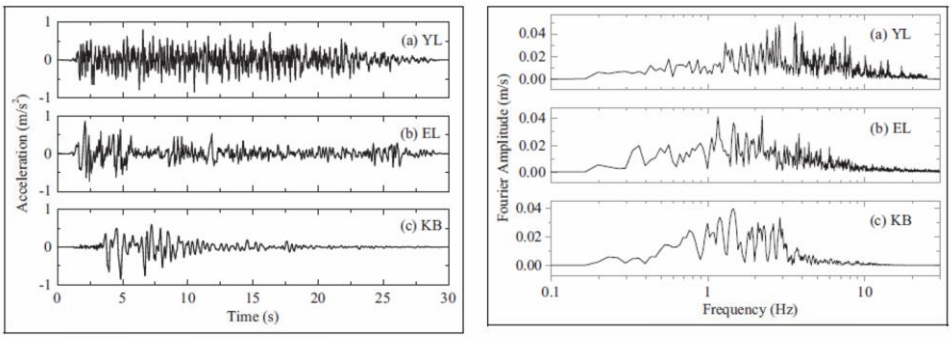

Figure 4.64. Responses in Time and Frequency Domain, (a) Artificial motion, (b) El Centro Earthquake, (c) Kobe Earthquake (Wang et. al., 2018).

Nakazawa et.al., 2020; performed shake table experiments of a full-scale road embankments reinforced with flexible container bags. The failure of highway embankments which are not already reinforced during major earthquakes and restoration process usually takes a long time and costs much money in Japan. This new method proposes placing flexible container bags at the bottom of the embankment slope to make an earthquake resistant highway embankment (Figure 4.65).

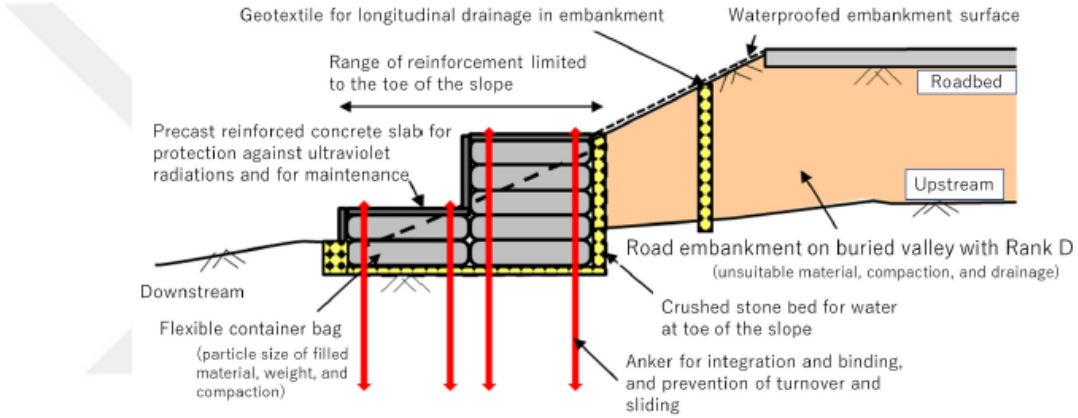

Figure 4.65. Method of using soil bags for embankments (Nakazawa et.al., 2020).

Two different full scale highway embankments were constructed. One of the models were constructed with one-tier type of flexible soil containers whereas the other one was constructed with two-tier type (Figure 4.66). Models were instrumented with accelerometers and 3D laser scanners. Shaking table experiments were performed on E-Defense. Input dynamic excitations were four individual acceleration scaled sine wave (5Hz and 40 cycle). Obtained results after dynamic performance tests reveal that two-tier type of reinforcement is more effective than the one-tier one by means of seismic performance as one-tier reinforced model was slightly damaged under dynamic loading. Also acceleration amplification rates near the crest of the embankment were less in two-tier reinforced model.

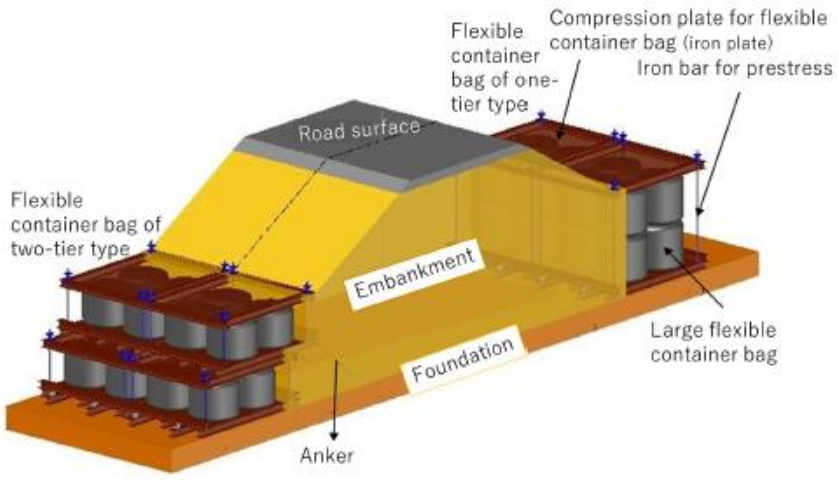

Figure 4.66. Outline of the experimental models (Nakazawa et.al., 2020).

Han et. al. (2021) conducted experiments using a shaking table to assess how well embankments reinforced with plastic geogrids perform under seismic conditions. A model test study of Zhounan Expressway in China was represented as a1:20 scale model in laboatory conditions (Figure 4.67). Various dynamic loads from real earthquake records to white noise were subjected to the unreinforced and reinforced embankment models. The test outcomes indicated that the reinforced embankment had an initial natural frequency that was 42.4% greater than the unreinforced embankment, and its initial damping ratio decreased by 19.4%. Reinforced embankment model experienced less acceleration amplification at the crest level.

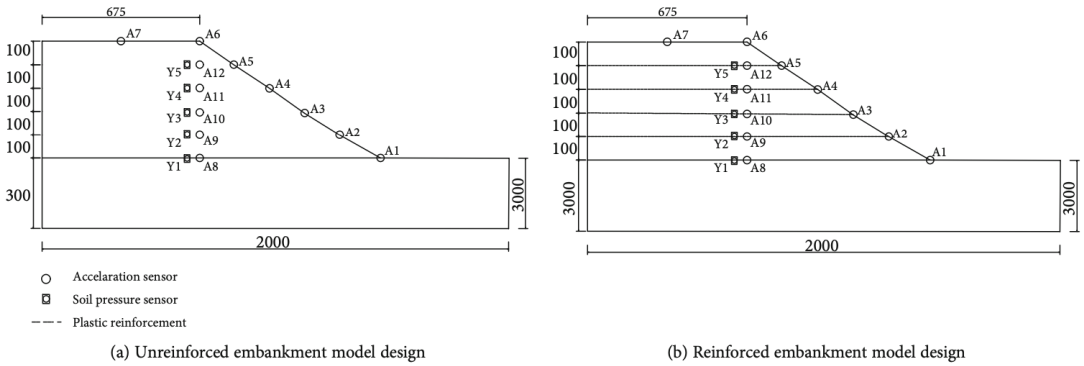

Figure 4.67. Experimental set-up (Han et. al., 2021).

Qin et al. (2024) conducted 1g shaking table tests to assess the effectiveness of a proposed hybrid pile system in mitigating excessive settlement and lateral spreading of highway embankments under dynamic loading. The experimental study included three cases of 1/50 scale reinforced highway embankment models, combining vertical and inclined piles with geogrid reinforcements. The numerical results demonstrated that the proposed hybrid pile system effectively performed by mitigating the lateral spreading and embankment settlements under the given two consecutive dynamic excitations, successfully controlling the dynamic induced deformations.

4.5. EPS Geofoam Embankments

Akay et al. (2013) performed an laboratory experiment to observe the effectiveness of EPS-block geofoam in remediating slopes under seepage flow. To assess the effectiveness of geofoam blocks, a study conducted 36 lysimeter experiments using three distinct constant water pressure levels. A Plexiglas box measuring 200x20x60cm was utilized to replicate real-world conditions and observe both immediate and lasting deformations. The laboratory configuration can be seen in Figure 4.68. The findings of the study indicate that the geofoam block system is particularly efficient to prevent the seapage induced deformations in slopes in comparison with the cases with no EPS-block geofoam.

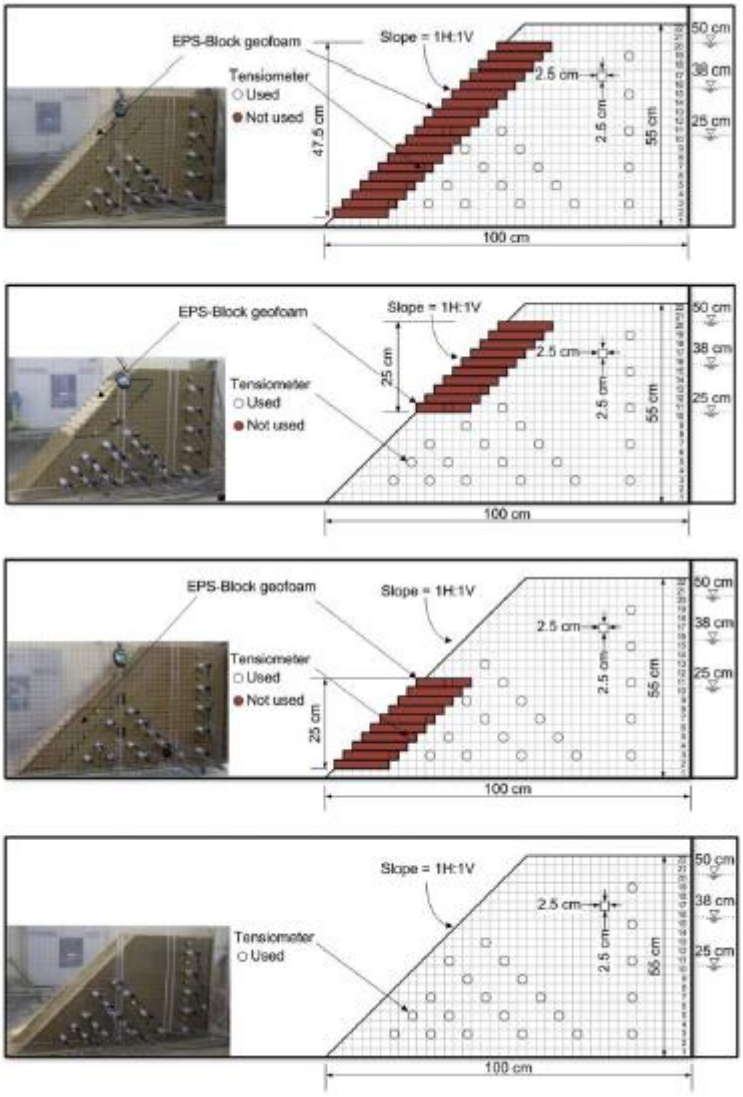

Figure 4.68. Experimental set-up and instrumentations (Akay *et al*., 2013).

A study performed by Neupane (2015) investigated the possible use of EPS geofoam in railway embankments. With the help of the numerical, laboratory and field techniques, static and dynamic deflections along the railway was investigated. In field experiments, data was collected on the vertical deflection of commuter and light rail lines by placing accelerometers on the sleepers. These accelerometers were attached to the concrete ties using glue, and were used to measure the deflection caused by a MTS machine. The results of the experiments showed

that the critical accelerations for sliding, sway, and rocking were 0.6 g, 0.2 g, and 0.3 g, respectively.

The first geofoam block roadway embankment of Turkey was constructed in 2017 in Istanbul (Ozer and Akinay, 2018). The decision to utilize geofoam blocks was made to safeguard the primary urban utility corridor concealed beneath the roadway and to minimize expenses.Both external and internal stability evaluations were performed due to the NCHRP guidelines and a total of 720m^3 of geofoam blocks were used during construction. 1 m high, 1.2 m wide and 2.5 m long blocks with a unit weight of 22 kg/m^3 were used to construct the 3 m high geofoam embankment (Figure 4.69). A number of five settlement plates were used to obtain the settlement data for over 10 months. At the completion of construction, the settlement of 16 mm on the crest was determined to be approximately 0.55% of the embankment height. The measured strain on geofoam blocks at the end of construction was lower than the strains that would cause permanent deformation. The overall cumulative geofoam block strains after construction was around 0.3%. It was suggested that, based on the settlement information, the pattern of post-construction settlements would probably be below the maximum deformation limit of 2% strain.

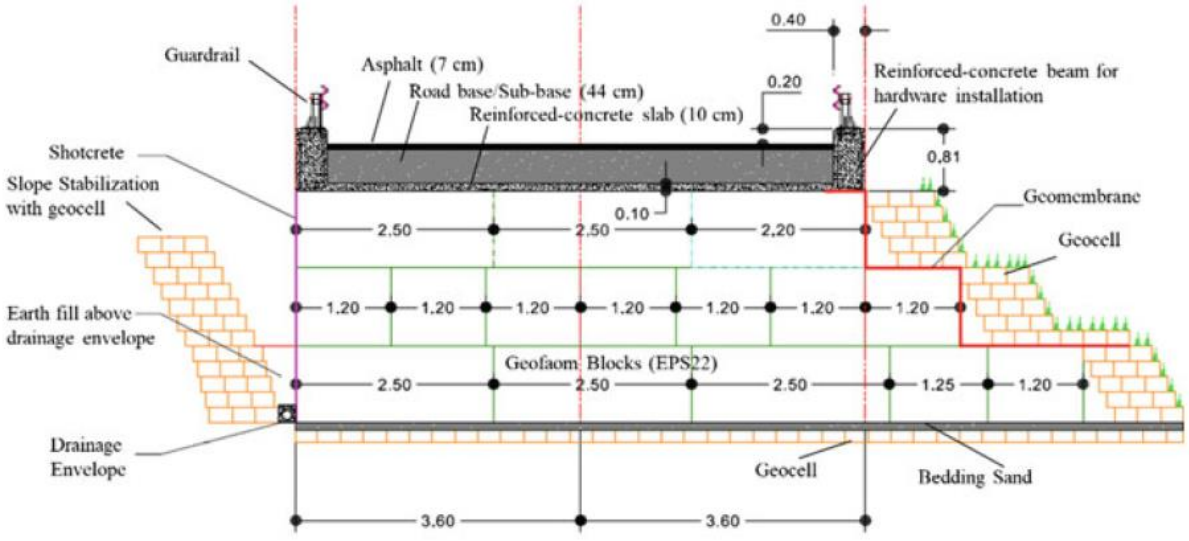

Figure 4.69. Cross section of the geofoam roadway (Ozer and Akinay, 2018).

Sloan, (2011) conducted tests on column-supported embankments and provided design recommendations. The procedure involves using columns to transfer the load of the embankment to a firm layer when building over soft ground. Sloan conducted five tests using 2 ft diameter columns arranged in a square array with varying center-to-center spacing of 6 ft to 10 ft. The instrumentation used included load cells, earth pressure cells, lead-wire extensometers, foil strain gages, and settlement profilers to measure geosynthetic strain and settlement. Surface settlement was measured using a total station. Test results revealed that adapting the Terzaghi Method is better to determine vertical stress on the geosynthetic reinforcement and adapting the Parabolic Method is preferable determine tension in the reinforcement. Figure 4.70 shows a simplified test facility and embankment.

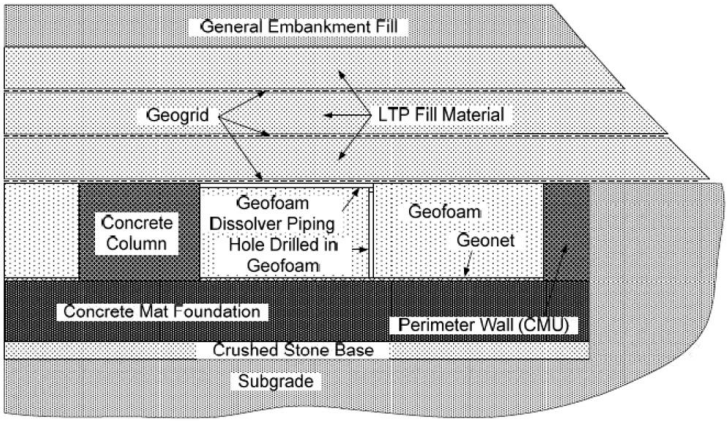

Figure 4.70. Cross section view of the embankment (Sloan, 2011).

A study by Puppala et.al., 2019 presents a case study about a bridge approach slab in Texas which experienced more than 40cm of settlement in 16 years of operation. Many different treatment methods were used to solve the settlement problem but all of them was ineffective. Finally, existing soil fill on the embankment was removed and replaced with lightweight EPS geofoam blocks. Top 1.8m of embankment soil was filled by EPS 22. Geofoam blocks were placed in three layers (60cm each) and encapsulated by a membrane to prevent water infiltration. Geofoam layers finally covered by flex base, hot mix asphalt concrete and concrete pavement as shown in Figure 4.71. During the rehabilitation with EPS geofoam blocks, four inclinometers

were instrumented at top of the geofoam layers beneath the asphalt concrete layer to measure the settlement data over time. Obtained results reveal that after the rehabillitation with EPS geofoam blocks, measured settlements were found to be only up to 2.8cm at crest level after three years of operation.

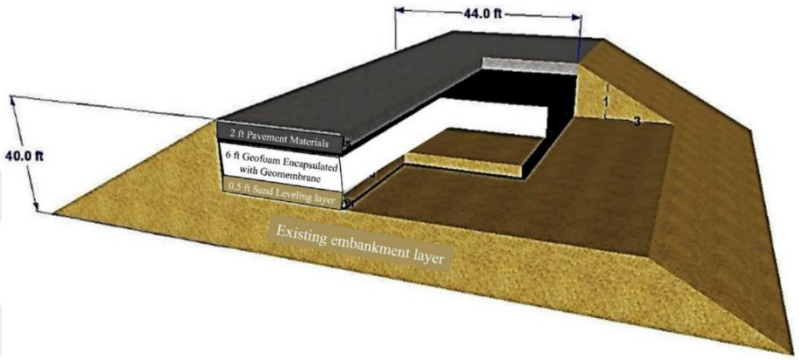

Figure 4.71. Rehabilitated highway embankment with EPS geofoam blocks (Puppala et. al., 2019).

Neto and Rodrigues (2021) conducted extensive tests on EPS geofoam embankments under various loading conditions. The embankment was tested with loads of 50,000 kg tractor placed on top of the embankment. The dimensions of the embankment were 31.4m in length, 10.8m in width, and 1.8m in height. EPS 22 material was used in three layers over a weak subgrade and covered by a 300mm cement treated base and 100mm of hot mix asphalt. The embankment was equipped with pressure cells to monitor the vertical stress propagation from the surface to the depth of the structure. The results of the field experiments showed that the elastic parameters determined in smaller samples of EPS geofoam blocks in laboratory conditions did not match the behavior observed in the field. This was due to the fact that large blocks were subjected to reduced deformation levels.

4.6. Embankments with Tire Chips-Sand Mixtures

Yoon et al. (2005) performed a study to evaluate the practicality of utilizing a combination of tire shreds and sand on road embankments. The study also examined the flammability characteristics of the mixture and assessed the potential for groundwater contamination resulting from the use of synthetic materials. To accomplish this, a trial embankment was built using a 50/50 volume ratio of tire shreds and sand and installed monitoring equipment to track the vertical settling and heat production within the mixture. Figure 4.72 shows the instrumented embankment model.

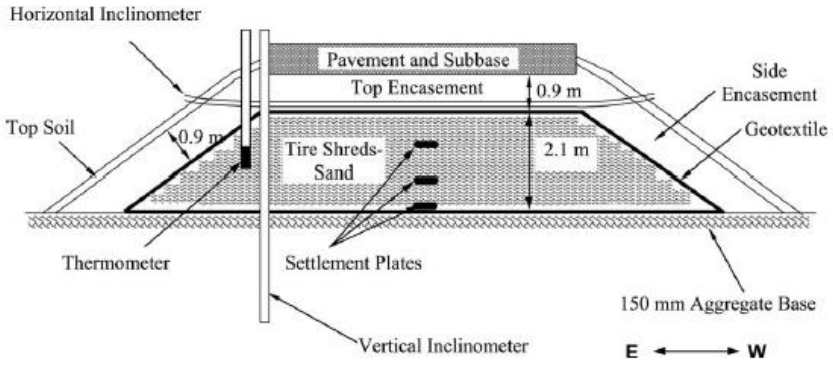

Figure 4.72. Instrumented Embankment Model (Yoon *et al*., 2005).

To improve the compressibility properties of a mixture used for embankments, a combination of scrap tire and sand were used. This mixture has the advantage of being sustainable and durable, as scrap tire is lightweight and does not biodegrade. It was observed that, settlements were only up to 10mm at crest after 360 days of operation and no signs of cracking or damage observed.

Embankment construction over soft ground may lead to some serious problems of instability and large settlements. Tanchaisawat et al. (2008) conducted a study to investigate the behavior of lightweight geomaterials made of a mixture of tire chips and sand reinforced with geogrids for use in embankment construction on soft ground. The study aimed to determine the

most suitable mixing ratio for the fill material. The researchers constructed a full-scale field test embankment with a precast wall facing at the Asian Institute of Technology (AIT) campus in Bangkok, Thailand. The geogrid reinforced embankment system was equipped with settlement plates, strain gauges, and inclinometers to measure settlement and lateral wall movement within the embankment and subsoil. The results showed that the 30:70% mixing ratio was the most suitable fill material, and the geogrid reinforced embankment system significantly reduced settlement at the ground surface by 67.5% compared to conventional backfill without foundation treatments. Additionally, the maximum lateral wall movement observed at the top of the wall 13 months after construction was 45% smaller than that of conventional sand backfill on untreated ground.

In a study conducted by Bosscher et al. in 1997, the design of highway embankments using tire chips as a lightweight material in highway construction was investigated. The study encompassed laboratory model studies, numerical analyses, and field performance evaluations of test fills. To carry out the research, a test embankment was constructed near a landfill in close proximity to Madison, Wisconsin. This location was chosen due to the presence of heavy truck traffic along the route. The test embankment consisted of eight different sections, each measuring 6 meters in length. These sections varied in terms of the thicknesses and types of tire chips used, as shown in Figure 4.73. The results of the experiments revealed some interesting findings. One notable discovery was that incorporating 30% sand by weight into the tire-chip matrix increased the modulus to a level comparable to that of pure sand. This suggests that the inclusion of sand can enhance the performance of tire chips in embankment construction.

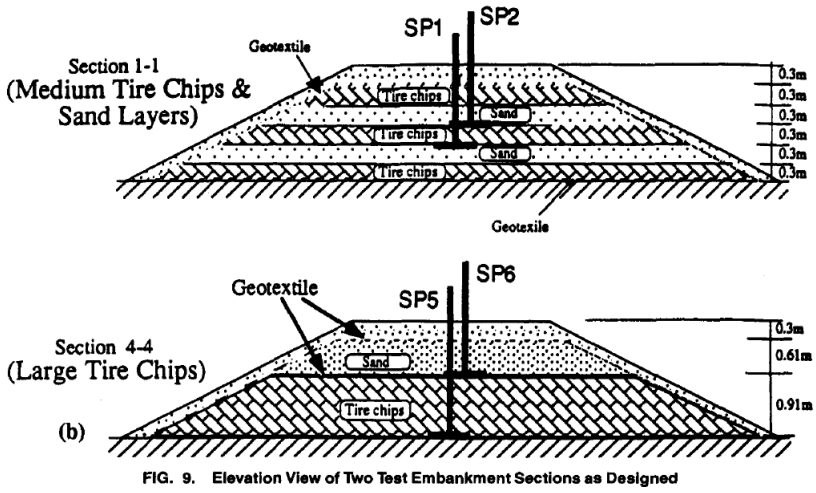

Figure 4.73. Two test section of highway embankments (Bosscher et. al., 1997).

4.7. Numerical Studies

Toksoy and Edinçliler (2023) performed numerical analyses in an attempt to simulate the field scale seismic performance tests of highway embankments by using a mobile seismic shaker as a dynamic source. To determine the local site conditions and wave propagation properties in the area, a range of geotechnical and geophysical tests were carried out, which included Pressuremeter tests, Multichannel Analysis of Surface Waves (MASW) tests, Electrical Resistance Tomography (ERT) tests, and laboratory tests. This data was then used to create two distinct models of a highway embankment, one with geogrid reinforcement and one without (Figure 4.74). These models were subjected to the dynamic motion, which is 1-100Hz sine wave, and the results were compared to evaluate the effectiveness of the geogrid reinforcement. Conclusion remarks include that the use of geogrid reinforcement reduced the peak transmitted accelerations by 78% and total displacements by 20% in comparison with the unreinforced model.

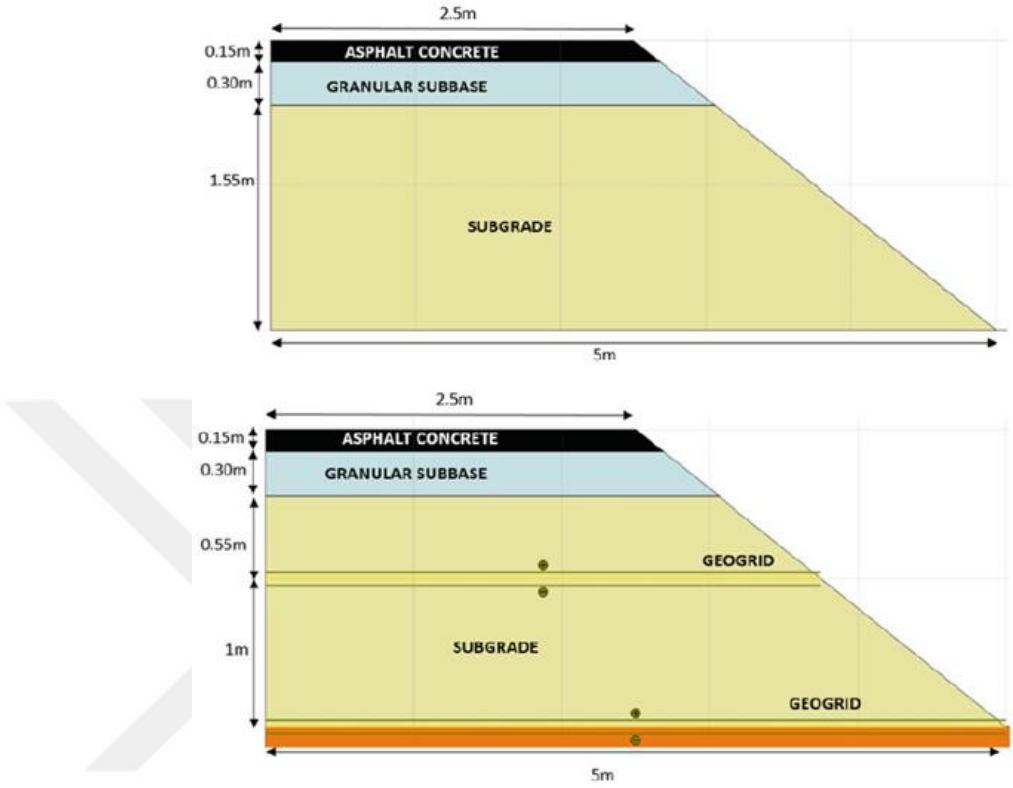

Figure 4.74. Highway Embankment Models (Toksoy and Edinçliler, 2023).

Edinçliler and Toksoy (2022) performed numerical analysis to determine the effects of geogrid reinforcement on the dynamic performance of lightweight embankments with EPS Geofoam inclusions for the first time in the literature. Non-linear seismic response analyses were performed using Gökçeada and Kocaeli Earthquake records. The 1993 AASHTO regulations were taken into consideration when defining the criteria for designing the embankment and selecting the appropriate materials. The geogrid material chosen has an ultimate tensile strength of 40kN/m^2 and meets the FHWA NHI-07-092 regulations. Additionally, the EPS geofoam material has a density of 20kg/m^3. Figure 4.75 presents the numerical model.

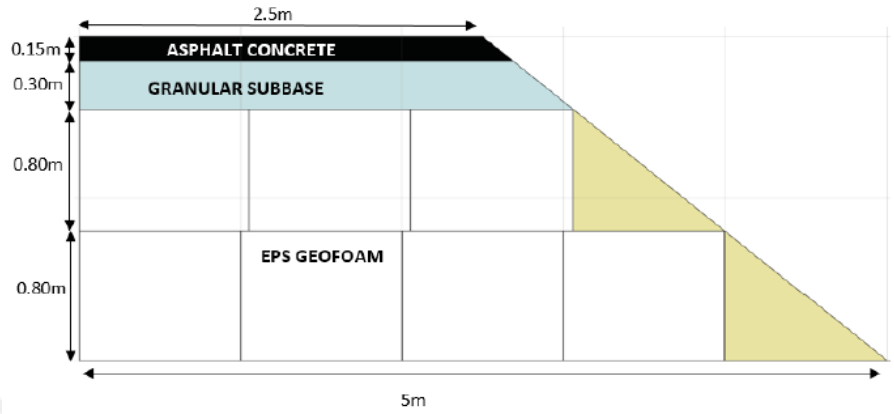

Figure 4.75. Dimensioning of the model (Edinçliler and Toksoy, 2022).

Obtained results were compared and evaluated in terms of total displacement and transmitted acceleration values. The proposed geogrid reinforcement in the foundation method could significantly reduce the total displacement values by up to 29% and the transmitted acceleration values up to 86%.

Chakraborty and Sawant (2024) investigated the dynamic response of an embankment model on liquefiable soil. Their numerical study examined the effectiveness of gravel berms and stone columns in mitigating liquefaction under various dynamic motions. FEM analyses conducted with PLAXIS 3D indicated that the stone column method is more effective than the gravel berm technique in mitigating liquefaction. The study also found that the pore pressure of the foundation soil and the settlement of the embankment are directly affected by the Arias Intensity of the dynamic input excitation.

In a recent research by Toksoy and Edincliler (2024), the dynamic performance of lightweight EPS Geofoam embankments were investigated by conducting 3D FEM analyses for the first time in the literature. A series of geotechnical and geophysical experiments were performed to assess the foundation soil properties and site response of the test area which were later integrated into the 3D FEM analyses. The numerical results revealed that total displacements and crest level settlements were impressively reduced by 82% and 89%, respectively in comparison to the Unreinforced Embankment model (Figure 4.76). Transmitted

accelerations were also found to be up to 77% less in EPS Geofoam Embankment model due to the cellular air bubble structure of the EPS which is capable of reducing the dynamic impact and vibration effects.

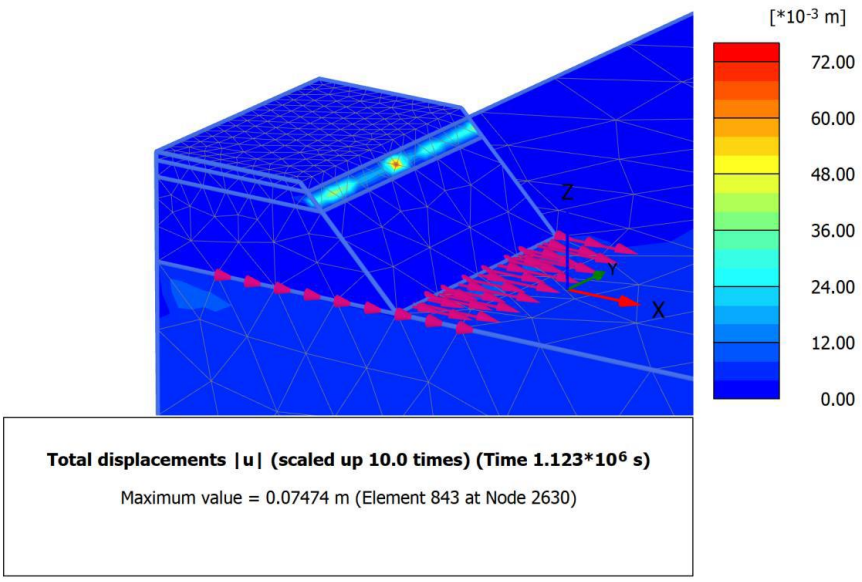

Figure 4.76. Total displacements in EPS Geofoam model (Toksoy and Edincliler, 2024).

5. EXPERIMENTAL STUDY

This chapter begins with the geotechnical and geophysical tests including site investigation, pressuremeter tests, microtremor tests, MASW tests, ERT tests, SASW tests, to determine the local site conditions and the wave propagation properties of the test area. Next, the design considerations, construction details and the obtained results from field scale seismic performance tests with MSS from highway embankment models are given.

5.1. Geotechnical and Geophysical Experiments

It is at utmost importance to know the site conditions on which full scale seismic performance tests to be performed. The most important part of the proposed studies within this thesis is the seismic performance tests with Mobile Seismic Shaker. Three different full scale highway embankments will be constructed at Boğaziçi University Kandilli Observatory and Earthquake Research Institute with the special permission of the university administration. This chapter covers the rehabilitation of the test area, pressuremeter tests, soil sampling with boreholes, microtremor tests, Multichannel Analysis of Surface Waves (MASW) method, Spectral Analysis of Surface Waves (SASW) method and Electrical Resistivity Tomography (ERT) to investigate the engineering properties of the proposed test area and explore the subsurface conditions.

5.1.1. Site Investigation and Rehabilitation of the Test Area

Investigation of the site conditions and preperation of the test area before experimental studies is very important. The construction of the full scale highway embankment models and their seismic performance tests with Mobile Seismic Shaker will be performed in the desired area in Figure 5.1.



Figure 5.1. Construction and Seismic Performance Test Area at KOERI.

The test area at KOERI was investigated in 2012 before the construction of the BTK building. Site investigation is based on six boreholes up to 20m depth (Safir Jeoteknik, 2012). The locations of those boreholes are shown in Figure 5.2.



Figure 5.2. Locations of Boreholes for the Site Investigation (Safir Jeoteknik, 2012).

Evaluation of the borehole based site investigation reveals that very firm silty clay layer exists from approximately 1m to 10m overlying the limestone layer (Baltalimanı Formation). No borehole drills coincide the pre-defined test area and it is seen that layer thicknesses may vary dramatically (from 2m to 10m) in relatively short distances as shown in Figure 5.3.

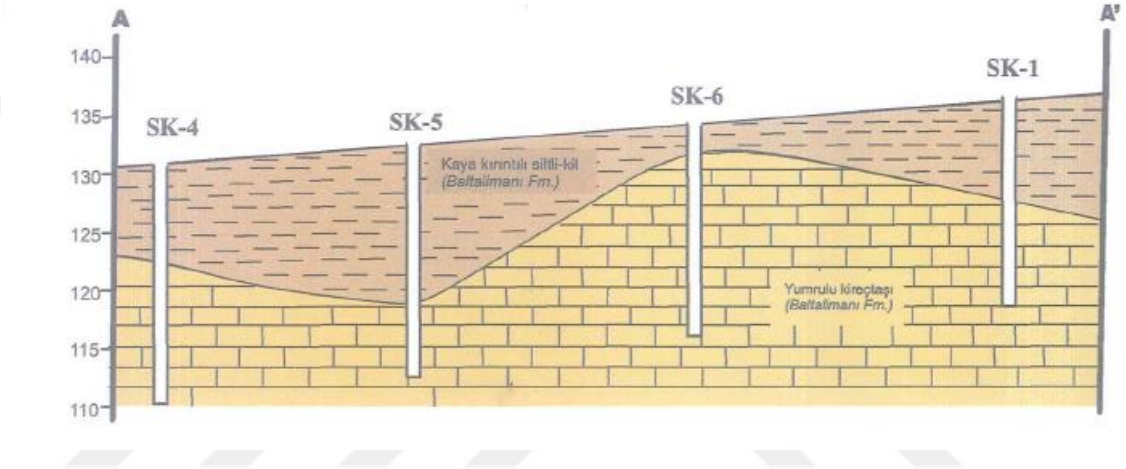

Figure 5.3. Geologic Horizontal Cross-Section (Safir Jeoteknik, 2012).

Even though the proposed test area is close to SK-4 borehole, it is essential to know the exact subsurface conditions with layer depths in this study which directly affects the seismic response of highway embankment models in the field and obtained data is used in numerical analyses for the calibration study. So that, additional subsurface exploration methods have been decided to be implemented in the proposed test area as given in the following sections.

Prior to the site investigation applications, the test area rehabilitated and leveled with the help of an excavator. The stages of this process is represented in Figure 5.4.



Figure 5.4. Rehabilitation of the Test Area.

5.1.2. Pressuremeter Tests

Subsurface exploration methods took place in the proposed test area after the rehabilitation and leveling process had completed. Four additional boreholes up to 10m have been drilled across the test area and undisturbed soil samples have been collected from every 1.5m for the laboratory tests. Concurrently, pressuremeter tests have been performed in the boreholes. This step is important because the data provided in Safir Jeoteknik (2012), even though it is very close, was not exactly coinside with the proposed test area. The data obtained from pressuremeter tests are important to for the calibration of the soil models in numerical analyses. pressuremeter tests were performed by a local company named Rumeli Zemin in 2019. During the proposed tests, the pressuremeter probe is inserted to the boreholes and applies pressure to the sidewalls of the borehole and measures the resultant deformation (Figure 5.5).



Figure 5.5. Pressuremeter Probe for Pressuremeter Tests.

After the calibration of pressure and volume, and taking into account the diameter of the probe, elastic modulus can be calculated (Table 5.1) and related elastic modulus profile of the test area can be drawn in Figure 5.6.

Table 5.1. Calculated Elastic Modulus Values for different boreholes and depths (Rumeli Zemin, 2019).

Depth (m)	Sondaj No	Em (MPa)
2.00	SK-4	7.76
4.00	SK-2	49.05
5.00	SK-4	60.77

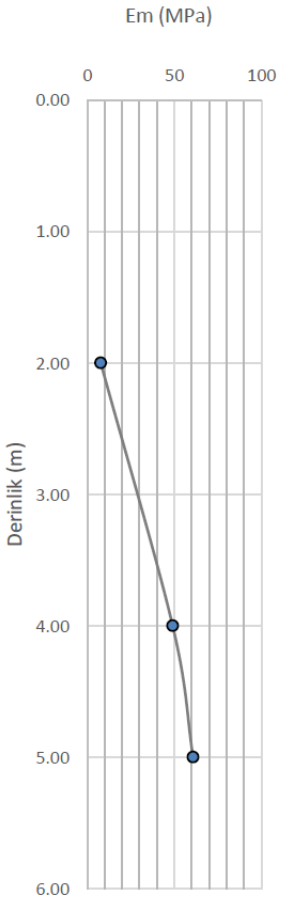

Figure 5.6. Elastic Modulus Profile of the Test Area (Rumeli Zemin, 2019).

Calculated net limit pressures from the performed Pressuremeter Tests on the test area are shown in Table 5.2.

Table 5.2. Net Limit Pressures from Experiments (Rumeli Zemin, 2019).

Depth (m)	**Net Limit Pressure (kPa)**
2.0	1484
4.0	1440
5.0	2068

Given net limit pressure values indicate that up to 4.0m depth of the borehole in the test area, the soil type is in the upper bounds of very stiff clay and sand whereas after 5.0m of depth, the soil type is in the range of hard clay and dense sand.

Provided Pressuremeter tests results are used to calculate the mechanical properties of the foundation soil such as the cohesion and internal friction angle. Following equation is used to calculate the cohesion of the foundation soil (Menard, 1957):

$$\mathbf{c = (p_1 - p_0) / 5.5}$$
$$\mathbf{= (94)/5.5 \approx 17 kN/m^2} \quad (5.1)$$

where **c** is cohesion, $\mathbf{p_1}$ is The maximum pressure in probe, $\mathbf{p_0}$ is Initial pressure in probe, respectively.

Provided Pressuremeter tests results are also used to calculate internal friction angle of the foundation soil. Following equation is used to calculate the cohesion of the foundation soil (Menard, 1975):

$$\mathbf{\tan \phi = 0.22 + 0.05.\log(E)}$$
$$\mathbf{= 0.22 + 0.05.\log(1.625) \approx 12°} \quad (5.2)$$

where, ϕ is internal friction angle and **E** is Elastic modulus of the soil, respectively.

5.1.3. Microtremor Tests

Microtremor tests were performed by a local company named Geometrik Mühendislik. During this study, Güralp CMG-6TD model, three component seismometer was used for microtremor recordings at three different locations across the test area (Figure 5.7). The microtremor coordinates were precisely determined by using a GPS device (Figure 5.8). The coordinates are given in Table 5.3.



Figure 5.7. Locations of Microtremors.

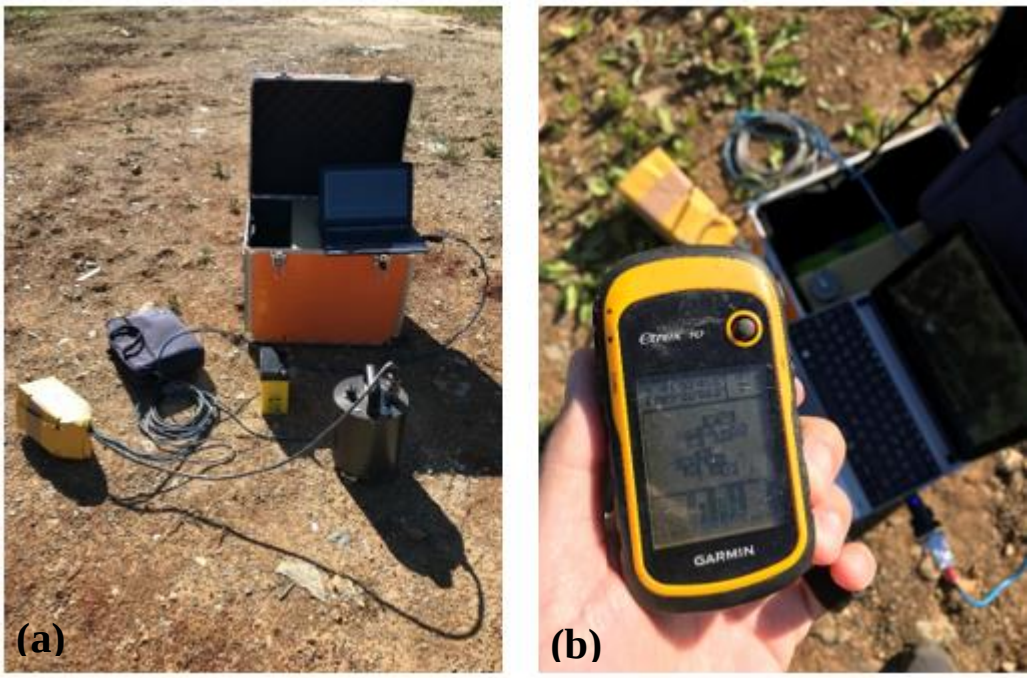

Figure 5.8. Microtremor Set-up (a) and Coordinate Readings (b).

Table 5.3. Coordinates of Microtremor Measurements.

	COORDINATES
M-1	41° 03’ 49.5” N 29° 03’ 50.0” E
M-2	41° 03’ 48.1” N 29° 03’ 51.7” E
M-3	41° 03’ 48.9” N 29° 03’ 50.6” E

Obtained H/V Spectra from M-1 data is given in Figure 5.9 and the obtained dynamic properties from the H/V spectra of test area are given in Table 5.4.

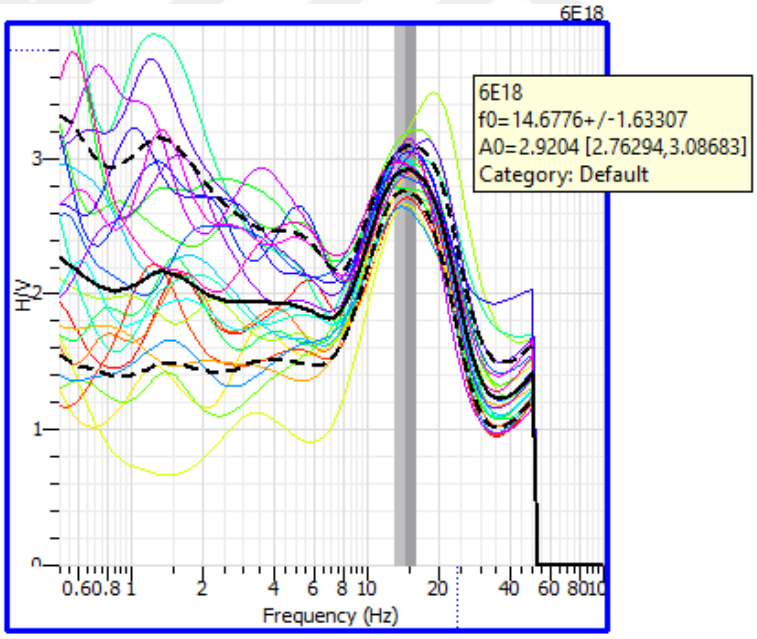

Figure 5.9. Obtained H/V Spectra from M-1 data (Geometrik Mühendislik, 2021).

Table 5.4. Site characteristics for M-1 location.

Location	Natural Frequency (Hz)	Predominant Period (s)	H/V Ratio
M-1	14.68	0.07	2.92

Obtained H/V Spectra from M-2 data is given in Figure 5.10 and the obtained dynamic properties from the H/V spectra of M-2 are given in Table 5.5.

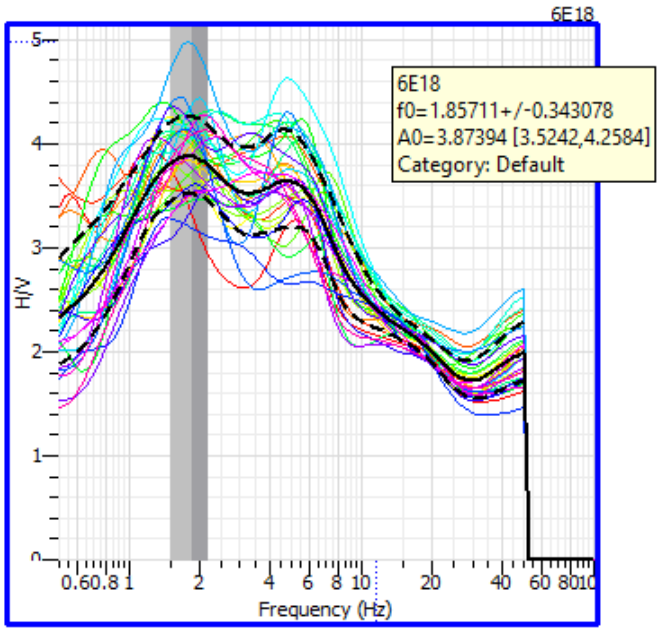

Figure 5.10. Obtained H/V Spectra from M-2 data (Geometrik Mühendislik, 2021).

Table 5.5. Site characteristics for M-2 location.

Location	Natural Frequency (Hz)	Predominant Period (s)	H/V Ratio
M-2	1.86	0.54	3.87

Obtained H/V Spectra from M-3 data is given in Figure 5.11 and the obtained dynamic properties from the H/V spectra of M-3 are given in Table 5.6.

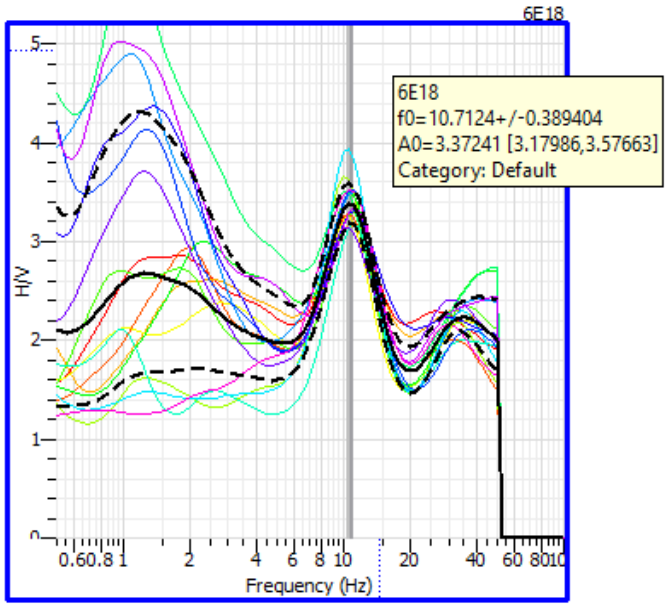

Figure 5.11. Obtained H/V Spectra from M-3 data (Geometrik Mühendislik, 2021).

Table 5.6. Site characteristics for M-3 location.

Location	Natural Frequency (Hz)	Predominant Period (s)	H/V Ratio
M-3	10.71	0.09	3.37

As shown in Table 5.6, obtained natural frequency is 10.71Hz and the predominant period is 0.09s. H/V ratio is determined as 3.37 based on the microtremor measurements from M-3.

5.1.4. Multichannel Analysis of Surface Waves (MASW) Tests

Seismic reflection tests have been performed across the test area in Boğaziçi University Kandilli Observatory and Earthquake Research Institute in order to accurately monitor and identify the subsurface soil layers, their thicknesses and Vs values (Figure 5.12). MASW technique (Multichannel Analyses of Surface Waves) has been adapted in this study as the depth

range of interest is between 0-30m. MASW tests were performed by Geometrik Mühendislik company in 2021. 12 channel, 4.5Hz geophones were placed in every 3 meters and along 47 meters for each and every 8 profiles (4+4). As a seismic source, a 10kg hammer was used. Seismic source was impacted at five different points along each profile (0, 4, 23.5, 43 and 47m from the start).



Figure 5.12. A view from MASW experiments.

Initially, this approach assesses the seismic surface waves produced by seismic sources and determines the velocities at which these waves propagate. Subsequently, it examines the variations in shear-wave velocity (Vs) beneath the surveyed region to construct a comprehensive two-dimensional (2D) representation of the distinct soil layers, each characterized by different Vs values. MASW profiles across the test area are represented in Figure 5.13.

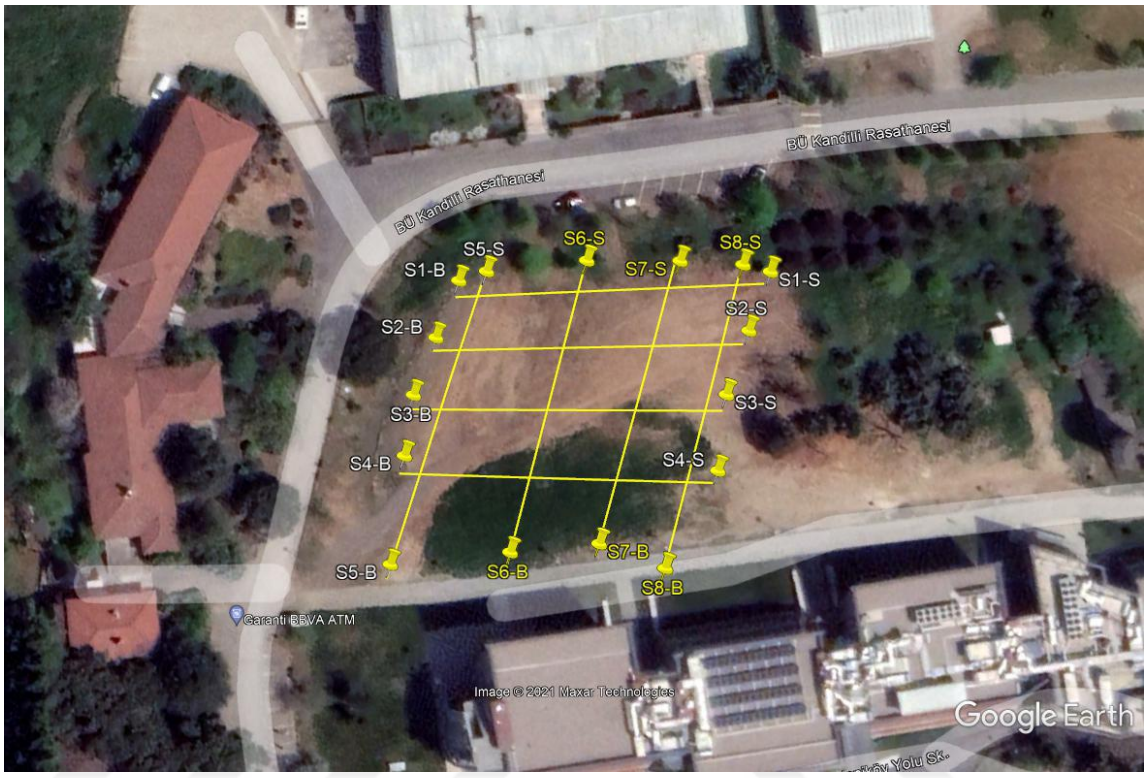

Figure 5.13. MASW Profiles across the test area.

After all dispersion data were carefully evaluated and processed, shear wave profiles along S1-S4 are given in Figures 5.14-5.17.

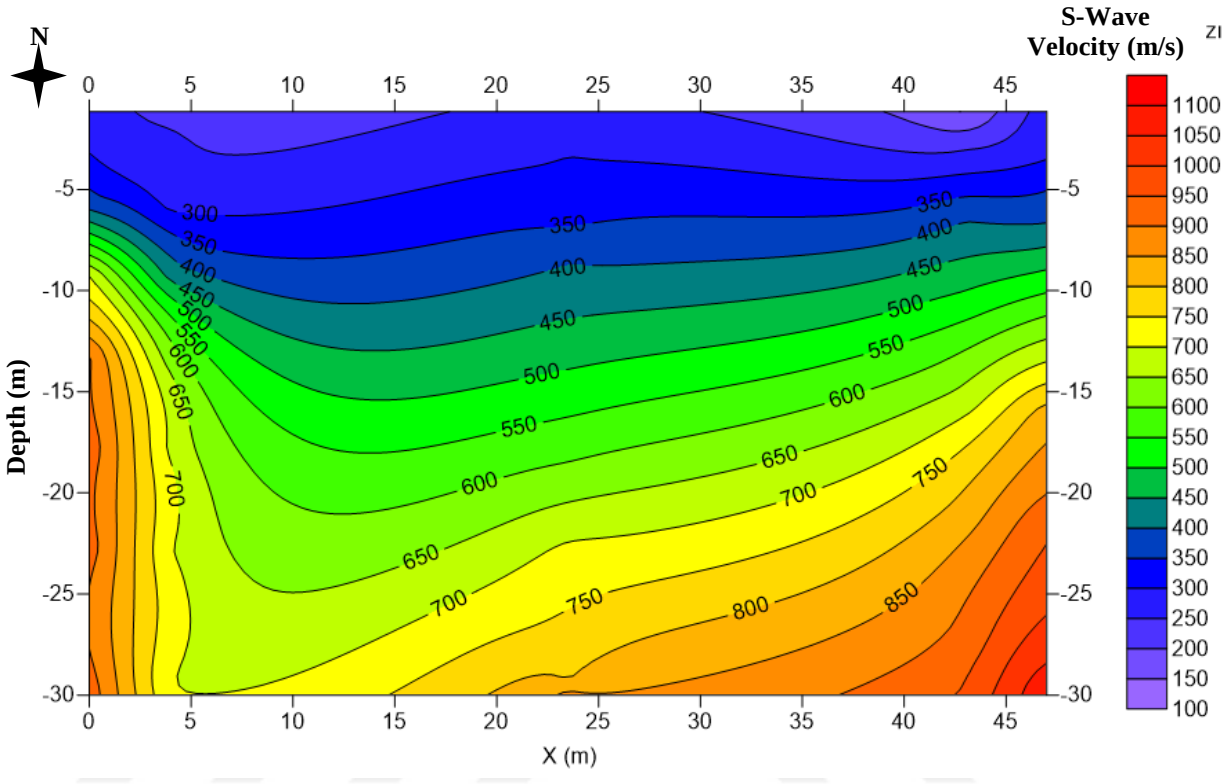

Figure 5.14. Shear wave profile along S1 (Geometrik Mühendislik, 2021).

As represented in Figure 5.14, shear wave profile along S1 is not uniform and shear wave velocities change in short distances especially at the beginning and at the end of the profile. The average Vs_{30} value obtained for profile S1 is 570m/s. Shear wave velocity profile along S2 is given in Figure 5.15.

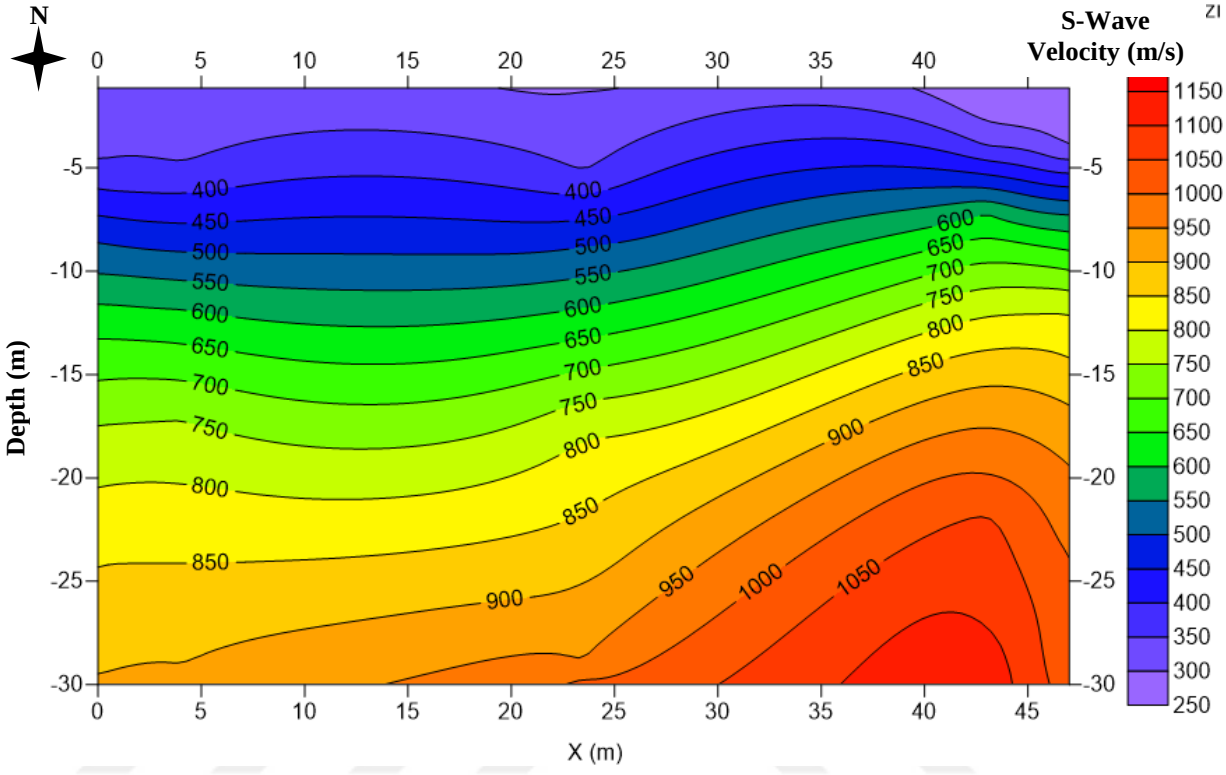

Figure 5.15. Shear wave profile along S2 (Geometrik Mühendislik, 2021).

As represented in Figure 5.15, shear wave profile along S2 is more uniform than S1 bu still shear wave velocities change in short distances especially at the end of the profile. The average Vs_{30} value obtained for profile S2 is 649m/s. Shear wave velocity profile along S3 is given in Figure 5.16.

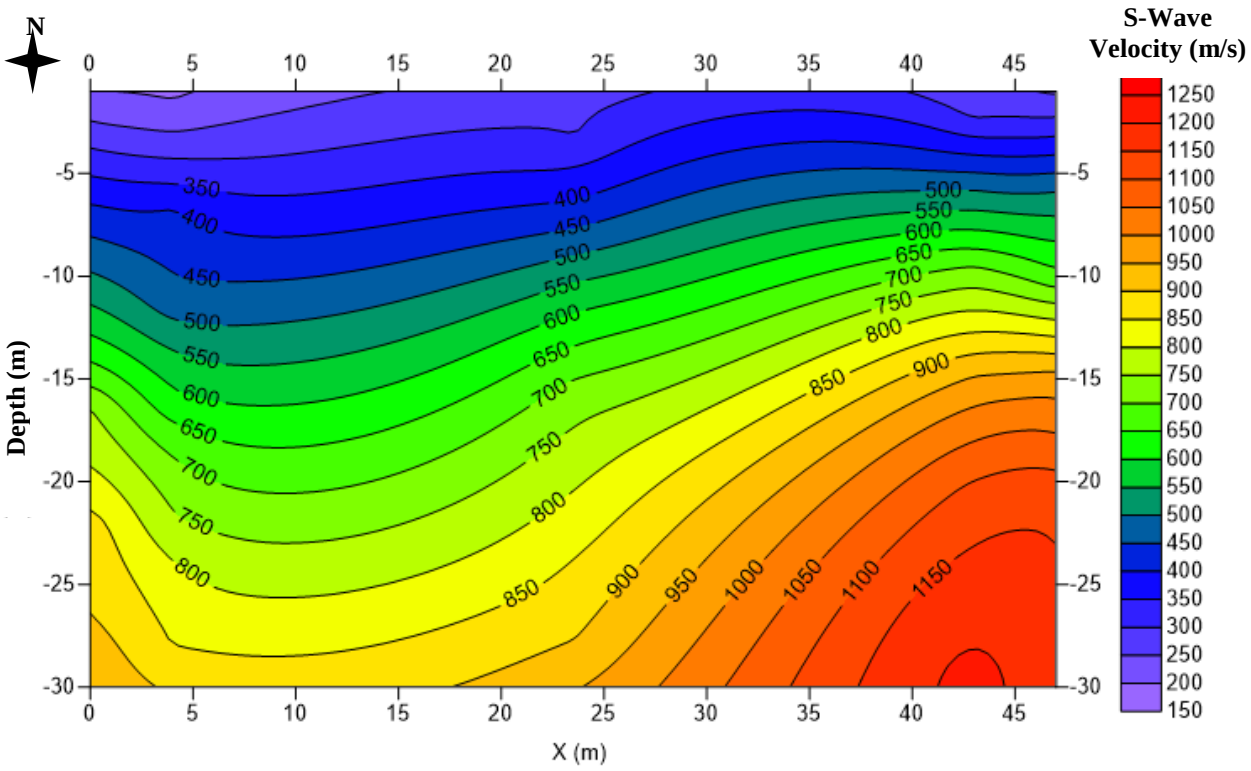

Figure 5.16. Shear wave profile along S3 (Geometrik Mühendislik, 2021).

As represented in Figure 5.16, shear wave profile along S3 is not uniform and shear wave velocities change in short distances especially at the end of the profile. The average Vs_{30} value obtained for profile S3 is 646m/s. Shear wave velocity profile along S4 is given in Figure 5.17.

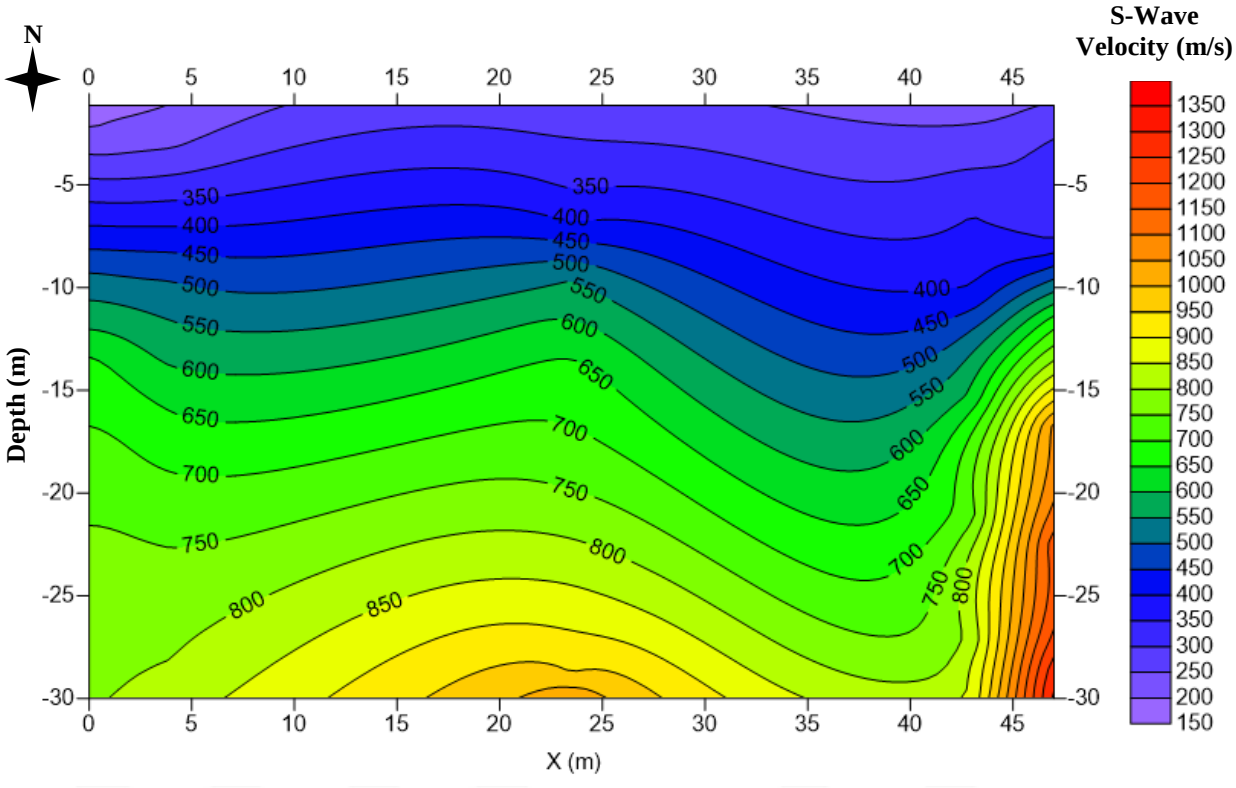

Figure 5.17. Shear wave profile along S4 (Geometrik Mühendislik, 2021).

As represented in Figure 5.17, shear wave profile along S4 is not uniform and shear wave velocities change in short distances especially at the end of the profile. The average Vs_{30} value obtained for profile S4 is 569m/s.

Site classifications according to obtained V_{S30} with respect to NEHRP (Table 5.7) and 2018 Turkish Earthquake Code (Table 5.8) are Site Class C and Site Class ZC, respectively.

Table 5.7. Site Classification according to NEHRP (1994).

Site Class	Generic Description	Range of V_{S30}
A	Hard rock	> 1500 m/s
B	Rock	760–1500 m/s
C	Very dense soil and soft rock (firm horizon)	360 < 760 m/s
D	Stiff Soil	180 < 360 m/s
E	Soil profile with soft clay	< 180 m/s
F	Site-specific geotechnical investigation required	

Table 5.8. Site Classification according to Turkish Earthquake Code (2018).

Yerel Zemin Sınıfı	Zemin Cinsi	Üst 30 metrede ortalama		
		$(V_s)_{30}$ [m/s]	$(N_{60})_{30}$ [darbe /30 cm]	$(c_u)_{30}$ [kPa]
ZA	Sağlam, sert kayalar	> 1500	–	–
ZB	Az ayrışmış, orta sağlam kayalar	760 – 1500	–	–
ZC	Çok sıkı kum, çakıl ve sert kil tabakaları veya ayrışmış, çok çatlaklı zayıf kayalar	360 – 760	> 50	> 250
ZD	Orta sıkı – sıkı kum, çakıl veya çok katı kil tabakaları	180 – 360	15 – 50	70 – 250
ZE	Gevşek kum, çakıl veya yumuşak – katı kil tabakaları veya $PI > 20$ ve $w > \%\ 40$ koşullarını sağlayan toplamda 3 metreden daha kalın yumuşak kil tabakası $(c_u < 25\ \text{kPa})$ içeren profiller	< 180	< 15	< 70
ZF	Sahaya özel araştırma ve değerlendirme gerektiren zeminler: 1) Deprem etkisi altında çökme ve potansiyel göçme riskine sahip zeminler (sıvılaşabilir zeminler, yüksek derecede hassas killer, göçebilir zayıf çimentolu zeminler vb.), 2) Toplam kalınlığı 3 metreden fazla turba ve/veya organik içeriği yüksek killer, 3) Toplam kalınlığı 8 metreden fazla olan yüksek plastisiteli (PI >50) killer, 4) Çok kalın (> 35 m) yumuşak veya orta katı killer.			

5.1.5. Electrical Resistivity Tomography (ERT) Tests

The resistivity survey technique has been in use since the 1920s and is considered one of the oldest and widely employed methods for geophysical exploration. The ERT method is a valuable approach to evaluate the electrical properties of materials beneath the surface. These differences can be used to create maps of geological structures, sinkholes, fractures, and groundwater. To set up the ERT field, a group of evenly spaced electrodes must be installed and connected to a central control unit using multi-core cables. ERT tests have been performed by

a local company named Geometrik Mühendislik in 2021. In this case study, 3D method is implemented and 7x8 lines, a total number of 56 electrodes have been used in 6m spacing. The distribution of the electrodes and the stages of the ERT test in test area is represented in Figure 5.18 and Figure 5.19.



Figure 5.18. Distribution of the electrodes in the test area (Geometrik Mühendislik, 2021).



Figure 5.19. Stages of ERT Testing, a) Driving the electrodes, b) Watering the electrodes for increased conductivity, c) Setting up connections, d) A view from the test area, e) Data acquisition system.

ERT test results clearly show the resistivity of the soil in proposed test area up to 18.8m of depth. The resistivity can easily be correlated with the Vs of the soil. In this legand, dark blue indicates a Vs value of 300m/s, green indicates a Vs value of 500m/s, yellow indicates a Vs value of 700m/s and red indicates a Vs value of 1000m/s. Generated 3-D resistivity map of the test area is shown in Figure 5.20.

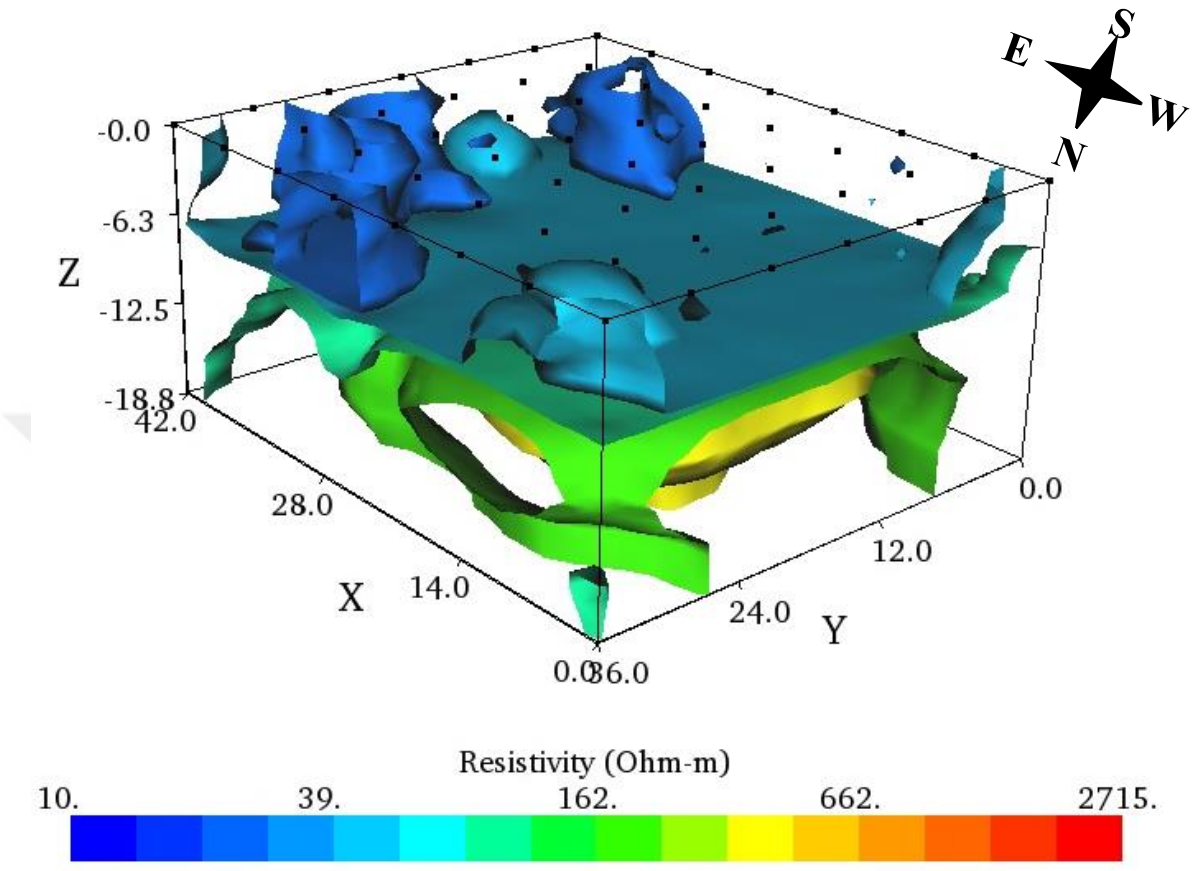

Figure 5.20. Generated 3-D resistivity map of the test area (Geometrik Mühendislik, 2021).

As shown in the 3-D map, approximately the first 6m of the test area consists of relatively low resistivity (low shear wave velocity approximately 300m/s) material and material properties dramatically change with depth.

5.1.6. Spectral Analysis of Surface Waves (SASW) Tests

The SASW method is a technique that utilizes Rayleigh surface waves to assess the shear wave velocity profiles of layered subsurface materials. This method involves measuring the Rayleigh wave velocity at various frequency ranges, which allows for the creation of a dispersion curve. The dispersion curve illustrates the relationship between Rayleigh wave

velocity and frequency, enabling the determination of the shear wave velocity profile of the layered media.

A dynamic circular load (such as the excitation plate of a mobile shaker) perpendicular to the surface of a half space generates P-waves S-waves, Rayleigh waves, and head waves (Foinquinos and Roesset 2000).

Mitra (1961) and Woods (1968) showed that the displacements both in the near field and far field are generally dominated by Rayleigh Waves.

Rayleigh waves carry the highest amount of energy, accounting for 67% of the total propagated energy. In contrast, S-waves carry 26% of the energy, and P-waves only carry 7%. In terms of attenuation, Rayleigh waves are less likely to attenuate compared to body waves. The attenuation of body waves occurs both within the mass (1/R) and along the surface ($1/R^2$), while Rayleigh waves attenuate with a rate of $1/R^{0.5}$, which is slower than body waves as can be seen in Figure 5.21. (Woods, 1968).

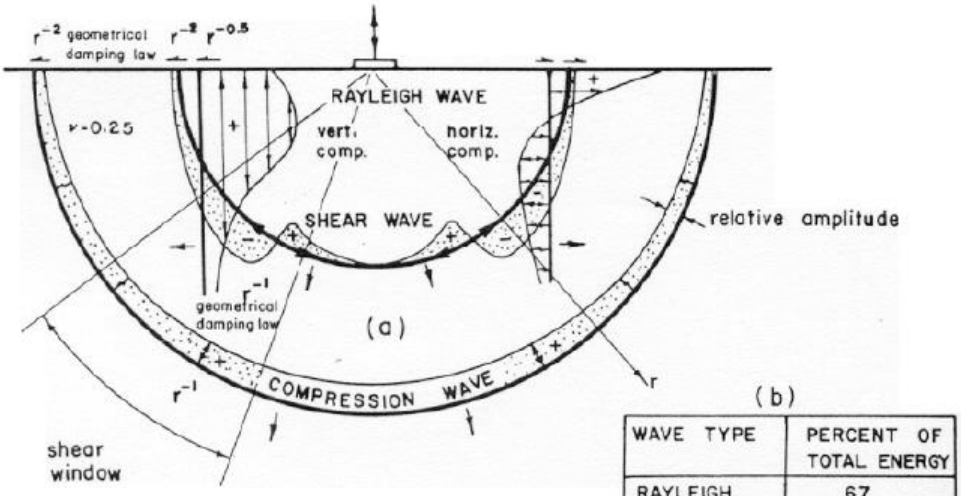

WAVE TYPE	PERCENT OF TOTAL ENERGY
RAYLEIGH	67
SHEAR	26
COMPRESSION	7

Figure 5.21. Wave propagation for dynamically loading circular footing on elastic half space (Chang, 2002).

In order to investigate the wave propagation properties and to determine the shear wave velocity profile in the test area SASW method was also implemented. Mobile Seismic Shaker is used as a dynamic source and the excitation plate of the mobile shaker perpendicular to the surface generated vibrations in the proposed test area of the campus. Generated vibrations were recorded by four accelerometers which are Güralp CMG-CD2453EAM type. Accelerometers were placed in 90cm intervals and distance of the first sensor to the mobile shaker was 1.2m. Seismic waves propagating from the excitation plate of the mobile shaker were simultaneously recorded by four broad-band accelerometers in all three components (N-S, E-W, U-D). Sensor 1 is the closest accelerometer to the mobile shaker and Sensor 4 is the farthest one (Figure 5.22). Configuration details and distances between sensors were taken from the literature (Chang, 2002). Test set-up is represented in Figure 5.23.

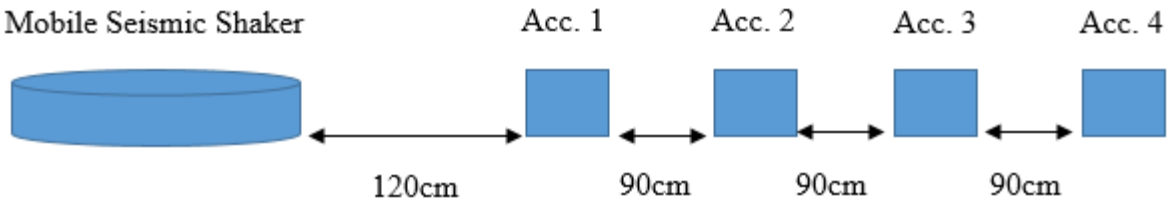

Figure 5.22. Instrumentation plan for the SASW tests.



Figure 5.23. Field vibration test set-up.

Dynamic inputs to be used in SASW tests were carefully selected by taking into consideration of the typcial earthquake characteristics (frequency range, amplitude, duration) and the capabilities of the MSS. It is known that most earthquakes generate dynamic motions in the frequency range of up to 100Hz and many of the destrcutive earthquakes generate dynamic motions with the pre-dominant frequency of 1-30Hz. MSS can apply up to 27kN of force so two

force levels of 10kN and 20kN were selected. In terms of duration, 10s and 30s were selected as the lower and upper bounds of the destructive earthquakes. A total of five field vibration tests were performed for the proposed SASW tests and the details of field vibration tests are represented in Table 5.9. Representative Acceleration Responses from Test 1 are given in Figure 5.24.

Table 5.9. Details of field vibration tests.

Test No	Frequency	Force	Duration
1	0-100Hz	10kN	30s
2	0-100Hz	20kN	30s
3	10Hz	10kN	10s
4	20Hz	10kN	10s
5	30Hz	10kN	10s

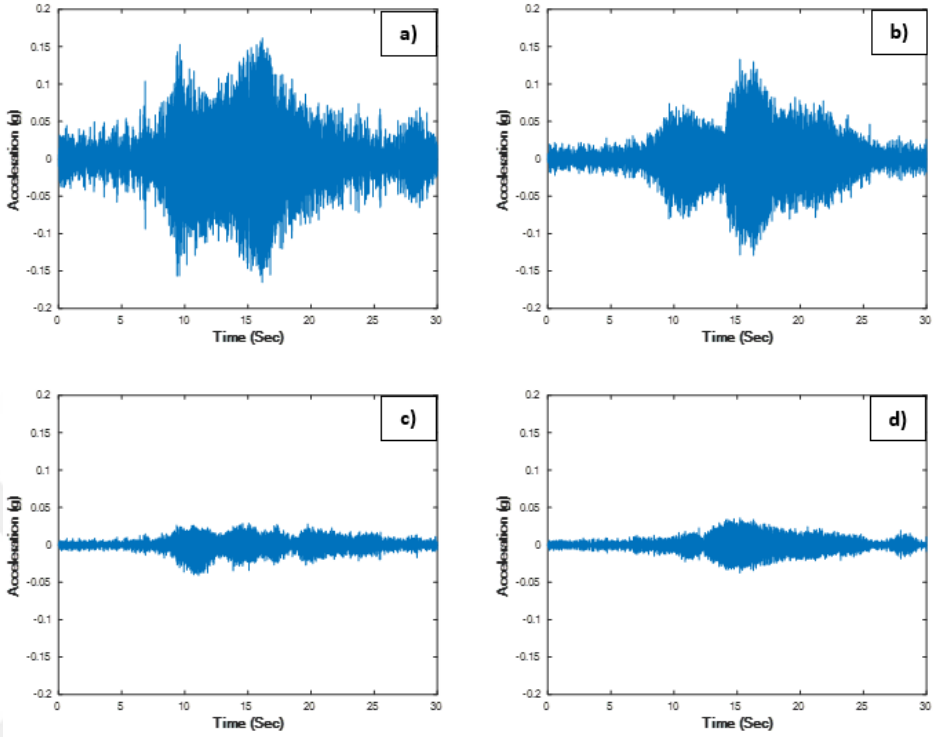

Figure 5.24. Acceleration Responses from Test 1 (E-W), a) Sensor 1, b) Sensor 2, c) Sensor 3, d) Sensor 4.

As represented in Figure 5.24, when the MSS applies 1-100Hz of motion at 10kN of force for 30s in U-D direction; Acc. 1, Acc.2, Acc.3 and Acc.4 measures 0.16g, 0.14g, 0.04g and 0.03g in the E-W direction, respectively. The amplitude of dynamic motion attenuates non-linearly with respect to distance from source. Field vibration tests were performed for the rest of the dynamic motions and directions and obtained results were evaluated.

Mobile Seismic Shaker (MSS) applied the dynamic loads in the vertical direction, thus U-D data were considered for further analysis that investigates the effect of force and frequency content on the results. Figure 5.25 represents the observed peak accelerations with respect to the varying force (10kN and 20kN) applied by the MSS during Test No:1 and 2.

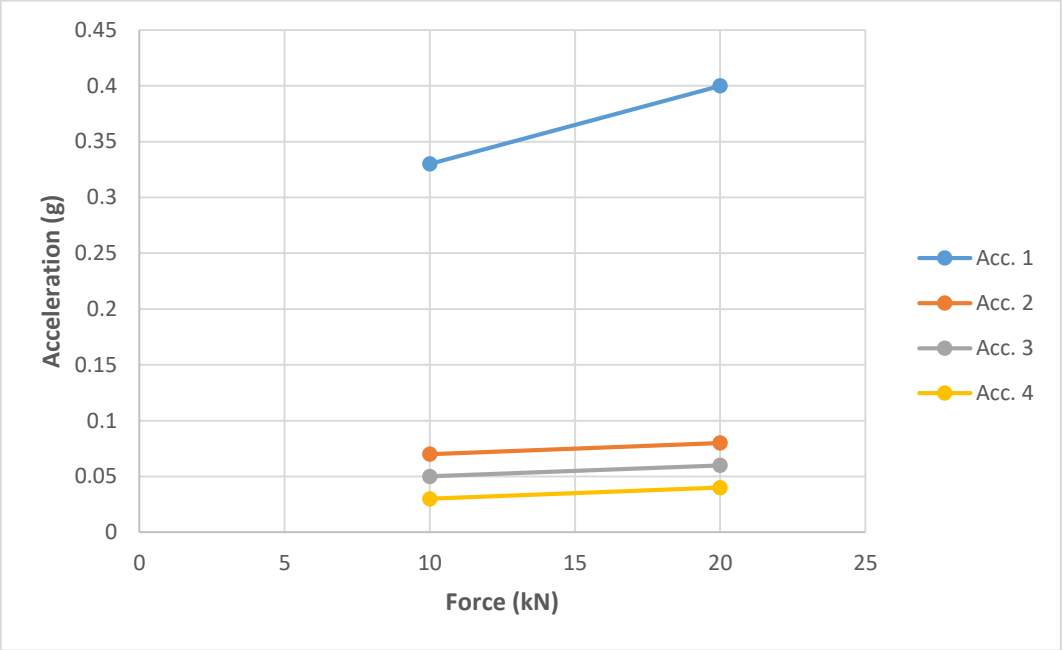

Figure 5.25. Measured Peak Accelerations (U-D) versus Applied Force by MSS.

As can be inferred from Figure 5.25, the closest accelerometer to the dynamic source (Acc. 1) measured the highest acceleration values (0.33g and 0.40g). Acceleration values were directly proportional to the increased force and inversely proportional to the increased distance to the dynamic source as expected.

Figure 5.26 represents the observed peak accelerations for each sensor with respect to the increasing pre-dominant frequency (10Hz-20Hz-30Hz) of the dynamic load applied by MSS during tests 3,4 and 5.

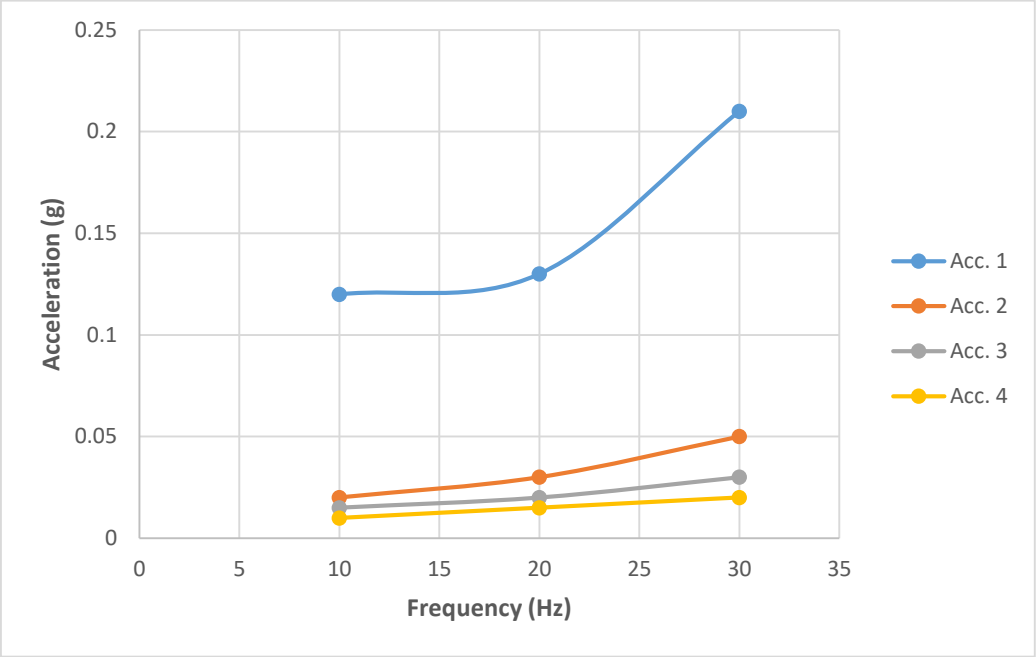

Figure 5.26. Measured Peak Accelerations (U-D) versus Frequency Content applied by MSS.

As can be seen in Figure 5.26, increasing frequency content (10Hz-20Hz-30Hz) of the dynamic excitation increased the peak accelerations. Peak acceleration value obtained from Acc. 1 under 10Hz of motion is 0.12g whereas it reaches up to 0.21g under 30Hz of sine wave. The maximum and the minimum acceleration values were obtained from Acc. 1 (closest one to the MSS) and Acc. 4 (farthest one to the MSS), respectively. It can also be inferred from the Figure 5.103 that due to the increasing frequency content (10Hz to 30Hz) of the dynamic source, the curvature of the lines in the graph reveal the nonlinear soil behaviour was observed especially for the data from Acc. 1.

As stated by Richart et.al, 1970; vertically propagating dynamic loads create Rayleigh type surface waves. Rayleigh waves propagate only 10% slower than S waves, thus average V_s profile of a site can easily be calculated.

Investigation of 30Hz data from Test No:5 shows that seismic loads propagating from MSS travel with 270m/s when the distance between source to Sensor 4 (2.9m) and the signal arrival time (0.0107s) are divided considering the equation of speed (2.9m/0.0107s = 270m/s).

As Rayleigh wave velocity is 10% slower than Shear wave, the average V_s can easily be calculated as 300m/s (270m/s x 1.1). Related wave length can be found as follows:

$$\lambda_R = V_R / f; \quad (5.3)$$

where λ_R is wave length, V_R is wave velocity and F is frequency, respectively.

Wave length was calculated as 9m (270/30), which reveals that the average V_S = 300m/s up to 9m depth of the test site. Calculations were confirmed by other frequency ranges. Obtained shear wave velocity profile is in correlation with the seismic reflection surveys. Obtained shear wave velocity profiles from MASW tests show that the average shear wave velocity for the first 9m is in the range of 325m/s to 375m/s (section 5.1.4).

5.2. Highway Embankment Design and Field Scale Experiments

This section of the thesis includes the design and material selection considerations with respect to specified guidelines and standards (FHWA NHI-05-037, 1993 AASHTO, 2013 KGM Technical Regulations, 2004 NCHRP) for the construction of the full scale highway embankment models. Also, proposed dynamic performance tests of full scale highway embankment models using mobile seismic shaker are given in detail.

5.2.1. Materials

A highway embankment or a pavement is an engineering structure composed of different layers. The pavement structure consists of layers of subbase, base and surface courses placed on a subgrade to support and distribute the traffic load (Figure 5.27).

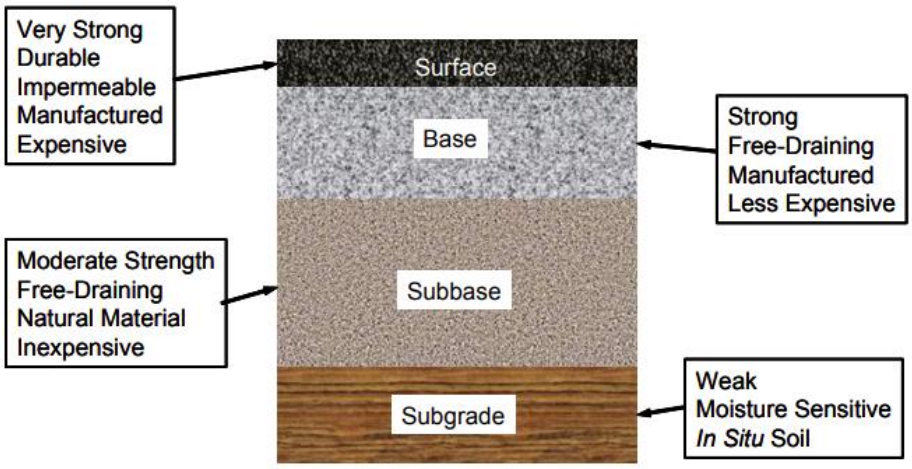

Figure 5.27. Typical layers of a flexible highway embankment (FHWA NHI-05-037).

The subgrade course is the in-situ natural soil on which the pavement is constructed. It serves as a supporting platform for the construction.

The subbase course is the layer which lays between subgrade and base courses and it has a designed thickness. It's primary purpose is to support the base course. The aggregate material used in subbase course is slightly lower quality than the one used in base course. A subbase layer is quite beneficial because it contributes to the structural capacity of the pavement system. It also serves as a filter to avoid fine-grained subgrade soils in the base course and provides drainage for the water in the system.

The base course is the layer which lays between asphalt concrete surface and subbase courses with a designed thickness. It serves as a uniform and stable support for the surface layer. It significantly improves the structural capacity of the system. This layer usually consists of high quality aggregates which require a specified gradation and typically compacted unbound.

The top most layer of a pavement system is the surface course which is exposed to traffic load and harsh climatic effects. The surface layer is typically asphalt concrete (bituminous) in flexible pavements and Portland Cement Concrete (PCC) in rigid pavements. The surface layer

is generally constructed on top of a base layer of unbound coarse aggregate. However it is commonly placed directly on the subgrade for the roads with low traffic load (FHWA NHI-05-037).

The coarse aggregate properties for unbound subbase and bases play a very important role for the stability of highway embankments. Particle shape of the aggregate should be more angular rather than round shaped due to the fact that round shaped aggregates displace and reorient.

5.2.1.1. Subbase and Base Material

The design of embankment models and the criteria for selecting materials for highway embankments comply with both the 1993 AASHTO and 2013 KGM Technical Regulations at the same time. In this study, the aggregate base and subbase materials are selected as Type-B for 2013 KGM Technical Regulation (Table 5.10 and Table 5.11) and Type-A for 1993 AASHTO (Table 5.12).

Table 5.10. Subbase Classifications of 2013 KGM Technical Regulation.

Tablo-401-1 Alttemel Malzemesi Gradasyon Limitleri

Elek Açıklığı		TİP-A	TİP-B
mm	in	% Geçen	% Geçen
75	3	100	
50	2	-	100
37,5	1 1/2	85 - 100	80 - 100
25	1	-	60 - 90
19	3/4	70 - 100	45 - 80
9,5	3/8	45 - 80	30 - 70
4,75	No.4	30 - 75	25 - 55
2,00	No.10	-	15 - 40
0,425	No.40	10 - 25	10 - 20
0,075	No.200	0 - 12	0 - 12

Table 5.11. Base Layer Classifications of 2013 KGM Technical Regulation.

Elek Açıklığı		% Geçen	
mm	in	Tip - I	Tip – II
37,5	1 ½	100	
25	1	72 - 100	100
19	¾	60 - 92	80 - 100
9,5	3/8	40 - 75	50 - 82
4,75	No.4	30 - 60	35 - 65
2,00	No.10	20 - 45	23 - 50
0,425	No.40	8 - 25	12 - 30
0,075	No.200	0 -10	2 - 12

Table 5.12. Subgrade Classifications of 1999 AASHTO.

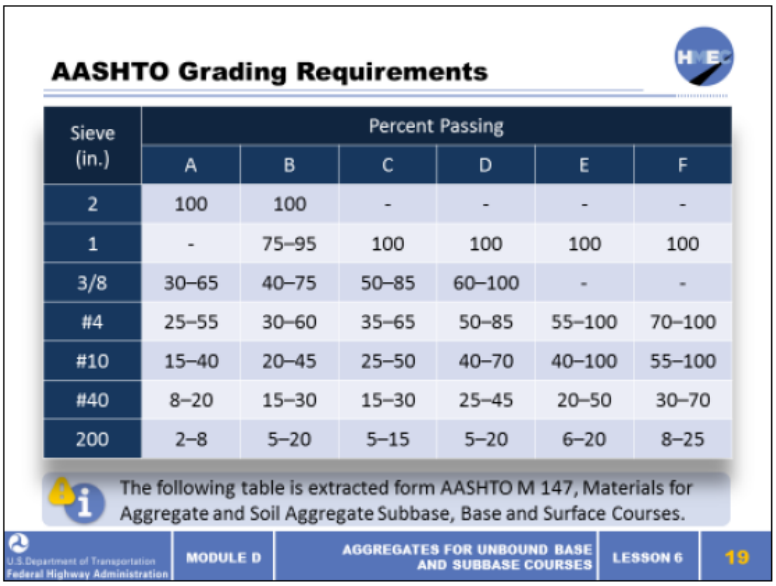

The thickness of surface (asphalt concrete) layer and the granular aggregate base layer have been chosen as 15cm and 30cm, respectively for all three models. GAB layer is located under the AC layer and above the subgrade layer.

The subbase and base material used for the construction of the highway embankments are obtained from “Ergenekon Ocak” in Istanbul. Subbase and base materials for the construction of highway embankment models are represented in Figure 5.28 and Figure 5.29, respectively.



Figure 5.28. Subbase material obtained from Ergenekon Ocak.



Figure 5.29. Base material obtained from Ergenekon Ocak.

Sieve analyses to obtain the grain-size distribution of subbase material were performed at Boğaziçi University Geotechnical Earthquake Engineering Laboratory. Sieve analyses were repeated three times in accordance with the ASTM Standard of D422.

Figure 5.30, represents the grain-size distribution of subbase material and Figure 5.31, represents the grain-size distribution of base material.

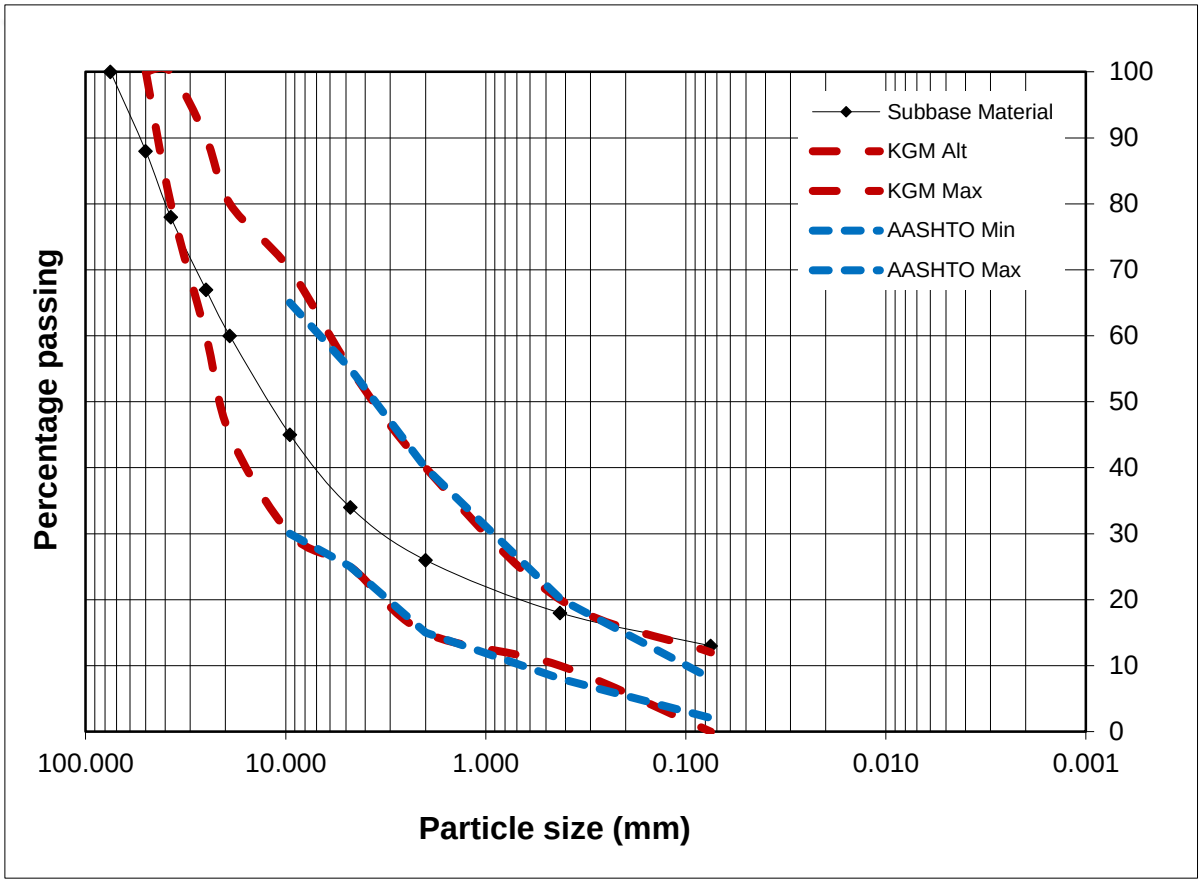

Figure 5.30. Particle size distribution of subbase material.

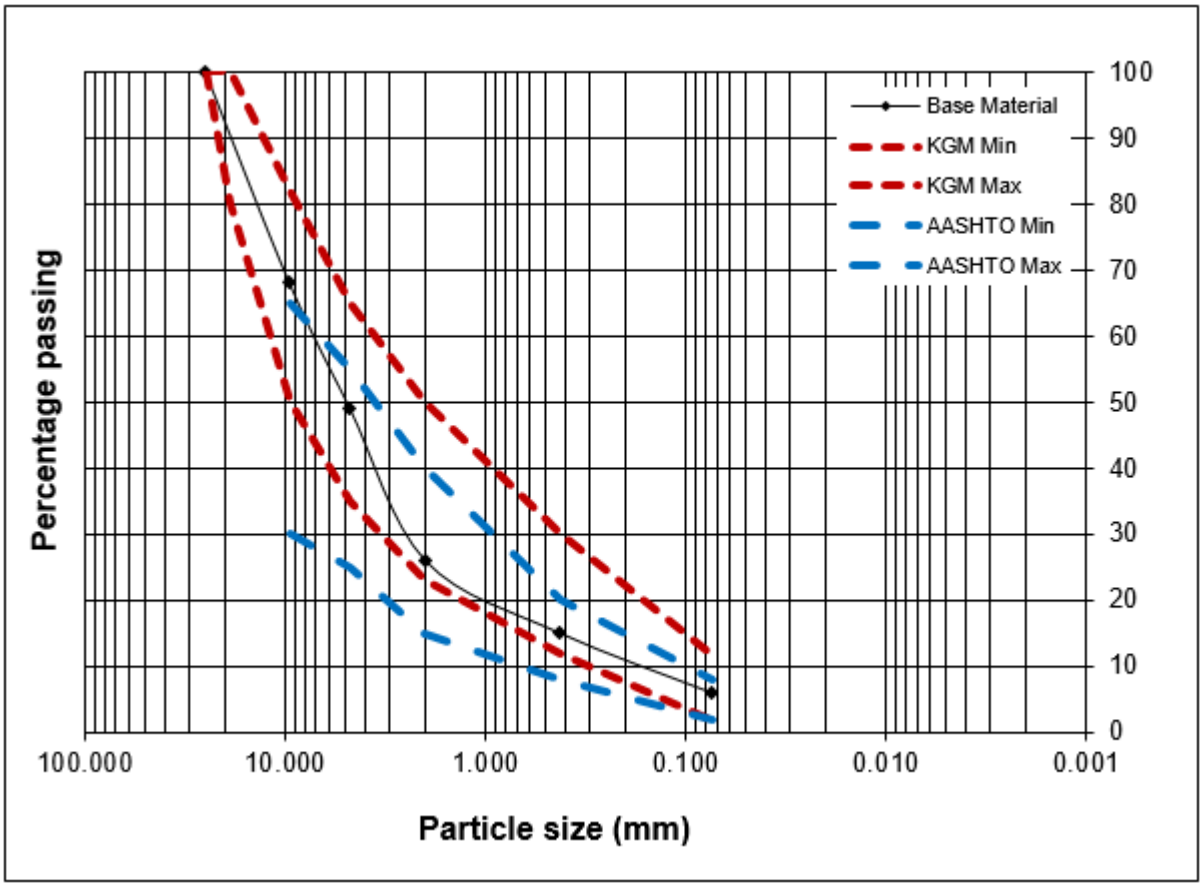

Figure 5.31. Particle size distribution of base material.

As represented in Figure 5.30 and Figure 5.31, the grain-size distribution of subbase and base materials were compared with the lower and upper limits of 2013 KGM and 1993 AASHTO regulations. Based on the test results, subbase material is mostly compatible with both regulations with few exceptions at lower (D≤0.075mm) and upper bounds (D≥50mm). The particle-size distribution of the base material is in a good aggrement with both regulations as represented in Figure 5.75 given that the particle size distribution of the base material is in the defined range of 2013 KGM and 1993 AASHTO.

5.2.1.2. Geogrid Material

For the geogrid reinforced highway embankment model, the selected geogrid material is bi-axial ForTex GG 40x40kN/m obtained from a local company named Istanbul Teknik in

Istanbul. The ultimate tensile strength (T_{ult}) is 40kN/m for both axes. Geogrid with T_{ult} : 40kN/m is commonly preffered for road and highway constructions. The geogrid material meets the requirements as given in FHWA NHI-07-092 (Table 5.13).

Table 5.13. Geogrid material requirements of FHWA NHI-07-092.

Property	Test Method	Units	Requirement		
SURVIVABILITY			Geogrid Class		
			CLASS 1[4]	CLASS 2	CLASS 3
Ultimate Multi-Rib Tensile Strength	ASTM D 6637	lb/ft (kN/m)	1230 (18)	820 (12)	820 (12)
Junction Strength[5]	GSI GRI GG2	lb (N)	25[5] (110[6])	25 (110)	8 (35)
Ultraviolet Stability (Retained Strength)	ASTM D 4355	%	50% after 500 hours of exposure		
OPENING CHARACTERISTICS					
Aperture Size	Direct measure	in. (mm)	0.5 to 3 in. (12.5 to 75 mm) and Aperture Size ≥ D50 of aggregate above geogrid Aperture Size ≤ 2·D85 of aggregate above geogrid		
Separation	ASTM D 422	mm	D85 of aggregate above geogrid < 5·D85 subgrade Other wise use separation geotextile with geogrid		

Two layers of geogrid layers with the given tensile strength have been previously found to be enough with respect to the preliminary finite element analysis and hand calculations.

5.2.1.3. EPS Geofoam Material

The EPS Geofoam material for the proposed field scale experiments was chosen following the guidelines and recommended standards outlined in the NCHRP (2004). In accordance with the requirements, the selected EPS Geofoam material has a density of 20kg/m^3 and is designated as EPS50, as proposed by AASHTO. As given in Table 5.14, minimum allowable full-block density of the EPS geofoam material should be 20kg/m^3 and the selected material meets the requirements. The material designation by the AASHTO for EPS geofoam blocks is based on the minimum elastic limit stress of the blocks (50kPa in this case). EPS geofoam blocks were arranged by Turkish EPS Geofoam Association, EPSDER. The design values of engineering parameters for the three typical EPS Geofoam blocks can be found in

Table 5.14. The effect of temperature and stress on expected strains for EPS geofoam with 20kg/m^3 density is given in Table 5.15.

Table 5.14. Engineering parameters of EPS geofoam blocks in NCHRP (2004).

Proposed AASHTO Material Designation	Design Values of Engineering Parameters			
	Minimum Allowable Full-Block Density, kg/m^3(lbf/ft^3)	California Bearing Ratio, CBR (%)	Initial Tangent Young's Modulus, E_{ti}, MPa(lbs/in^2)	Resilient Modulus, M_R, MPa(lbs/in^2)
EPS50	20 (1.25)	2	5 (725)	5 (725)
EPS70	24 (1.5)	3	7 (1015)	7 (1015)
EPS100	32 (2.0)	4	10 (1450)	10 (1450)

Table 5.15. The effect of temperature and stress on expected strains for 20kg/m^3 density EPS geofoam NCHRP (2004).

Density	Temperature	Stress	Duration	Strain	Strain Increase
20 kg/m^3 (1.25 lbs/ft^3)	+23 °C (+73°F)	30 kPa (626 lbs/ft²)	2,400 hours (approx. 3 months)	0.8%	0%
	+60 °C (+140 °F)			1.5%	88%
	+23 °C (+73 °F)	40 kPa (835 lbs/ft²)	2,400 hours (approx. 3 months)	1.1%	0%
	+60 °C (+140 °F)			3.25%	195%

5.2.2. Embankment Design Considerations

Field scale seismic performance tests require a number of considerations right from the design stage. The success of the proposed experimental studies are highly depended on the five pre-defined critera to meet. These are damage criteria, MSS criteria, Site Characteristics criteria, Natural Frequency of the Models criteria and the Budget criteria.

- Damage Critera: Unreinforced model must experience damage while reinforced model and EPS geofoam model should get severe damage in order to assess the effectiveness of the geogrid reinforcement and lightweight material on the seismic performance

- MSS Criteria: The bias between the input and output dynamic excitation must be minimal in order to successfully excite the embankment models.

- Site Characteristics Criteria: The fundamental period of the test area should not coincide the fundamental period of the embankment models.

- Natural Frequency of the Models Criteria: The natural frequency of embankment models should be in the range of what MSS can successfully apply. Resonance phenomenon should be observed to achieve the maximum response.

- Budget Criteria: Construction costs should not exceed the pre-arranged budget.

5.2.3. Mobile Seismic Shaker (MSS)

Dynamic field testing of geotechnical and structural systems has become possible with the development of large-scale mobile shakers which are also called as vibroseis or thumoer truck. Excitations generated by these large mobile shakers can be controlled in direction (vertically or horizontally), frequency, and load amplitude. The use of mobile seismic shakers is quite appropriate for subsurface imaging (2D/3D), In-Situ liquefaction tests, structural health monitoring and soil structure interaction studies.

Mobile seismic shakers offer great advantages, especially for large-scale dynamic testing, in earthquake engineering and civil engineering fields to ensure accurate and realistic testing. One of the biggest disadvantages of shake table testing is to be have to work on small-scale models due to the size and weight limitations. Thus, the compatibility between the

dynamic behavior of small-scale structures and their prototypes can often be debated by authorities.

One of the greatest advantages of mobile seismic shakers is the ability to work easily with large-scale and real-sized structures without any limitations. In this way, the results obtained from numerical analyses can be compared much more accurately with reality.

There are only a few mobile shakers in the world and one of those is currently operated by Boğaziçi University Kandilli Observatory and Earthquake Research Institute which is the only one of a kind in Turkey. It is specially designed by the Earthquake Engineering Department for the "Geotechnical Earthquake Engineering Research Center Project" funded by T.C. Cumhurbaşkanlığı Strateji ve Bütçe Başkanlığı. Proposed field scale experimental studies will be performed by use of this vehicle. The Mobile Seismic Shaker (MSS) will be used as a dynamic source. The MSS can generate horizontal and vertical dynamic forces up to 27kN in a frequency range of 10-225Hz. The self-weight of the vehicle is 10 tons. The vehicle is represented in Figure 5.32.



Figure 5.32. The mobile seismic shaker (MSS).

5.2.4. Construction of the Highway Embankment Models

Three different full scale highway embankments were constructed at the proposed test area of with respect to the regulation and standards of the 1993 AASHTO, 2013 KGM Technical Regulations, FHWA NHI-05-037 and 2004 NCHRP. The types of embankments are namely unreinforced embankment, geogrid reinforced embankment and lightweight EPS Geofoam embankment. Construction of the embankment models were done by a local company named Irem Inşaat.

Field scale seismic performance tests require a number of considerations right from the design stage. In the design stage; hand calculations and preliminary numerical analyses were performed to obtain the exact dimensions of the embankment models in accordance with the previously defined design considerations.

The dimensions of the Unreinforced Embankment model are 9m x 9m on the ground, 5x 5m at crest level with 2m of height and the slope inclination of 45° as represented in Figure 5.33.

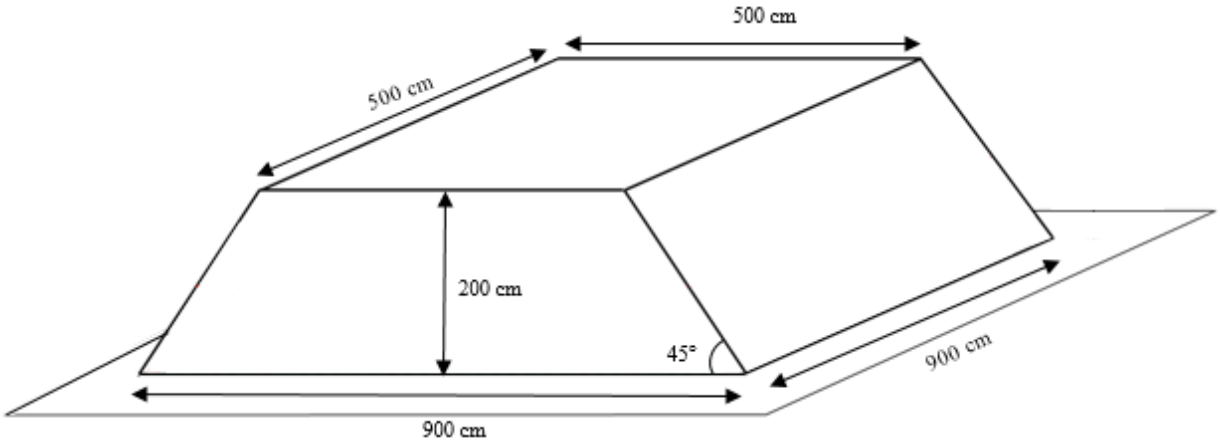

Figure 5.33. Dimensions of the Unreinforced Embankment Model (not to scale).

Construction of different types highway embankments involves several different important processes. Step by step construction process of the unreinforced highway embankment model is given in Figure 5.34.



Figure 5.34. Construction steps of the unreinforced embankment, a) Preperation of the site, b) Excavation, c) Preperation of the foundation, d) Construction of the subbase, e) Construction of the base, f) Asphalt paving.

As represented in Figure 5.34, any vegetation, bushes, debris and rock is removed from the construction site in the first place (a). First, top most soil layer on the construction site is removed with the help of an excavator to reach the foundation soil (b). Second, the foundation layer is leveled and compacted with the self weight of the excavator (c). Then, the subbase material is laid with the help of an excavator to the construction site of interest in a controlled manner to ensure uniformity. The material properties of the subbase material were previously determinded by a series of laboratory experiments. The unit weight of the subbase material is $20kN/m^3$ with $20kN/m^2$ of cohesion and 35° of internal friction angle. It is important to lay the subbase material in approximately 30cm layers and to compact each layer with the help of a hand operated roller until the desired relative density D_r of around 70% is achieved. The thickness of the subbase layer is 155cm (d). Similar to the previous stage, the base material laid over the subbase material with the help of an excavator in a controlled manner to ensure uniformity. The material properties of the base material were previously determinded by a series of laboratory experiments. The unit weight of the material is $22kN/m^3$ with $30kN/m^2$ of cohesion and 45° of internal friction angle. The base material is compacted with the help of a hand operated roller until the desired relative density D_r of around 90% is achieved. The thickness of the base layer is 30cm (e). Finally, the embankment surface layer is paved with bituminous asphalt concrete layer. Asphalt mix is carried from the plant to the construction site with the help of a insulated truck to maintain the required temperature. The asphalt mix is spread over the base layer quickly and carefully and the asphalt mix is compacted with the hand operated roller until the desired 15cm of thickness is achieved (f).

The dimensions of the Geogrid Reinforced Embankment model are 9m x 9m on the ground, 5m x 5m at crest level with 2m of height and the slope inclination of 45°. Two layers of geogrid reinforcement, one layer at the base of the embankment and one layer at mid-height of the embankment was previously found to be enough with respect to the hand calculations and used during the construction process (Figure 5.35). The geogrid reinforced embankment is identical to the unreinforced highway embankment model except the geogrid reinforcement.

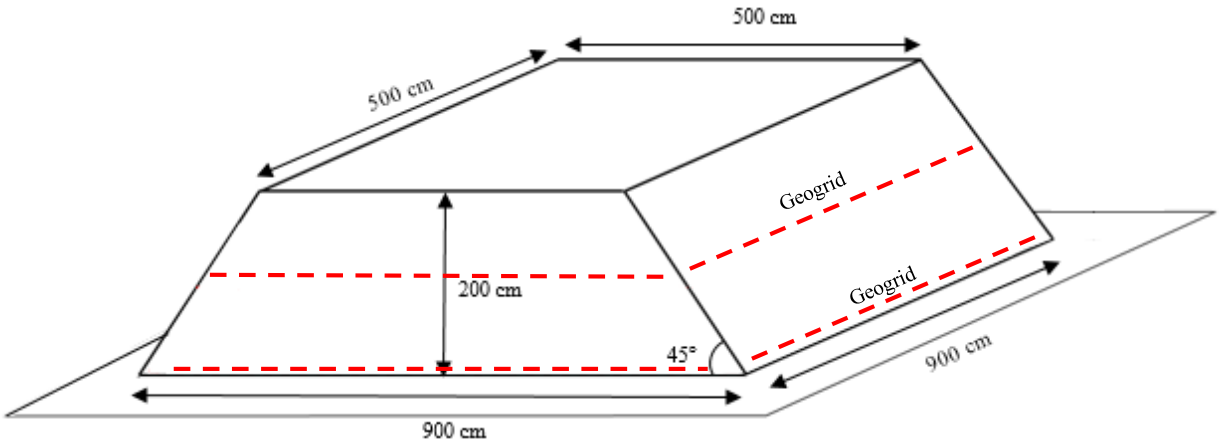

Figure 5.35. Dimensions of the Geogrid Reinforced Embankment Model (not to scale).

Construction of geogrid reinforced highway embankments requires important steps and disciplines that needs to take into account. The construction sequence is represented in Figure 5.36.



Figure 5.36. Construction steps of the geogrid reinforced embankment, a) Rolling the first geogrid layer, b) Construction of the subbase, c) Rolling the second geogrid layer, d) Construction of the base, e) Asphalt paving.

As represented in Figure 5.36; similar to the construction stages of the unreinforced embankment; any vegetation, bushes, debris and rock was removed from the construction site, top most soil layer on the construction site was removed with the help of an excavator to reach the foundation soil and the foundation layer was leveled and compacted with the self weight of the excavator to provide the required strength and stability to the embankment model before the construction of the geogrid reinforced embankment model. After, the first geogrid reinforcement layer was rolled over the foundation soil and under the subbase layer (a). The subbase material was laid with the help of an excavator over the first geogrid layer very carefully. The material properties of the subbase material were previously determinded by a series of laboratory experiments. The unit weight of the material is $20kN/m^3$ with $20kN/m^2$ of cohesion and 35° of internal friction angle. As mentioned previously, it is important to lay the subbase material in approximately 30cm layers and to compact each layer with the help of a hand operated roller until the desired relative density D_r of 70% is achieved (b). When the thickness of the subbase layer is exactly 100cm (mid-height of the embankment), the second layer of geogrid was installed over the existing part of the subbase layer (c). After, an additional 55cm of subbase material is laid and compacted over the second layer of reinforcement. The base material was laid over the subbase material with the help of an excavator in a controlled manner to ensure uniformity. The material properties of the base material were also previously determinded by a series of laboratory experiments. The unit weight of the material is $22kN/m^3$ with $30kN/m^2$ of cohesion and 45° of internal friction angle. After, the base material is compacted with the help of a hand operated roller until the desired relative density D_r of 90% is achieved. The thickness of the base layer is 30cm (d). Finally, the embankment surface layer was paved with bituminous asphalt concrete layer. Asphalt mix was carried from the plant to the construction site with the help of a insulated truck to maintain the required temperature. The asphalt mix was spread over the base layer quickly and carefully and the asphalt mix was compacted with the hand operated roller until the desired 15cm of thickness is achieved (e).

Dimensions of the EPS Geofoam highway embankment model are 9m x 9m on the ground, 5m x 5m at crest level with 2m of height. Proposed EPS geofoam blocks are shown in Figure 5.37.

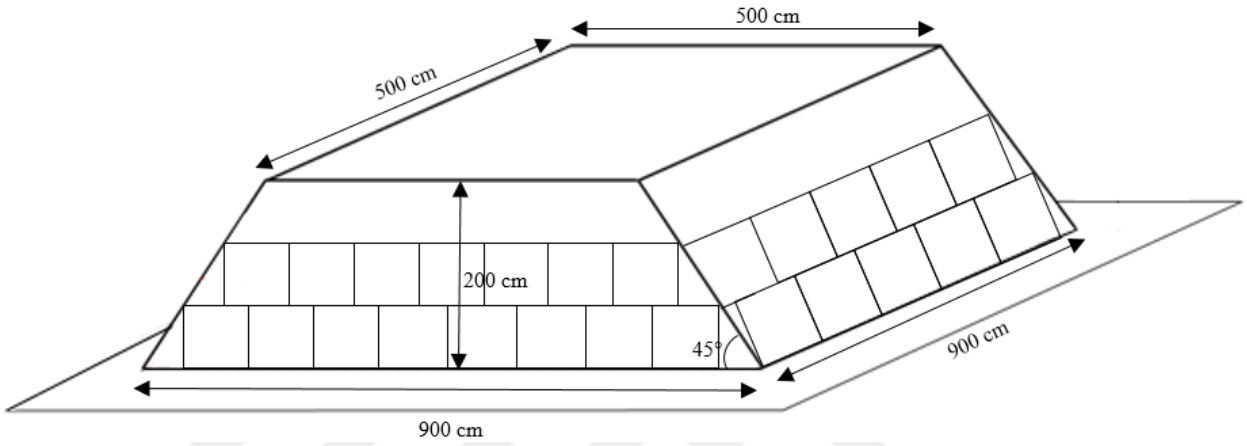

Figure 5.37. Dimensions of the EPS Geofoam Embankment Model (not to scale).

The construction sequence of the EPS geofoam embankment is represented in Figure 5.38.



Figure 5.38. Construction steps of the EPS geofoam embankment, a) Levelling the EPS geofoam blocks, b) EPS geofoam blocks as subbase, c) Construction of the base, d) Asphalt concrete paving, e) Protection layer.

Given in Figure 5.38; just like it was the case for the unreinforced and geogrid reinforced embankment; any vegetation, bushes, debris and rock was removed from the construction site, top most soil layer on the construction site was removed with the help of an excavator to reach the foundation soil and the foundation layer was leveled and compacted with the self weight of the excavator to provide the required strength and stability to the embankment model before the construction of the EPS geofoam embankment model too. As represented in Figure 5.38a, levelling process is a key stage for the construction with EPS geofoam blocks to make sure every single block is aligned and fit tightly together to minimize gaps between blocks and to ensure the uniform load distribution. EPS geofoam blocks are used as the subbase layer itself for the EPS geofoam highway embankment model. Each geofoam block has dimensions of 100x100x75cm and using a total of 74 blocks, 55.5m^3 of EPS geofoam blocks were used for the construction. Material properties of the EPS geofoam are given in detail in Section 5.2.1.3. As recommended in NCHRP (2004), minimum two layers of EPS geofoam were used. The blocks were carefully placed to consider the slope angle of 45°. The second layer of blocks were unevenly distributed with respect to the first layer of blocks (b). After, the base material laid over the subbase material with the help of an excavator in a controlled manner to ensure uniformity. The material properties of the base material were also previously determinded by a series of laboratory experiments. The unit weight of the material is 22kN/m^3 with 30kN/m^2 of cohesion and 45° of internal friction angle. The base material is compacted with the help of a hand operated roller until the desired relative density D_r of 90% was achieved. The thickness of the base layer is 30cm (c). Then, the embankment surface layer was paved with bituminous asphalt concrete layer. Asphalt mix was carried from the plant to the construction site with the help of a insulated truck to maintain the required temperature. The asphalt mix was spread over the base layer quickly and carefully and the asphalt mix was compacted with the hand operated roller until the desired 15cm of thickness was achieved (d). After the completion of the construction, EPS blocks were covered with fine grained fill material to protect the EPS blocks from UV rays and wheatering (e). The completed highway embankment models after the construction is given in Figure 5.39.

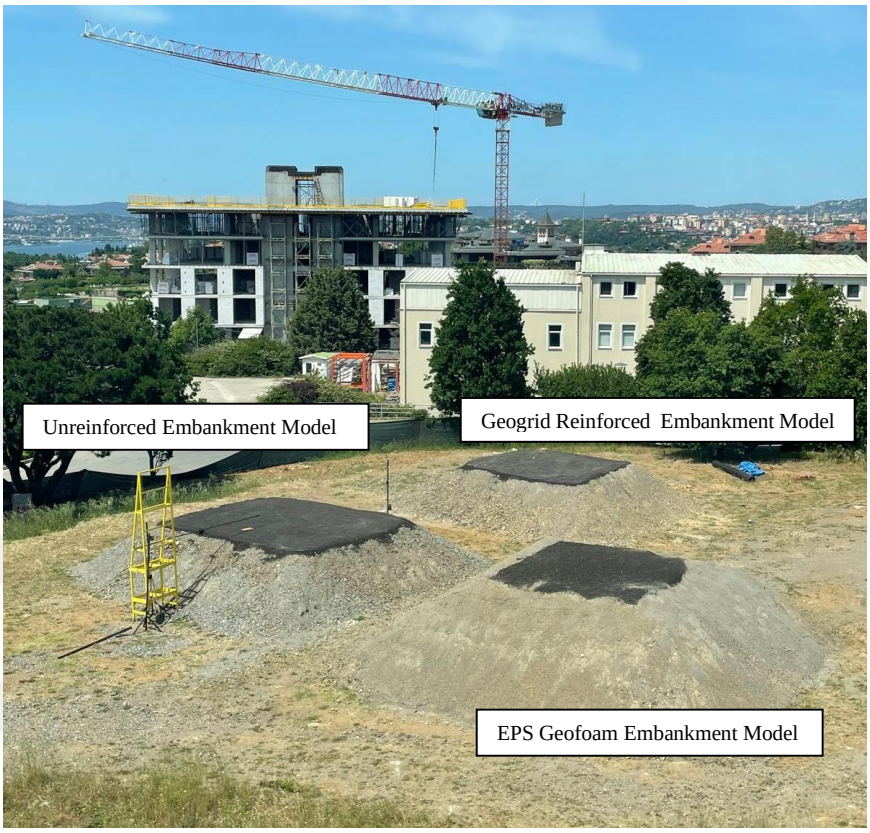

Figure 5.39. The completed highway embankment models after construction.

5.2.5. Instrumentation Plan

A true instrumentation plan is very important for experimental studies. Determining sensor locations for a field-scale seismic performance test of highway embankment models involves a strategic approach to capture the critical responses of the embankment models subjected to dynamic motions. Obtained results from preliminary numerical analysis were considered for the determination of the sensor locations.

Instrumentation plan for field scale seismic performance tests consists of 12 accelerometers (A) and 4 LVDT's (D). Accelerometers are to be placed at various heights and locations from toe to crest of the embankment models to better understand the variation of transmitted accelerations for each and every model. A1 is located on the ground, next to the

embankment to capture the input dynamic motion from Mobile Seismic Shaker. A2, A3 and A4 are located on the slope of the embankment at different heights of h/4, 2h/4 and 3h/4, respectively in order to understand the amplification/deamplification effects with respect to embankment height. A total of seven accelerometers were employed at the crest of the embankment models at various locations to gain a better insight about the dynamic response of embankment models as crest is the most important part of an highway embankment model. A5, A6, A7 and A8 are located at the crest linearly along the center of the embankment. So that linear/non-linear regression analysis could be performed between the acceleration response and distance to source. A9 is located at the noth-east corner, A10 is located at the south-east corner, A11 is located at the south-west corner, and A12 is located at the north-west corner of the crest. Güralp CMG-CD2453EAM model accelerometers are used. Accelerometers are fixed to the asphalt concrete layer by using two-sided tapes and super-strong adhesives (Figure 5.40).



Figure 5.40. Fixing the accelerometers on asphalt concrete layer.

D1, D2 and D3 are displacement transducers to measure the horizontal displacements located on the slope of the embankment at different heights of h/4, 2h/4 and 3h/4, respectively in order to understand how horizontal displacements are influenced by the embankment height. D4 is located at the center of the crest to measure the vertical displacements (settlements). Horizontal displacements on the road alignment and vertical displacements on the crest of the embankment models will be measured with Leuze ODS10L1-25M.8/LAK-M12 model LVDT sensors. The measurement range is 25m with the resolution of 1mm.

The instrumentation plan remains the same for all embankment models (Unreinforced, Geogrid Reinforced, EPS Geofoam) and both directions (along the road direction and perpendicular to the road direction). The instrumentation plan along the road direction is represented in Figure 5.41 and the instrumentation plan perpendicular to the road direction is represented in Figure 5.42.

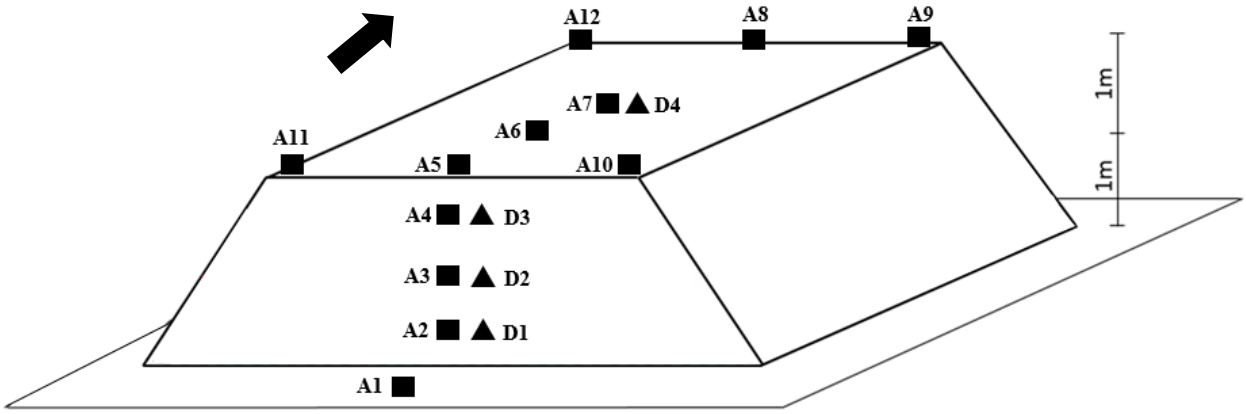

Figure 5.41. Instrumentation Plan along the Road Direction.

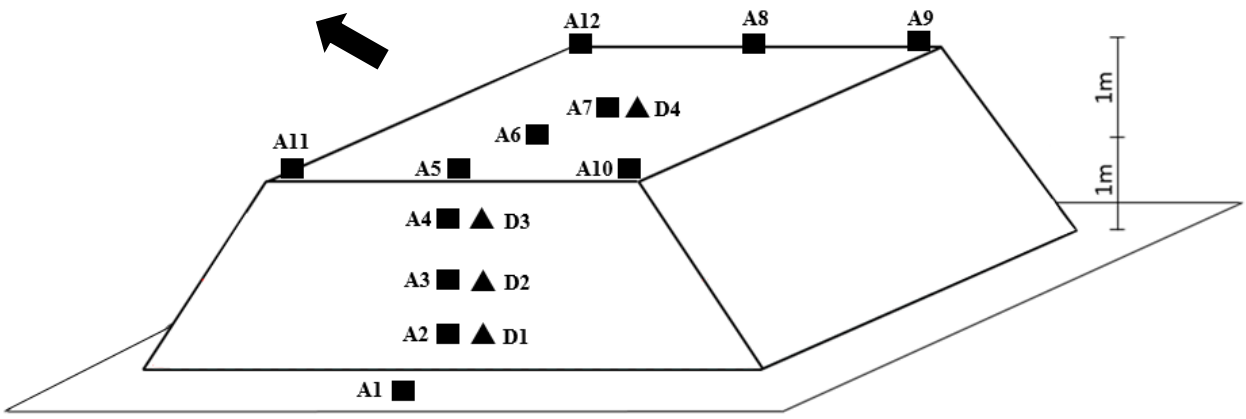

Figure 5.42. Instrumentation Plan Perpendicular to the Road Direction.

Instrumented Unreinforced Embankment Model prior to seismic performance tests is shown in Figure 5.43.



Figure 5.43. Unreinforced Embankment Model prior to seismic performance tests, a) along the road direction, b) perpendicular to the road direction.

Instrumented Geogrid Reinforced Embankment Model prior to seismic performance tests is shown in Figure 5.44.



Figure 5.44. Geogrid reinforced Embankment Model prior to seismic performance tests, a) along the road direction, b) perpendicular to the road direction.

Instrumented EPS Geofoam Embankment Model prior to seismic performance tests is shown in Figure 5.45.

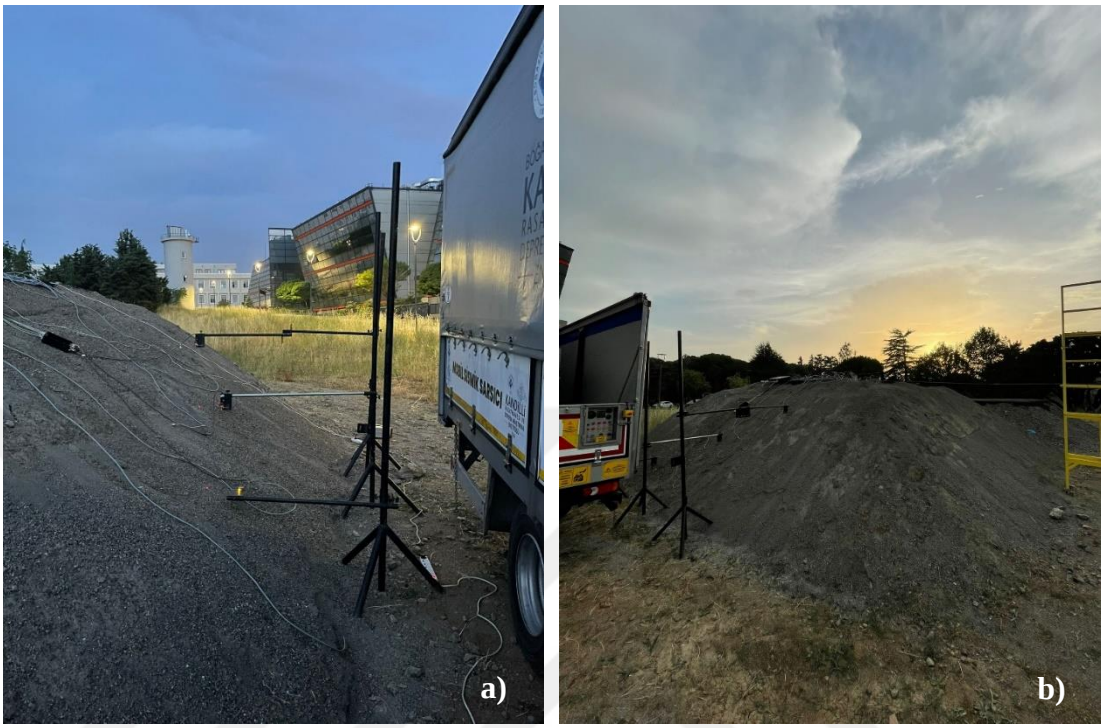

Figure 5.45. EPS Geofoam Embankment Model prior to seismic performance tests, a) along the road direction, b) perpendicular to the road direction.

Obtained data from all sensors are collected with the help of 16-channel data acquisition system and saved in the laptop (Figure 5.46).



Figure 5.46. Conducting the seismic performance tests.

Embankment locations on the test area were precisely determined with respect to the obtained results from a series of geophysical experiments including MASW Tests (section 5.1.4) and ERT Tests. Due to the nature of wave propagation, subsurface conditions under embankments should be as similar as possible to avoid any disturbance by site effects. Figure 5.47 represents the precise embankment locations at the test site and the shear wave velocity profiles beneath each embankment.

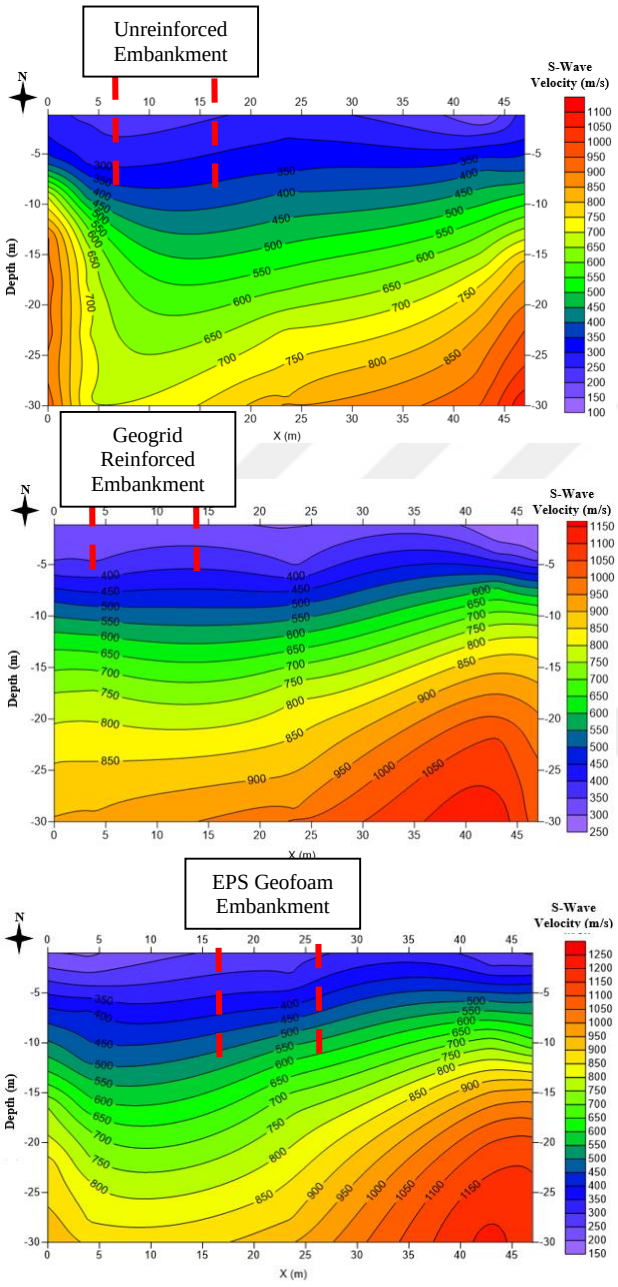

Figure 5.47. Shear wave velocity conditions under embankments by MASW Tests (Geometrik Mühendislik, 2021).

Coordinates and Vs_{30} values of embankment models are given Table 5.16 and Table 5.17, respectively for the west-end, middle and east-end sides of the models.

Table 5.16. Embankment Location Coordinates.

	Coordinates (West-Middle-East)
Unreinforced Embankment	41° 03’ 49.7” N - 41° 03’ 49.6” N - 41° 03’ 49.6” N 29° 03’ 50.4” E - 29° 03’ 50.5” E - 29° 03’ 50.6” E
Geogrid Reinforced Embankment	41° 03’ 49.5” N - 41° 03’ 49.4” N - 41° 03’ 49.4” N 29° 03’ 50.0” E - 29° 03’ 50.2” E - 29° 03’ 50.4” E
EPS Geofoam Embankment	41° 03’ 49.2” N - 41° 03’ 49.1” N - 41° 03’ 49.1” N 29° 03’ 49.6” E - 29° 03’ 49.9” E - 29° 03’ 50.1” E

Table 5.17. Vs30 Variation under Embankments.

	Vs_{30} (m/s) (West-Middle-East)
Unreinforced Embankment	505 – 506 - 507
Geogrid Reinforced Embankment	607 – 620 - 615
EPS Geofoam Embankment	523 – 525 - 529

Figure 5.48 represents the precise embankment locations at the test site due to the ERT results and the inverted resistivity profiles beneath each embankment. From low to high resistivity, the color of the graph changes from blue to red. As provided detailly in section 5.1.5, electrical resistivity is correlated with the shear wave velocities. Inverted resistivity to Vs_{30} convertion with respect to Figure 5.48 is given in Table 5.18.

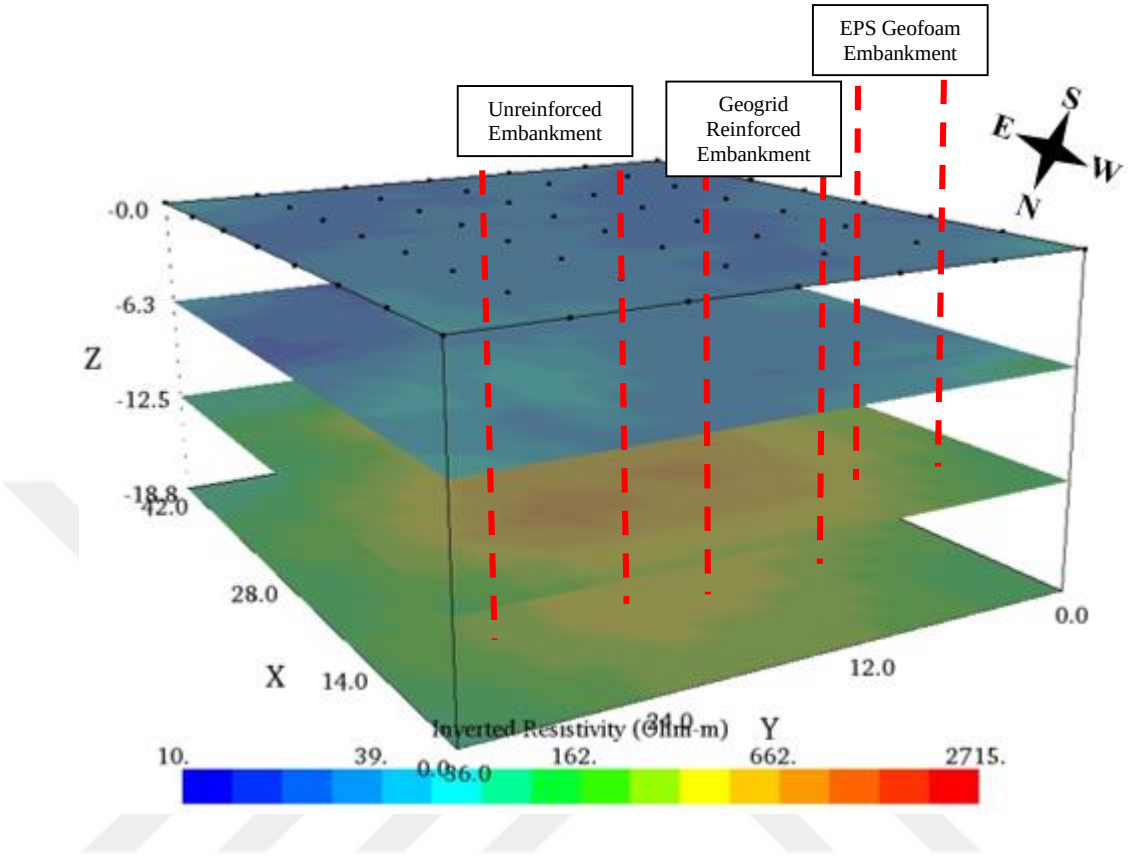

Figure 5.48. Sub-Surface conditions under embankments (Geometrik Mühendislik, 2021).

Table 5.18. Inverted Resistivity to Vs30 Conversion.

Inverted Resistivity from ERT	**Vs_{30} (m/s)**
Dark Blue	300
Green	500
Yellow	700
Red	1000

5.2.6. Dynamic Excitations

Field scale seismic performance tests of unreinforced highway embankment, geogrid reinforced highway embankment and EPS geofoam highway embankment are to be performed at the proposed test area located in Boğaziçi University Kandilli Observatory and Earthquake Research Instituite. Mobile Seismic Shaker is used as a dynamic excitation source in the field.

Dynamic excitations are selected carefully to observe the effect of different characteristics of seismic motions such as the frequency content, amplitude and duration on the dynamic performance of highway embankments. Capabilites of the MSS were also taken into consideration for the selection of the input motions for the applied frequency ranges and the force levels. Table 5.19, gives the detailed information about the input motions to be used throughout the full scale experimental studies in the field.

Table 5.19. Input motions to be applied by MSS for the full scale experiments.

Input Motions Applied by MSS	Frequency (Hz)	Duration (s)	Force (kN)
1)	1-100	30	15
2)	1-100	30	27
3)	1-250	30	15
4)	1-250	30	27
5)	1-250	120	27

5.2.7. Test Results Obtained from Field Scale Experimental Studies

Experimental results from full-scale unreinforced, geogrid reinforced and EPS geofoam highway embankment models for perpendicular to the road direction are given in this section. Experimental results are represented as Acceleration Responses and Displacement Responses.

5.2.7.1. Test Results for Unreinforced Embankment Model

Test results of the Unreinforced Embankment model for the perpendicular to the road direction are represented in this section. Test results are represented as Acceleration Responses and Displacement Responses for the selected accelerometers of A1, A3, A7, A11 and selected two LVDT's (D3 and D4). A1 is located on the ground, next to the embankment to capture the input dynamic motion from Mobile Seismic Shaker. A3 is located on the slope of the embankment at h/2 of the embankment. A7 is located at the crest along the center of the embankment and A11 is located at the south-west corner of the crest. D3 is displacement transducer to measure the horizontal displacements located on the slope of the embankment at

3h/4 and D4 is located at the center of the crest to measure the vertical displacements (settlements).

5.2.7.1.1. Test Results for Unreinforced Embankment Model under 1-100Hz

Obtained results under the input dynamic motions of 1-100Hz 15kN 30s and 1-100Hz 27kN 30s are given in this section. A1 is a uni-axial accelerometer located 1m away from the actuator of the Mobile Seismic Shaker on the ground and measures the accelerations. When the MSS applies incremental 1-100Hz sine wave at 15kN of force for 30s, the measured peak acceleration value is 0.32g as given in Figure 5.49a. When the MSS applies incremental 1-100Hz sine wave at 27kN of force for 30s, the measured peak acceleration value by A1 is 0.38g as given in Figure 5.49b.

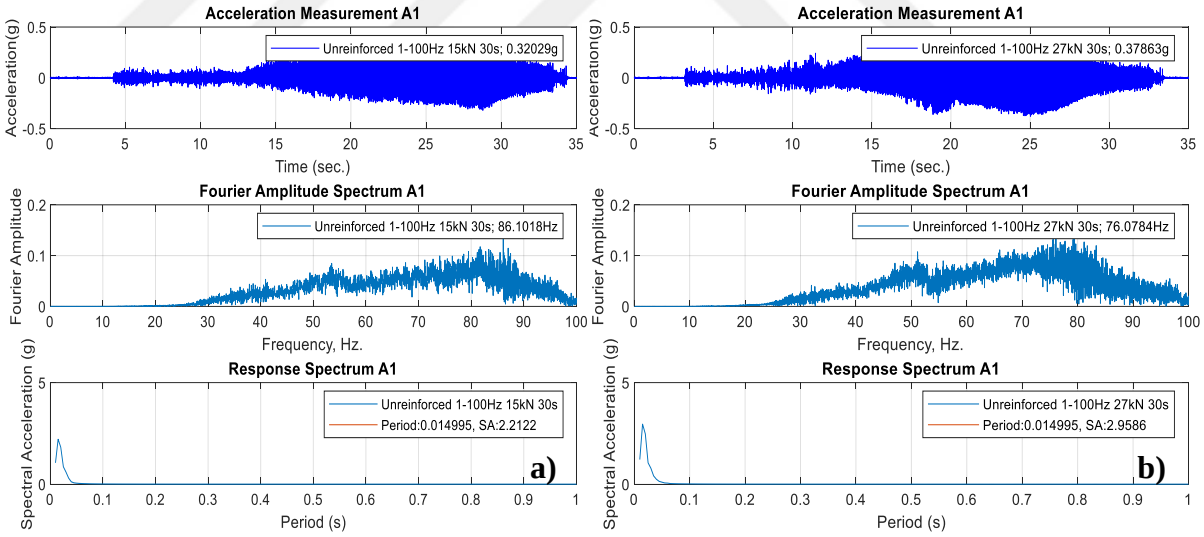

Figure 5.49. Acceleration Response of A1, a) 1-100Hz 15kN 30s, b) 1-100Hz 27kN 30s.

A3 is a uni-axial accelerometer located on the slope of the embankment at h/2 from the ground and measures the accelerations. When the MSS applies incremental 1-100Hz sine wave at 15kN of force for 30s, the measured peak acceleration value of A3 is 0.21g with Sa of 1.57g as given in Figure 5.50a. Under the incremental 1-100Hz sine wave at 27kN of force for 30s, the measured peak acceleration of the measured peak acceleration value of A3 is 0.24g with Sa

of 1.94g (Figure 5.50b). Peak accelerations at the slope of the embankment decrease with respect to height and the distance from the source.

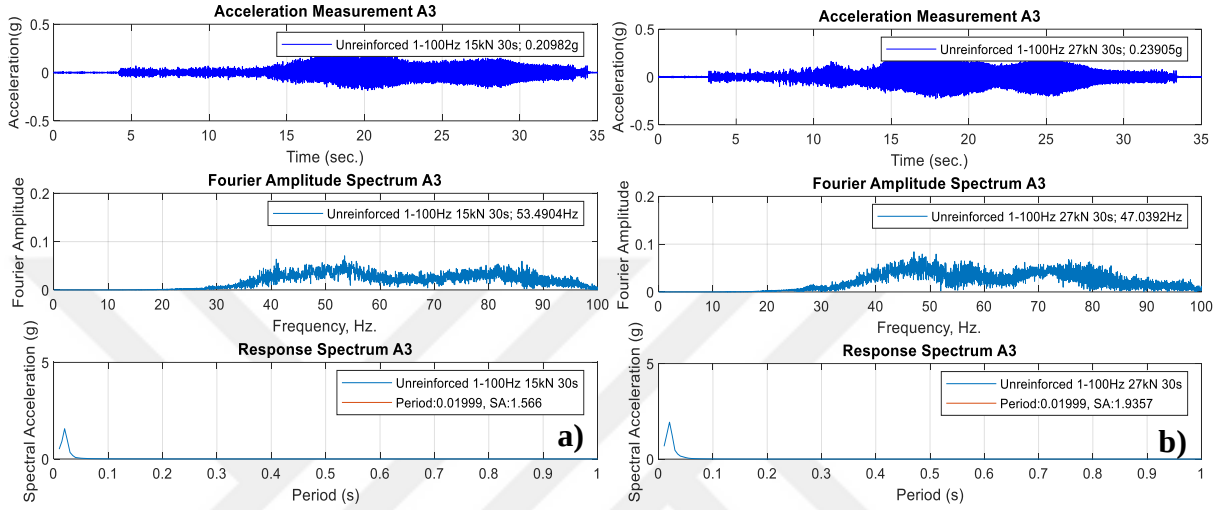

Figure 5.50. Acceleration Response of A3, a) 1-100Hz 15kN 30s, b) 1-100Hz 27kN 30s.

A7 is a uni-axial accelerometer located at the center of the crest of the embankment. As given in Figure 5.51a; when the MSS applies incremental 1-100Hz sine wave at 15kN of force for 30s, the measured peak acceleration value of A7 is 0.08g with Sa of 0.57g and under the incremental 1-100Hz sine wave at 27kN of force for 30s; the measured peak acceleration value of A7 is 0.09g with Sa of 0.69g (Figure 5.51b). Peak accelerations increase with respect to force.

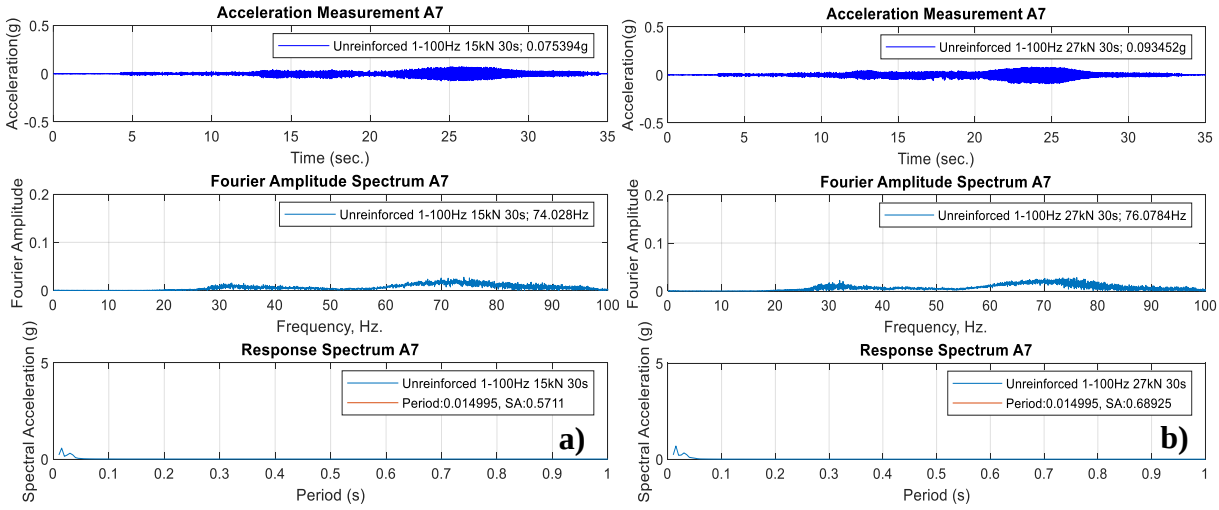

Figure 5.51. Acceleration Response of A7, a) 1-100Hz 15kN 30s, b) 1-100Hz 27kN 30s.

A11 is a uni-axial accelerometer located on the crest of the embankment at the south-west corner. As given in Figure 5.52a, when the MSS applies incremental 1-100Hz sine wave at 15kN of force for 30s, the measured peak acceleration value of A11 is 0.15g with Sa of 1.10g and under the 1-100Hz 27kN 30s, the measured peak acceleration value of A11 is 0.17g with Sa of 1.19g (Figure 5.52b). Transmitted and spectral accelerations increase with respect to force.

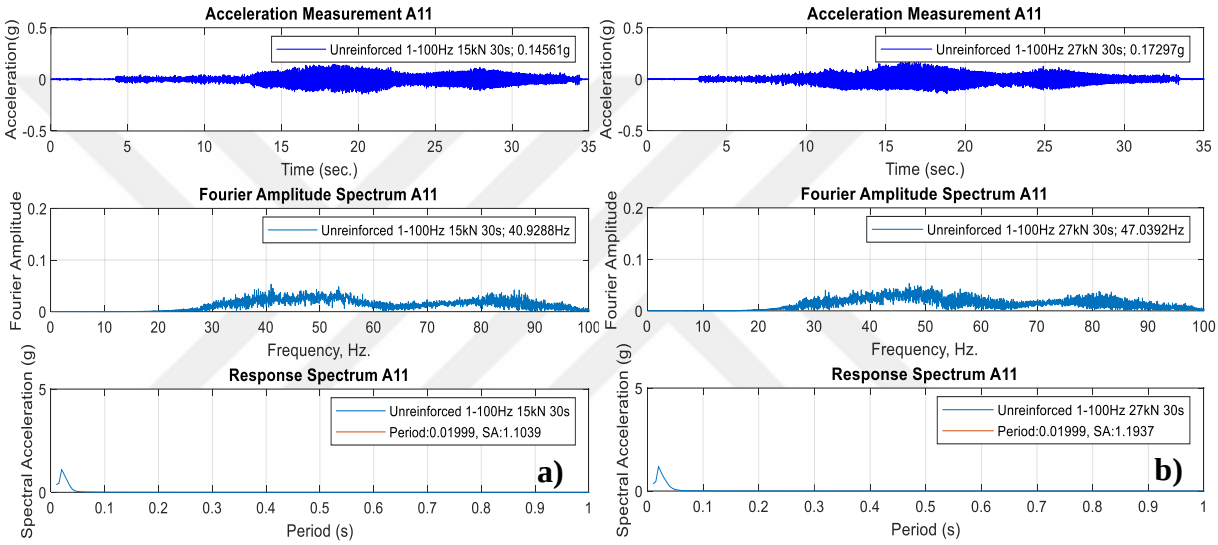

Figure 5.52. Acceleration Response of A11, a) 1-100Hz 15kN 30s, b) 1-100Hz 27kN 30s.

D3 is LVDT displacement transducers to measure the horizontal displacements located on the slope of the embankment at 3h/4. When the MSS applies incremental 1-100Hz sine wave at 15kN of force for 30s, the measured peak horizontal displacement values is measured as 0.36cm for D3 (Figure 5.53a) and when the force is increased to 27kN, the measured peak horizontal displacement values is measured as 0.79cm (Figure 5.53b).

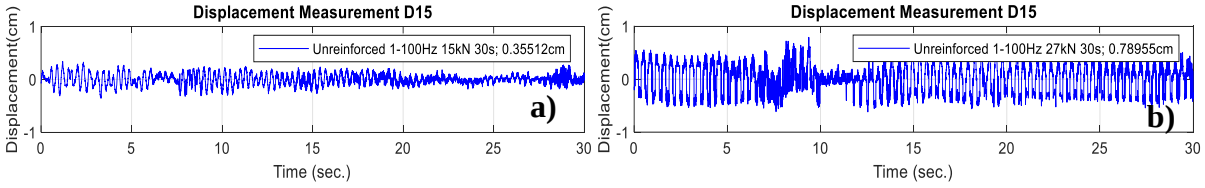

Figure 5.53. Displacement Response of D3, a) 1-100Hz 15kN 30s, b) 1-100Hz 27kN 30s.

D4 is a LVDT displacement transducer to measure the vertical displacements (settlements) located at crest. When the MSS applies incremental 1-100Hz sine wave at 15kN of force for 30s, the measured peak vertical displacement value from D4 is 1.01cm as given in Figure 5.54a. Under the 1-100Hz sine wave at 27kN of force for 30s, settlements increase to 1.51cm (Figure 5.54b). Displacement responses increase with respect to force.

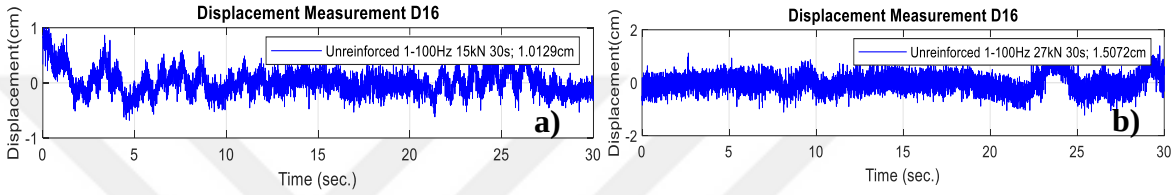

Figure 5.54. Displacement Response of D4, a) 1-100Hz 15kN 30s, b) 1-100Hz 27kN 30s.

5.2.7.1.2. Test Results for Unreinforced Embankment Model under 1-250Hz

Obtained results under the input dynamic motions of 1-250Hz 15kN 30s and 1-250Hz 27kN 30s are given in this section. When the MSS applies incremental 1-250Hz sine wave at 15kN of force for 30s, the measured peak acceleration value by A1 is 0.40g as given in Figure 5.55a. When the force level increases to 27kN, A1 measures 0.43g as given in Figure 5.55b.

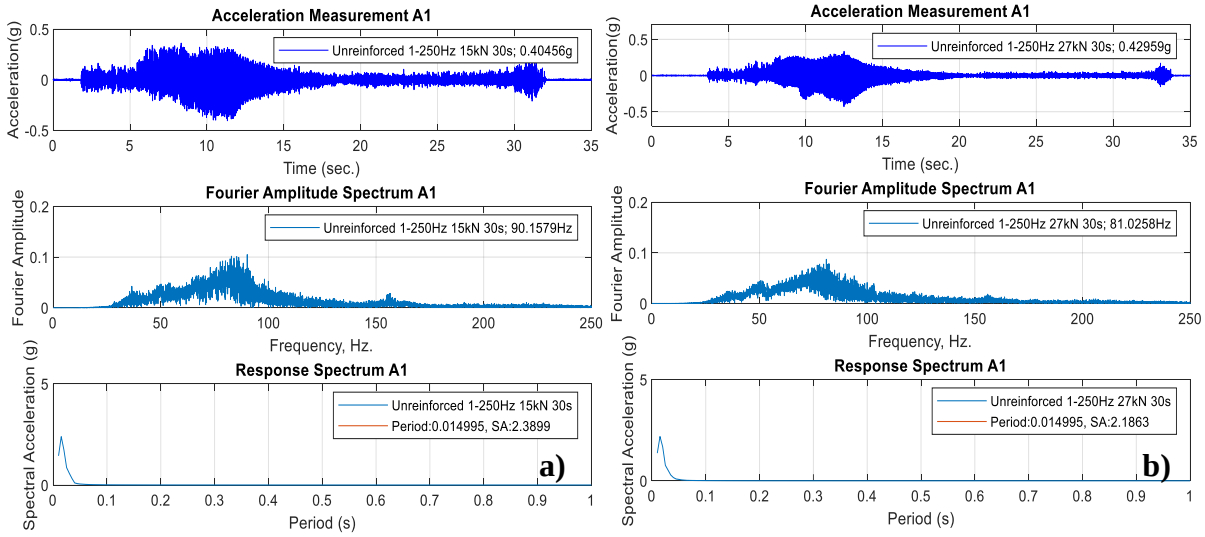

Figure 5.55. Acceleration Response of A1, a) 1-250Hz 15kN 30s, b) 1-250Hz 27kN 30s.

A3 is a uniaxial accelerometer on the embankment slope at a height of h/2 from the ground, measuring accelerations. When the MSS generates an incremental sine wave of 1-250Hz at a force of 15kN for 30 seconds, A3 records a peak acceleration of 0.25g, with a spectral acceleration (Sa) of 1.74g, as shown in Figure 5.56a. For a sine wave of the same frequency range but with a force of 27kN for 30 seconds, A3 measures a peak acceleration of 0.27g, and an Sa of 1.75g, as given in Figure 5.56b.

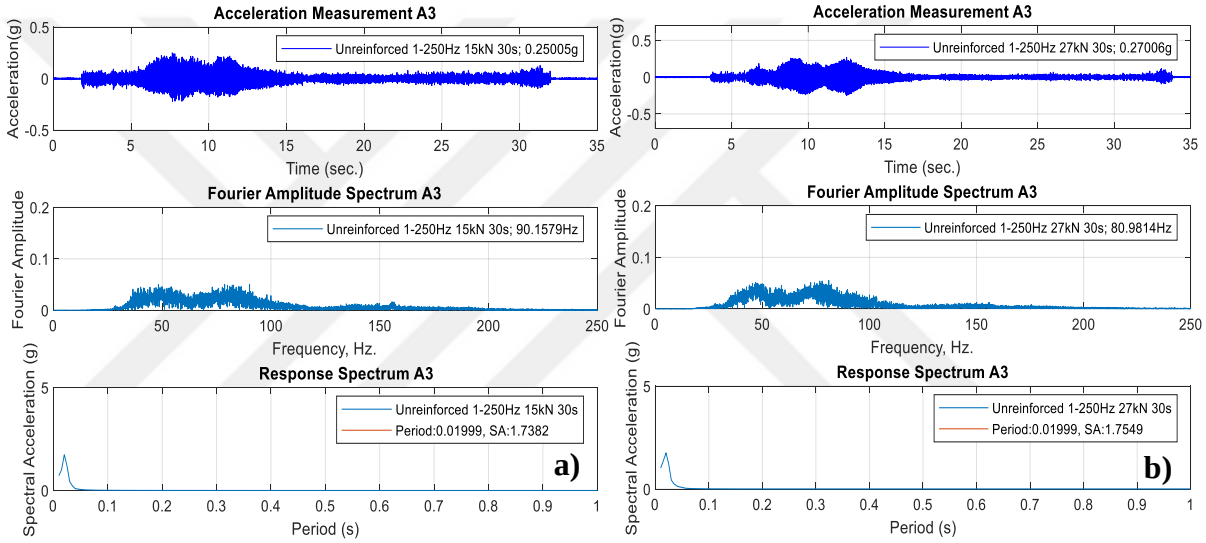

Figure 5.56. Acceleration Response of A3, a) 1-250Hz 15kN 30s, b) 1-250Hz 27kN 30s.

A7 is located at the center of the crest of the embankment. As given in Figure 5.57a, when the MSS applies incremental 1-250Hz sine wave at 15kN of force for 30s, the measured peak acceleration value of A7 is 0.09g with Sa of 0.67g and when the MSS applies incremental 1-250Hz sine wave at 27kN of force for 30s, the measured peak acceleration value of A7 is 0.10g with Sa of 0.64g (Figure 5.57b). Increased force leads to increased acceleration responses.

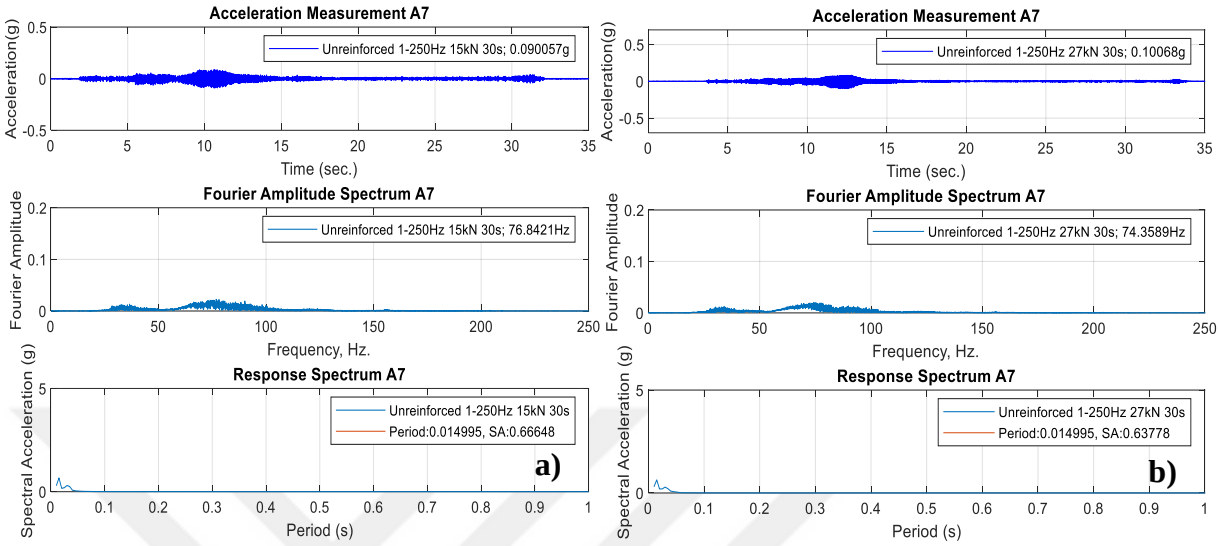

Figure 5.57. Acceleration Response of A7, a) 1-250Hz 15kN 30s, b) 1-250Hz 27kN 30s.

A11 is located on the crest of the embankment at the south-west corner. As given in Figure 5.58a, when the MSS applies incremental 1-250Hz sine wave at 15kN of force for 30s, the measured peak acceleration value of A11 is 0.18g with Sa of 1.14g and under the 1-250Hz 27kN 30s, the measured peak acceleration value of A11 is 0.20g with Sa of 1.20g (Figure 5.58b). Transmitted and spectral accelerations increase with respect to force.

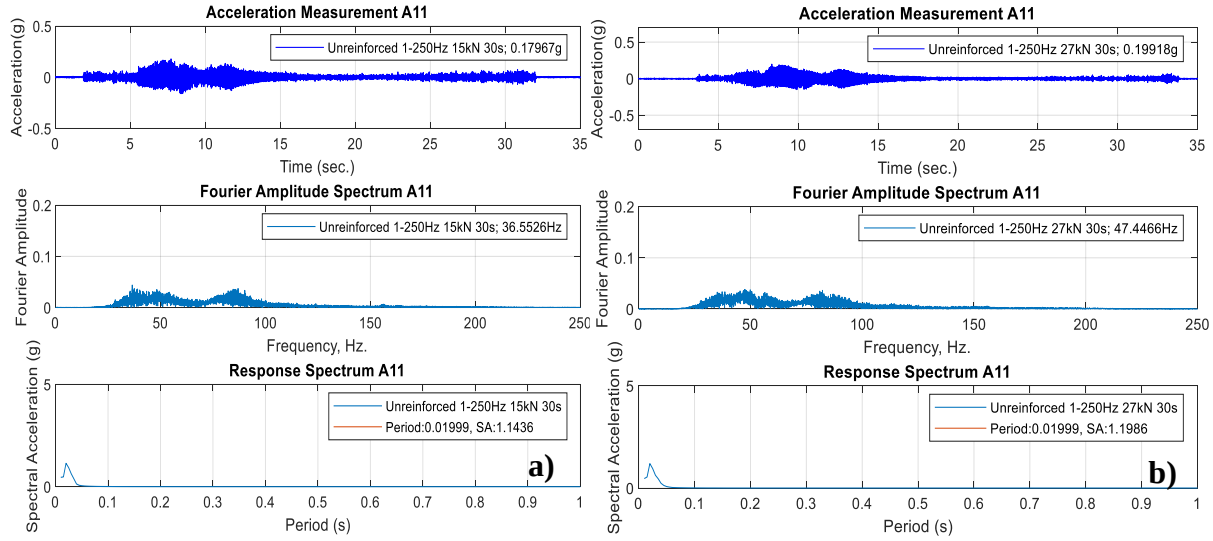

Figure 5.58. Acceleration Response of A11, a) 1-250Hz 15kN 30s, b) 1-250Hz 27kN 30s.

D3 is LVDT displacement transducers to measure the horizontal displacements located on the slope of the embankment at 3h/4. When the MSS applies incremental 1-250Hz sine wave at 15kN of force for 30s, the measured peak horizontal displacement value on the slope is measured as 1.56cm for D3 (Figure 5.59a) and when the force level is increased to 27kN, the measurement of D3 is obtained as 1.68cm (Figure 5.59b).

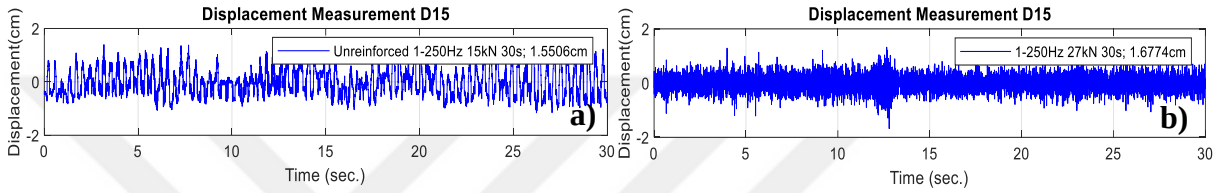

Figure 5.59. Displacement Response of D3, a) 1-250Hz 15kN 30s, b) 1-250Hz 27kN 30s.

D4 measures the vertical displacements (settlements) located at crest. When the MSS applies incremental 1-250Hz sine wave at 15kN of force for 30s, the measured peak vertical displacement value is 1.18cm as given in Figure 5.60a. Under the incremental 1-250Hz sine wave at 27kN of force for 30s, the measured peak settlement value is 1.27cm as given in Figure 5.60b. Increased force and frequency range has a direct effect on increased displacement responses.

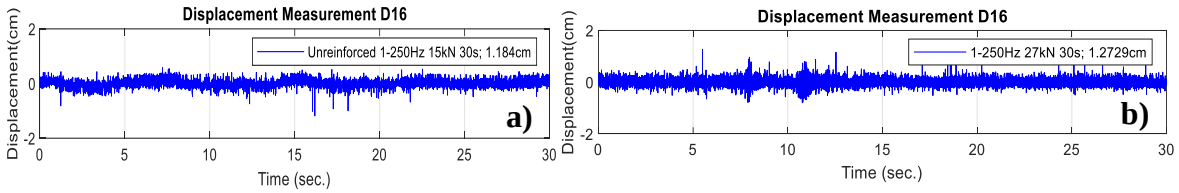

Figure 5.60. Displacement Response of D4, a) 1-250Hz 15kN 30s, b) 1-250Hz 27kN 30s.

5.2.7.1.3. Test Results for Unreinforced Embankment Model under 1-250Hz 27kN 120s

When the MSS applies incremental 1-250Hz sine wave at 27kN of force for 120s, the measured peak acceleration value by A1 is 0.50g as given in Figure 5.61.

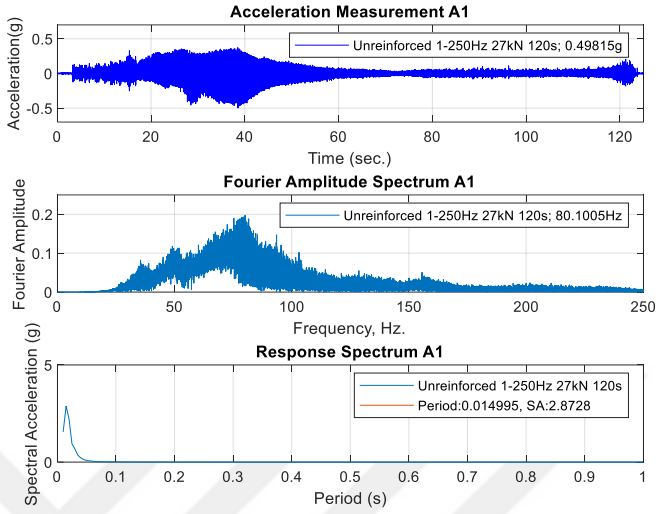

Figure 5.61. Acceleration Response of A1.

A3 is located on the slope of the embankment at h/2 from the ground and measures the accelerations. When the MSS applies incremental 1-250Hz sine wave at 27kN of force for 120s, the measured peak acceleration of A3 is 0.30g with Sa of 2.14g as given in Figure 5.62.

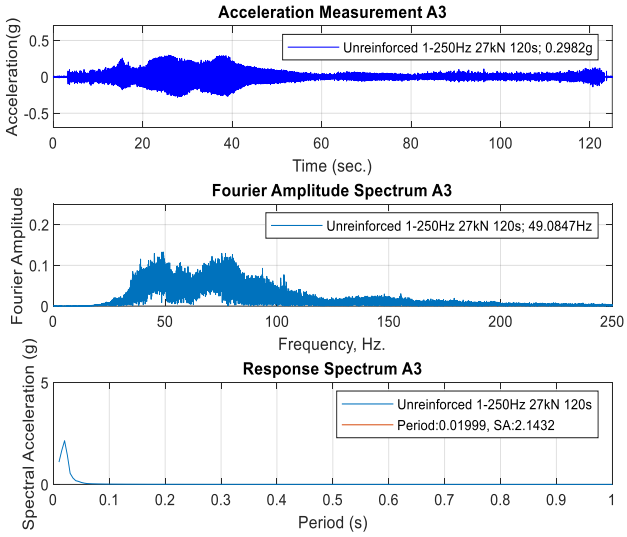

Figure 5.62. Acceleration Response of A3.

A7 is a uni-axial accelerometer located at the center of the crest of the embankment. As given in Figure 5.63, when the MSS applies incremental 1-250Hz sine wave at 27kN of force for 120s, the measured peak acceleration value of A7 is 0.09g with Sa of 0.61g.

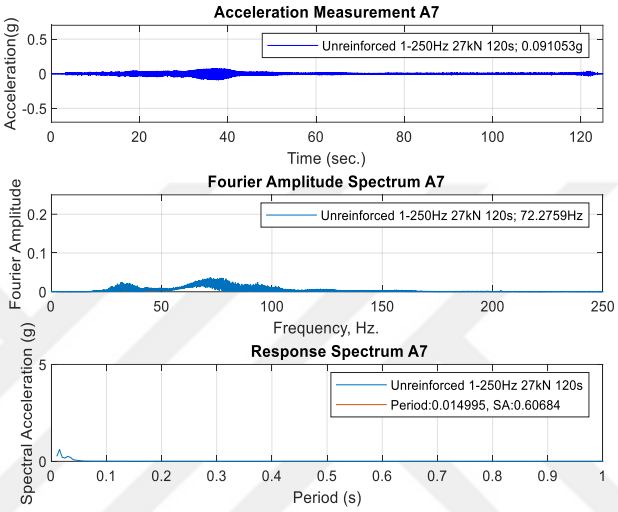

Figure 5.63. Acceleration Response of A7.

A11 is located on the crest of the embankment at the south-west corner. As given in Figure 5.64, when the MSS applies incremental 1-250Hz sine wave at 27kN of force for 120s, the measured peak acceleration value of A11 is 0.23g with Sa of 1.54g. Increased force and frequency range has a direct effect on increased acceleration responses.

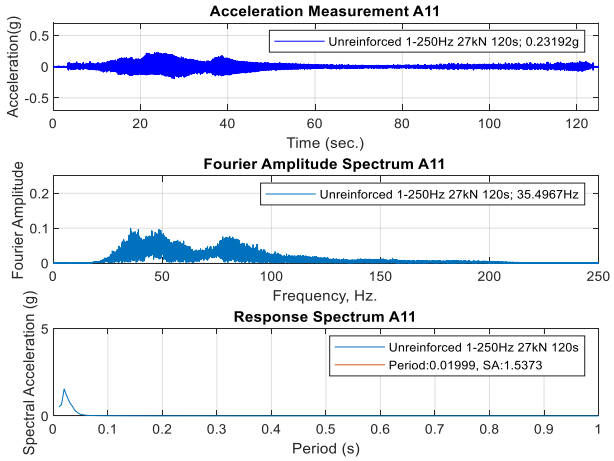

Figure 5.64. Acceleration Response of A11.

D3 is LVDT displacement transducers to measure the horizontal displacements located on the slope of the embankment at 3h/4. When the MSS applies incremental 1-250Hz sine wave at 27kN of force for 120s, the measured peak horizontal displacement values is 1.88cm for D3. Measured horizontal displacements increase with respect to duration and force (Figure 5.65).

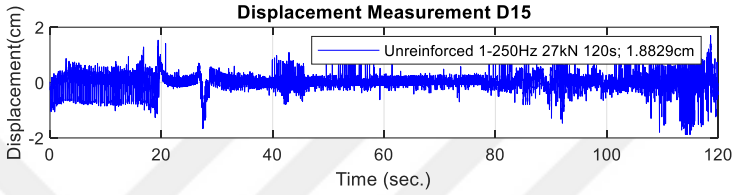

Figure 5.65. Displacement Response of D3.

D4 is a LVDT displacement transducer to measure the vertical displacements (settlements) located at crest. When the MSS applies incremental 1-250Hz sine wave at 27kN of force for 120s, the measured peak vertical displacement value is 1.38cm as given in Figure 5.66. Settlements increase with respect to duration and force of the applied motion.

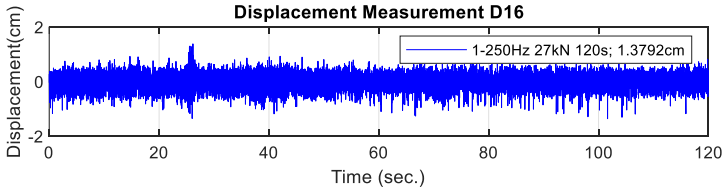

Figure 5.66. Displacement Response of D4.

5.2.7.2. Test Results for Geogrid Reinforced Embankment Model

Test results of the Geogrid Reinforced Embankment model for the perpendicular to the road direction are represented in this section. Test results are represented as Acceleration Responses and Displacement Responses for the selected accelerometers of A1, A3, A7, A11 and selected two LVDT's (D3 and D4).

5.2.7.2.1. Test Results for Geogrid Reinforced Embankment Model under 1-100Hz

Obtained results under the input dynamic motions of 1-100Hz 15kN 30s and 1-100Hz 27kN 30s are given in this section. A1 is a uni-axial accelerometer located 1m away from the actuator of the Mobile Seismic Shaker on the ground and measures the accelerations. When the MSS applies incremental 1-100Hz sine wave at 15kN of force for 30s, the measured peak acceleration value is 0.33g as given in Figure 5.67a. The measured peak acceleration value is 0.37g when the force of the MSS increases to 27kN (Figure 5.67b).

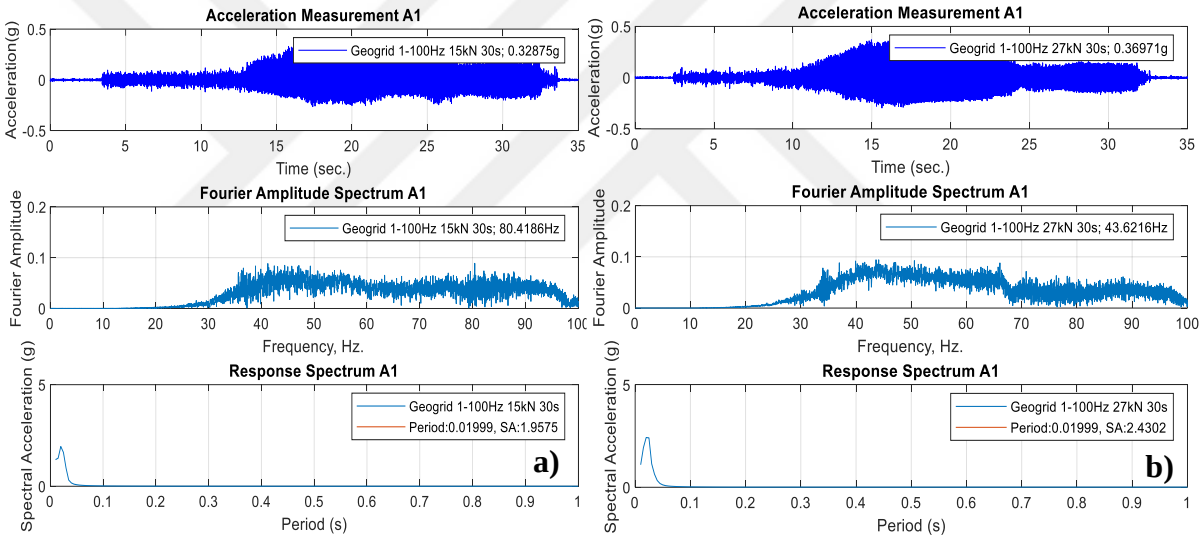

Figure 5.67. Acceleration Response of A1, a) 1-100Hz 15kN 30s, b) 1-100Hz 27kN 30s.

A3 is located on the slope of the embankment at h/2 from the ground and measures the accelerations. When the MSS applies incremental 1-100Hz sine wave at 15kN of force for 30s, the measured peak acceleration of A3 is 0.17g with Sa of 1.15g as given in Figure 5.68a. When the force level is increased to 27kN, the measured peak acceleration of A3 increases to 0.20g with 1.61g of Sa as given in Figure 5.68b.

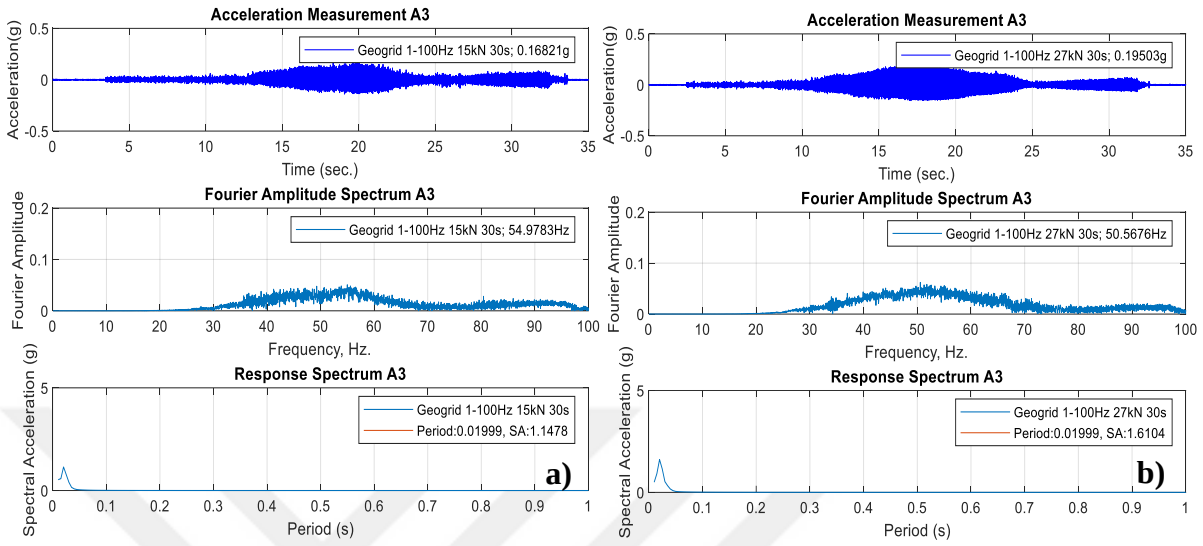

Figure 5.68. Acceleration Response of A3, a) 1-100Hz 15kN 30s, b) 1-100Hz 27kN 30s.

A7 is located at the center of the crest of the embankment. As given in Figure 5.69a, when the MSS applies incremental 1-100Hz sine wave at 15kN of force for 30s, the measured peak acceleration value of A7 is 0.05g with Sa of 0.31g and when the MSS applies incremental 1-100Hz sine wave at 27kN of force for 30s, the measured peak acceleration value of A7 increases to 0.06g with Sa of 0.47g as given in Figure 5.69b.

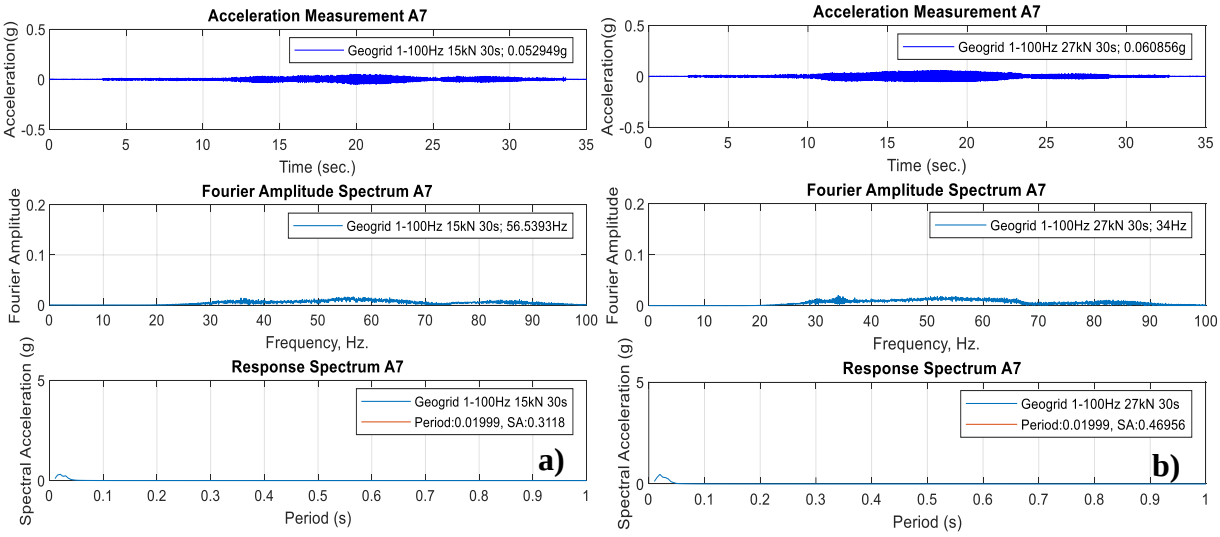

Figure 5.69. Acceleration Response of A7, a) 1-100Hz 15kN 30s, b) 1-100Hz 27kN 30s.

A11 is located on the crest of the embankment at the south-west corner. As given in Figure 5.70, when the MSS applies incremental 1-100Hz sine wave at 15kN of force for 30s, the measured peak acceleration value of A11 is 0.06g with Sa of 0.48g. Due to the increased force level of the MSS, A11 measured 0.06g with Sa of 0.44g. Similarly, acceleration responses with respect to force.

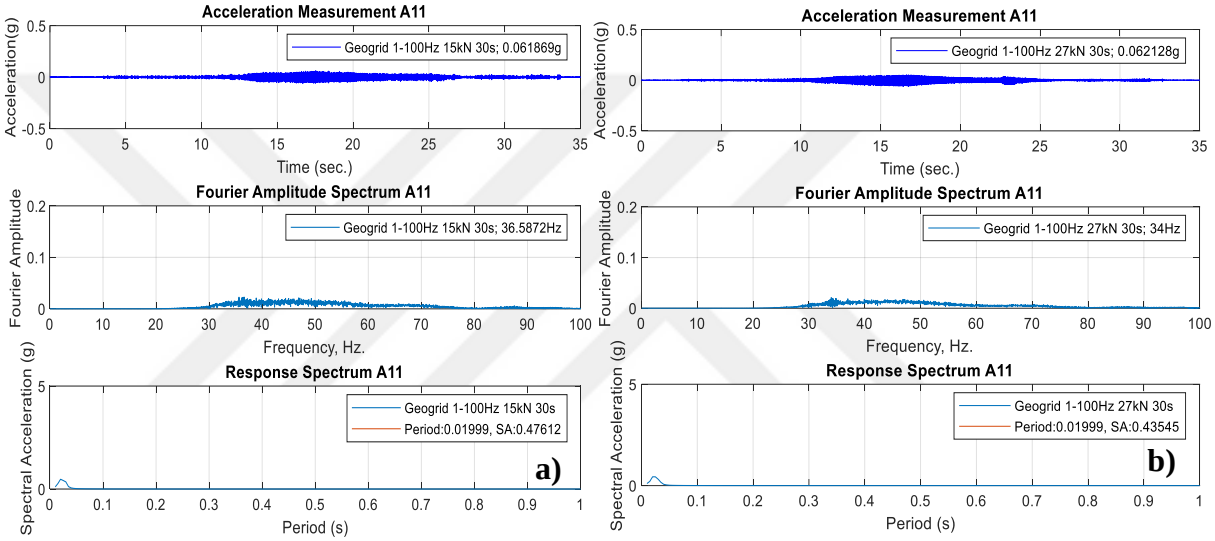

Figure 5.70. Acceleration Response of A11, a) 1-100Hz 15kN 30s, b) 1-100Hz 27kN 30s.

D3 is LVDT displacement transducers to measure the horizontal displacements located on the slope of the embankment at 3h/4. When the MSS applies incremental 1-100Hz sine wave at 15kN of force for 30s, the measured peak horizontal displacement value is measured as 0.19cm for D3 (Figure 5.71a). When the force level is increased to 27kN, the measurement of D3 is increased to 0.28cm (Figure 5.71b).

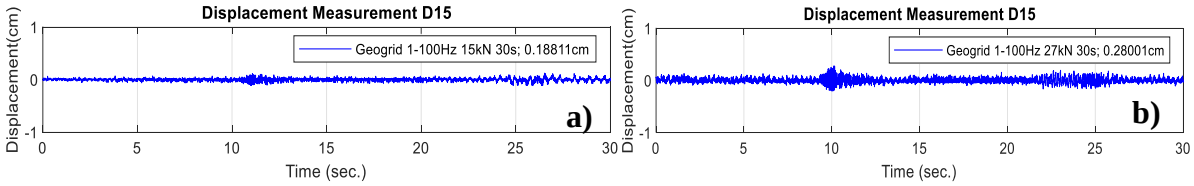

Figure 5.71. Displacement Response of D3, a) 1-100Hz 15kN 30s, b) 1-100Hz 27kN 30s.

D4 is a LVDT displacement transducer to measure the vertical displacements (settlements) located at crest. When the MSS applies incremental 1-100Hz sine wave at 15kN of force for 30s, the measured peak vertical displacement value is 0.05cm as given in Figure 5.72a. When the force level is increased to 27kN, the measurement of D4 is increased to 0.11cm (Figure 5.72b).

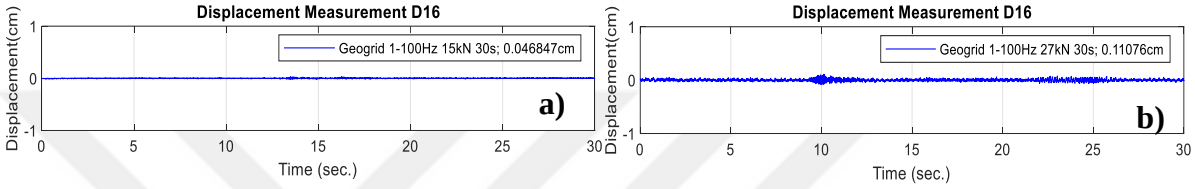

Figure 5.72. Displacement Response of D4, a) 1-100Hz 15kN 30s, b) 1-100Hz 27kN 30s.

5.2.7.2.2. Test Results for Geogrid Reinforced Embankment Model under 1-250Hz

Obtained results under the input dynamic motions of 1-250Hz 15kN 30s and 1-250Hz 27kN 30s are given in this section. When the MSS applies incremental 1-250Hz sine wave at 15kN of force for 30s, the measured peak acceleration value by A1 is 0.40g as given in Figure 5.73a. As the force increases to 27kN, A1 measures 0.44g under 1-250Hz 27kN 30s s given in Figure 5.73b.

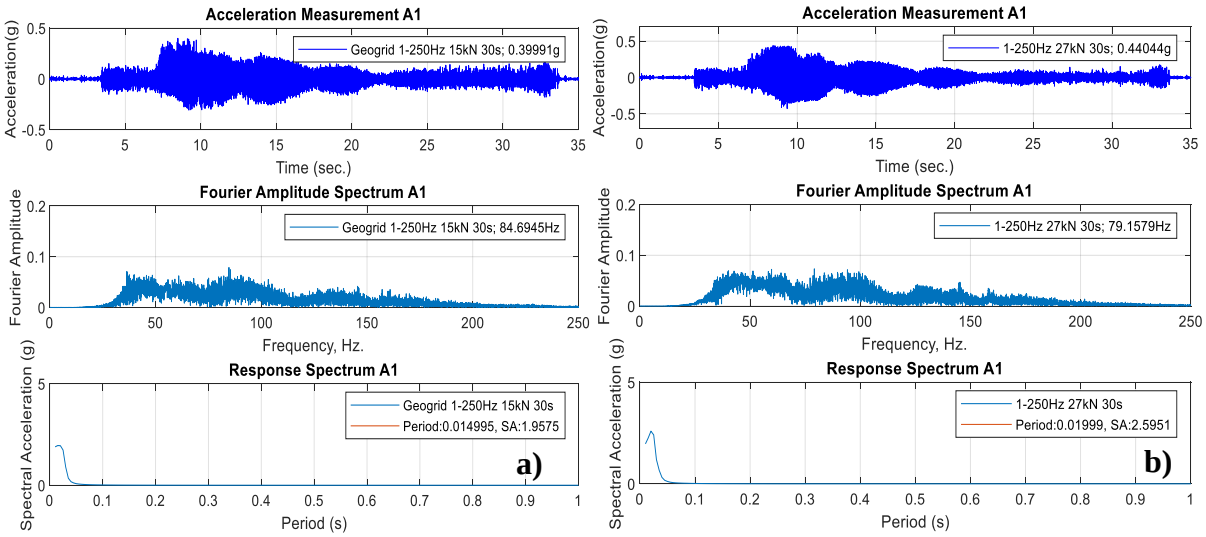

Figure 5.73. Acceleration Response of A1, a) 1-250Hz 15kN 30s, b) 1-250Hz 27kN 30s.

A3 is a uni-axial accelerometer located on the slope of the embankment at h/2 from the ground and measures the accelerations. When the MSS applies incremental 1-250Hz sine wave at 15kN of force for 30s, the measured peak acceleration of A3 is 0.18g with Sa of 1.21g as given in Figure 5.74a. Similarly, he measured peak acceleration value of A3 is 0.20g with Sa of 1.50g under the 1-250Hz sine wave at 27kN of force for 30s (Figure 5.74b).

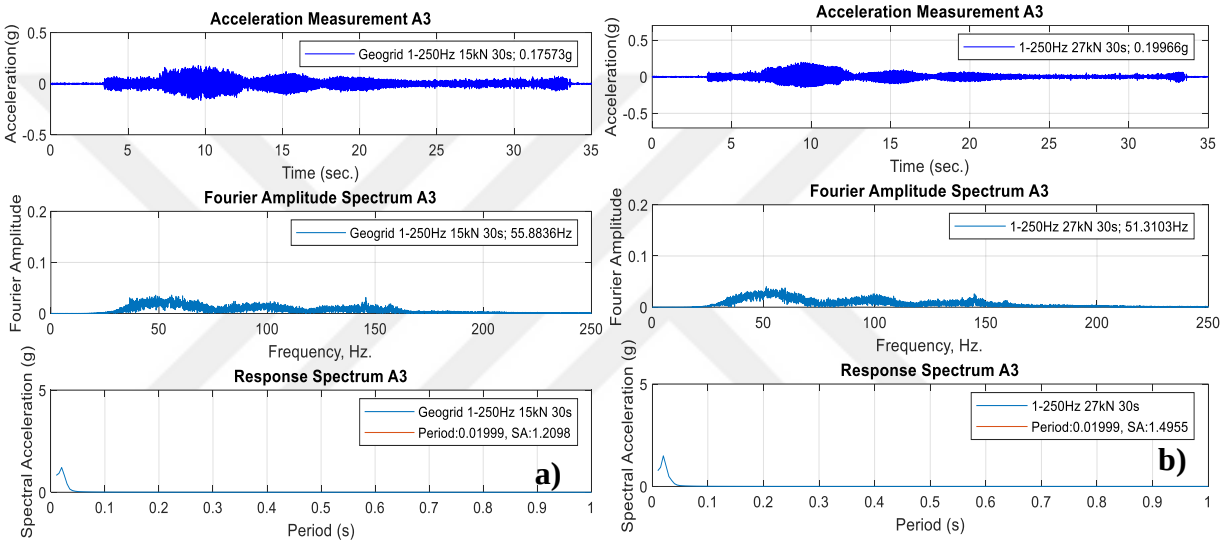

Figure 5.74. Acceleration Response of A3, a) 1-250Hz 15kN 30s, b) 1-250Hz 27kN 30s.

A7 is a uni-axial accelerometer located at the center of the crest of the embankment. As given in Figure 5.75, when the MSS applies incremental 1-250Hz sine wave at 15kN of force for 30s, the measured peak acceleration value of A7 is 0.05g with Sa of 0.32g. Similarly, he measured peak acceleration value of A7 is 0.06g with Sa of 0.40g under the 1-250Hz sine wave at 27kN of force for 30s.

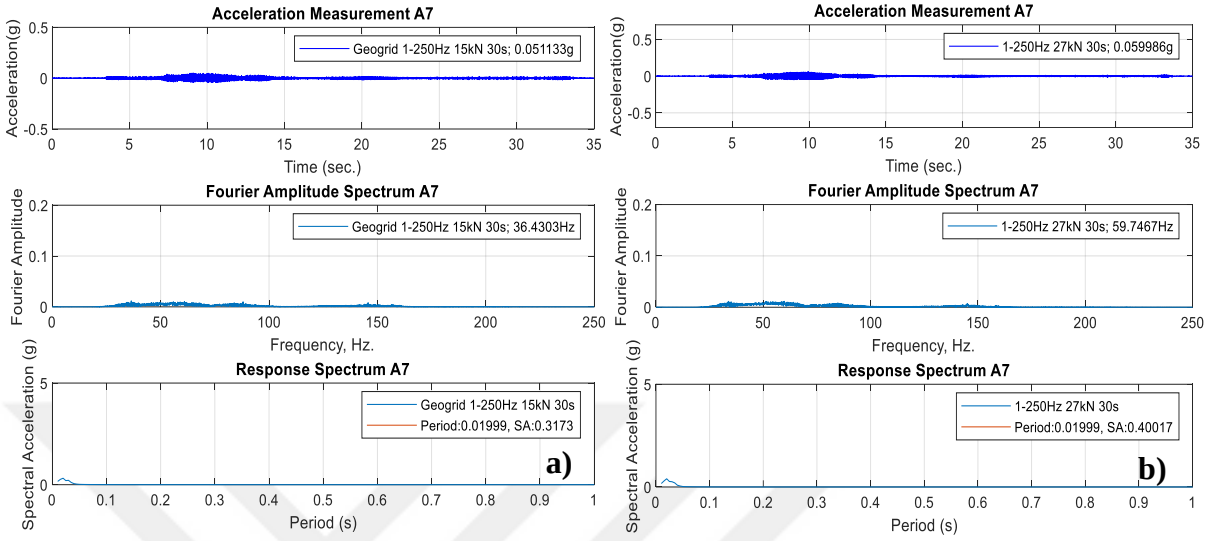

Figure 5.75. Acceleration Response of A7, a) 1-250Hz 15kN 30s, b) 1-250Hz 27kN 30s.

A11 is a uni-axial accelerometer located on the crest of the embankment at the south-west corner. As given in Figure 5.76, when the MSS applies incremental 1-250Hz sine wave at 15kN of force for 30s, the measured peak acceleration value of A11 is 0.06g with Sa of 0.38g. When the MSS force level is increased to 27kN, A11 measures 0.08g with Sa of 0.56g.

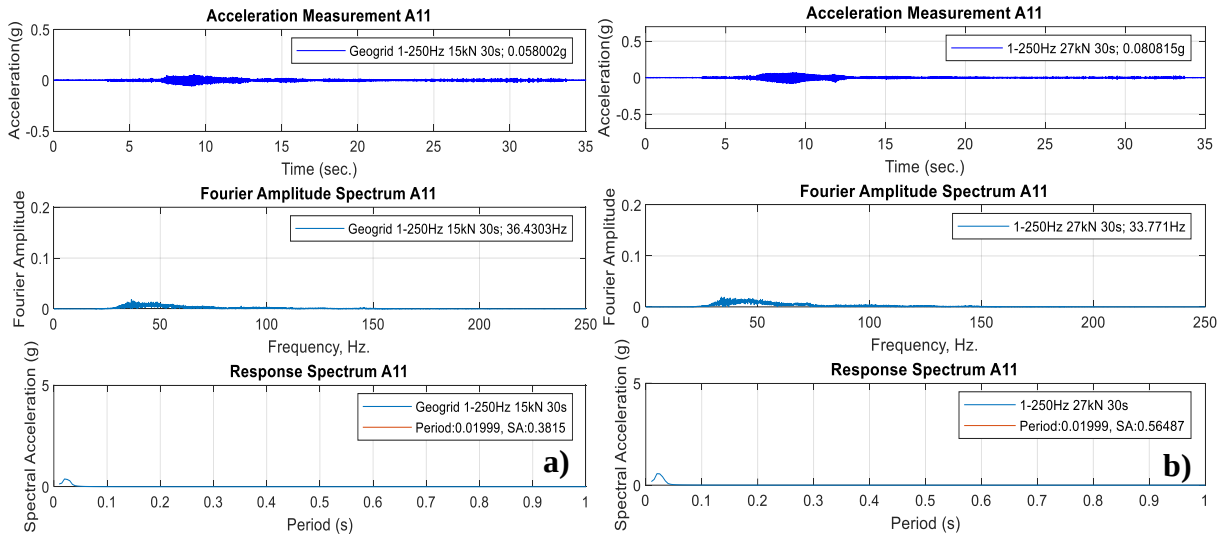

Figure 5.76. Acceleration Response of A11, a) 1-250Hz 15kN 30s, b) 1-250Hz 27kN 30s.

D3 is LVDT displacement transducers to measure the horizontal displacements located on the slope of the embankment at 3h/4. When the MSS applies incremental 1-250Hz sine wave at 15kN and 27kN of force for 30s, the measured peak horizontal displacement values are measured as 0.33cm and 0.26cm for D3, respectively as given in Figure 5.77.

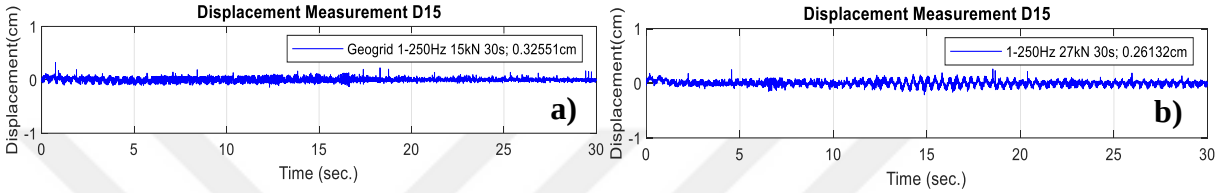

Figure 5.77. Displacement Response of D3, a) 1-250Hz 15kN 30s, b) 1-250Hz 27kN 30s.

D4 is a LVDT displacement transducer to measure the vertical displacements (settlements) located at crest. When the MSS applies incremental 1-250Hz sine wave at 15kN and 27kN of force for 30s, the measured peak vertical displacement values are 0.10cm and 0.14cm as given in Figure 5.78a and Figure 5.78b, respectively.

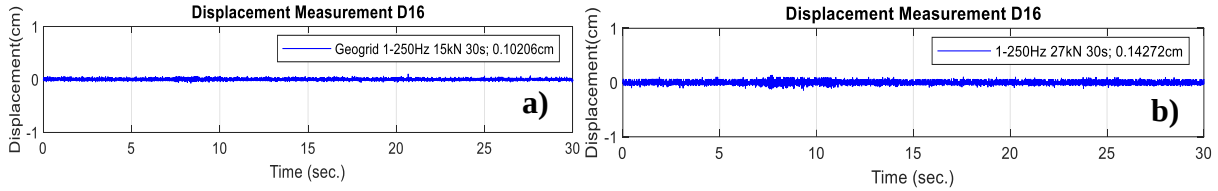

Figure 5.78. Displacement Response of D4, a) 1-250Hz 15kN 30s, b) 1-250Hz 27kN 30s.

5.2.7.2.3. Test Results for Geogrid Reinforced Embankment Model under 1-250Hz 27kN 120s

When the MSS applies incremental 1-250Hz sine wave at 27kN of force for 120s, the measured peak acceleration value by A1 is 0.49g as given in Figure 5.79.

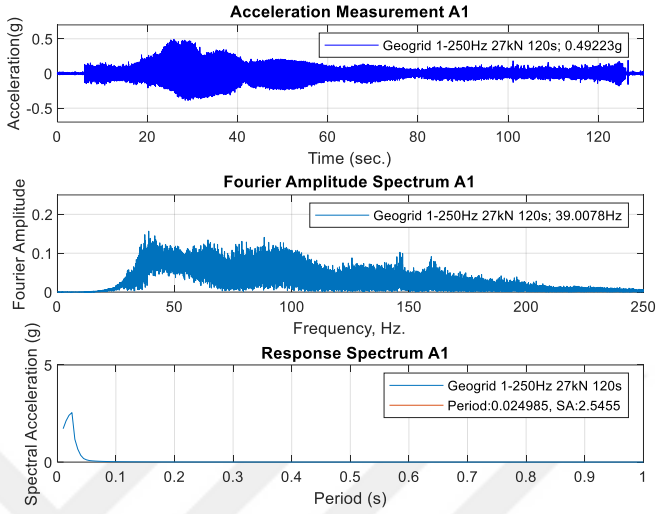

Figure 5.79. Acceleration Response of A1.

A3 is a uni-axial accelerometer located on the slope of the embankment at h/2 from the ground and measures the accelerations. When the MSS applies incremental 1-250Hz sine wave at 27kN of force for 120s, the measured peak acceleration of A3 is 0.21g with Sa of 1.47g as given in Figure 5.80.

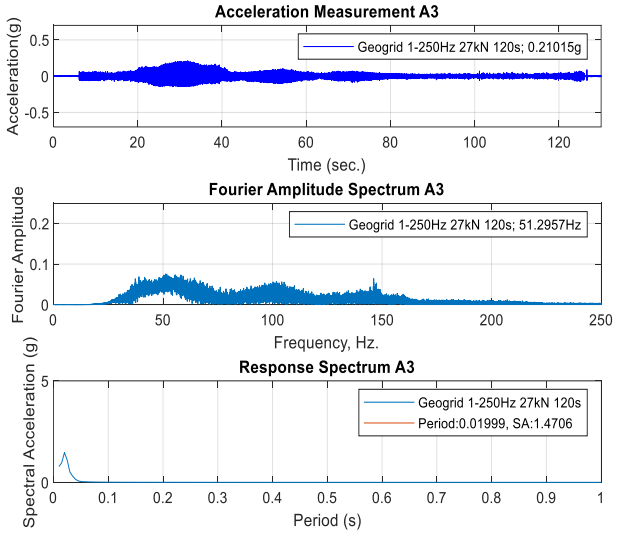

Figure 5.80. Acceleration Response of A3.

A7 is a uni-axial accelerometer located at the center of the crest of the embankment. As given in Figure 5.81, when the MSS applies incremental 1-250Hz sine wave at 27kN of force for 120s, the measured peak acceleration value of A7 is 0.07g with Sa of 0.48g.

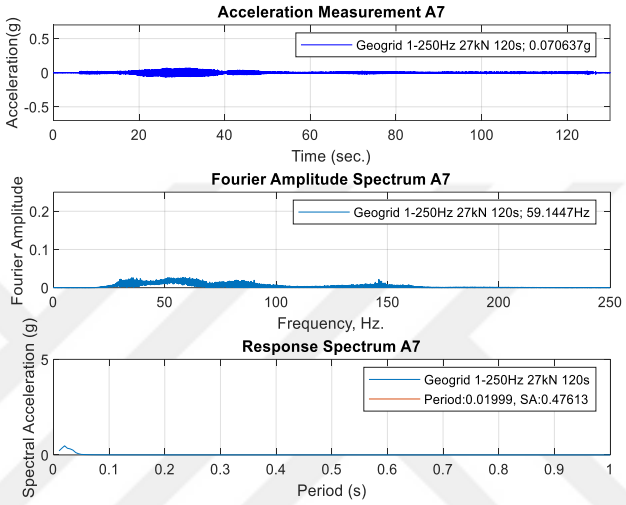

Figure 5.81. Acceleration Response of A7.

A11 is a uni-axial accelerometer located on the crest of the embankment at the south-west corner. As given in Figure 5.82, when the MSS applies incremental 1-250Hz sine wave at 27kN of force for 120s, the measured peak acceleration value of A11 is 0.09g with Sa of 0.62g.

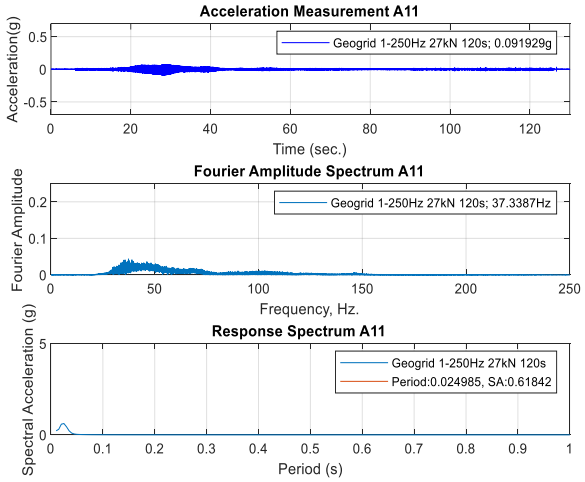

Figure 5.82. Acceleration Response of A11.

D3 is LVDT displacement transducers to measure the horizontal displacements located on the slope of the embankment at 3h/4. When the MSS applies incremental 1-250Hz sine wave at 27kN of force for 120s, the measured peak horizontal displacement value at D3 is measured as 0.31cm (Figure 5.83).

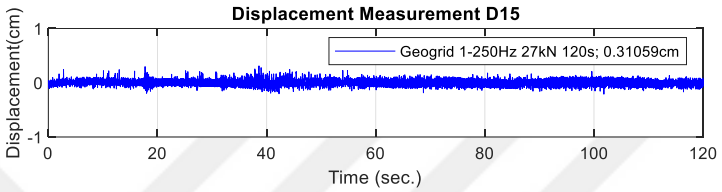

Figure 5.83. Displacement Response of D3.

D4 is a LVDT displacement transducer to measure the vertical displacements (settlements) located at crest. When the MSS applies incremental 1-250Hz sine wave at 27kN of force for 120s, the measured peak vertical displacement value is 0.16cm as given in Figure 5.84. Due to the geogrid reinforcement, measured horizontal and vertical displacement values are successfully reduced.

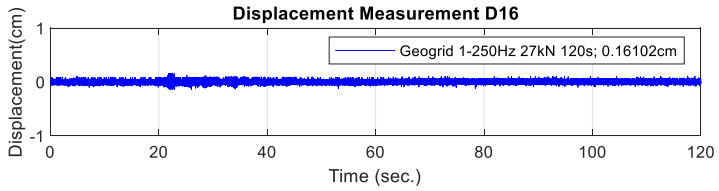

Figure 5.84. Displacement Response of D4.

5.2.7.3. Test Results for EPS Geofoam Embankment Model

Test results of the EPS Geofoam Embankment model for the perpendicular to the road direction are represented in this section. Test results are represented as Acceleration Responses and Displacement Responses for the selected accelerometers of A1, A3, A7, A11 and selected two LVDT's (D3 and D4).

5.2.7.3.1. Test Results for EPS Geofoam Embankment Model under 1-100Hz

Obtained results under the input dynamic motions of 1-100Hz 15kN 30s and 1-100Hz 27kN 30s are given in this section. A1 is a uni-axial accelerometer located 1m away from the actuator of the Mobile Seismic Shaker on the ground and measures the accelerations. When the MSS applies incremental 1-100Hz sine wave at 15kN and 27kN of force for 30s, the measured peak acceleration value is 0.32g and 0.36g as given in Figure 5.85a and Figure 5.85b, respectively.

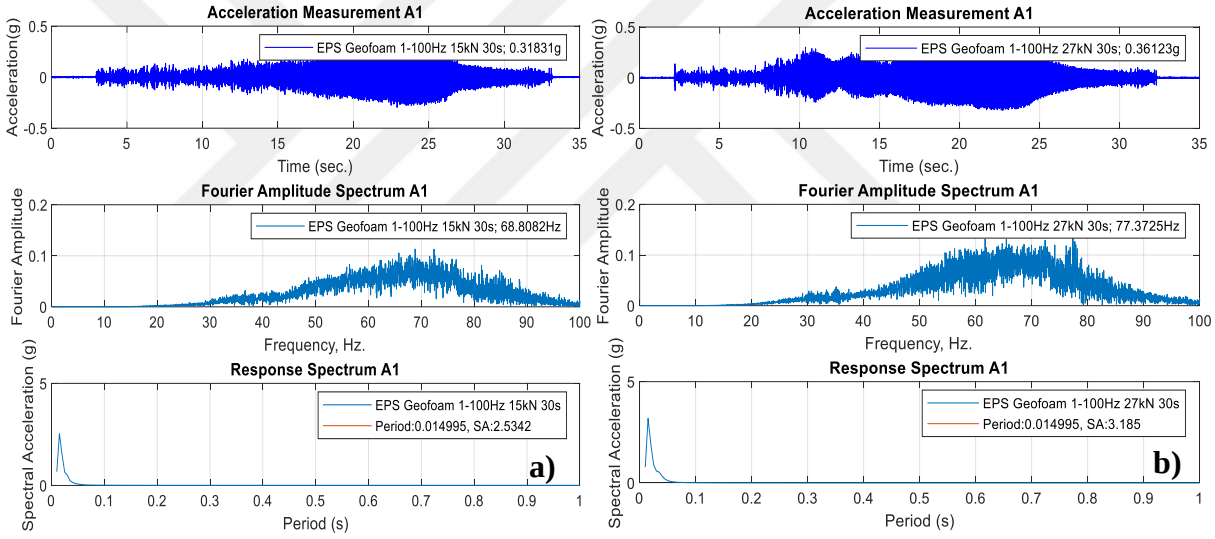

Figure 5.85. Acceleration Response of A1, a) 1-100Hz 15kN 30s, b) 1-100Hz 27kN 30s.

A3 is located on the slope of the embankment at h/2 from the ground and measures the accelerations. When the MSS applies incremental 1-100Hz sine wave at 15kN of force for 30s, the measured peak acceleration of A3 is 0.12g with Sa of 0.83g as given in Figure 5.86a. Under 1-100Hz sine wave at 27kN of force for 30s, A3 measures 0.14g with Sa of 0.91g (Figure 5.86b).

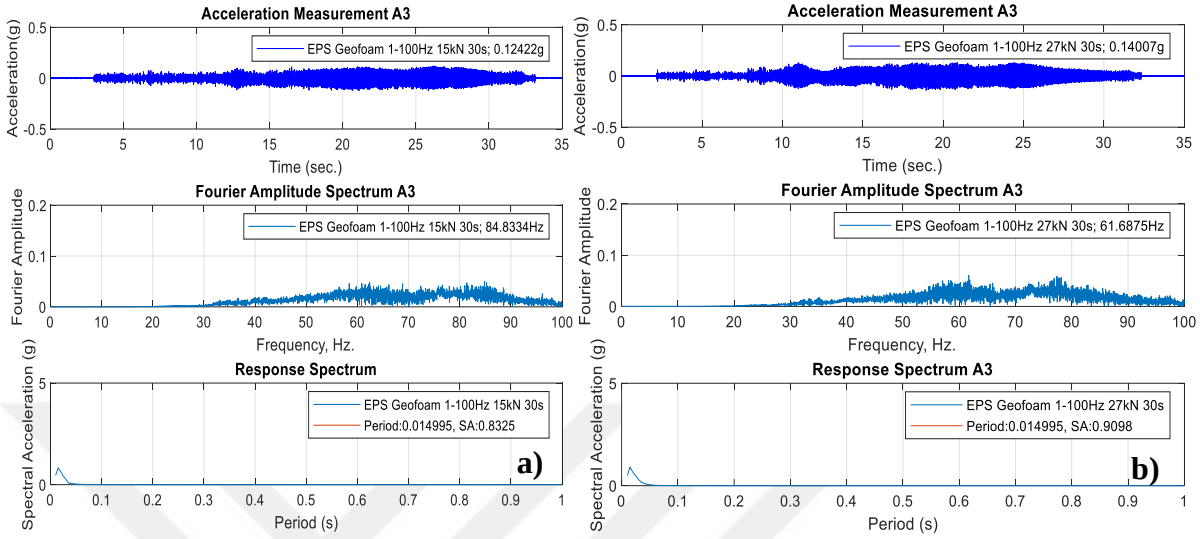

Figure 5.86. Acceleration Response of A3, a) 1-100Hz 15kN 30s, b) 1-100Hz 27kN 30s.

A7 is located at the center of the crest of the embankment. As given in Figure 5.87a, when the MSS applies incremental 1-100Hz sine wave at 15kN of force for 30s, the measured peak acceleration value of A7 is 0.05g with Sa of 0.38g. When the force level is increased, A7 measures 0.05g with Sa of 0.44g (Figure 5.87b).

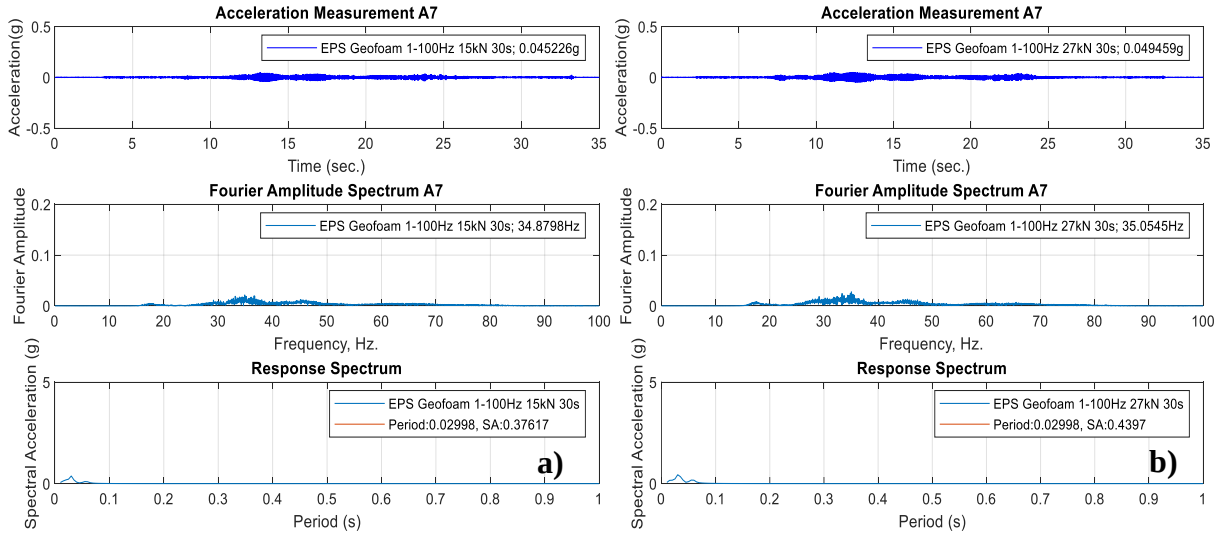

Figure 5.87. Acceleration Response of A7, a) 1-100Hz 15kN 30s, b) 1-100Hz 27kN 30s.

As given in Figure 5.88a, when the MSS applies incremental 1-100Hz sine wave at 15kN of force for 30s, the measured peak acceleration value of A11 is 0.03g with Sa of 0.19g. Due to the increased force level, A11 measures 0.05g with 0.33g of Sa (Figure 5.88b).

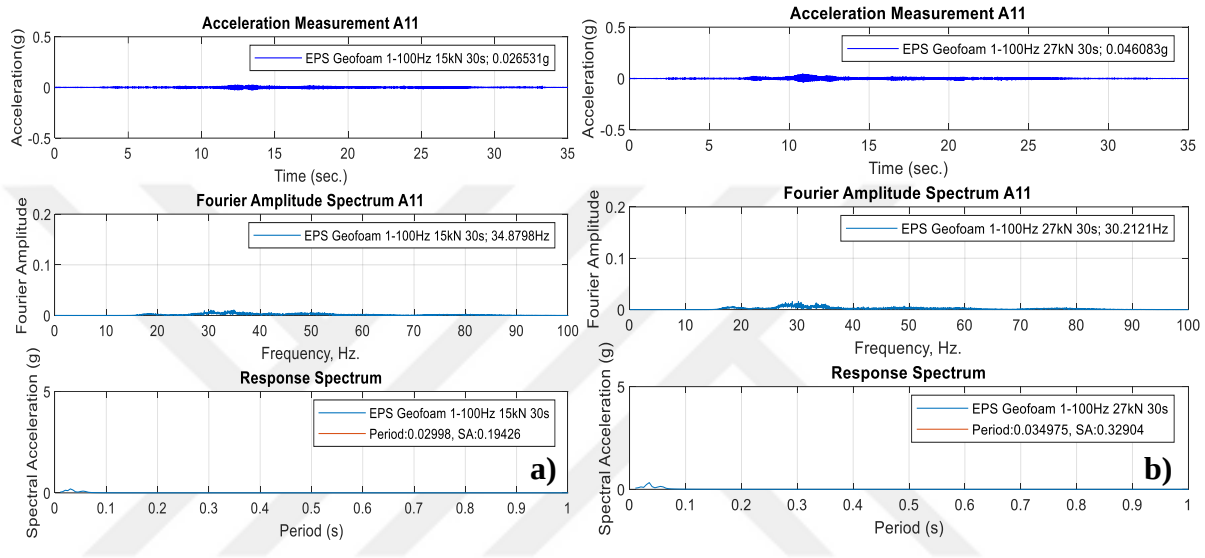

Figure 5.88. Acceleration Response of A11, a) 1-100Hz 15kN 30s, b) 1-100Hz 27kN 30s.

D3 is LVDT displacement transducers to measure the horizontal displacements located on the slope of the EPS Geofoam embankment at 3h/4. As given in Figure 5.89, when the MSS applies incremental 1-100Hz sine wave at 15kN and 27kN of force for 30s, the measured peak horizontal displacement (D3) values are measured as 0.06cm and 0.08cm for D3, respectively.

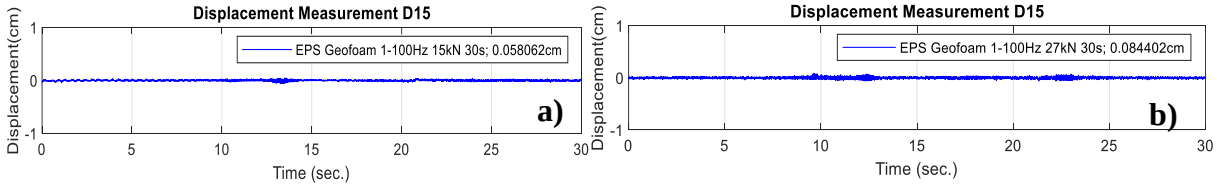

Figure 5.89. Displacement Response of D3, a) 1-100Hz 15kN 30s, b) 1-100Hz 27kN 30s.

D4 is a LVDT displacement transducer to measure the vertical displacements (settlements) located at crest. When the MSS applies incremental 1-100Hz sine wave at 15kN

and 27kN of force for 30s, the measured peak vertical displacement (D4) values are 0.01cm as given in Figure 5.90a and Figure 5.90b, respectively.

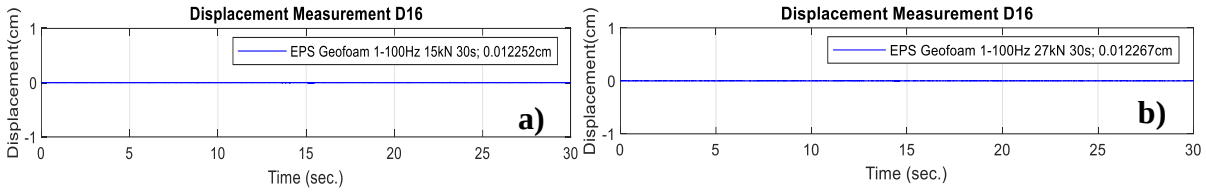

Figure 5.90. Displacement Response of D4, a) 1-100Hz 15kN 30s, b) 1-100Hz 27kN 30s.

5.2.7.3.2. Test Results for EPS Geofoam Embankment Model under 1-250Hz

Obtained results under the input dynamic motions of 1-250Hz 15kN 30s and 1-250Hz 27kN 30s are given in this section. When the MSS applies incremental 1-250Hz sine wave at 15kN of force for 30s, the measured peak acceleration value by A1 is 0.41g as given in Figure 5.91a, and under the 1-250Hz 27kN 30s, A1 measures 0.43g as given in Figure 5.91b.

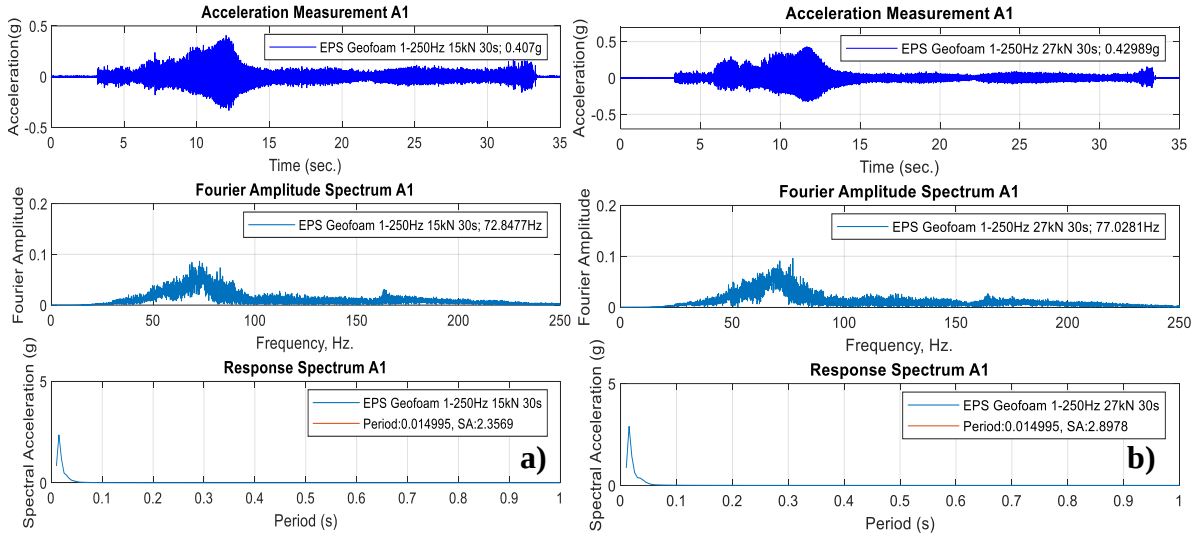

Figure 5.91. Acceleration Response of A1, a) 1-250Hz 15kN 30s, b) 1-250Hz 27kN 30s.

A3 is located on the slope of the embankment at h/2 from the ground and measures the accelerations. When the MSS applies incremental 1-250Hz sine wave at 15kN and 27kN of

force for 30s, the measured peak acceleration of A3 is 0.15g with Sa of 0.49g and 0.16g with Sa of 0.58g, respectively. Increased force levels lead to a slight increase in acceleration response at the slope of the embankment (Figure 5.92).

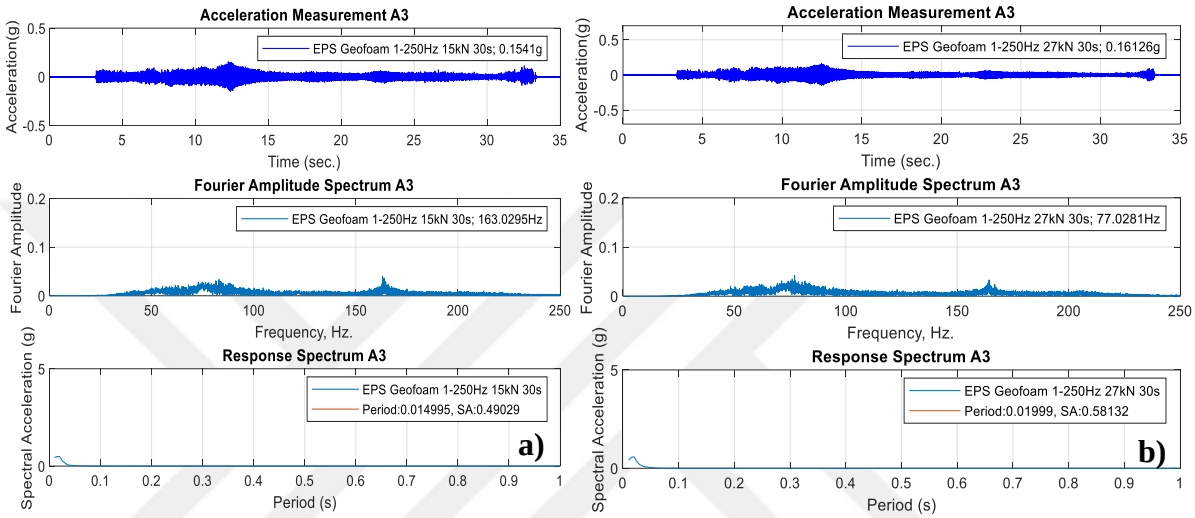

Figure 5.92. Acceleration Response of A3, a) 1-250Hz 15kN 30s, b) 1-250Hz 27kN 30s.

A7 is located at the center of the crest of the embankment. As given in Figure 5.93, when the MSS applies incremental 1-250Hz sine wave at 15kN and 27kN of force for 30s, the measured peak acceleration values of A7 are 0.05g with Sa of 0.39g.

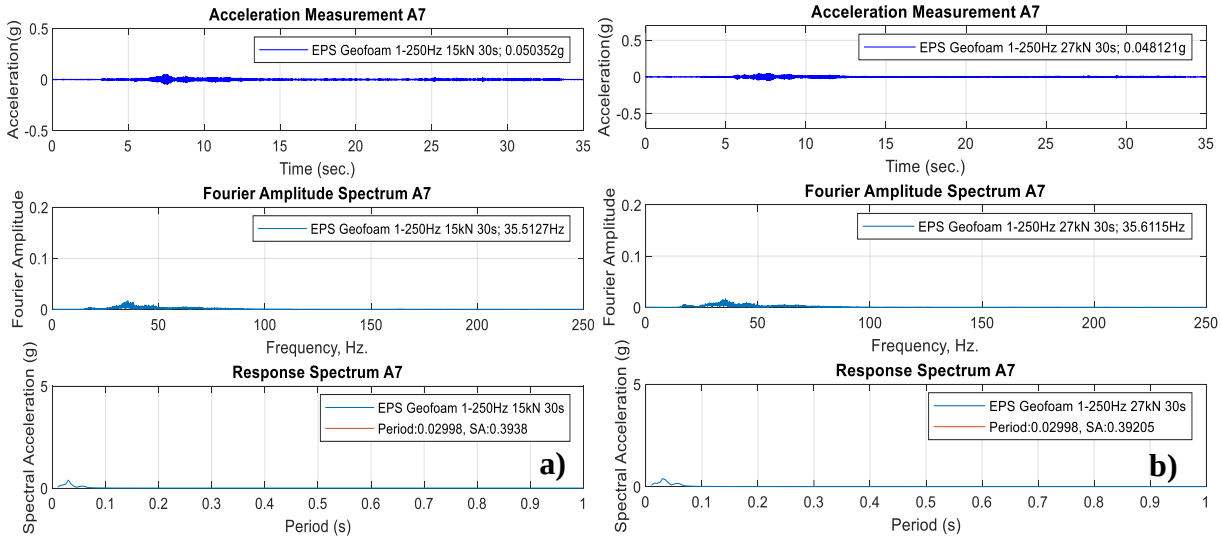

Figure 5.93. Acceleration Response of A7, a) 1-250Hz 15kN 30s, b) 1-250Hz 27kN 30s.

A11 is located on the crest of the embankment at the south-west corner. As given in Figure 5.94a, when the MSS applies incremental 1-250Hz sine wave at 15kN of force for 30s, the measured peak acceleration value of A11 is 0.04g with Sa of 0.25g, and the measured peak acceleration value of A11 is 0.05g with Sa of 0.31g when the force is increased to 27kN (Figure 5.94b). Increased force leads to increased displacement responses in EGE too.

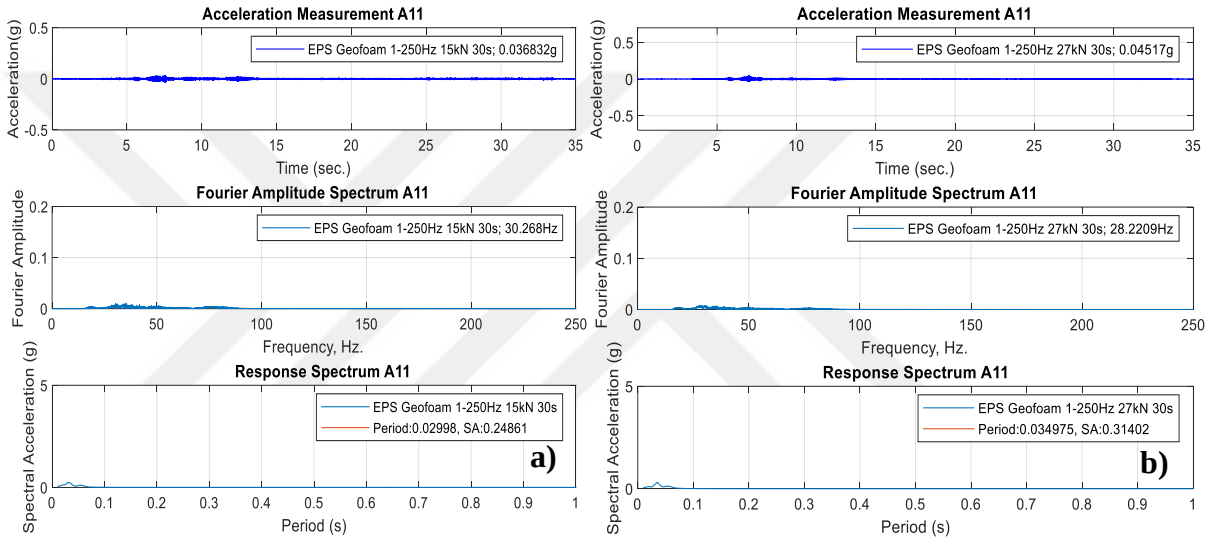

Figure 5.94. Acceleration Response of A11, a) 1-250Hz 15kN 30s, b) 1-250Hz 27kN 30s.

D3 is LVDT displacement transducers to measure the horizontal displacements located on the slope of the EPS Geofoam embankment at 3h/4. As given in Figure 5.95, under the incremental 1-250Hz sine wave at 15kN and 27kN of force for 30s, the measured peak horizontal displacement (D3) values are measured as 0.07cm and 0.08cm, respectively.

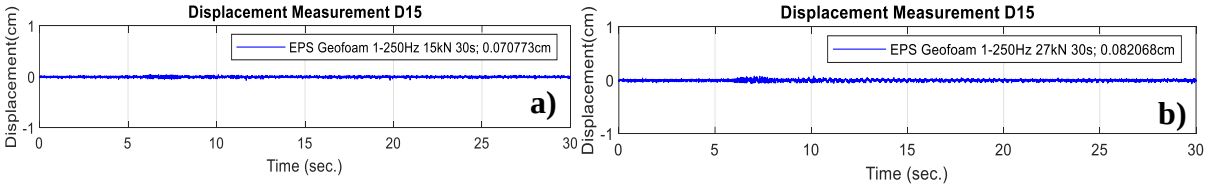

Figure 5.95. Displacement Response of D3, a) 1-250Hz 15kN 30s, b) 1-250Hz 27kN 30s.

D4 is a LVDT displacement transducer to measure the vertical displacements (settlements) located at crest. When the MSS applies incremental 1-250Hz sine wave at 15kN of force for 30s, the measured peak vertical displacement value is 0.03cm as given in Figure 5.96a. Similarly, under the incremental 1-250Hz sine wave at 27kN of force for 30s, 0.02cm of settlement is measured (Figure 5.96b).

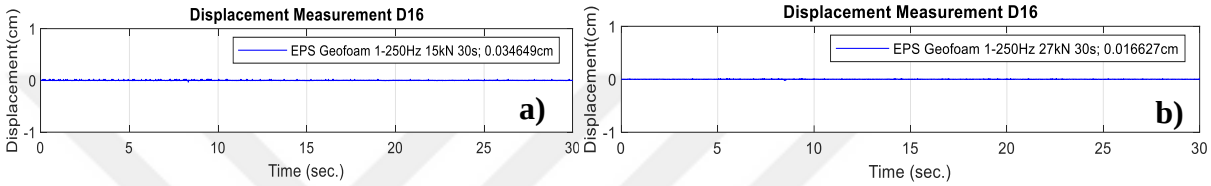

Figure 5.96. Displacement Response of D4, a) 1-250Hz 15kN 30s, b) 1-250Hz 27kN 30s.

5.2.7.2.3. Test Results for EPS Geofoam Embankment Model under 1-250Hz 27kN 120s

When the MSS applies incremental 1-250Hz sine wave at 27kN of force for 120s, the measured peak acceleration value by A1 is 0.49g as given in Figure 5.97.

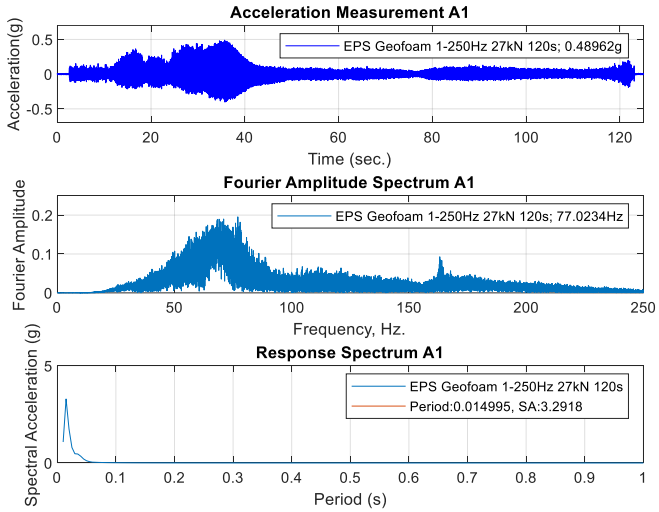

Figure 5.97. Acceleration Response of A1.

A3 is located on the slope of the embankment at h/2 from the ground and measures the accelerations. When the MSS applies incremental 1-250Hz sine wave at 27kN of force for 120s, the measured peak acceleration of A3 is 0.16g with Sa of 0.59g (Figure 5.98).

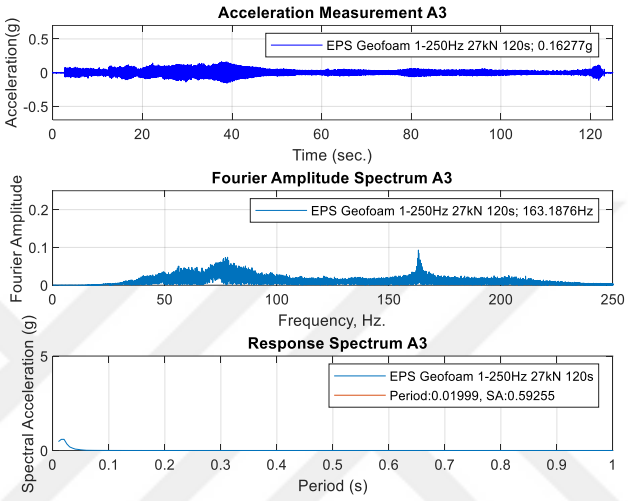

Figure 5.98. Acceleration Response of A3.

A7 is located at the center of the crest of the embankment. As given in Figure 5.99, when the MSS applies incremental 1-250Hz sine wave at 27kN of force for 120s, the measured peak acceleration value of A7 is 0.05g with Sa of 0.42g.

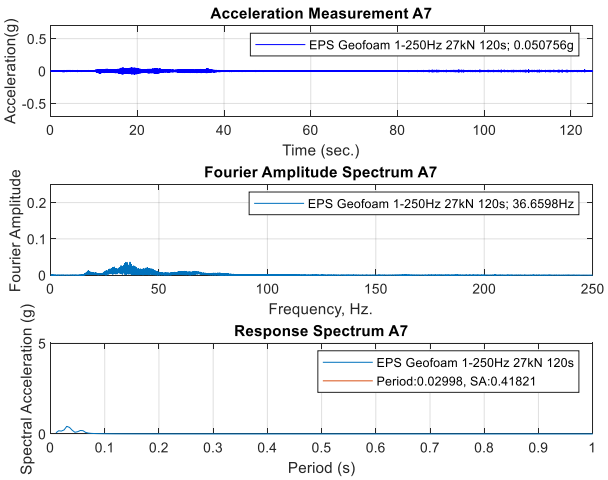

Figure 5.99. Acceleration Response of A7.

A11 is located on the crest of the embankment at the south-west corner. As given in Figure 5.100, when the MSS applies incremental 1-250Hz sine wave at 27kN of force for 120s, the measured peak acceleration value of A11 is 0.05g with Sa of 0.35g. Accelerations responses are less when compared to URE and GRE due to the damping properties of the EPS geofoam.

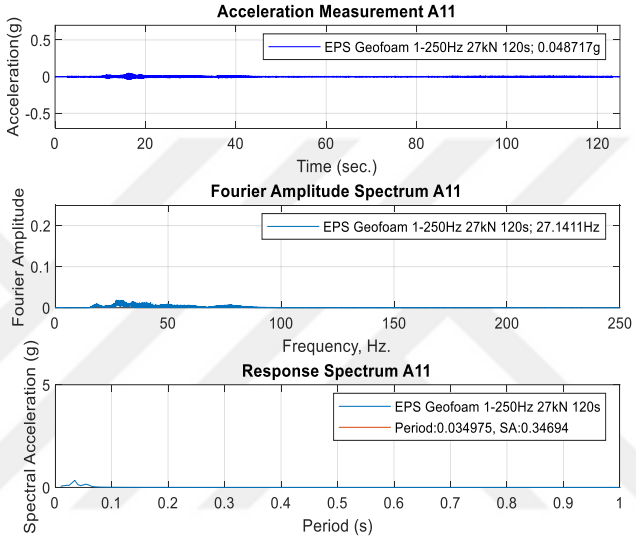

Figure 5.100. Acceleration Response of A11.

D3 is LVDT displacement transducers to measure the horizontal displacements located on the slope of the embankment at 3h/4. Given in Figure 5.101, when the MSS applies incremental 1-250Hz sine wave at 27kN of force for 120s, the measured peak horizontal displacement value is measured as 0.10cm (D3).

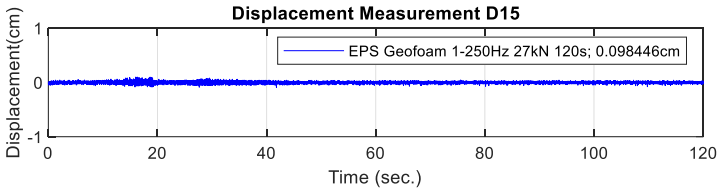

Figure 5.101. Displacement Response of D3.

D4 is a LVDT displacement transducer to measure the vertical displacements (settlements) located at crest. When the MSS applies incremental 1-250Hz sine wave at 27kN

of force for 120s, the measured peak vertical displacement value is 0.04cm as given in Figure 5.102.

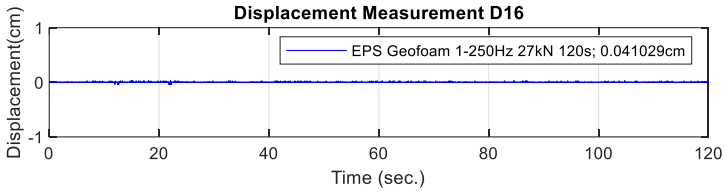

Figure 5.102. Displacement Response of D4.

5.3. Shaking Table Experiments

Shaking table experiments were performed at the shaking table laboratory at Boğaziçi University Kandilli Observatory and Earthquake Research Institute. Experiments were performed as a simulation of the field scale experiments to observe the effect of geogrid reinforcement and EPS geofoam fill on 1/10 scaled unreinforced highway embankment model, geogrid reinforced highway embankment model and EPS geofoam highway embankment model inside a plexiglass box. The shaking table used for the proposed experiments is the ANCO R-148. This shaking table is a uni-axial horizontal vibration table that is driven by a servo-hydraulic actuator which has a maximum payload capacity of 10 tons and features a 3 m x 3 m table. It is capable of producing vibrations with a maximum acceleration of 2g. The hydraulic actuator used in this shaking table is able to generate a stroke of +/- 12 cm, resulting in a total stroke of 24 cm. The actuator in the shaking table is equipped with a 3-stage servo-valve. The valve is controlled by an analog inner-loop control system that is displacement-based. Additionally, there is a digital outer-loop control system that utilizes acceleration feedback for control. For table motion and data acquisition, a Data Physics 550 WIN digital data control system is employed. This system is responsible for controlling the shaking table's motion and collecting data during the experiments.

5.3.1. Materials

A few stages and disciplines were followed for the preparation of the test setup which are to decide the proper embankment prototype. It was assessed that a 1/10 scale of the field-scale highway embankment models is optimal for the laboratory tests.

5.3.1.1. Sand

'Silivri Sand' has been used during the shaking table experiments which is common around Istanbul region. Figure 5.103 displays the grain-size distribution of Silivri Sand in accordance with the ASTM Standard of D422.According to the USCS system, the specimen is classified as poorly graded sand (SP) with C_u: 2.29 and C_c : 1.1.

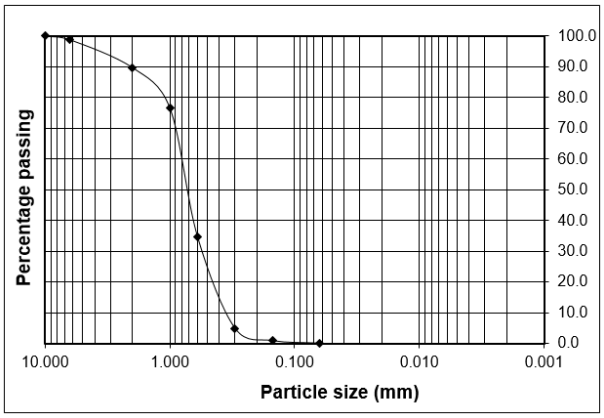

Figure 5.103. Particle size distribution of Silivri Sand.

5.3.1.2. Geogrids

The material utilized for reinforcement in this study is a bi-axial type geogrid. As per the scaling laws of Iai (1989), the geogrid material used in the experiments should typically be scaled down to 1/10th of its original size.

However, bi-axial geogrid material with T_{ult}: 40kN/m is to be used in field scale experiments and the minimum available geogrid reinforcement available in the market has a tensile strength of T_{ult}: 20kN/m. Due to the limitation of finding a geogrid reinforcement material with less tensile strength, and to differentiate between two geogrids by means of seismic performance, two geogrid reinforcements with T_{ult}: 20kN/m and T_{ult}: 40kN/m were both used as different cases.

5.3.1.3. Plexiglass Soil Box

To conduct reduced scale shaking table experiments, a soil box with dimensions of 90x40x50cm was used. The box's sides are constructed from plexiglass material that is 15mm thick. Figure 5.104 displays the soil box utilized in the shaking table experiments.

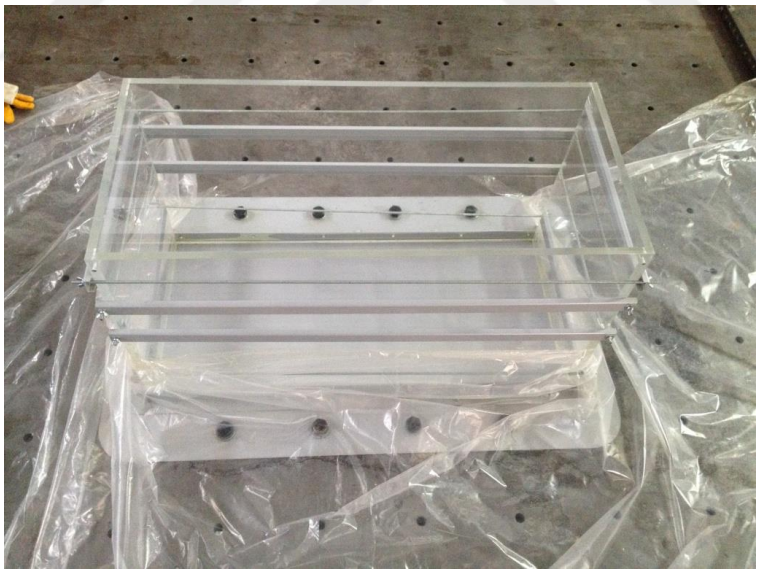

Figure 5.104. The plexiglass soil box (Toksoy, 2014).

5.3.2. Methods

This part of the thesis covers the pleksiglass soil box performance check, preperation of the reduced scale embankment models and their instrumentation prior to shaking table tests.

5.3.2.1. Performance Check of the Soil Box

To perform shaking table experiments, it is necessary to utilize a soil box that creates simulated soil layer boundary conditions. According to Taylor and Crewe (1996) , this is a crucial component of the process. Toksoy (2014) conducted performance check tests on the pleksiglas soil box when it was produced and brought to the shaking table facility. Sides of the soil box was covered with gres oil to minimize the friction in the first place The box was filled to half of its height with sand and instrumented using five accelerometers placed at the same level. The sand was compacted until the relative density of about 70% was achieved. The soil box should exhibit the same dynamic behavior measured from the accelerometers inserted into the sand located at the center and each corner of the box. Proposed performance tests for the soil box were conducted using the records of 1940 El Centro Earthquake (0.36g), 1995 Kobe Earthquake (0.68g) and 1999 Kocaeli Earthquake (0.23g) and a incremental 1-50Hz sinusoidal motion up to 0.5g. All records were obtained from BU-KOERI database. Acceleration responses from each sensor were recorded and analysed. It was found that acceleration responses from all accelerometers were almost identical under given dynamic loads which revealed that the pleksiglass soil box provides desired boundary conditions for the proposed shaking table experiments.

5.3.2.2. Preperation of the Reduced Scale Highway Embankment Models

Shaking table tests were conducted as a reduced scale field tests. Various dynamic motions were used to conduct shaking table tests on embankment models. These models were scaled in terms of dimensions. The materials used in shaking table experiments are not scaled. Namely, Unreinforced, geogrid reinforced and EPS geofoam highway embankments are studied during shaking table experiments.

Reduced scale embankment models were prepared with respect to 1:10 scale of the prototype in the field experiments. All models are prepared on the same foundation soil layer which has a density of 16.5kN/m^3 and the relative density of Dr: 60%. All embankment models

are dimensionally identical with H:20cm, L:25cm with slope inclination of 45°. Unreinforced embankment model is shown in Figure 5.105.



Figure 5.105. Physical appearance of unreinforced embankment model.

Due to the obtained results from the preliminary numerical studies, two layers of geogrid reinforcement was found to be sufficient to meet the required FOS. One layer is positioned below the embankment, while the second layer is placed at the mid-height of the embankment model. (Figure 5.106). Two different bi-axial geogrid reinforcement materials with T_{ult}: 20kN/m and T_{ult}: 40kN/m were used in different cases. Geogrid reinforced embankment model is shown in Figure 5.107.



Figure 5.106. Placement of a geogrid layer.



Figure 5.107. Physical appearance of geogrid reinforced embankment model.

EPS geofoam material to be used for the field scale experiments has a density of 20kg/m^3 based on the NCHRP (2004) requirements. This study utilized the similitude approach for 1 g tests, as described in previous studies by Iai (1989; 1997), and Iai and Sugano (1999), to create models of embankments. The similitude law ensures that the material density remains constant. Therefore, the same EPS geofoam material with a density of 20kg/m^3 was used in reduced scale shaking table tests. Table 5.20 provides further information on the scaling factors employed in this study.

Table 5.20. Adopted Scaling Laws (Iai and Sugano, 1999).

Variables	Generalized scaling factors (prototype/model)	"Scale factors in practice" (prototype/model) ($\lambda_\rho = 1$ and $\lambda_\varepsilon = 1$)
x (length)	λ	λ
ρ_s (density of soil)	λ_ρ	1
ε (strain of soil)	λ_ε	1
t (time)	$(\lambda\lambda_\varepsilon)^{0.5}$	$(\lambda)^{0.5}$
σ (stress in soil)	$\lambda\lambda_\rho$	λ
u (displacement)	$\lambda\lambda_\varepsilon$	λ
$\ddot{u}$ (acceleration)	1	1
Frequency	$\lambda^{-0.5}$	$\lambda^{-0.5}$

Based on the NCHRP (2004) requirements, at least two layers of EPS geofoam materials shall be used in highway embankments and the top most layer should be covered with at least 30cm of fill. Dimensions of the geofoam blocks and the thickness of the top most layer was adapted to the proposed 1:10 scaling law. EPS geofoam embankment model prior to shaking table tests are shown in Figure 5.108.

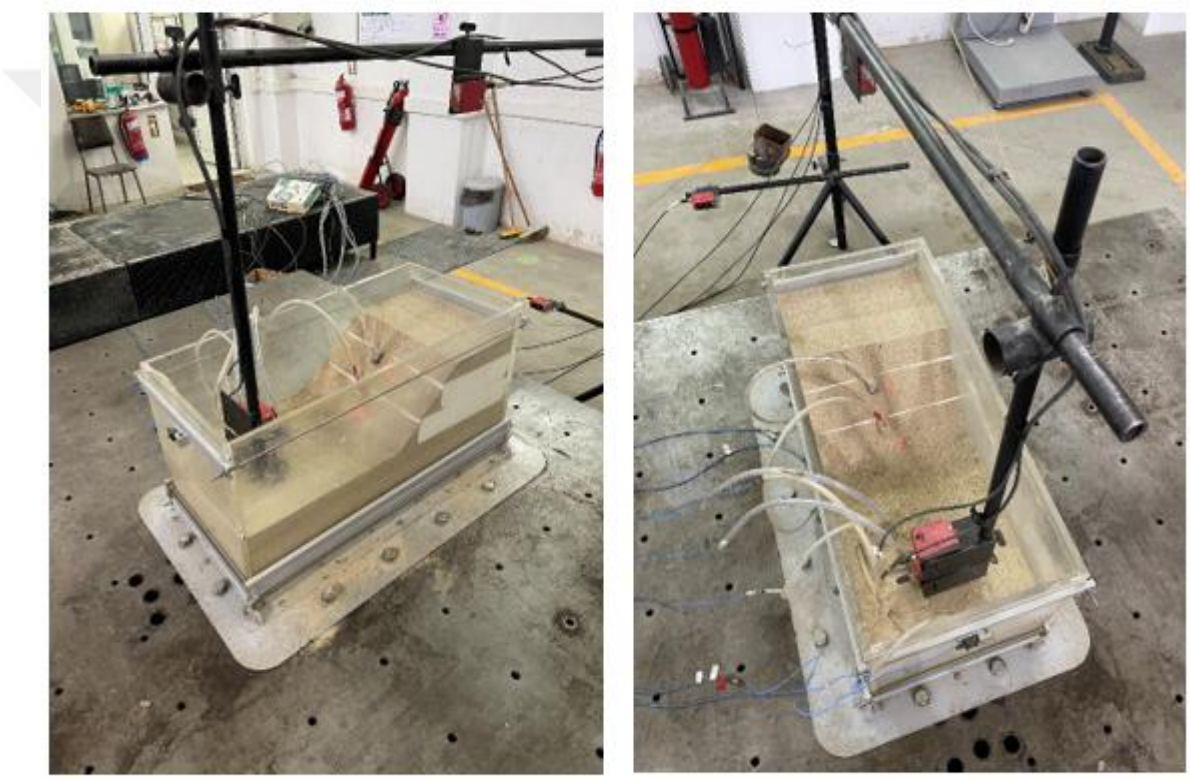

Figure 5.108. EPS Geofoam embankment model.

5.3.2.3. Instrumentation

The instrumentation plan for the shaking table experiments consists of nine accelerometers and four displacement sensors (LVDT). Accelerometers and LVDTs are symbolized with letters of “A” and “D” respectively. Accelerometer A1 is located on the shaking table and measures the input dynamic motion. A2 is fixed on the pleksiglas soil box, A3, A4, A5 and A6 are buried inside the sand foundation and are placed linearly at mid-height.

A7 is placed five centimeters below the geogrid layer at the bottom of the embankment. A8 is located between two geogrid reinforcement layers inside the embankment and five centimeters above the toe; and A9 is placed five centimeters below the crest of the embankment. D11 is the LVDT to measure the toe level displacements on the slope of the embankment models while D12 measures the crest level displacements on the slope of the models. D13 is located to measure the vertical displacement (settlement) at the crest of the embankment models. Instrumentation remains the same for all models and the representative instrumentation plan is given in Figure 5.109.

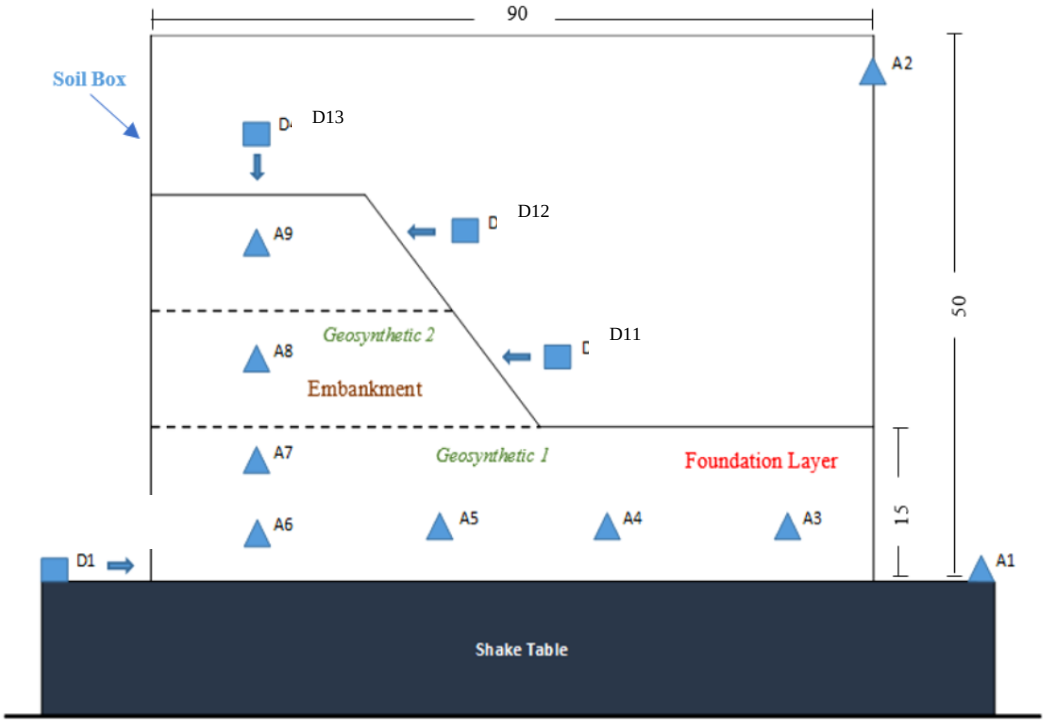

Figure 5.109. Instrumentation plan for shaking table experiments.

5.3.3. Shaking Table Experiments

Reduced scale dynamic performance tests of unreinforced highway embankment, geogrid reinforced highway embankment and EPS geofoam highway embankment models were performed. Input motions are selected to observe the effect of different characteristics of dynamic motions such as the frequency content, amplitude and duration on the dynamic performance of highway embankments. Due to the scaling laws, the duration of the dynamic motions were reduced by a factor of $\sqrt{10}$ for the shaking table experiments.

Table 5.21, gives the detailed information about the input motions to be used throughout the laboratory experiments. Acceleration-Time histories of input dynamic motions used during the shaking table experiments are represented in Figure 5.110.

Table 5.21. Input motions for the shaking table experiments.

	Frequency (Hz)	**Duration (s)**	**Input Acceleration (g)**
1)	1-30	9.5	0.30
2)	1-30	38	0.29
3)	1-50	9.5	0.54
4)	1-50	38	0.50
5)	10	9.5	0.35
6)	10	38	0.35
7)	20	9.5	0.46
8)	20	38	0.42
9)	30	9.5	0.36
10)	30	38	0.34

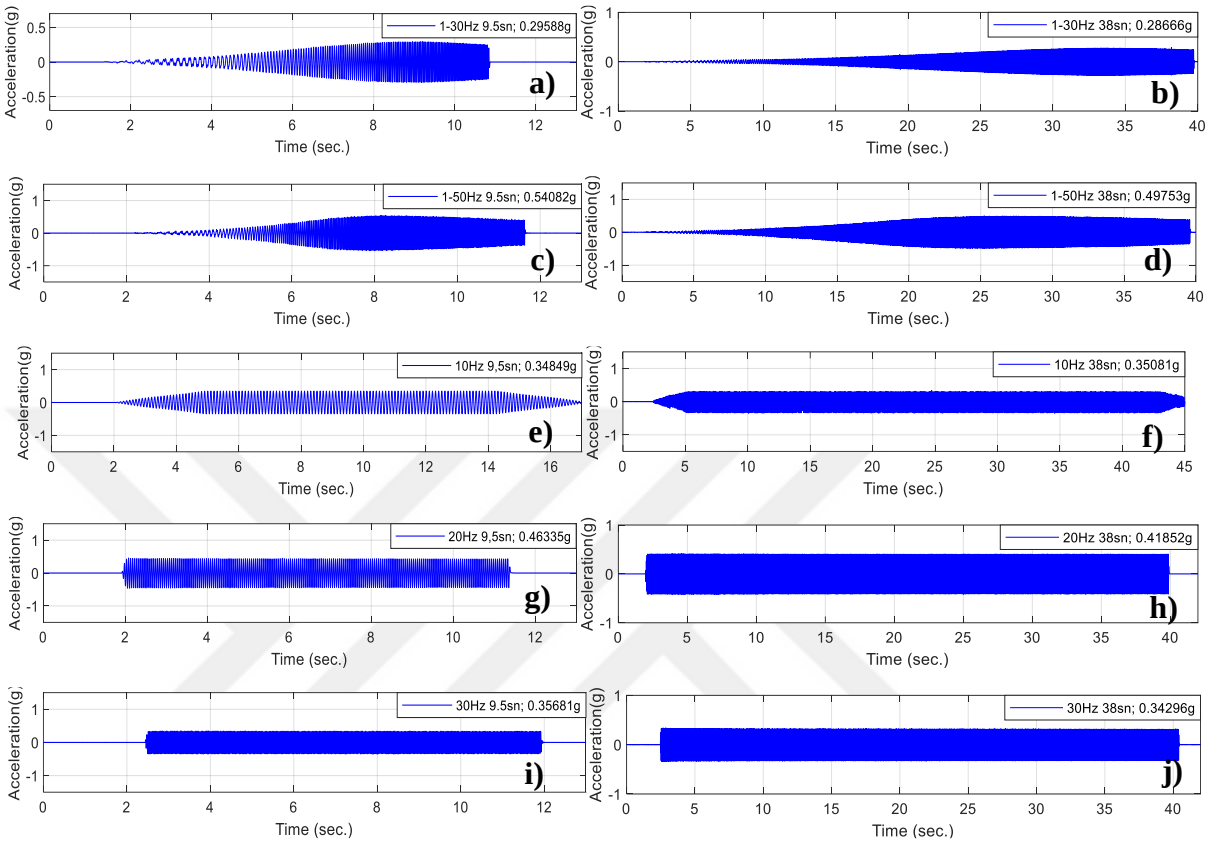

Figure 5.110. Input motions used in shaking table experiments, a) 1-30Hz 9.5s incremental sine wave, b) 1-30Hz 38s incremental sine wave, c) 1-50Hz 9.5s incremental sine wave, d) 1-50Hz 38s incremental sine wave, e) 10Hz 9.5s sine wave, f) 10Hz 38s sine wave, g) 20Hz 9.5s sine wave, h) 20Hz 38s sine wave, i) 30Hz 9.5s sine wave, j) 30Hz 38s sine wave.

5.3.4. Shaking Table Test Results

Experimental results for reduced scale unreinforced, geogrid reinforced (T_{ult}:20kN/m and T_{ult}:40kN/m) and EPS geofoam highway embankment models are given in this section. Experimental results are given as acceleration responses and displacement responses.

5.3.4.1. Test Results for Unreinforced Case

Shaking table test results of the unreinforced embankment model are represented in this section. Test results are represented as acceleration responses and displacement responses of the crest for the selected sensors of A9 and D12 and D13. A9 is placed at the crest of the embankment. D12 measures the horizontal displacements at the crest of the models and D13 is located to measure the vertical displacement (settlement) at the crest of the embankment models.

5.3.4.1.1. Test Results for Unreinforced Case under 1-30Hz

Shaking table test results for unreinforced case under 1-30Hz 9.5s and 1-30Hz 38s are given in this section.

The input dynamic motion of 1-30Hz 9.5s has a peak acceleration of 0.30g. The accelerometers located at the same height in the foundation layer (A3-A6) measured around 0.37g. Transmitted accelerations increase within the embankment body due to the increased height and the amplitude of acceleration reaches to 0.46g (A8) and 0.47g (A9) (Figure 5.111a). Fourier amplitudes under the given motion reach to their peak at 28.48Hz. Spectral accelerations on the unreinforced embankment model are 4.34g and 4.19g for A8 and A9, respectively. Relatedly, the structural periods are obtained in the range of 0.03 to 0.04s (Figure 5.111a).

The input dynamic motion of 1-30Hz 38s has a peak acceleration value of 0.29g and the accelerometers located at the same height in the foundation layer (A3-A6) measures around 0.36g. The amplitude of transmitted accelerations increase within the embankment body with respect to the increased height and reaches to 0.44g (A8) and 0.46g (A9) (Figure 5.111b). Fourier amplitudes reach to their peak at 24.4Hz. Spectral accelerations on the unreinforced embankment model in this case are 4.13g and 4.31g for A8 and A9, respectively. Structural periods are obtained as 0.04s (Figure 5.111b).

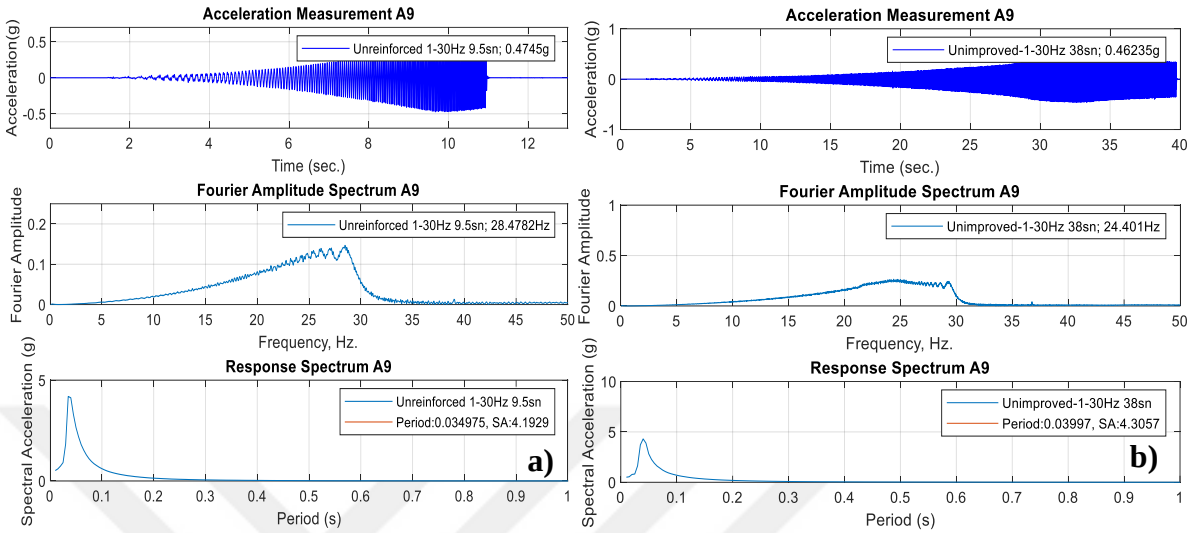

Figure 5.111. Acceleration Response of A9, a) 1-30 Hz 9.5s, b) 1-30 Hz 38s.

The crest of the embankment model (D12) displaces 38mm and 1.26cm horizontally under the 1-30hz 9.5s and 1-30Hz 38s, respectively as given in Figure 5.112a and Figure 5.112b. Similarly, the crest of the embankment (D13) settles 11mm and 23mm vertically under the 1-30Hz 9.5s and 1-30Hz 38s, respectively as represented in Figure 5.113a and Figure 5.113b. Deformed shape under the given dynamic excitation is shown in Figure 5.114.

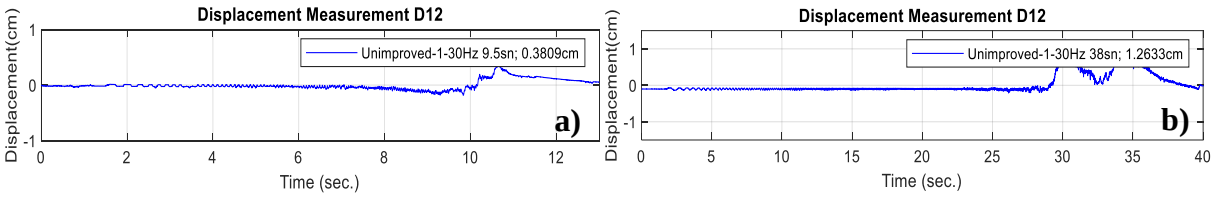

Figure 5.112. Displacement Response of D12, a) 1-30 Hz 9.5s, b) 1-30 Hz 38s.

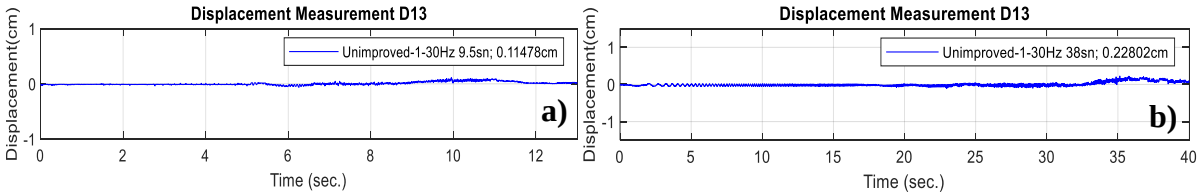

Figure 5.113. Displacement Response of D13, a) 1-30 Hz 9.5s, b) 1-30 Hz 38s.



Figure 5.114. Deformed shape of the unreinforced embankment model under 1-30Hz-9.5s.

5.3.4.1.2. Test Results for Unreinforced Case under 1-50Hz

Shaking table test results for unreinforced case under 1-50Hz 9.5s and 1-50Hz 38s are given in this section.

The dynamic excitation has a peak acceleration of 0.54g under 1-50Hz 9.5s. The amplitude of transmitted accelerations increase within the embankment body with respect to the increased height and reaches to 1.24g (A8) and 1.31g (A9) (Figure 5.115a). Fourier amplitudes reach to their peak at 47.9Hz. Spectral accelerations on the unreinforced embankment model in this case are 8.30g and 7.37g for A8 and A9, respectively. Structural periods are obtained in the range of 0.02s and 0.03s (Figure 5.115a).

Under 1-50Hz 38s, the input dynamic motion has a peak acceleration value of 0.50g and the accelerometers located at the same height in the foundation layer (A3-A6) measures around 0.75g. The amplitude of transmitted accelerations increase within the embankment body with respect to the increased height and reaches to 1.23g (A8) and 1.43g (A9) (Figure 5. 115b). Fourier amplitudes reach to their peak at 39.7Hz. Spectral accelerations on the unreinforced

embankment model in this case are obtained as 8.26g for A8 and A9. Structural periods are in the range of 0.02s and 0.03s (Figure 5. 115b).

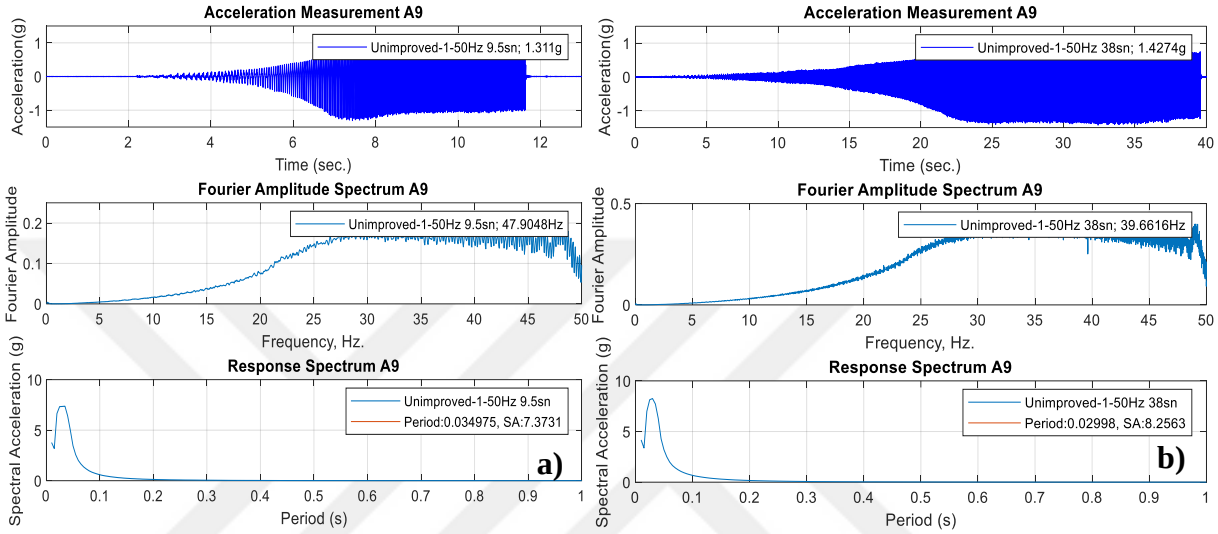

Figure 5.115. Acceleration Response of A9, a) 1-50 Hz 9.5s, b) 1-50 Hz 38s.

The crest of the embankment model (D12) displaces 1.21cm and 1.40cm horizontally under the 1-50hz 9.5s and 1-50Hz 38s, respectively as given in Figure 5.116a and Figure 5.116b. Similarly, the crest of the embankment (D13) settles 67mm and 12mm vertically under the 1-50Hz 9.5s and 1-50Hz 38s, respectively as represented in Figure 5.117a and Figure 5.117b.

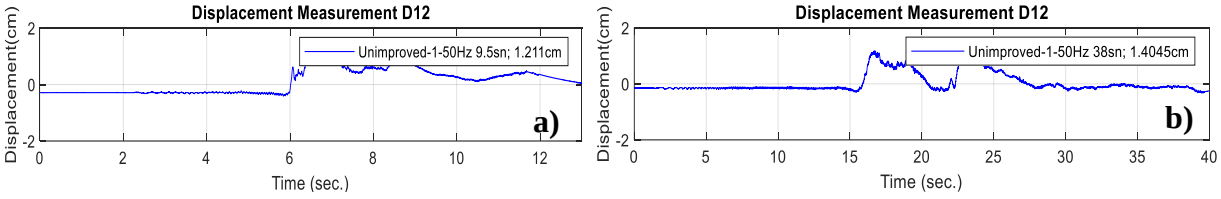

Figure 5.116. Displacement Response of D12, a) 1-50 Hz 9.5s, b) 1-50 Hz 38s.

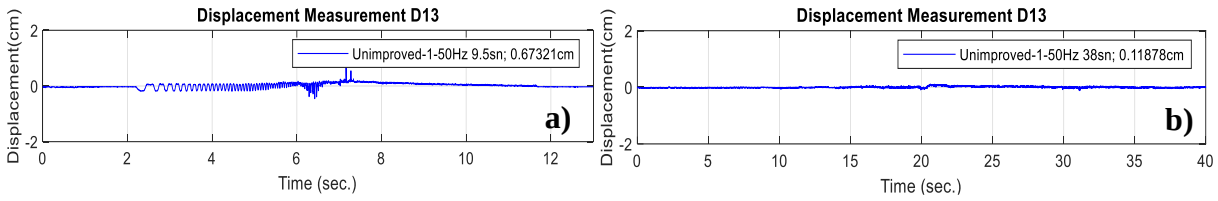

Figure 5.117. Displacement Response of D13, a) 1-50 Hz 9.5s, b) 1-50 Hz 38s.

Deformed shape of the unreinforced embankment model subjected to incremental 1-50Hz of vibration for 38s is shown in Figure 5.118.



Figure 5.118. Deformed shape of the unreinforced embankment model under 1-50Hz-38s.

5.3.4.1.3. Test Results for Unreinforced Case under 10Hz

Applied input dynamic motion of 10Hz 9.5s has a peak acceleration value of 0.35g and the accelerometers located at the same height in the foundation layer (A3-A6) also measures approximately 0.35g. The amplitude of transmitted accelerations increase within the embankment body is measured as 0.36g (Figure 5.119a). Fourier amplitudes reach to their peak at 10Hz as expected. Spectral accelerations on the unreinforced embankment model in this case are obtained as 3.59g and 3.64g for A8 and A9, respectively. Structural periods are obtained as 0.1s (Figure 5.119a).

Under the input motion of 10Hz 38s is 0.35g for the given case and the accelerometers in the foundation soil also measure the same amount of acceleration. Transmitted accelerations increase slightly due to the increased height of the embankment and reach 0.36g (A9) (Figure 5.119b). Fourier amplitudes reach to their peak at 10Hz. Spectral accelerations on the unreinforced embankment model in this case are obtained as 3.61g and 3.66g for A8 and A9, respectively. Structural periods are obtained as 0.1s (Figure 5.119b).

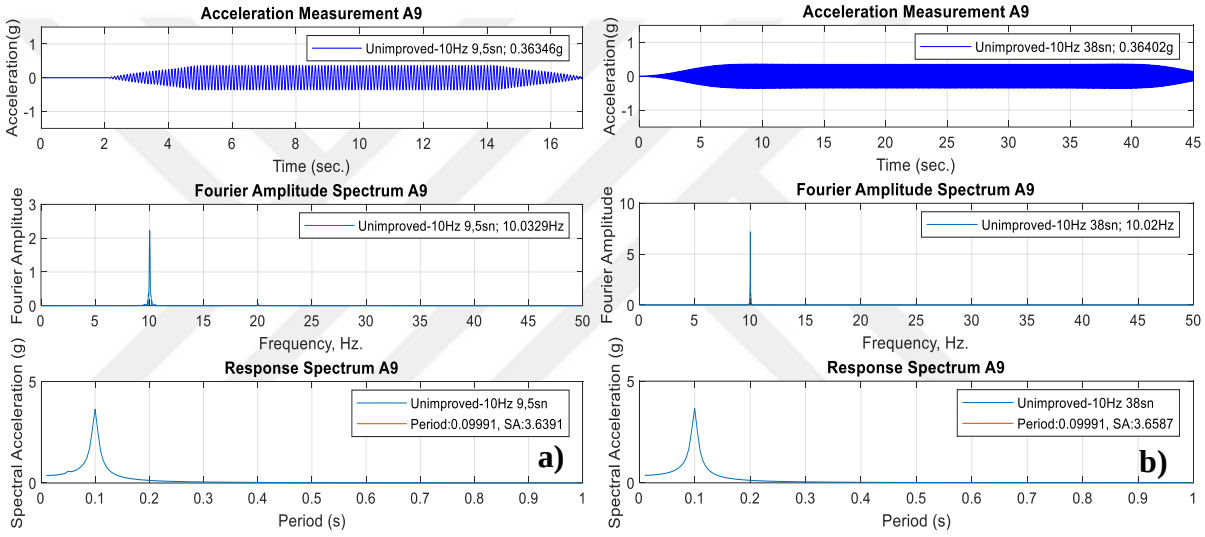

Figure 5.119. Acceleration Response of A9, a) 10Hz 9.5s, b) 10Hz 38s.

The crest of the embankment model (D12) displaces 29mm and 1.09cm horizontally under the 10Hz 9.5s and 10Hz 38s, respectively as given in Figure 5.120a and Figure 5.120b. Similarly, the crest of the embankment (D13) settles 8mm and 7mm vertically under the 10Hz 9.5s and 10Hz 38s, respectively as represented in Figure 5.121a and Figure 5.121b.

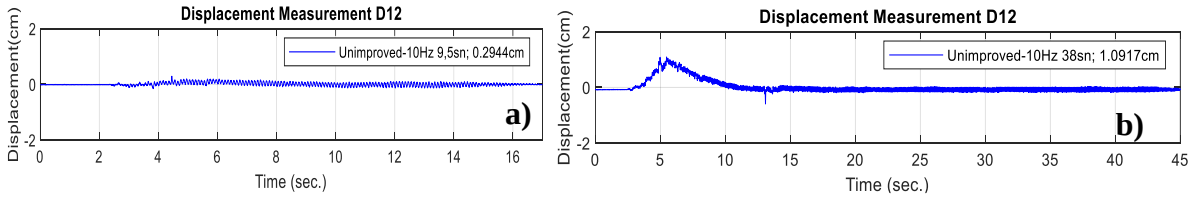

Figure 5.120. Displacement Response of D12, a) 10Hz 9.5s, b) 10Hz 38s.

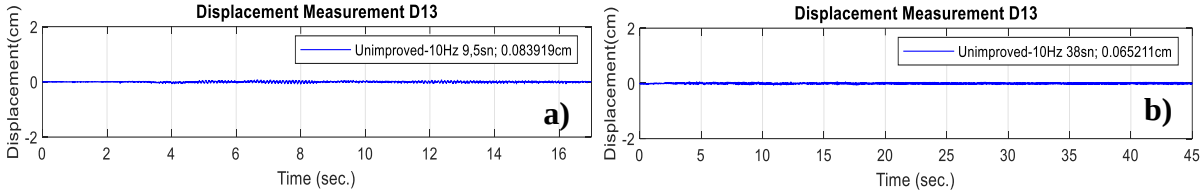

Figure 5.121. Displacement Response of D13, a) 10Hz 9.5s, b) 10Hz 38s.

5.3.4.1.4. Test Results for Unreinforced Case under 20Hz

The input acceleration is 0.46g under 20Hz 9.5s and the measurement of accelerometers in the foundation soil are in the range of 0.49g to 0.51g. Transmitted accelerations increase slightly due to the increased height of the embankment and reach 0.57g (A8) and 0.60g (A9) (Figure 5.122a). Fourier amplitudes reach to their peak at 20Hz as expected. Spectral accelerations on the unreinforced embankment model in this case are obtained as 5.48g and 5.73g for A8 and A9, respectively. Structural periods are obtained as 0.05s (Figure 5.122a).

The input dynamic motion of 20Hz 38s has a peak acceleration value of 0.42g and the accelerometers located at the same height in the foundation layer (A3-A6) measures approximately 0.45g. The amplitude of transmitted accelerations increase within the embankment body is measured as 0.51g (A8) and 0.54g (A9) (Figure 5.122b). Fourier amplitudes reach to their peak at 20Hz. Spectral accelerations on the unreinforced embankment model in this case are obtained as 5.17g and 5.41g for A8 and A9, respectively. Structural periods are obtained as 0.05s (Figure 5.122b).

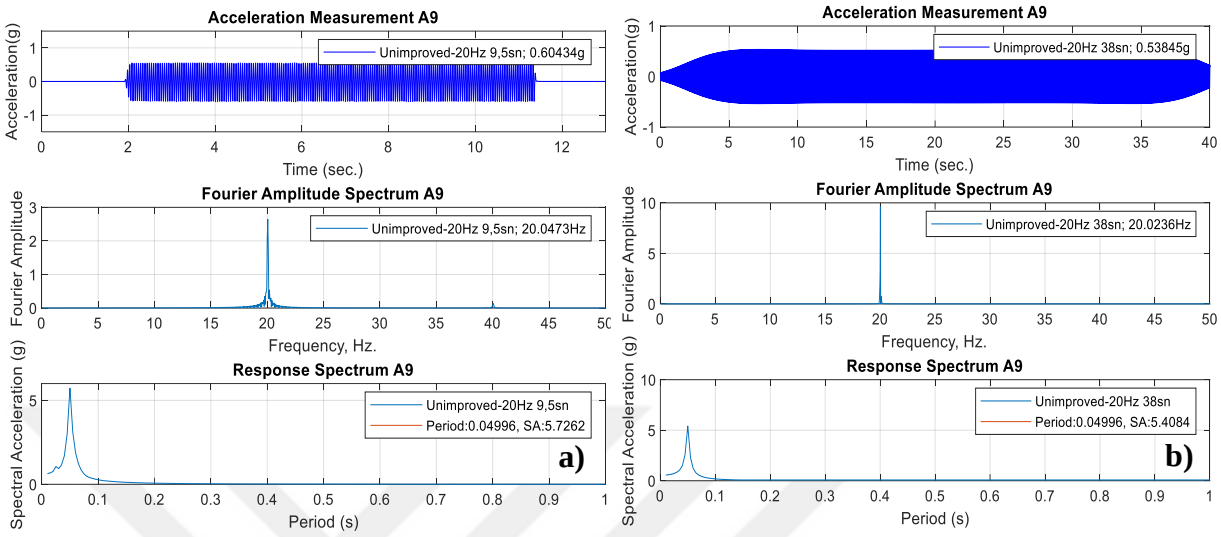

Figure 5.122. Acceleration Response of A9, a) 20Hz 9.5s, b) 20Hz 38s.

The crest of the embankment model (D12) displaces 78mm and 95mm horizontally under the 20Hz 9.5s and 20Hz 38s, respectively as given in Figure 5.123a and Figure 5.123b. Similarly, the crest of the embankment (D13) settles 16mm and 12mm vertically under the 20Hz 9.5s and 20Hz 38s, respectively as represented in Figure 5.124a and Figure 5.124b.

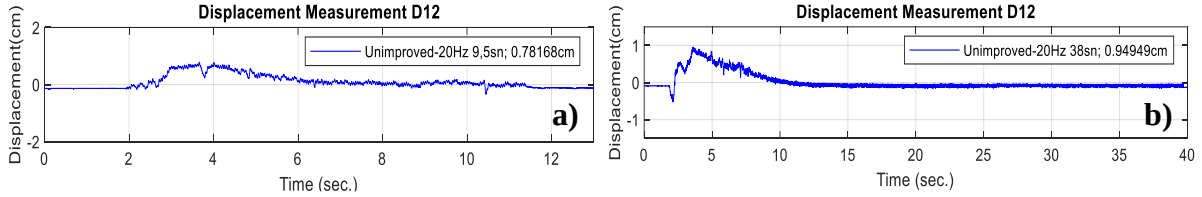

Figure 5.123. Displacement Response of D12, a) 20Hz 9.5s, b) 20Hz 38s.

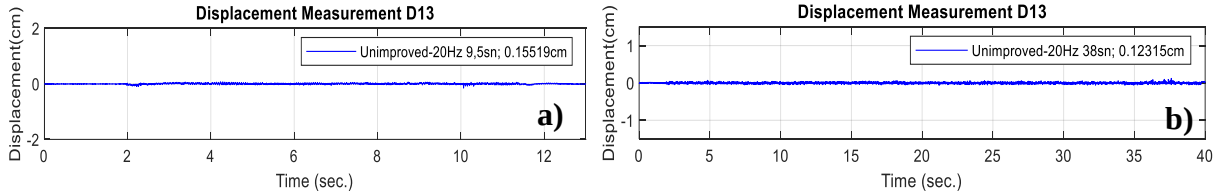

Figure 5.124. Displacement Response of D13, a) 20Hz 9.5s, b) 20Hz 38s.

5.3.4.1.5. Test Results for Unreinforced Case under 30Hz

The input dynamic motion of 30Hz 9.5s has a peak acceleration value of 0.36g. Obtained results show that, the amplitude of transmitted accelerations within the embankment body is measured as 0.72g (A8) and 0.84g (A9) (Figure 5.125a). Fourier amplitudes reach to their peak at 30Hz. Spectral accelerations on the unreinforced embankment model in this case are obtained as 3.91g and 4.26g for A8 and A9, respectively. Structural periods are obtained as 0.03s (Figure 5.125a).

30Hz 38s of motion has a peak acceleration value of 0.34g. No significant differences are observed in measured accelerations in the foundation soil as acceleration values are around 0.50g. Obtained results show that, the amplitude of transmitted accelerations increase within the embankment body is measured as 0.70g (A8) and 0.82g (A9) (Figure 5.125b). Fourier amplitudes reach to their peak at 30Hz as expected. Spectral accelerations on the unreinforced embankment model in this case are obtained as 3.78g and 4.18g for A8 and A9, respectively. Structural periods are obtained as 0.03s (Figure 5.125b).

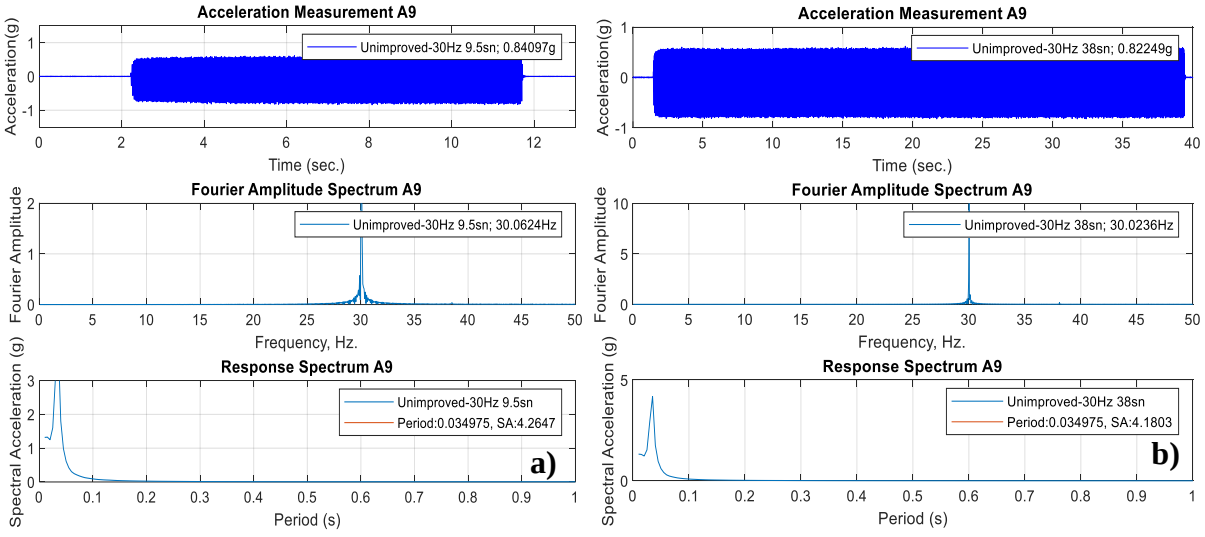

Figure 5.125. Acceleration Response of A9, a) 30Hz 9.5s, b) 30Hz 38s.

The crest of the embankment model (D12) displaces 81mm and 1.06cm horizontally under the 30Hz 9.5s and 30Hz 38s, respectively as given in Figure 5.126a and Figure 5.126b. Similarly, the crest of the embankment (D13) settles 18mm and 54mm vertically under the 30Hz 9.5s and 30Hz 38s, respectively as represented in Figure 5.127a and Figure 5.127b.

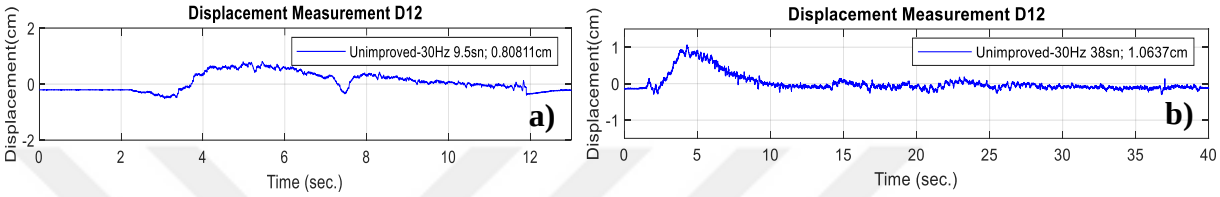

Figure 5.126. Displacement Response of D12, a) 30Hz 9.5s, b) 30Hz 38s.

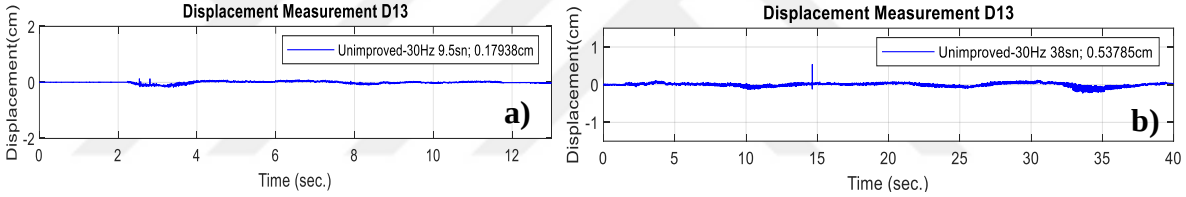

Figure 5.127. Displacement Response of D13, a) 30Hz 9.5s, b) 30Hz 38s.

Deformed shape of the unreinforced model under 30Hz of vibration for 9.5s is shown in Figure 5.128.

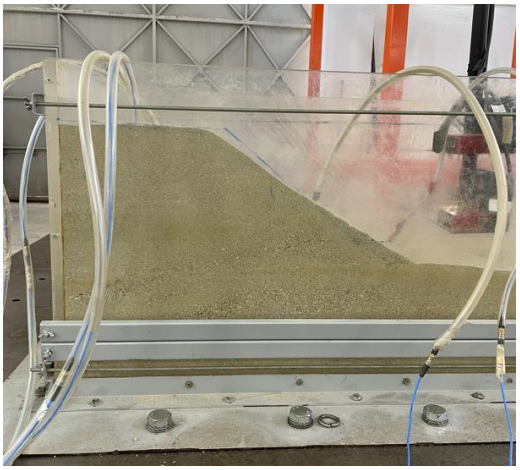

Figure 5.128. Deformed shape of the unreinforced embankment model subjected to 30Hz-9.5s.

5.3.4.2. Test Results for Geogrid Reinforced (Tult:20kN/m) Case

Shaking table test results of the geogrid reinforced embankment model (T_{ult}:20kN/m) are represented in this section. Test results are represented as acceleration responses and displacement responses for the selected sensors of A9 and D12 and D13. A9 is placed five centimeters below the crest of the embankment. D12 measures the crest level displacements on the slope of the models and D13 is located to measure the vertical displacement (settlement) at the crest of the embankment models.

5.3.4.2.1. Test Results for Geogrid Reinforced (Tult:20kN/m) Case under 1-30Hz

Given input dynamic motion of 1-30Hz 9.5s in current case has a peak acceleration value of 0.30g. No significant differences are observed in measured accelerations in the foundation soil as accelerationn values are around 0.33g. Obtained results show that, the amplitude of transmitted accelerations increase within the embankment body is measured as 0.41g (A8 and A9) (Figure 5.129a). Fourier amplitudes reach to their peak at 28.6Hz. Spectral accelerations in this case are obtained as 3.78g and 3.74g for A8 and A9, respectively. Structural periods are obtained as 0.04s (Figure 5.129a).

Under 1-30Hz 38s, the input dynamic motion has a peak acceleration value of 0.29g. No significant differences are observed in measured accelerations in the foundation soil as accelerationn values are around 0.32g. Obtained results show that, the amplitude of transmitted accelerations increase within the embankment body is measured as 0.41g on (A8) and 0.46g on (A9) (Figure 5.129b). Fourier amplitudes reach to their peak at 29.2Hz. Spectral accelerations in this case are obtained as 3.82g and 4.27g for A8 and A9, respectively. Structural periods are obtained as 0.03s and 0.04s for A8 and A9, respectively (Figure 5.129b).

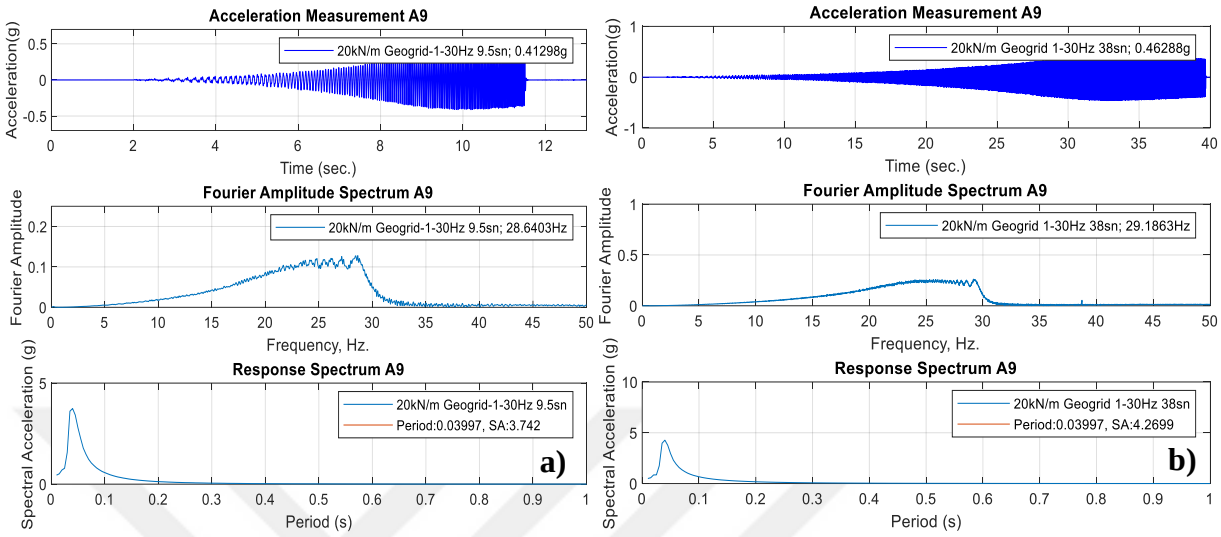

Figure 5.129. Acceleration Response of A9, a)1-30Hz 9.5s, b) 1-30Hz 38s.

The crest of the embankment model (D12) displaces 34mm and 42mm horizontally under the 1-30Hz 9.5s and 1-30Hz 38s, respectively as given in Figure 5.130a and Figure 5.130b. Similarly, the crest of the embankment (D13) settles 10mm and 15mm vertically under the 1-30Hz 9.5s and 1-30Hz 38s, respectively as represented in Figure 5.131a and Figure 5.131b.

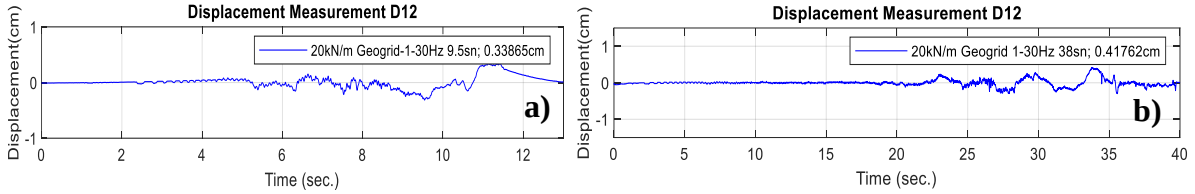

Figure 5.130. Displacement Response of D12, a)1-30Hz 9.5s, b) 1-30Hz 38s.

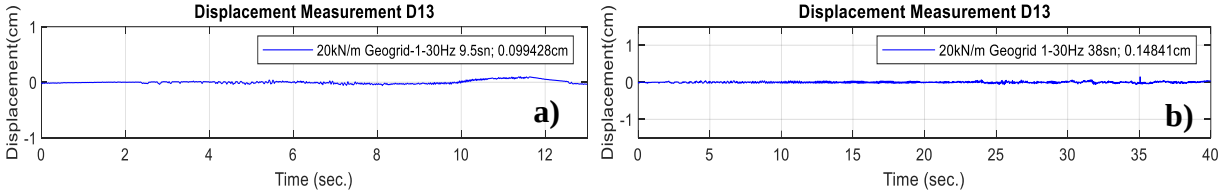

Figure 5.131. Displacement Response of D13, a)1-30Hz 9.5s, b) 1-30Hz 38s.

Deformation of the embankment model under defined input motion is shown in Figure 5.132.

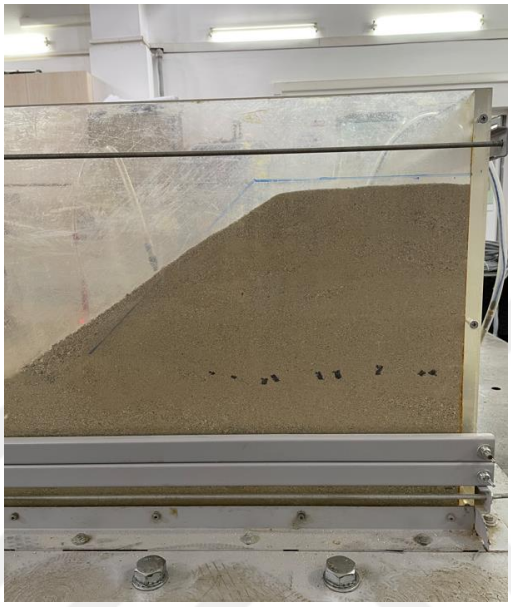

Figure 5.132. Deformed shape of the geogrid reinforced embankment model (T_{ult}:20kN/m) under 1-30Hz-9.5s.

5.3.4.2.2. Test Results for Geogrid Reinforced (Tult:20kN/m) Case under 1-50Hz

Applied input dynamic motion of 1-50Hz 9.5s has a peak acceleration value of 0.54g. Obtained results show that, the amplitude of transmitted accelerations increase within the embankment body is measured as 0.97g (A8) and 1.43g (A9) (Figure 5.133a). Fourier amplitudes reach to their peak at 47.9Hz. Spectral accelerations on the unreinforced embankment model in this case are obtained as 8.00g and 8.01g for A8 and A9, respectively. Structural period is obtained as 0.03s (Figure 5.133a).

The input dynamic motion of 1-50Hz 38s has a peak acceleration value of 0.50g. Obtained results show that, the amplitude of transmitted accelerations increase within the embankment body is measured as 0.93g (A8) and 1.50g (A9) (Figure 5.133b). Fourier amplitudes reach to their peak at 48.9Hz. Spectral accelerations on the unreinforced

embankment model in this case are obtained as 7.99g and 8.30g for A8 and A9, respectively. Structural period is obtained as 0.03s (Figure 5.133b).

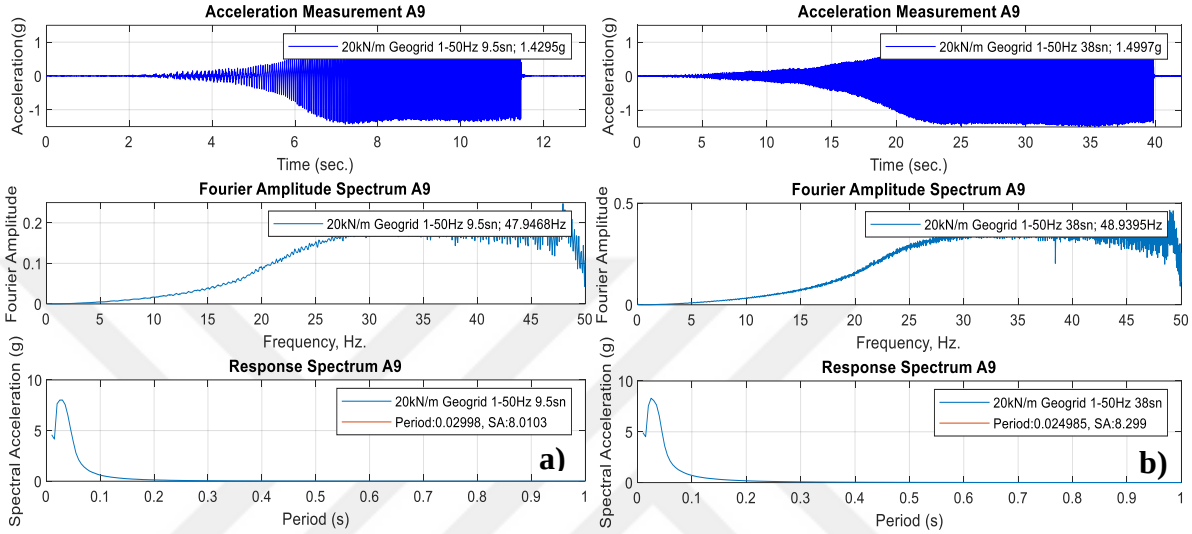

Figure 5.133. Acceleration Response of A9, a)1-50Hz 9.5s, b) 1-50Hz 38s.

The crest of the embankment model (D12) displaces 53mm and 42mm horizontally under the 1-50Hz 9.5s and 1-50Hz 38s, respectively as given in Figure 5.134a and Figure 5.134b. Similarly, the crest of the embankment (D13) settles 11mm and 15mm vertically under the 1-50Hz 9.5s and 1-50Hz 38s, respectively as represented in Figure 5.135a and Figure 5.135b.

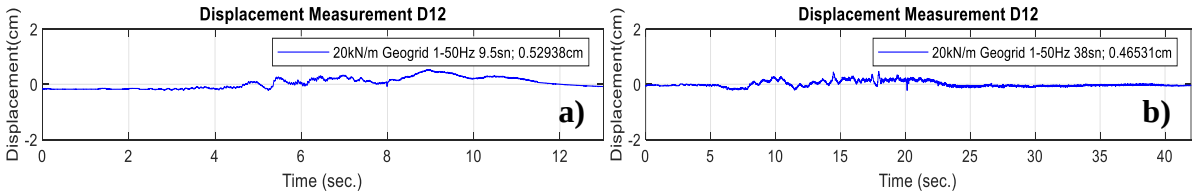

Figure 5.134. Displacement Response of D12, a)1-50Hz 9.5s, b) 1-50Hz 38s.

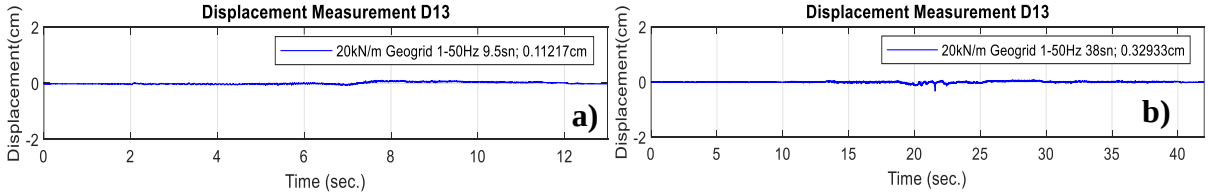

Figure 5.135. Displacement Response of D13, a)1-50Hz 9.5s, b) 1-50Hz 38s.

5.3.4.2.3. Test Results for Geogrid Reinforced (Tult:20kN/m) Case under 10Hz

Applied input dynamic motion of 10Hz 9.5s has a peak acceleration value of 0.35g and the accelerometers located at the same height in the foundation layer (A3-A6) also measures approximately 0.35g. The amplitude of transmitted accelerations increase within the embankment body is measured as 0.36g (A8) and 0.37g (A9) (Figure 5.136a). Fourier amplitudes reach to their peak at 10Hz as expected. Spectral accelerations on the unreinforced embankment model in this case are obtained as 3.59g and 3.73g for A8 and A9, respectively. Structural periods are obtained as 0.1s (Figure 5.136a).

The amplitude of the input motion of 10Hz 38s is 0.35g for the given case and the accelerometers in the foundation soil also measure approximately the same acceleration. Transmitted accelerations increase slightly due to the increased height of the embankment and reach 0.37g (A9) (Figure 5.136b). Fourier amplitudes reach to their peak at 10Hz. Spectral accelerations on the unreinforced embankment model in this case are obtained as 3.59g and 3.72g for A8 and A9, respectively. Structural periods are obtained as 0.1s (Figure 5.136b).

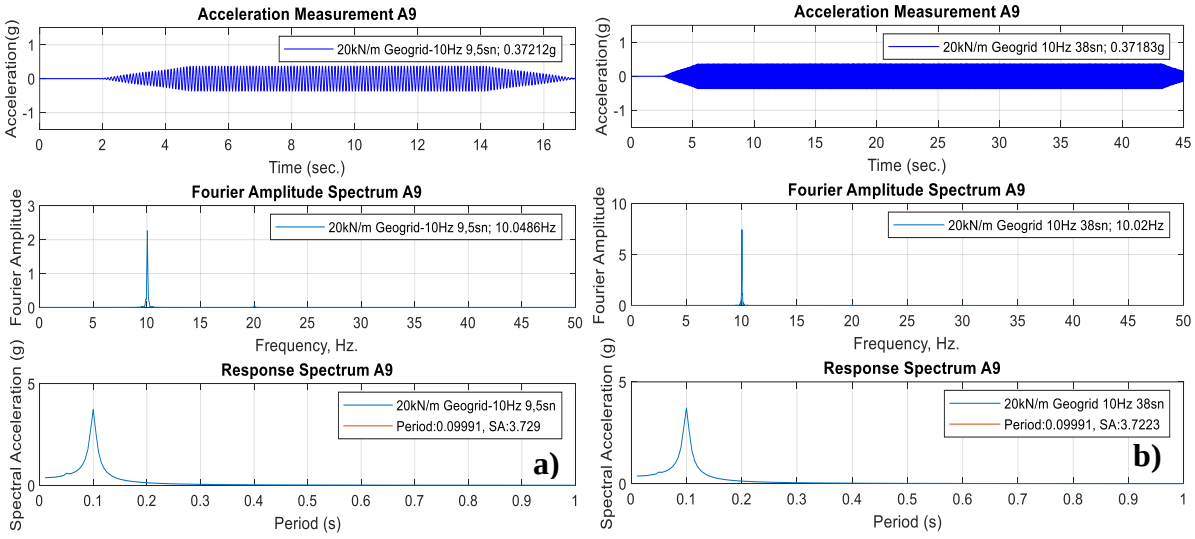

Figure 5.136. Acceleration Response of A9, a) 10Hz 9.5s, b) 10Hz 38s.

The crest of the embankment model (D12) displaces 26mm and 15mm horizontally under the 10Hz 9.5s and 10Hz 38s, respectively as given in Figure 5.137a and Figure 5.137b. Similarly, the crest of the embankment (D13) settles 4mm and 5mm vertically under the 10Hz 9.5s and 10Hz 38s, respectively as represented in Figure 5.138a and Figure 5.138b.

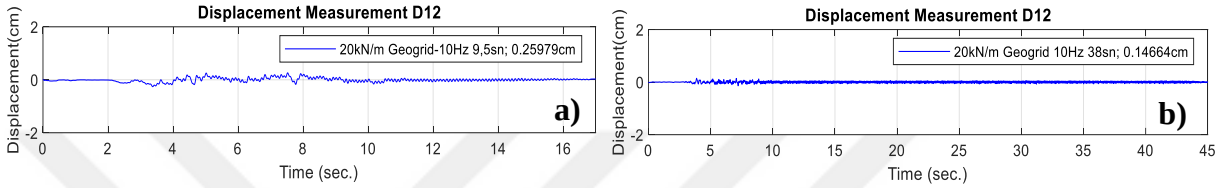

Figure 5.137. Displacement Response of D12, a) 10Hz 9.5s, b) 10Hz 38s.

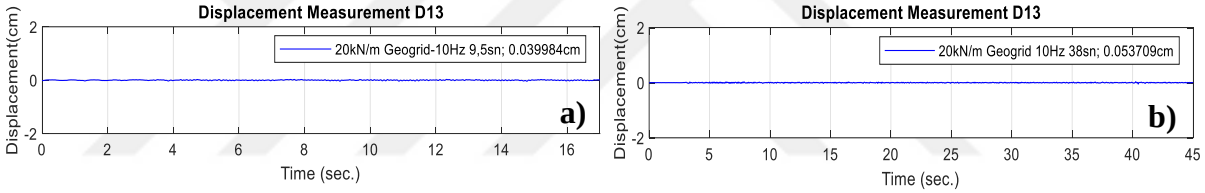

Figure 5.138. Displacement Response of D13, a) 10Hz 9.5s, b) 10Hz 38s.

Embankment model experienced deformation under defined dynamic motion is given in Figure 5.139.

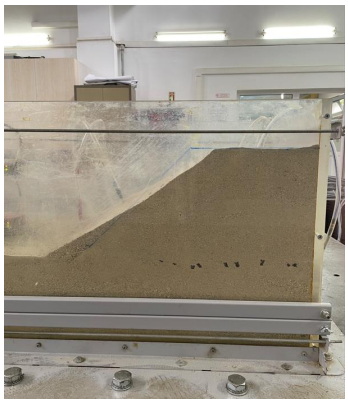

Figure 5.139. Deformed shape of the geogrid reinforced embankment model (T_{ult}:20kN/m) under 10Hz 9.5s.

5.3.4.2.4. Test Results for Geogrid Reinforced (Tult:20kN/m) Case under 20Hz

Input acceleration is 0.46g for the input motion of 20Hz 9.5s and the measurement of accelerometers in the foundation soil are in the range of 0.49g to 0.52g. Transmitted accelerations increase slightly due to the increased height of the embankment and reach 0.57g (A8) and 0.69g (A9) (Figure 5.140a). Fourier amplitudes reach to their peak at 20Hz as expected. Spectral accelerations on the unreinforced embankment model in this case are obtained as 5.52g and 6.50g for A8 and A9, respectively. Structural periods are obtained as 0.05s (Figure 5.140a).

Applied input dynamic motion of 20Hz 38s has a peak acceleration value of 0.42g and the accelerometers located at the same height in the foundation layer (A3-A6) measures approximately 0.46g. The amplitude of transmitted accelerations increase within the embankment body is measured as 0.52g (A8) and 0.63g (A9) (Figure 5.140b). Fourier amplitudes reach to their peak at 20Hz. Spectral accelerations on the unreinforced embankment model in this case are obtained as 5.00g and 5.94g for A8 and A9, respectively. Structural periods are obtained as 0.05s (Figure 5.140b).

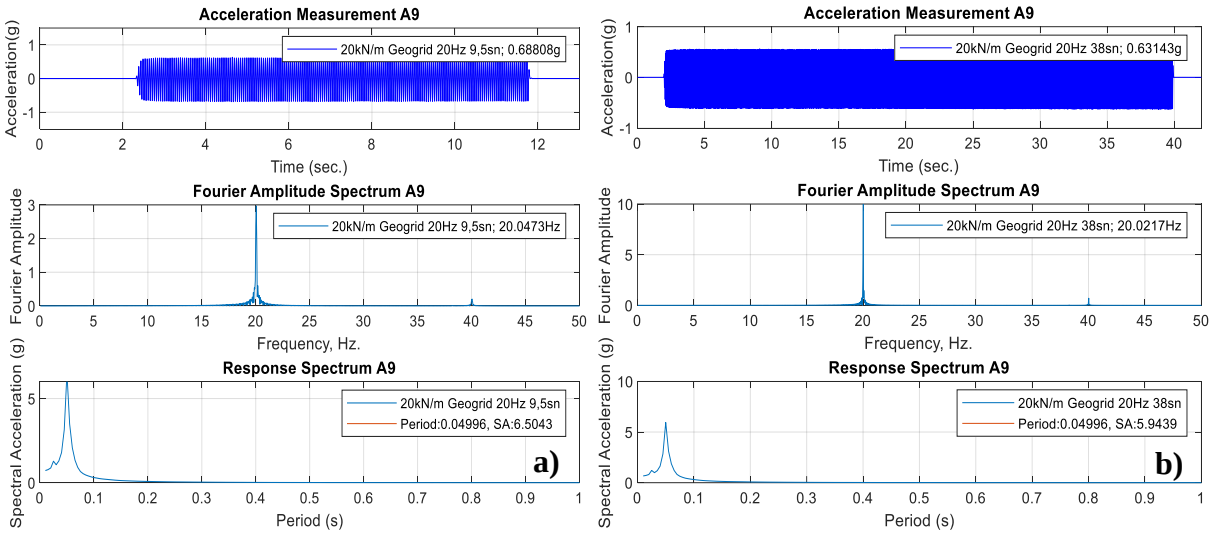

Figure 5.140. Acceleration Response of A9, a) 20Hz 9.5s, b) 20Hz 38s.

The crest of the embankment model (D12) displaces 75mm and 45mm horizontally under the 20Hz 9.5s and 20Hz 38s, respectively as given in Figure 5.141a and Figure 5.141b. Similarly, the crest of the embankment (D13) settles 7mm and 14mm vertically under the 20Hz 9.5s and 20Hz 38s, respectively as represented in Figure 5.142a and Figure 5.142b.

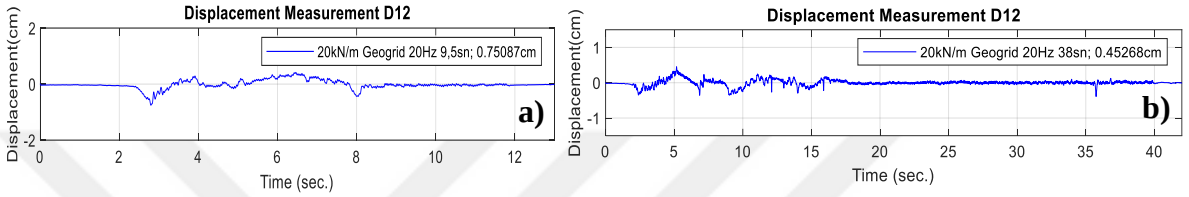

Figure 5.141. Displacement Response of D12, a) 20Hz 9.5s, b) 20Hz 38s.

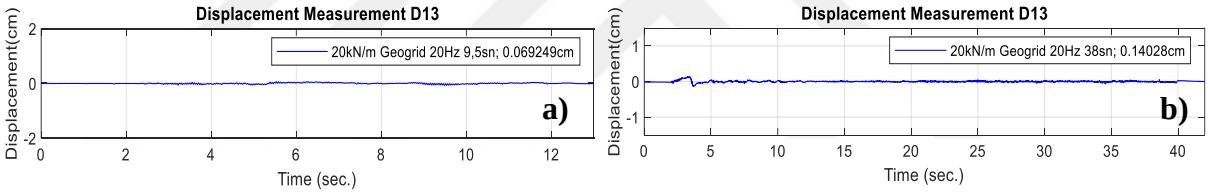

Figure 5.142. Displacement Response of D13, a) 20Hz 9.5s, b) 20Hz 38s.

5.3.4.2.5. Test Results for Geogrid Reinforced (Tult:20kN/m) Case under 30Hz

Applied input dynamic motion of 30Hz 9.5s has a peak acceleration value of 0.36g. Obtained results show that, the amplitude of transmitted accelerations increase within the embankment body is measured as 0.65g (A8) and 1.00g (A9). (Figure 5.143a). Fourier amplitudes reach to their peak at 30Hz. Spectral accelerations on the unreinforced embankment model in this case are obtained as 3.52g and 4.36g for A8 and A9, respectively. Structural periods are obtained as 0.03s (Figure 5.143a).

Given input dynamic motion of 30Hz 38s has a peak acceleration value of 0.34g. No significant differences are observed in measured accelerations in the foundation soil as accelerationn values are around 0.49g. Obtained results show that, the amplitude of transmitted

accelerations increase within the embankment body is measured as 0.61g on (A8) and 0.97g on (A9) (Figure 5.143b). Fourier amplitudes reach to their peak at 30Hz as expected. Spectral accelerations on the unreinforced embankment model in this case are obtained as 3.53g and 4.50g for A8 and A9, respectively. Structural periods are obtained as 0.03s (Figure 5.143b).

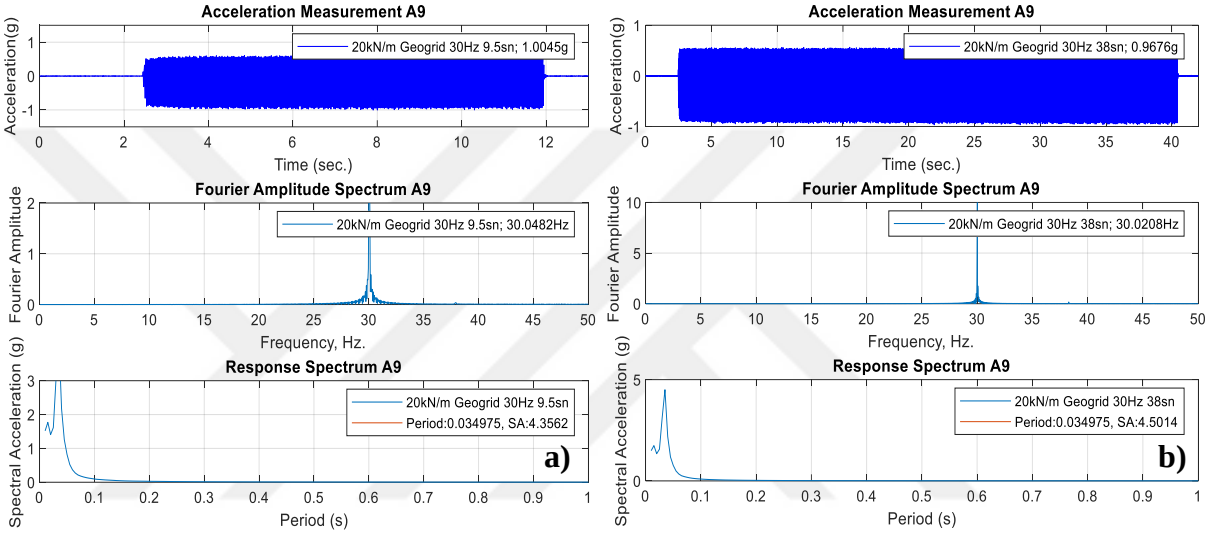

Figure 5.143. Acceleration Response of A9, a) 30Hz 9.5s, b) 30Hz 38s.

The crest of the embankment model (D12) displaces 76mm horizontally under the 30Hz 9.5s and 30Hz 38s, respectively as given in Figure 5.144a and Figure 5.144b. Similarly, the crest of the embankment (D13) settles 50mm and 70mm vertically under the 30Hz 9.5s and 30Hz 38s, respectively as represented in Figure 5.145a and Figure 5.145b.

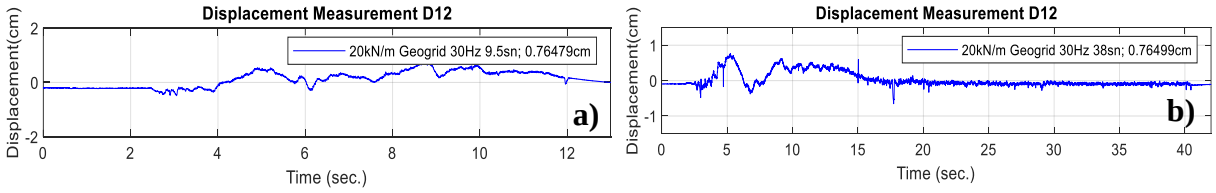

Figure 5.144. Displacement Response of D12, a) 30Hz 9.5s, b) 30Hz 38s.

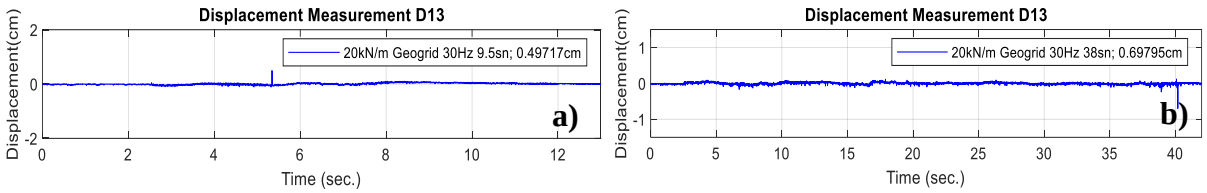

Figure 5.145. Displacement Response of D13, a) 30Hz 9.5s, b) 30Hz 38s.

5.3.4.3. Test Results for Geogrid Reinforced (Tult:40kN/m) Case

Shaking table test results of the geogrid reinforced embankment model (T_{ult}:40kN/m) are represented in this section. Test results are represented as acceleration responses and displacement responses for the selected sensors of A9 and D12 and D13. A9 is placed five centimeters below the crest of the embankment. D12 measures the crest level displacements on the slope of the models and D13 is located to measure the vertical displacement (settlement) at the crest of the embankment models.

5.3.4.3.1. Test Results for Geogrid Reinforced (Tult:40kN/m) Case under 1-30Hz

Given input dynamic motion of 1-30Hz 9.5s has a peak acceleration value of 0.30g. No significant differences are observed in measured accelerations in the foundation soil as accelerationn values are around 0.34g. Obtained results show that, the amplitude of transmitted accelerations increase within the embankment body is measured as 0.40g (A8) and 0.47g (A9). (Figure 5.146a). Fourier amplitudes reach to their peak at 28.5Hz. Spectral accelerations in this case are obtained as 3.77g and 4.19g for A8 and A9, respectively. Structural periods are obtained as 0.03s (Figure 5.146a).

The input excitation of 1-30Hz 38s has a peak acceleration value of 0.29g for this case. No significant differences are observed in measured accelerations in the foundation soil as accelerationn values are around 0.33g. Obtained results show that, the amplitude of transmitted accelerations increase within the embankment body is measured as 0.38g on (A8) and 0.47g on (A9) (Figure 5.146b). Fourier amplitudes reach to their peak at 29.2Hz. Spectral accelerations

in this case are obtained as 3.67g and 4.34g for A8 and A9, respectively. Structural periods are obtained as 0.03s and 0.04s for A8 and A9, respectively (Figure 5.146b).

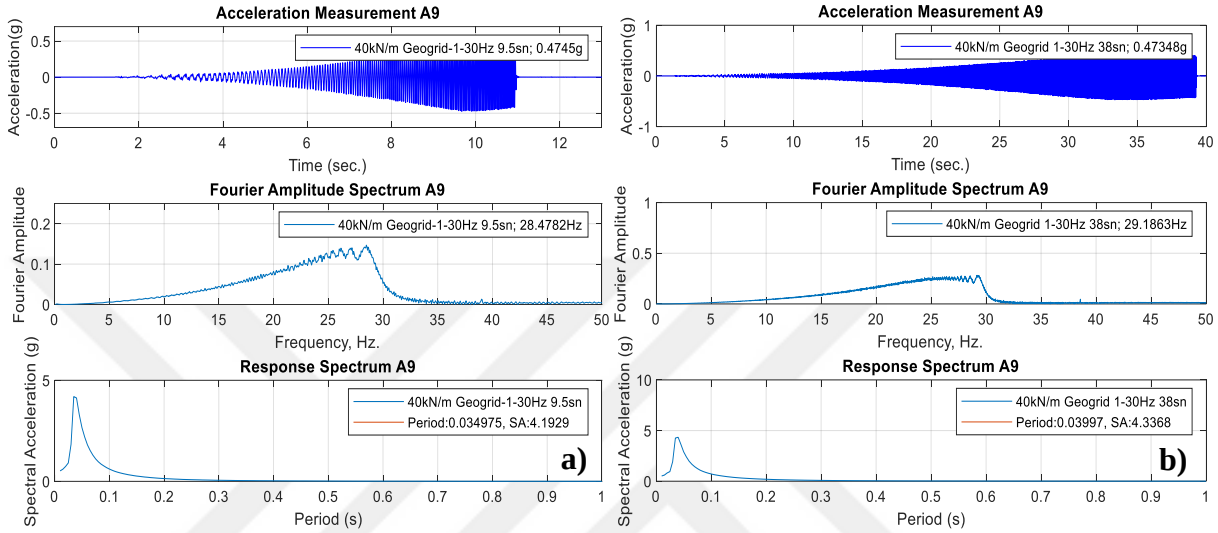

Figure 5.146. Acceleration Response of A9, a) 1-30Hz 9.5s, b) 1-30Hz 38s.

The crest of the embankment model (D12) displaces 53mm and 56mm horizontally under the 1-30Hz 9.5s and 1-30Hz 38s, respectively as given in Figure 5.147a and Figure 5.147b. Similarly, the crest of the embankment (D13) settles 7mm and 6mm vertically under the 1-30Hz 9.5s and 1-30Hz 38s, respectively as represented in Figure 5.148a and Figure 5.148b.

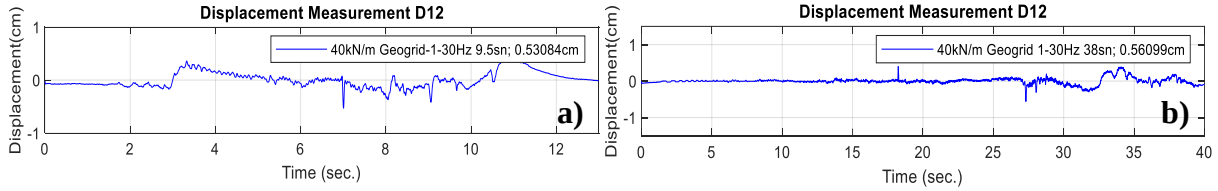

Figure 5.147. Displacement Response of D12, a) 1-30Hz 9.5s, b) 1-30Hz 38s.

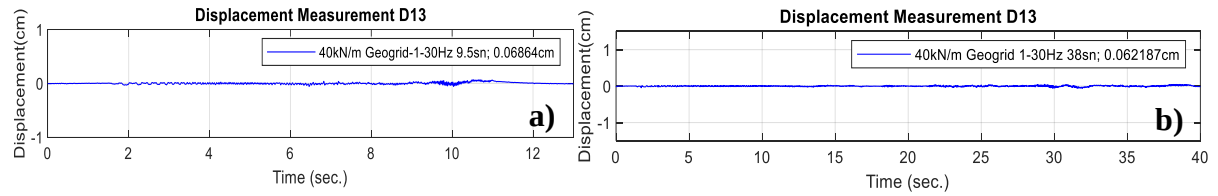

Figure 5.148. Displacement Response of D13, a) 1-30Hz 9.5s, b) 1-30Hz 38s.

5.3.4.3.2. Test Results for Geogrid Reinforced (Tult:40kN/m) Case under 1-50Hz

Applied input dynamic motion of 1-50Hz 9.5s has a peak acceleration value of 0.54g. Obtained results show that, the amplitude of transmitted accelerations increase within the embankment body is measured as 0.94g (A8) and 1.29g (A9) (Figure 5.149a). Fourier amplitudes reach to their peak at 48.1Hz. Spectral accelerations on the unreinforced embankment model in this case are obtained 7.53g and 7.46g for A8 and A9, respectively. Structural period is obtained as 0.02s (Figure 5.149a).

The input dynamic motion of 1-50Hz 38s has a peak acceleration value of 0.50g. Obtained results show that, the amplitude of transmitted accelerations increase within the embankment body is measured as 0.74g (A8) and 0.95g (A9) (Figure 5.149b). Fourier amplitudes reach to their peak at 38.6Hz. Spectral accelerations on the unreinforced embankment model in this case are obtained as 7.17g and 7.93g for A8 and A9, respectively. Structural period is obtained as 0.03s (Figure 5.149b).

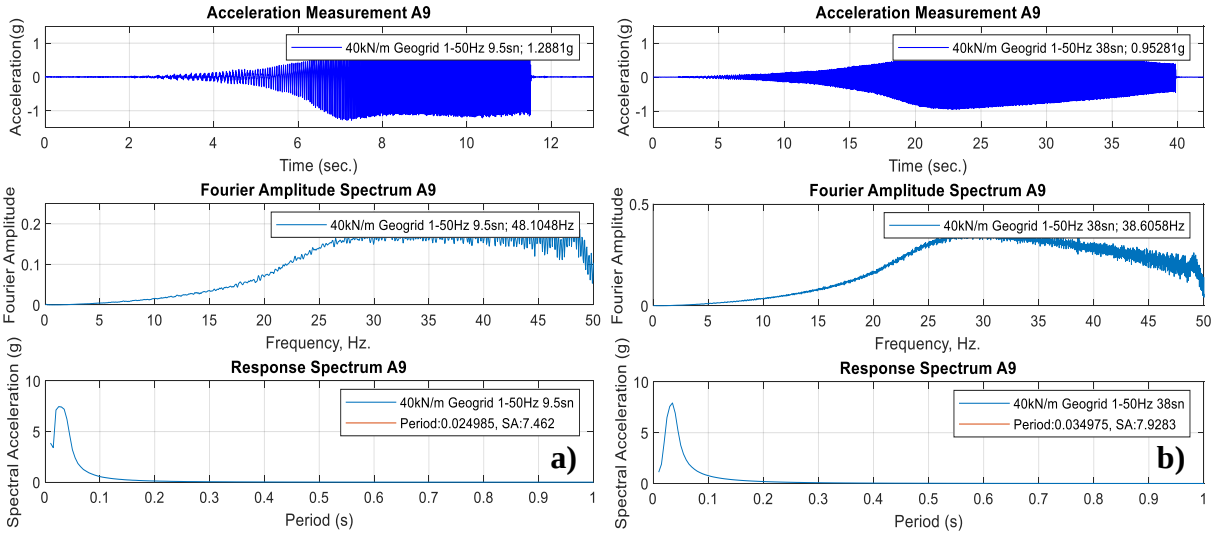

Figure 5.149. Acceleration Response of A9, a) 1-50Hz 9.5s, b) 1-50Hz 38s.

The crest of the embankment model (D12) displaces 51mm and 45mm horizontally under the 1-50Hz 9.5s and 1-50Hz 38s, respectively as given in Figure 5.150a and Figure 5.150b. Similarly, the crest of the embankment (D13) settles 11mm and 32mm vertically under the 1-50Hz 9.5s and 1-50Hz 38s, respectively as represented in Figure 5.151a and Figure 5.151b.

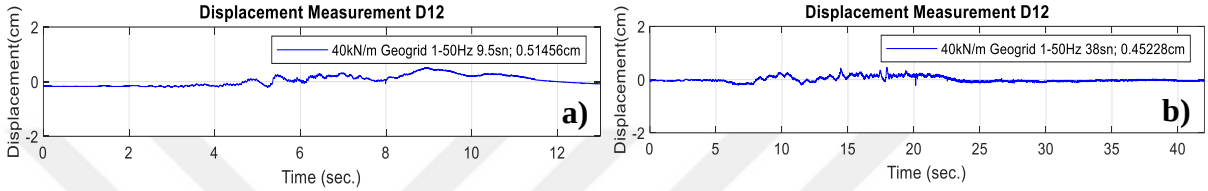

Figure 5.150. Displacement Response of D12, a) 1-50Hz 9.5s, b) 1-50Hz 38s.

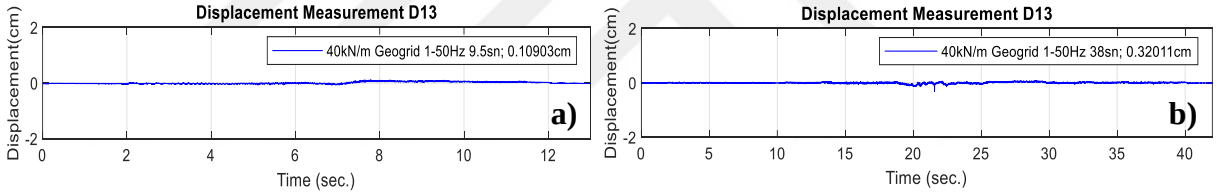

Figure 5.151. Displacement Response of D13, a) 1-50Hz 9.5s, b) 1-50Hz 38s.

5.3.4.3.3. Test Results for Geogrid Reinforced (Tult:40kN/m) Case under 10Hz

The input dynamic motion of 10Hz 9.5s has a peak acceleration value of 0.35g and the accelerometers located at the same height in the foundation layer (A3-A6) also measures approximately 0.35g. The amplitude of transmitted accelerations increase within the embankment body is measured as 0.36g (A8) level and 0.37g (A9) level (Figure 5.152a). Fourier amplitudes reach to their peak at 10Hz as expected. Spectral accelerations on the unreinforced embankment model in this case are obtained as 3.57g and 3.68g for A8 and A9, respectively. Structural periods are obtained as 0.1s (Figure 5.152a).

Applied input acceleration of 10Hz 38s is 0.35g for current case and the accelerometers in the foundation soil also measure approximately the same acceleration. Transmitted

accelerations increase slightly due to the increased height of the embankment and reach 0.37g (A9) (Figure 5.152b). Fourier amplitudes reach to their peak at 10Hz. Spectral accelerations on the unreinforced embankment model in this case are obtained as 3.58g and 3.67g for A8 and A9, respectively. Structural periods are obtained as 0.1s (Figure 5.152b).

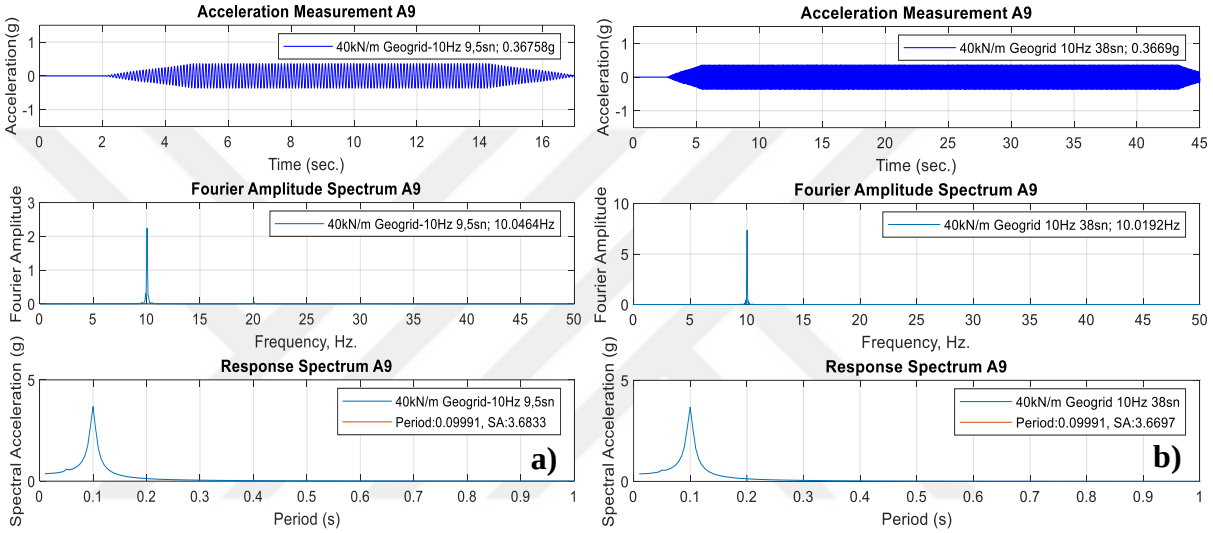

Figure 5.152. Acceleration Response of A9, a) 10Hz 9.5s, b) 10Hz 38s.

The crest of the embankment model (D12) displaces 25mm and 14mm horizontally under the 10Hz 9.5s and 10Hz 38s, respectively as given in Figure 5.153a and Figure 5.153b. Similarly, the crest of the embankment (D13) settles 4mm and 5mm vertically under the 10Hz 9.5s and 10Hz 38s, respectively as represented in Figure 5.154a and Figure 5.154b.

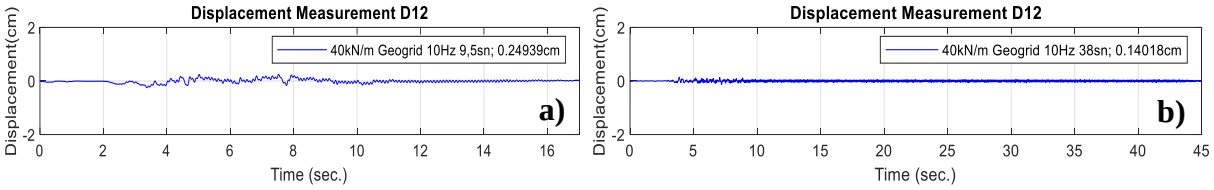

Figure 5.153. Displacement Response of D12, a) 10Hz 9.5s, b) 10Hz 38s.

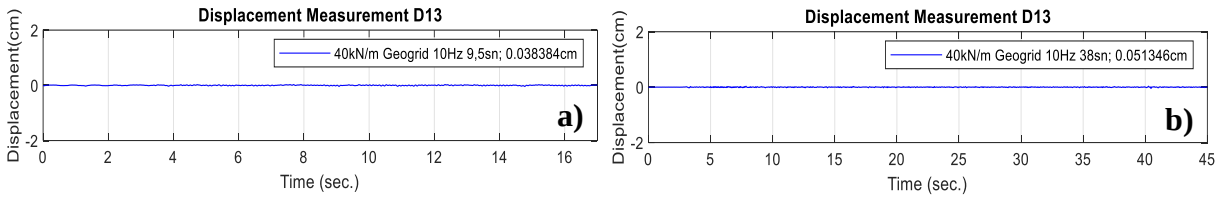

Figure 5.154. Displacement Response of D13, a) 10Hz 9.5s, b) 10Hz 38s.

5.3.4.3.4. Test Results for Geogrid Reinforced (Tult:40kN/m) Case under 20Hz

The input acceleration of 20Hz 9.5s is 0.46g and the measurement of accelerometers in the foundation soil are in the range of 0.49g to 0.51g. Transmitted accelerations increase slightly due to the increased height of the embankment and reach 0.55g (A8) and 0.65g (A9) (Figure 5.155a). Fourier amplitudes reach to their peak at 20Hz as expected. Spectral accelerations on the unreinforced embankment model in this case are obtained as 5.22g and 6.14g for A8 and A9, respectively. Structural periods are obtained as 0.05s (Figure 5.155a).

Applied input dynamic motion of 20Hz 38s has a peak acceleration value of 0.42g and the accelerometers located at the same height in the foundation layer (A3-A6) measures approximately 0.46g. The amplitude of transmitted accelerations increase within the embankment body is measured as 0.52g (A8) and 0.61g (A9) (Figure 5.155b). Fourier amplitudes reach to their peak at 20Hz. Spectral accelerations on the unreinforced embankment model in this case are obtained as 4.96g and 5.77g for A8 and A9, respectively. Structural periods are obtained as 0.05s (Figure 5.155b).

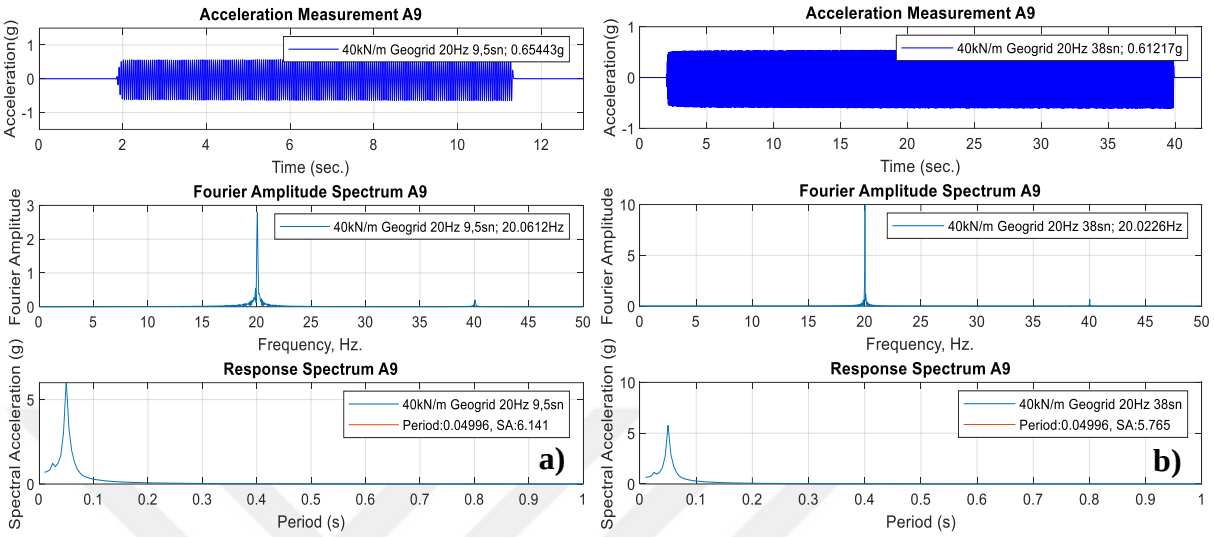

Figure 5.155. Acceleration Response of A9, a) 20Hz 9.5s, b) 20Hz 38s.

The crest of the embankment model (D12) displaces 75mm and 14mm horizontally under the 20Hz 9.5s and 20Hz 38s, respectively as given in Figure 5.156a and Figure 5.156b. Similarly, the crest of the embankment (D13) settles 7mm and 5mm vertically under the 20Hz 9.5s and 20Hz 38s, respectively as represented in Figure 5.157a and Figure 5.157b.

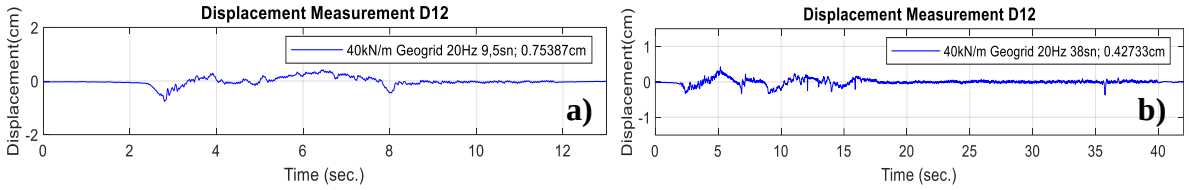

Figure 5.156. Displacement Response of D12, a) 20Hz 9.5s, b) 20Hz 38s.

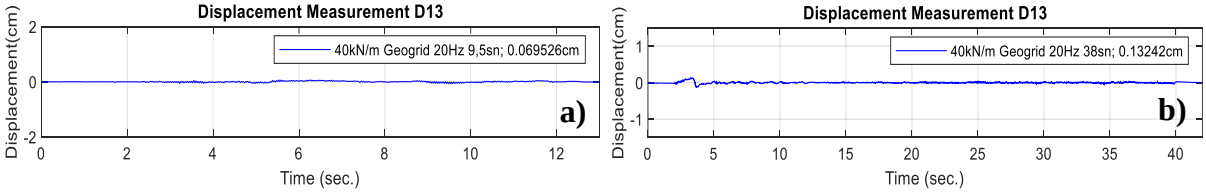

Figure 5.157. Displacement Response of D13, a) 20Hz 9.5s, b) 20Hz 38s.

5.3.4.3.5. Test Results for Geogrid Reinforced (Tult:40kN/m) Case under 30Hz

Applied input dynamic motion of 30Hz 9.5s has a peak acceleration value of 0.36g. Obtained results show that, the amplitude of transmitted accelerations increase within the embankment body is measured as 0.60g (A8) and 1.05g (A9) (Figure 5.158a). Fourier amplitudes reach to their peak at 30Hz. Spectral accelerations on the unreinforced embankment model in this case are obtained as 3.51g and 4.72g for A8 and A9, respectively. Structural periods are obtained as 0.03s (Figure 5.158a).

Given input dynamic motion of 30Hz 38s has a peak acceleration value of 0.34g. No significant differences are observed in measured accelerations in the foundation soil as acceleration values are around 0.46g. Obtained results show that, the amplitude of transmitted accelerations increase within the embankment body is measured as 0.59g (A8) and 1.04g (A9) (Figure 5.158b). Fourier amplitudes reach to their peak at 30Hz as expected. Spectral accelerations on the unreinforced embankment model in this case are obtained as 3.36g and 4.33g for A8 and A9, respectively. Structural periods are obtained as 0.03s (Figure 5.158b).

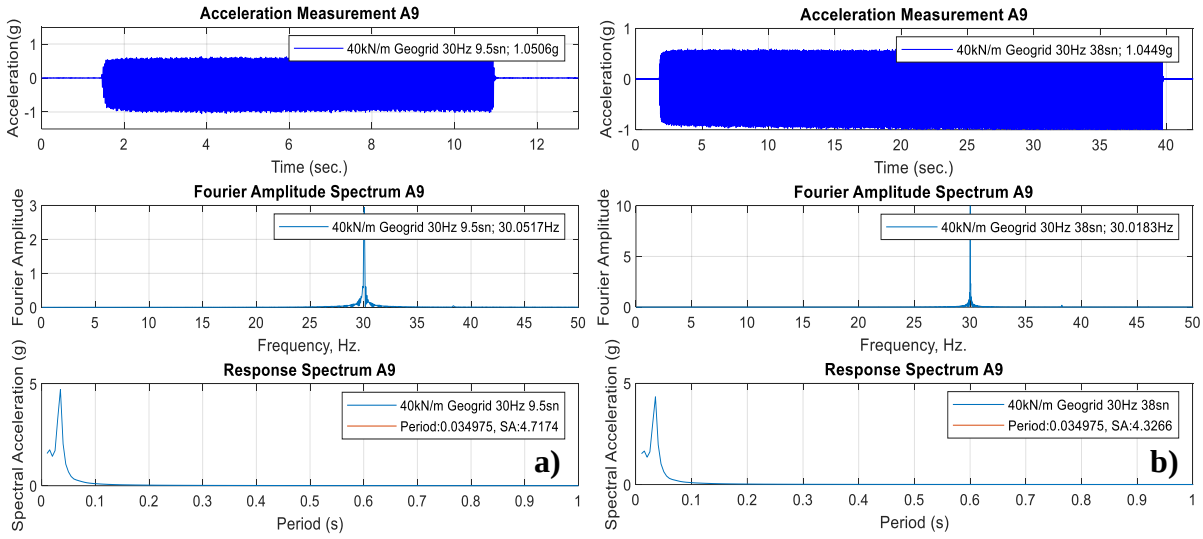

Figure 5.158. Acceleration Response of A9, a) 30Hz 9.5s, b) 30Hz 38s.

The crest of the embankment model (D12) displaces 32mm and 70mm horizontally under the 30Hz 9.5s and 30Hz 38s, respectively as given in Figure 5.159a and Figure 5.159b. Similarly, the crest of the embankment (D13) settles 21mm and 64mm vertically under the 30Hz 9.5s and 30Hz 38s, respectively as represented in Figure 5.160a and Figure 5.160b.

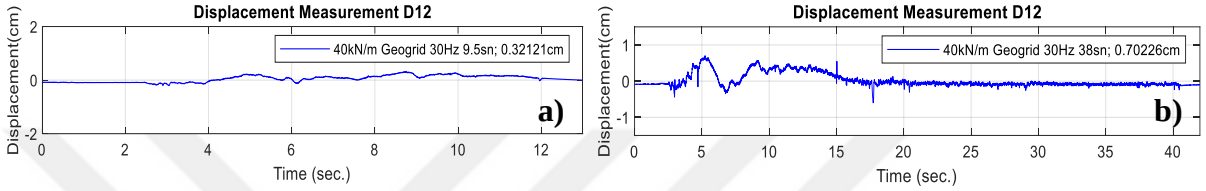

Figure 5.159. Displacement Response of D12, a) 30Hz 9.5s, b) 30Hz 38s.

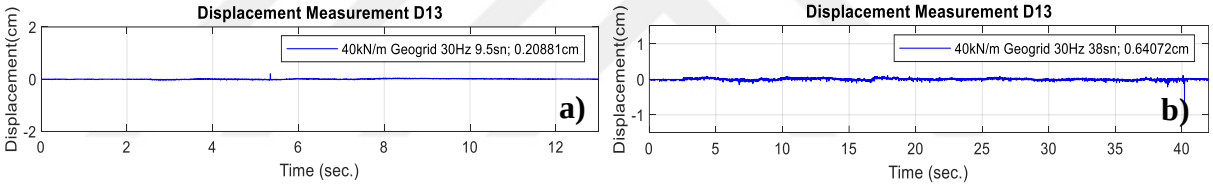

Figure 5.160. Displacement Response of D13, a) 30Hz 9.5s, b) 30Hz 38s.

5.3.4.4. Test Results for EPS Geofoam Case

Shaking table test results of the EPS geofoam embankment are represented in this section. Test results are represented as acceleration responses and displacement responses for the selected sensors of A9 and D12 and D13. A9 is placed five centimeters below the crest of the embankment. D12 measures the crest level displacements on the slope of the models and D13 is located to measure the vertical displacement (settlement) at the crest of the embankment models.

5.3.4.4.1. Test Results for EPS Geofoam Case under 1-30Hz

Given input dynamic motion of 1-30Hz 9.5s has a peak acceleration value of 0.30g. No significant differences are observed in measured accelerations in the foundation soil as accelerationn values are around 0.33g. Obtained results show that, the amplitude of transmitted accelerations increase within the EPS geofoam embankment is measured as 0.37g (A8) and 0.45g (A9) (Figure 5.161a). Fourier amplitudes reach to their peak at 28.6Hz. Spectral accelerations in this case are obtained as 3.47g and 4.11g for A8 and A9, respectively. Structural periods are obtained in the range of 0.03s and 0.04s (Figure 5.161a).

Peak acceleration value of the input motion 1-30Hz 38s is 0.29g for the current case. No significant differences are observed in measured accelerations in the foundation soil as acceleration values are around 0.32g. Obtained results show that, the amplitude of transmitted accelerations increase within the embankment body is measured as 0.36g on (A8) and 0.42g on (A9) (Figure 5.161b). Fourier amplitudes reach to their peak at 29.3Hz. Spectral accelerations in this case are obtained as 3.48g and 3.92g for A8 and A9, respectively. Structural periods are obtained as 0.03s and 0.04s for A8 and A9, respectively (Figure 5.161b).

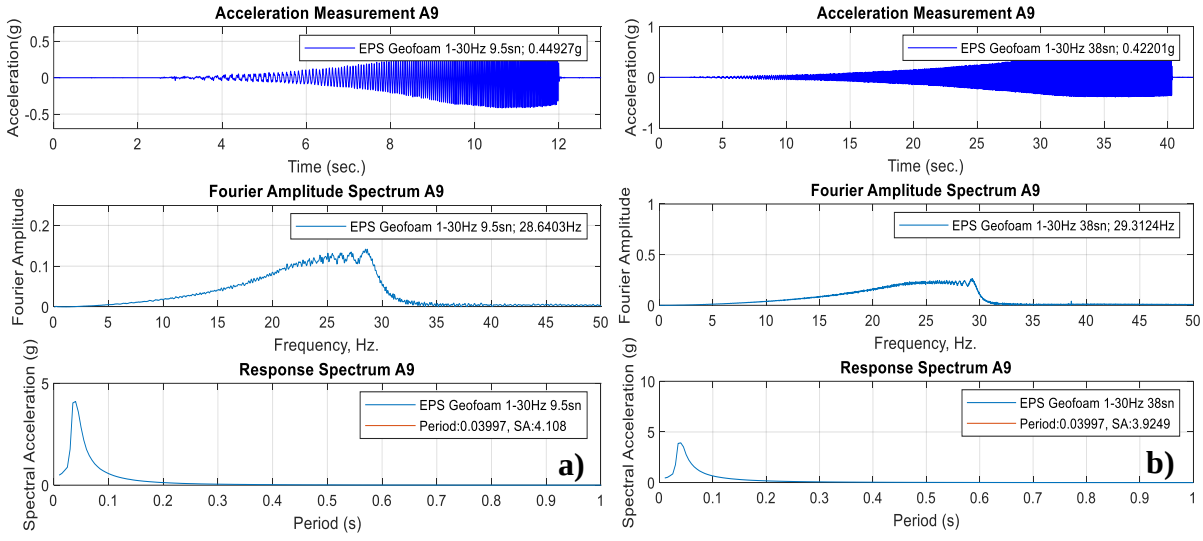

Figure 5.161. Acceleration Response of A9, a) 1-30Hz 9.5s, b) 1-30Hz 38s.

The crest of the embankment model (D12) displaces 29mm and 52mm horizontally under the 1-30Hz 9.5s and 1-30Hz 38s, respectively as given in Figure 5.162a and Figure 5.162b. Similarly, the crest of the embankment (D13) settles 6mm and 5mm vertically under the 1-30Hz 9.5s and 1-30Hz 38s, respectively as represented in Figure 5.163a and Figure 5.163b.

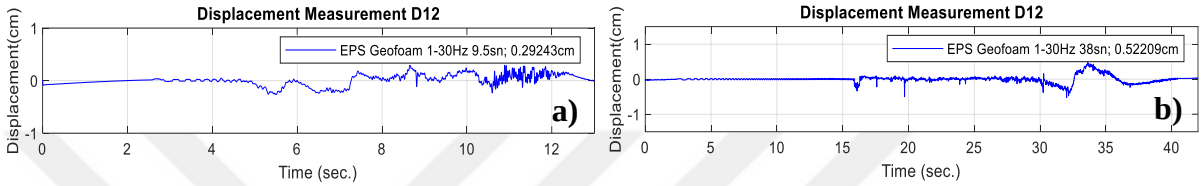

Figure 5.162. Displacement Response of D12, a) 1-30Hz 9.5s, b) 1-30Hz 38s.

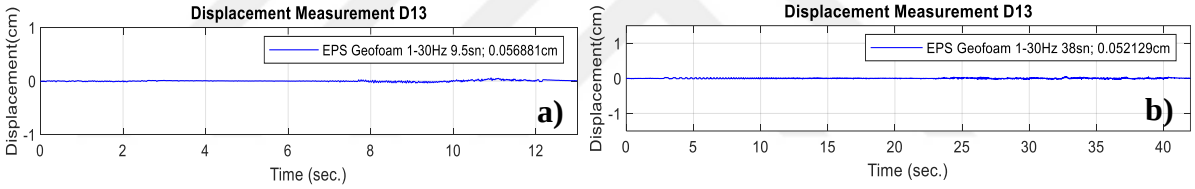

Figure 5.163. Displacement Response of D13, a) 1-30Hz 9.5s, b) 1-30Hz 38s.

Deformed shape of the EPS geofoam embankment model subjected to 1-30Hz-9.5s is shown in Figure 5.164.

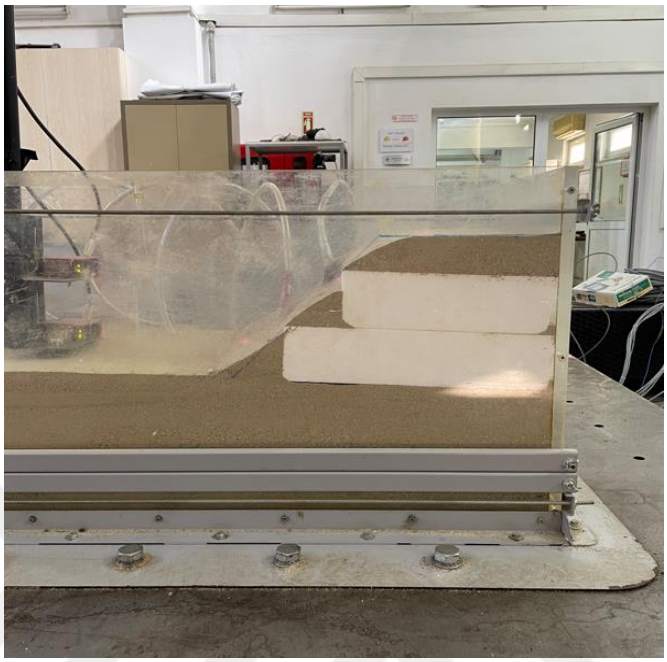

Figure 5.164. Deformed shape of the EPS geofoam embankment model subjected to 1-30Hz 9.5s.

5.3.4.4.2. Test Results for EPS Geofoam Case under 1-50Hz

Applied input dynamic motion of 1-50Hz 9.5s has a peak acceleration value of 0.54g. Obtained results show that, the amplitude of transmitted accelerations increase within the embankment body is measured as 0.98g (A8) and 1.04g (A9) (Figure 5.165a). Fourier amplitudes reach to their peak at 41.9Hz. Spectral accelerations on the unreinforced embankment model in this case are obtained 8.29g and 8.30g for A8 and A9, respectively. Structural period is obtained as 0.02s (Figure 5.165a).

The input dynamic motion of 1-50Hz 38s has a peak acceleration value of 0.50g. Obtained results show that, the amplitude of transmitted accelerations increase within the embankment body is measured as 1.04g (A8) and 1.01g (A9) (Figure 5.165b). Fourier amplitudes reach to their peak at 42.7Hz. Spectral accelerations on the unreinforced

embankment model in this case are obtained as 7.80g and 7.90g for A8 and A9, respectively. Structural period is obtained as 0.03s (Figure 5.165b).

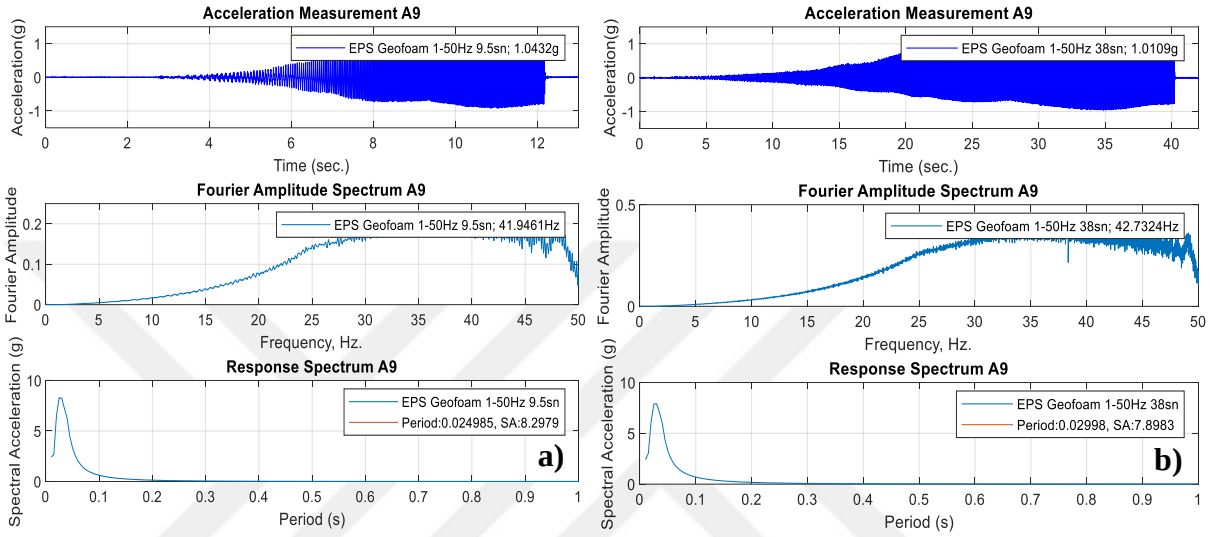

Figure 5.165. Acceleration Response of A9, a) 1-50Hz 9.5s, b) 1-50Hz 38s.

The crest of the embankment model (D12) displaces 1.04cm and 1.26cm horizontally under the 1-50Hz 9.5s and 1-50Hz 38s, respectively as given in Figure 5.166a and Figure 5.166b. Similarly, the crest of the embankment (D13) settles 15mm and 21mm vertically under the 1-50Hz 9.5s and 1-50Hz 38s, respectively as represented in Figure 5.167a and Figure 5.167b.

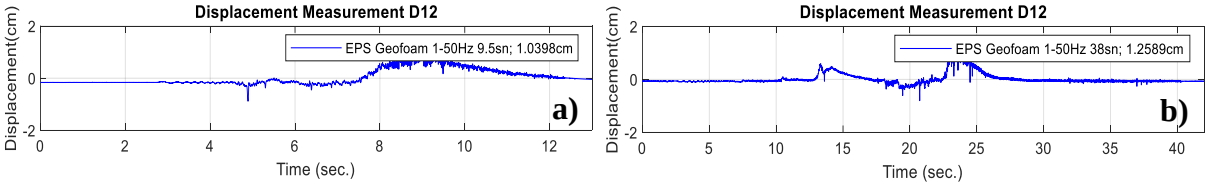

Figure 5.166. Displacement Response of D12, a) 1-50Hz 9.5s, b) 1-50Hz 38s.

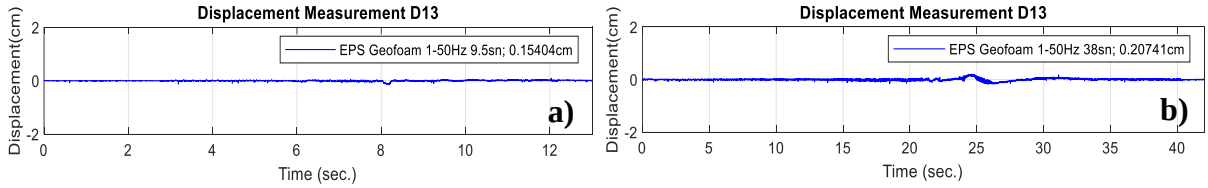

Figure 5.167. Displacement Response of D13, a) 1-50Hz 9.5s, b) 1-50Hz 38s.

Deformed shape of the EPS geofoam embankment model subjected to 1-50Hz-38s is shown in Figure 5.168.

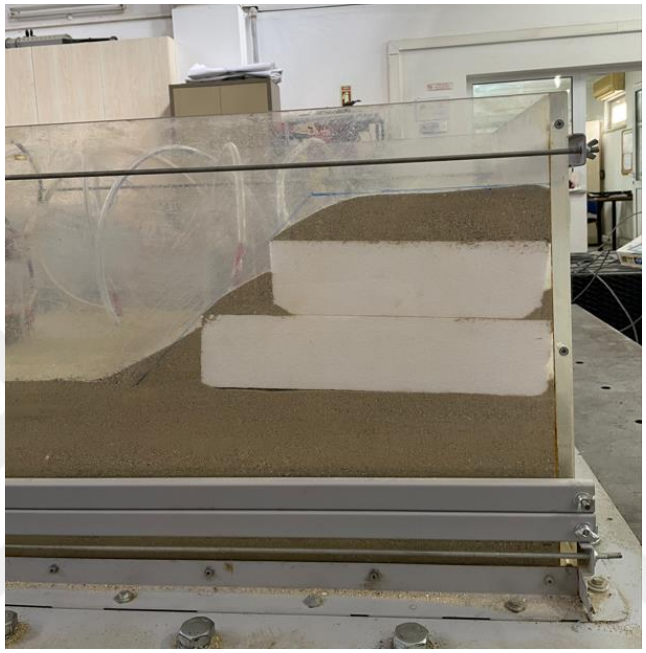

Figure 5.168. Deformed shape of the EPS geofoam embankment model subjected to 1-30Hz 9.5s.

5.3.4.4.3. Test Results for EPS Geofoam Case under 10Hz

Applied input dynamic motion of 10Hz 9.5s has a peak acceleration value of 0.35g and the accelerometers located at the same height in the foundation layer (A3-A6) also measures approximately 0.35g. The amplitude of transmitted accelerations increase within the embankment body is measured as 0.35g (A8) and 0.36g (A9) (Figure 5.169a). Fourier amplitudes reach to their peak at 10Hz as expected. Spectral accelerations on the unreinforced embankment model in this case are obtained as 3.55g and 3.64g for A8 and A9, respectively. Structural periods are obtained as 0.1s (Figure 5.169a).

Peak acceleration value of the input 10Hz 38s is 0.35g for the given case and the accelerometers in the foundation soil also measure approximately the same acceleration. Transmitted accelerations increase slightly due to the increased height of the embankment and reach 0.36g (A9) (Figure 5.169b). Fourier amplitudes reach to their peak at 10Hz. Spectral accelerations on the unreinforced embankment model in this case are obtained as 3.56g and 3.64g for A8 and A9, respectively. Structural periods are obtained as 0.1s (Figure 5.169b).

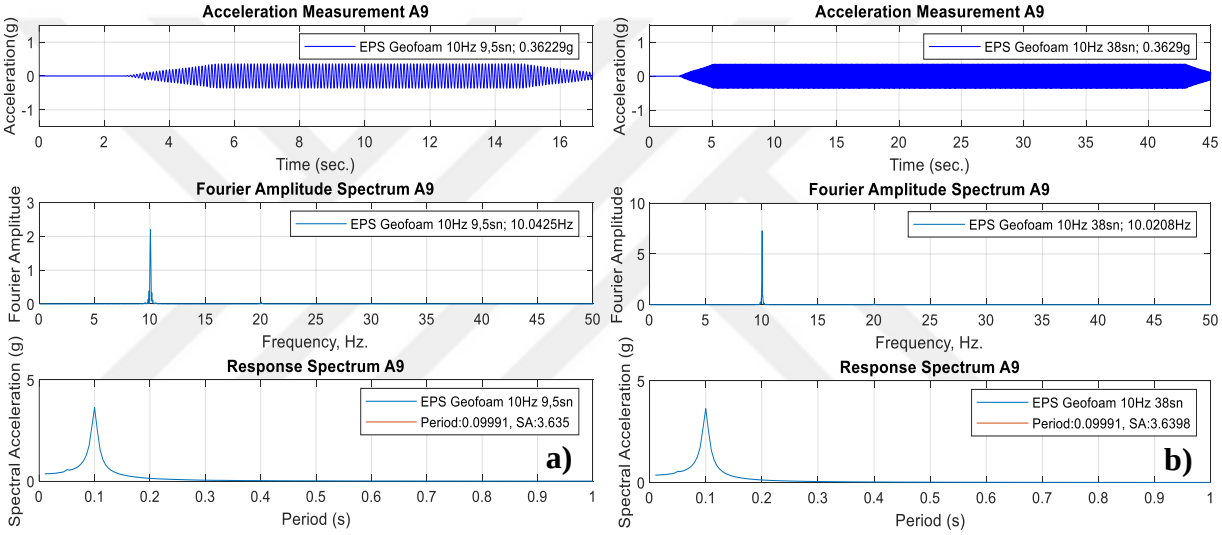

Figure 5.169. Acceleration Response of A9, a) 10Hz 9.5s, b) 10Hz 38s.

The crest of the EPS geofoam embankment model (D12) displaces 83mm and 27mm horizontally under the 10Hz 9.5s and 10Hz 38s, respectively as given in Figure 5.170a and Figure 5.170b. Similarly, the crest of the embankment (D13) settles 3mm and 4mm vertically under the 10Hz 9.5s and 10Hz 38s, respectively as represented in Figure 5.171a and Figure 5.171b.

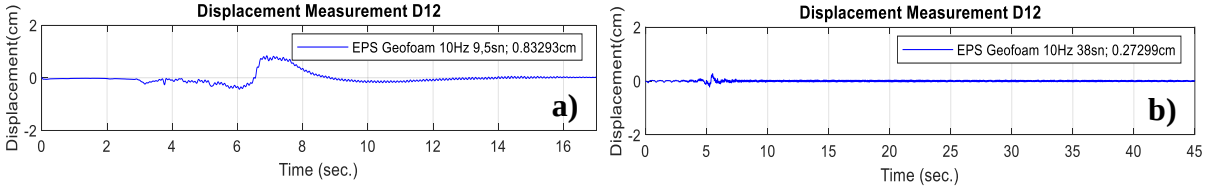

Figure 5.170. Displacement Response of D12, a) 10Hz 9.5s, b) 10Hz 38s.

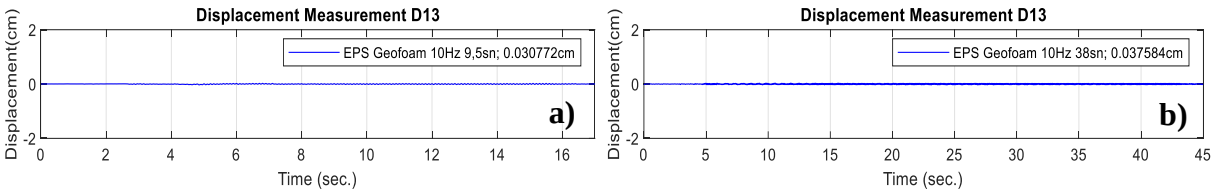

Figure 5.171. Displacement Response of D13, a) 10Hz 9.5s, b) 10Hz 38s.

5.3.4.4.4. Test Results for EPS Geofoam Case under 20Hz

Input acceleration is 0.46g for the 20Hz 9.5s motion and the measurement of accelerometers in the foundation soil are in the range of 0.49g to 0.51g. Transmitted accelerations increase slightly due to the increased height of the embankment and reach 0.53g (A8) and 0.59g (A9) (Figure 5.172a). Fourier amplitudes reach to their peak at 20Hz as expected. Spectral accelerations on the unreinforced embankment model in this case are obtained as 5.15g and 5.61g for A8 and A9, respectively. Structural periods are obtained as 0.05s (Figure 5.172a).

Applied input dynamic motion of 20Hz 38s has a peak acceleration value of 0.42g and the accelerometers located at the same height in the foundation layer (A3-A6) measures approximately 0.44g. The amplitude of transmitted accelerations increase within the embankment body is measured as 0.49g (A8) and 0.54g (A9). (Figure 5.172b). Fourier amplitudes reach to their peak at 20Hz. Spectral accelerations on the unreinforced embankment model in this case are obtained as 4.69g and 5.13g for A8 and A9, respectively. Structural periods are obtained as 0.05s (Figure 5.172b).

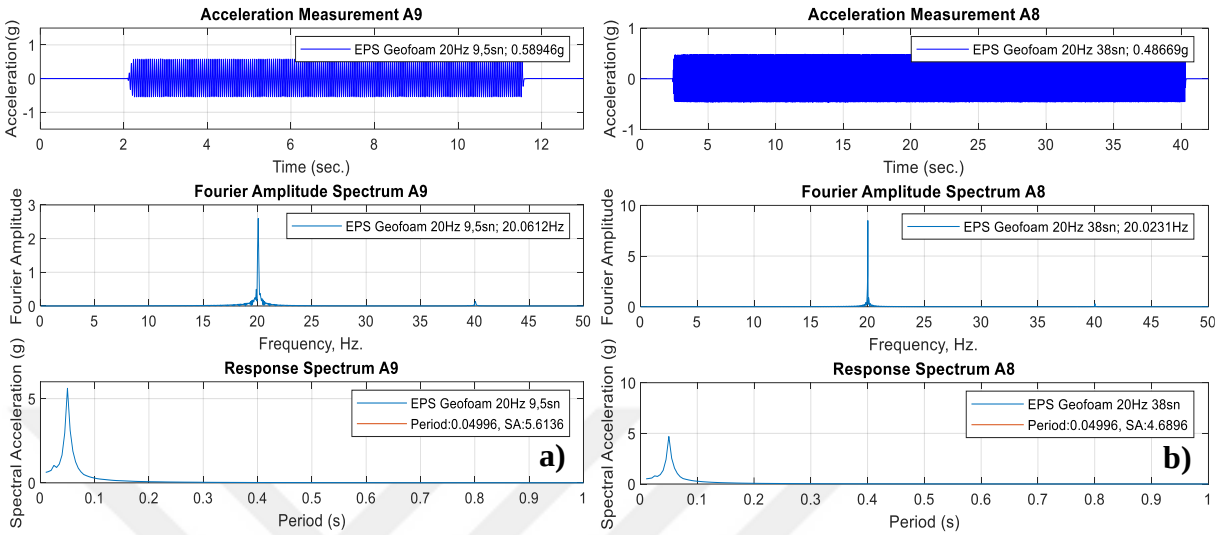

Figure 5.172. Acceleration Response of A9, a) 20Hz 9.5s, b) 20Hz 38s.

The crest of the EPS geofoam embankment model (D12) displaces 69mm and 33mm horizontally under the 20Hz 9.5s and 20Hz 38s, respectively as given in Figure 5.173a and Figure 5.173b. Similarly, the crest of the embankment (D13) settles 5mm vertically under the 20Hz 9.5s and 20Hz 38s, respectively as represented in Figure 5.174a and Figure 5.174b.

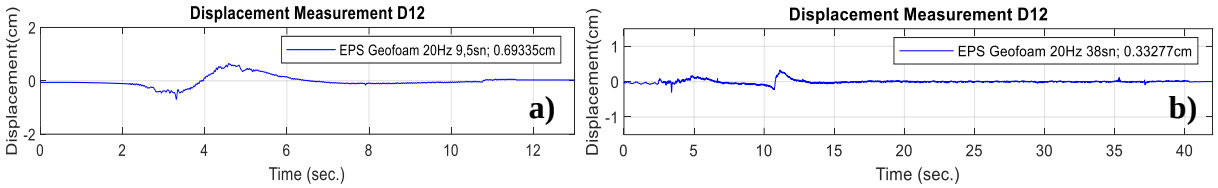

Figure 5.173. Displacement Response of D12, a) 20Hz 9.5s, b) 20Hz 38s.

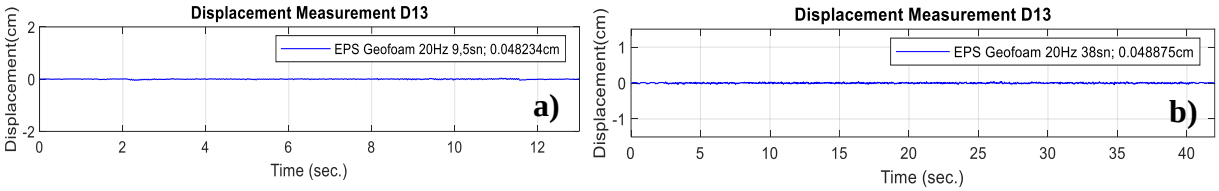

Figure 5.174. Displacement Response of D13, a) 20Hz 9.5s, b) 20Hz 38s.

5.3.4.4.5. Test Results for EPS Geofoam Case under 30Hz

The input dynamic motion of 30Hz 9.5s has a peak acceleration value of 0.36g. Obtained results show that, the amplitude of transmitted accelerations increase within the embankment body is measured as 0.62g (A8) and 0.93g (A9) (Figure 5.175a). Fourier amplitudes reach to their peak at 30Hz. Spectral accelerations on the unreinforced embankment model in this case are obtained as 3.32g and 4.26g for A8 and A9, respectively. Structural periods are obtained as 0.03s (Figure 5.175a).

Given input dynamic motion of 30Hz 38s has a peak acceleration value of 0.34g. No significant differences are observed in measured accelerations in the foundation soil as acceleration values are around 0.44g. Obtained results show that, the amplitude of transmitted accelerations increase within the embankment body is measured as 0.59g (A8) and 1.04g (A9). (Figure 5.175b). Fourier amplitudes reach to their peak at 30Hz as expected. Spectral accelerations on the unreinforced embankment model in this case are obtained as 3.18g and 4.28g for A8 and A9, respectively. Structural periods are obtained as 0.03s (Figure 5.175b).

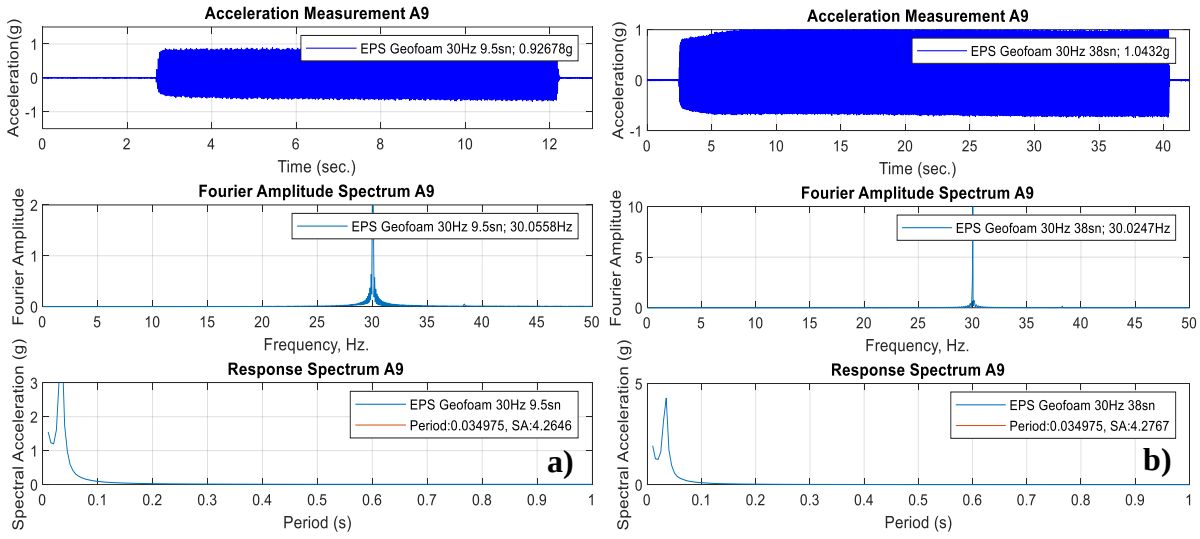

Figure 5.175. Acceleration Response of A9, a) 30Hz 9.5s, b) 30Hz 38s.

The crest of the EPS geofoam embankment model (D12) displaces 96mm and 69mm horizontally under the 30Hz 9.5s and 30Hz 38s, respectively as given in Figure 5.176a and Figure 5.176b. Similarly, the crest of the embankment (D13) settles 14mm and 31mm vertically under the 30Hz 9.5s and 30Hz 38s, respectively as represented in Figure 5.177a and Figure 5.177b.

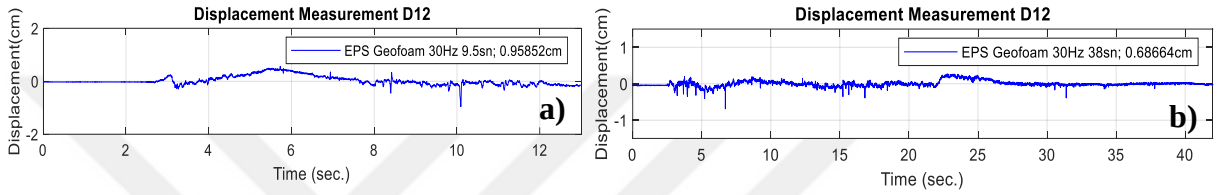

Figure 5.176. Displacement Response D12, a) 30Hz 9.5s, b) 30Hz 38s.

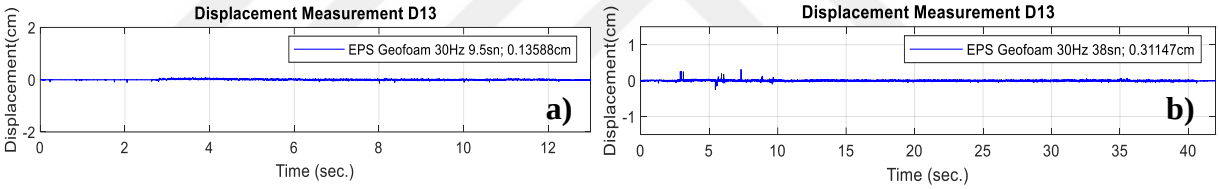

Figure 5.177. Displacement Response of D13, a) 30Hz 9.5s, b) 30Hz 38s.

6. DISCUSSIONS ON SEISMIC PERFORMANCE OF EMBANKMENT MODELS

Obtained experimental results from shaking table experiments and seismic performance tests of full scale field tests are further evaluated in this section of the thesis.

6.1. Shaking Table Tests

Shaking table experiments were performed as a 1/10 reduced scale simulation of the full-scale seismic performance tests with MSS on field conditions. Reduced scale unreinforced highway embankment model, geogrid reinforced highway embankment model and EPS geofoam highway embankment model were subjected to dynamic motions with different characteristics as 10Hz 9.5s, 10Hz 38s, 20Hz 9.5s, 20Hz 38s, 30Hz 9.5s, 30Hz 38s, 1-30Hz 9.5s, 1-30Hz 38s, 1-50Hz 9.5s and 1-50Hz 38s. Performance indicators defined for the discussion part are acceleration and displacement responses and seismic demand.

6.1.1. Effects of Geogrid Reinforcement on Seismic Response of Embankment Models

Shaking table test results with all details are given for unreinforced embankment model in Section 5.3.4.1 and for geogrid reinforced embankment model (T_{ult}:20kN/m) in Section 5.3.4.2. Comparison of the seismic performances of unreinforced and geogrid reinforced embankment model (T_{ult}:20kN/m) in terms of transmitted accelerations clearly show that effect of geogrid reinforcement is highly dependent on the input dynamic motion. When the obtained shaking table results provided in abovementioned sections are compared, it is seen that geogrid reinforced embankment model perform much better in terms of dynamic performance when subjected to incremental sine sweep excitations instead of fixed frequency input motions. Transmitted accelerations are up to 24.4% and 10.9% (A8) less in geogrid reinforced embankment model under 1-50Hz and 1-30Hz sine sweep excitations in comparison with the unreinforced case. Initial and after test conditions of the URE subjected to 1-50Hz 38s is given in Figure 6.1.



Figure 6.1. a) Initial conditions of URE, b) Deformed shape of the URE subjected to 1-50Hz 38s of motion.

Given in Figure 6.1, URE suffered from excessive horizontal and vertical displacements during shaking table tests. URE experienced up to 1.4cm of horizontal displacement and almost 1cm of settlement under 1-50Hz 38s of motion. Failure surface is deep and extends through the embankment body regardless the dynamic motion (Figure 6.1).

Tensile strength of the geogrid reinforcement layers significantly reduces the displacements on the embankment model. Shaking table test results indicate that horizontal displacements measured from the toe (D11) and the crest (D12) of the geogrid reinforced embankment model with T_{ult}:20kN/m are 73.1% and 86.2% less, respectively when compared to unreinforced model. Similarly, vertical displacements (settlements) at crest level (D13) are 83.6% less. Slip surfaces are usually shallow to very shallow due to the provided tensile strength (Figure 6.1). The effect of geogrid reinforcement is best achieved under 10Hz of excitation

(Figure 6.2) and 1-50Hz sine sweep. Due to the resonance phenomenon, measured displacements tend to increase especially under 30Hz of excitation. Duration of the dynamic excitations has a direct influence on measured displacements as expected. However, the effect of duration on geogrid efficiency is not observed.



Figure 6.2. a) Initial conditions of GRE, b) Deformed shape of the geogrid reinforced embankment model (T_{ult}:20kN/m) under 10Hz 9.5s of motion.

The efficiency of geogrid reinforcement on Spectral Acceleration (SA) values is best observed under incremental sine sweep excitations especially under 1-50Hz dynamic motion. Due to the A8 and A9, SA values are 13.3% and 10.7% less in geogrid reinforced model compared to unreinforced case. In addition, the efficiency of geogrid reinforcement in terms of period shift effect is also observed. Structural period at crest level shifts from 0.02s to 0.03s under 1-50Hz input excitation.

Figure 6.3 represents the acceleration measurements at the toe (A8), where the effect of geogrid reinforcement is clearly observed, for URE and GRE with T_{ult}:20kN/m under 1-50Hz 38s of motion. Also Figure 6.4 represents the horizontal displacement measurement at crest

(D12) for URE and GRE with T_{ult}:20kN/m under 10Hz 38s of motion where the effect of geogrid reinforcement can be seen.

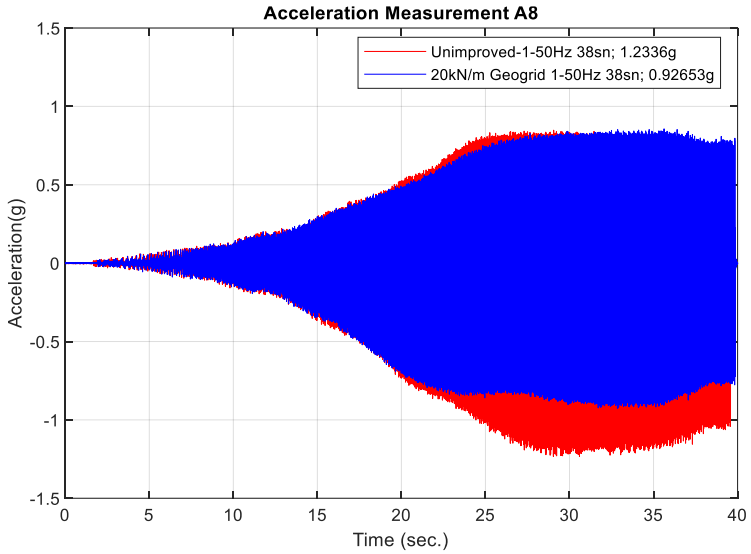

Figure 6.3. Comparison of the Transmitted Accelerations at toe (A8) for Unreinforced and T_{ult}:20kN/m Geogrid Reinforced Models under 1-50Hz 38s of motion.

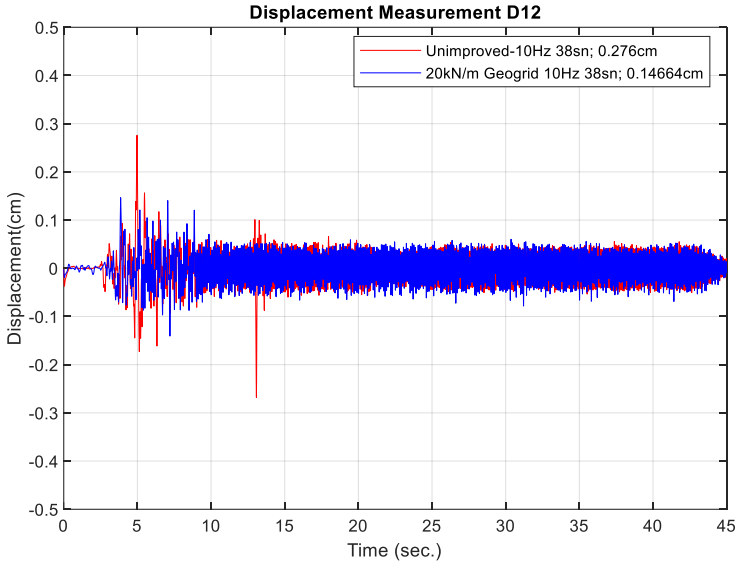

Figure 6.4. Comparison of the Horizontal Displacements at D12 for Unreinforced and Tult:20kN/m Geogrid Reinforced Models under 10Hz-38s of motion.

Evaluation of the seismic performances of unreinforced and geogrid reinforced embankment models (T_{ult}:40kN/m) in terms of transmitted accelerations also indicate that geogrid reinforcement efficiency depends on the input dynamic motion. Results show one more time that geogrid reinforced embankment model perform much better in terms of dynamic performance when subjected to incremental sine sweep excitations instead of fixed frequency input motions. Transmitted accelerations measured at toe and at crest are 39.8% (A8) and 33.6% (A9) less in geogrid reinforced embankment model under 1-50Hz sine sweep excitations in comparison with the unreinforced case. As a result of the resonance phenomenon is observed during experiments with fixed frequency motions especially for the 20Hz and 30Hz input cases, obtained results are unable to reveal the effect of reinforcement. Instead, the transmitted accelerations in geogrid reinforced model are up to 25% higher under 30Hz input motion.

The provided additional tensile strength by the geogrid reinforcement successfully reduces the measured displacements on the embankment model. Experimental results show that horizontal displacements measured from the toe (D11) and the crest (D12) of the geogrid reinforced embankment model T_{ult}:40kN/m are 74.6% and 87.2% less, respectively when compared to unreinforced model. Similarly, vertical displacements (settlements) at crest level (D13) are 83.6% less. The effect of geogrid reinforcement is best achieved under 10Hz of excitation and 1-50Hz sine sweep. Due to the resonance phenomenon, measured displacements tend to increase especially under 30Hz of excitation. Duration of the input motions directly affect the measured displacements. However, no effect of duration on geogrid efficiency is inferred due to the obtained results.

The efficiency of geogrid reinforcement on Spectral Acceleration (SA) values is best observed under incremental sine sweep excitations especially under 1-50Hz dynamic motion SA values are 13.2% (A8) and 4% (A9) less in geogrid reinforced model compared to unreinforced case. Comparison of the Transmitted Accelerations at toe (A8) for Unreinforced and T_{ult}:40kN/m Geogrid Reinforced Models under 1-50Hz-38s of motion is given in Figure 6.5.

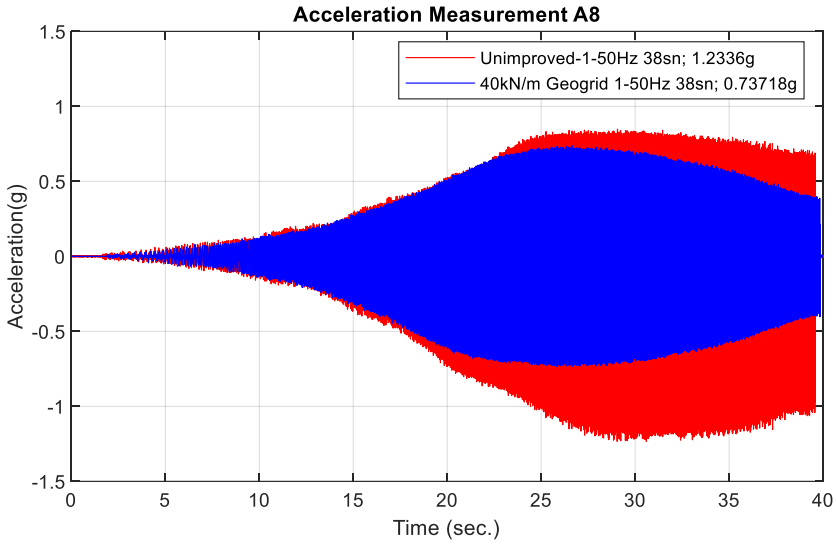

Figure 6.5. Comparison of the Transmitted Accelerations at toe (A8) for Unreinforced and T_{ult}:40kN/m Geogrid Reinforced Models under 1-50Hz-38s of motion.

In addition, the efficiency of geogrid reinforcement in terms of period shift effect is also observed. Structural periods within the embankment shifts from 0.02s to 0.03s under 1-50Hz input excitation. This is due to the fact that the friction and interlocking between the geogrid and the surrounding soil layer and as the soil deforms, this interaction helps dissipate energy. Seismic demand reduction due to the geogrid reinforcement (13.3%) is represented in Figure 6.6 at toe (A8).

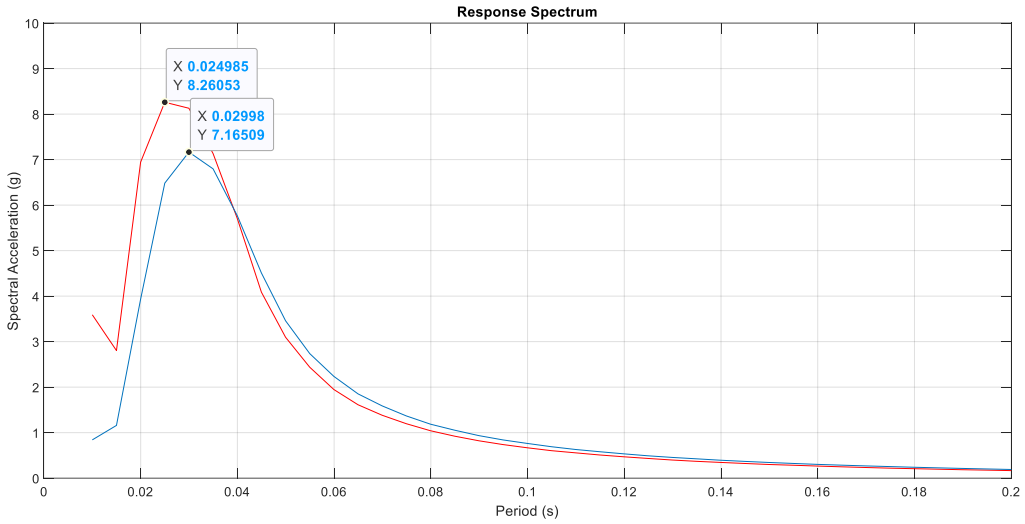

Figure 6.6. Seismic Demand Reduction on T_{ult}:40kN/m Geogrid Reinforced Model Compared to Unreinforced Model at toe (A8) under 1-50Hz-38s of motion.

6.1.2. Effects of Geofoam Fill on Seismic Response of Embankment Models

Superior material properties of EPS geofoam significantly reduce the resultant displacements throughout the experimental study. Horizontal displacements obtained from the toe (D11) and the crest (D12) of the geogrid reinforced embankment model are 71.6% and 75.2% less to that of the unreinforced model. Similarly, vertical displacements (settlements) at crest level (D13) are 78.3% less. Represented in Figure 6.7, EGE models remain very stable with very shallow sliding deformation on the slope of the embankment and no deformation on the embankment body. EPS geofoam significantly reduces displacements in highway embankments due to its low density and its high compressibility, which absorbs energy from dynamic loads. It reduces stress on foundation soils, limits settlement, and offers strong resistance to deformation which contribute to enhanced stability and minimal displacement under various dynamic motions.

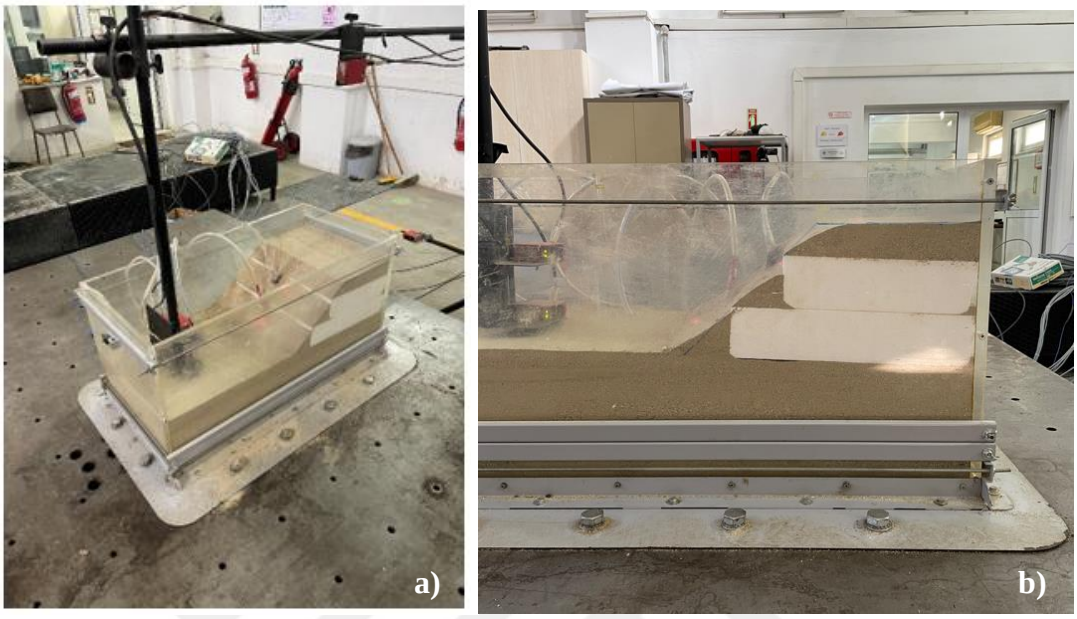

Figure 6.7. a) Initial conditions of EGE, b) Deformed shape of the EGE subjected to 1-30Hz 9.5s of motion.

The effect of lightweight EPS geofoam material is best achieved under incremental sine sweeps and 10Hz of excitation. It is also inferred from the results that the effect of resonance phenomenon is almost compensated in terms of displacements. Duration of the dynamic excitation is found to be related with measured displacements as expected. However, no direct influence of duration on dynamic behavior of the EPS geofoam embankment is found due to the tabulated results.

Comparison of the dynamic performances of unreinforced and EPS Geofoam embankment models in terms of transmitted accelerations clearly show that the dynamic performance of lightweight EPS geofoam is highly dependent on the frequency content of the input dynamic motion. Similar to other cases, EPS embankment model performs much better in terms of dynamic performance when subjected to incremental sine sweep excitations instead of fixed frequency input motions. Transmitted accelerations measured at toe and at crest are 21% (A8) and 29.4% (A9) less in EPS geofoam embankment model under 1-50Hz sine sweep

excitations in comparison with the unreinforced case. Figure 6.8 represents the comparison of the transmitted accelerations at toe (A9) for URE and EGE under 1-50Hz 38s of motion.

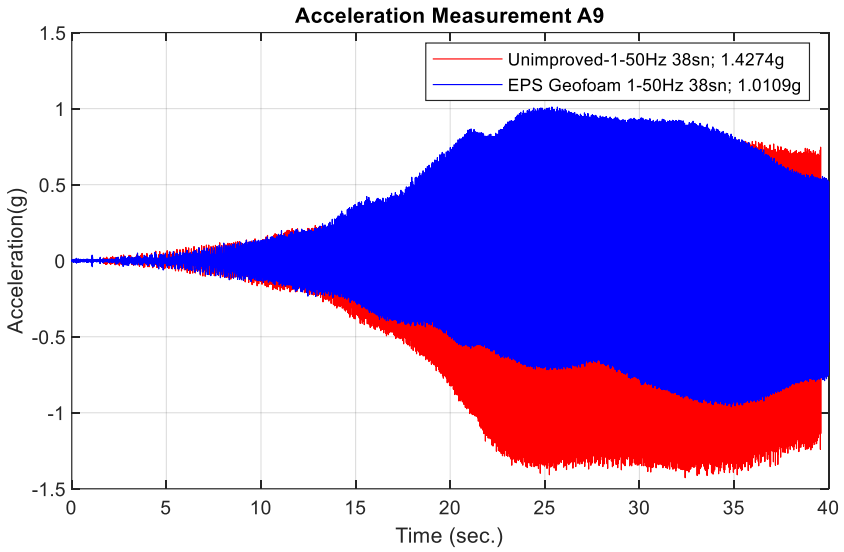

Figure 6.8. Comparison of the Transmitted Accelerations at Crest for Unreinforced and EPS Geofoam Models under 1-50Hz-38s of motion.

The efficiency EPS geofoam on Spectral Acceleration (SA) values can be seen under all given dynamic motions of this study. However, SA reduction is best observed under incremental sine sweep excitations especially under 1-30Hz dynamic motion. SA value is 20% less at toe (A8) in EPS geofoam model compared to unreinforced embankment case. Also, the efficiency of geogrid reinforcement in terms of period shift effect is also achieved. Structural period at crest level shifts from 0.02s to 0.03s under 1-50Hz input excitation and from 0.03s to 0.04s under 1-30Hz of excitation.

6.1.3. Discussions on the Effect of Geogrid Tensile Strength on Seismic Performance

The effect of geogrid strength has also been investigated through shaking table experiments in this study. The variation of amplification factors (AF) obtained with respect to

relative height for unreinforced, T_{ult}: 20kN/m geogrid reinforced and T_{ult}:40kN/m reinforced embankment models is represented in Figure 6.9 for A6, A7, A8 and A9 under the dynamic input motion of 1-50Hz 38s of motion which clearly reflects the effect of tensile strength in terms of AF. Similar results were achieved from the other input motions as well.

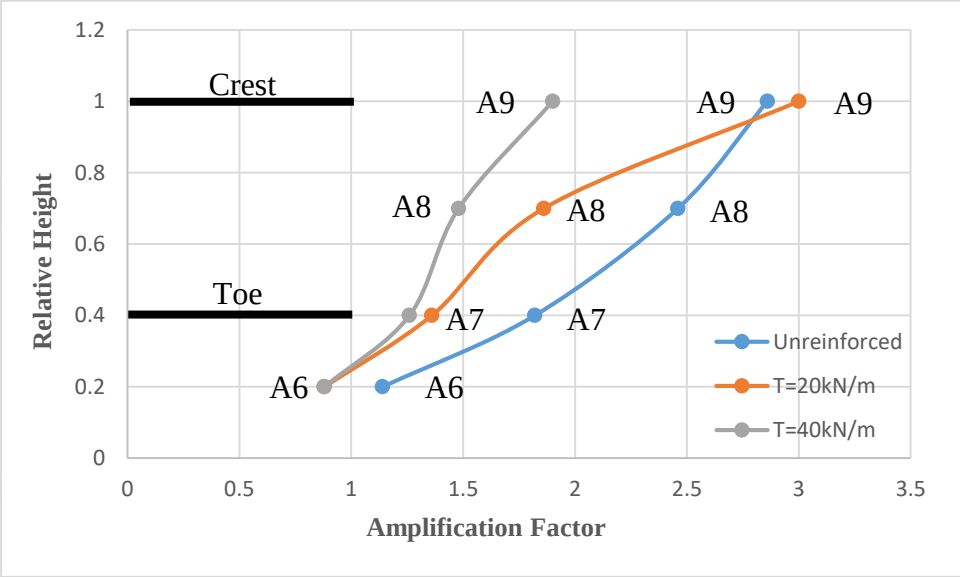

Figure 6.9. Variation of Amplification Factors with Respect to Relative Height under 1-50Hz 38s of motion for URE, GRE (T_{ult} :20kN/m) and GRE (T_{ult} :40kN/m).

As represented in Figure 6.9, performing 1/10 reduced scale experiments, obtained results by means of selected dynamic performance indicators are similar between geogrid reinforced embankment models with two different geogrid strength. However, the embankment model with a tensile strength of T_{ult}: 40kN/m exhibits a better dynamic performance (less AF values) than the embankment model with a tensile strength of T_{ult}: 20kN/m, which is an expected result due to the relatively increased strength of the embankment model. The effect of geogrid reinforcement is visible even in the foundation soil (A6). As can be inferred from Figure 6.9, calculated AF values in the foundation soil (A6) for GRE models with T_{ult}: 20kN/m and T_{ult}: 40kN/m are 0.88 (de-amplification) whereas the calculated AF value for URE is 1.14 under the proposed input motion. Amplification factors increase due to relative height of the embankment models. AF values are higher in unreinforced model than other two geogrid

reinforced models (Figure 6.9). Due to the addition of tensile strength to the system and the resultant soil-geogrid interaction, the degree of AF values decreases with increased geogrid tensile strength. The soil-geogrid interaction resists the horizontal displacements, distributes the dynamic loads along the embankments more uniformly and the interlocking between soil and geogrid layers increases the shear resistance which reduces the AF values. At toe level, AF values are 25% and 31% less in GRE model with T_{ult}: 20kN/m and GRE model with T_{ult}: 40kN/m, respectively. Similarly at crest level, AF values are 39% less in GRE model with T_{ult}: 40kN/m. This is due to the fact that, geogrid with higher tensile strength can resist higher horizontal forces generated by seismic or dynamic loads. This resistance reduces the tendency of soil to displace and concurrently reduces the calculated AF values. Meanwhile, as given in Figure 6.9, the calculated AF value for GRE model with T_{ult}: 20kN/m at crest (A9) is slightly higher than the unreinforced case, which is probably a measurement error.

6.1.4. Discussions on Normalized Accelerations and Displacements of All Embankment Models

Evaluation of the experimental results by means of normalized accelerations and displacements are given in this section. Normalized Accelerations are calculated based on the data from toe (A8) and crest (A9) under 1-50Hz 38s of motion, the input motion of which the efficiency of geogrid reinforcement (section 5.3.4.2.4 and section 5.3.4.3.4) and lightweight EPS geofoam inclusion (section 5.3.4.4.4) is best observed. Similarly, Normalized Displacements are calculated based on the data from crest (D12 horizontal and D13 vertical) under 10Hz 38s of motion, the input motion of which the efficiency of geogrid reinforcement (section 5.3.4.2.6 and section 5.3.4.3.6) and lightweight EPS geofoam inclusion (section 5.3.4.4.6) is best observed in terms of displacements. The variation of normalized acceleration at crest and toe is given in Figure 6.10.

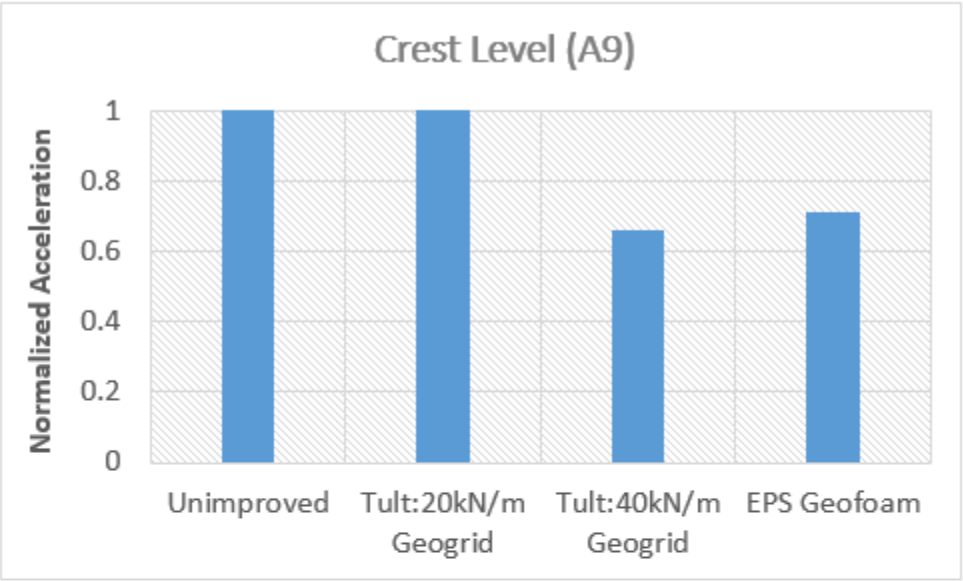

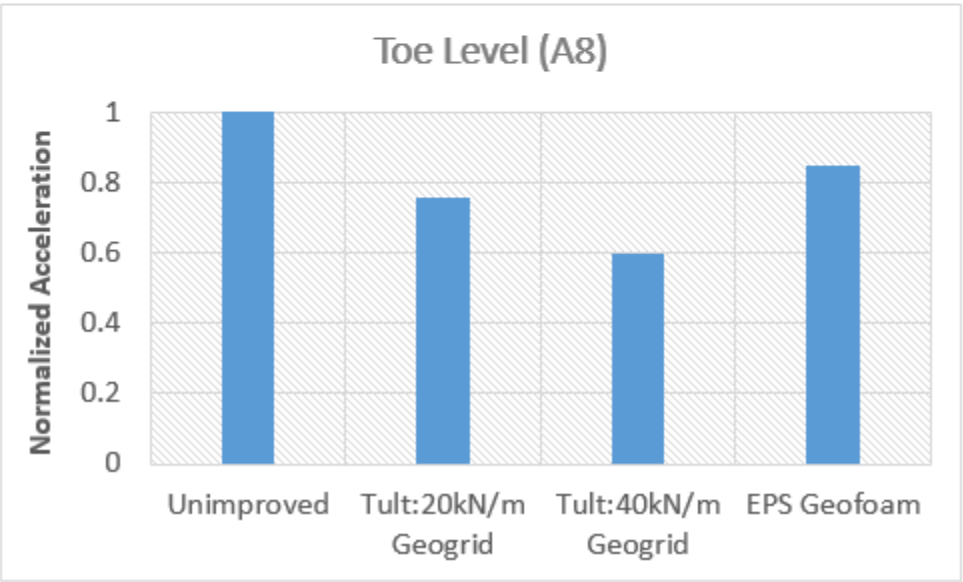

Figure 6.10. The variation of normalized acceleration at crest (A9) and toe (A8) under 1-50Hz 38s of motion.

As shown in Figure 6.10, crest level acceleration in geogrid reinforcement with T_{ult}: 20kN/m does not decrease when compared to unreinforced case. On the other hand, up to 34% normalized acceleration reduction is calculated in geogrid reinforced embankment model with T_{ult}: 40kN/m. Crest level normalized accelerations are 29% less in lightweight EPS geofoam

embankment model in comparison with the unreinforced case. This is probably due to the fact that EPS geofoam material is better at absorbing higher frequency dynamic forces than geogrid material and vice versa. Thus, GRE performed better than URE under given dynamic motion. Also, normalized accelerations are 24% and 40% less in geogrid reinforced embankment models with T_{ult}: 20kN/m and T_{ult}: 40kN/m, respectively in comparison with the unreinforced case (Figure 6.10). Increased tensile strength improved the seismic performance of the GRE as expected. Calculated normalized acceleration reduction ratio for EPS geofoam embankment model is limited to 15%. As mentioned, geogrid material typically perform better in terms of mitigation of transmitted accelerations under low-frequency motions than EPS geofoam due to its interlocking effect with the surrounding soil. The variation of normalized horizontal displacements at crest level is represented for all models in Figure 6.11.

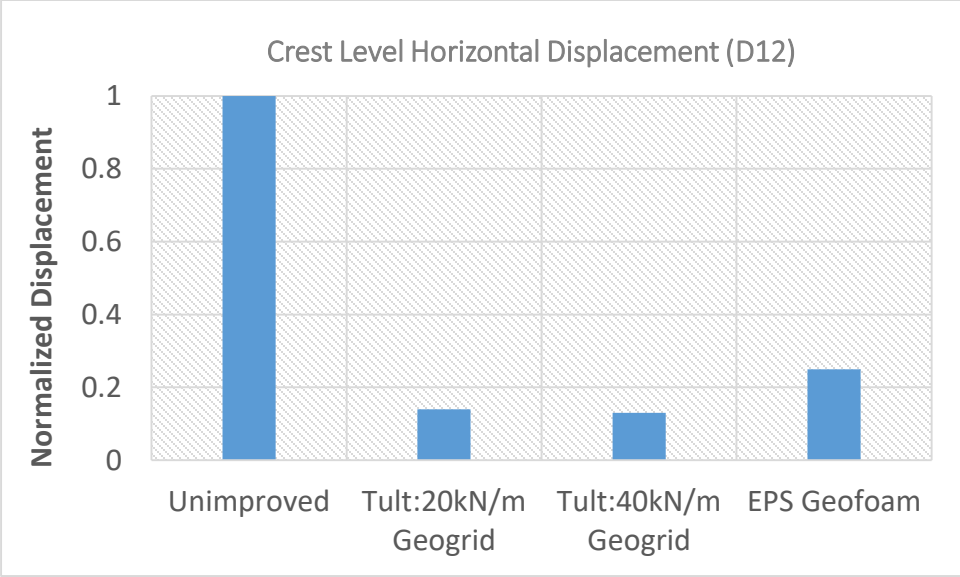

Figure 6.11. The variation of normalized horizontal displacement at crest (D12) under 10Hz 38s of motion.

As can be inferred from the Figure 6.11, crest level normalized horizontal displacements are reduced by 86% and %87 in geogrid reinforced embankment models with T_{ult}: 20kN/m and T_{ult}: 40kN/m, respectively. It is seen that geogrid reinforcement layers provide the required

additional tensile strength to withstand the induced displacements. In addition, the calculated reduction ratio in normalized displacements is found to be 75% in EPS geofoam embankment model. Similar results were achieved with other input motions as well but the reduction of normalized horizontal displacements is higher for the given motion. The variation of normalized vertical displacements at crest level is represented for all embankment models in Figure 6.12.

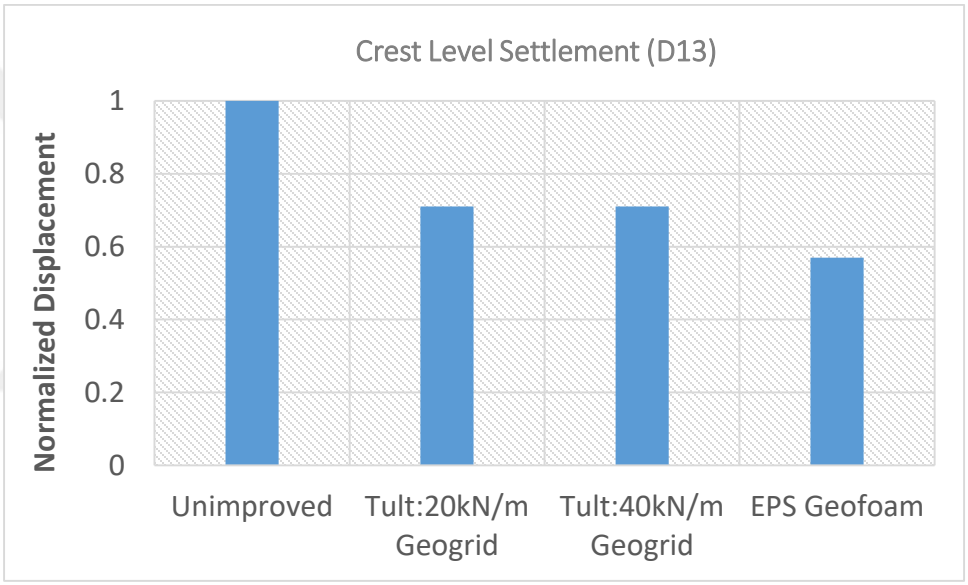

Figure 6.12. The variation of normalized vertical displacement at crest (D13) under 10Hz 38s of motion.

As can be inferred from Figure 6.12, normalized vertical displacements at crest level clearly show the effectiveness of EPS geofoam inclusions in mitigation of the degree of settlements as calculated normalized displacements are 43% less in comparison with the unimproved case. The reduction of normalized displacements is 29% in both geogrid reinforced embankment models (D13). Similar results were achieved with other input motions as well but the reduction of normalized vertical displacements is higher for the given motion. Geogrid reinforcement in this study is found to be more effective in limiting the horizontal displacements than vertical displacements (settlements). EPS geofoam's extremely low density greatly reduces

the embankment's self-weight. As a result, the gravitational forces on the embankment are minimized, leading to reduced deformation and displacement under dynamic loads.

6.2. Full Scale Seismic Performance Tests

Full scale seismic performance tests of URE, GRE and EGE were performed at the proposed test area located in Boğaziçi University Kandilli Observatory and Earthquake Research Instituite. MSS is used as a dynamic excitation source on the field. Dynamic excitations are selected carefully to observe the effect of different characteristics of seismic motions such as the frequency content, amplitude and duration on the dynamic performance of highway embankments. Capabilites of the MSS were also taken into consideration for the selection of the input motions for the applied frequency ranges and the force levels (section 5.2.7).

Evaluation of the obtained data from seismic performance test with URE shows that, recorded acceleration values decrease with respect to the distance from the source for all cases and directions. A1 gives the highest acceleration measurements as it is closest to the MSS, which is the dynamic source. Measured acceleration values from A2, A3 and A4 decreases with respect to height. Accelerometers located at the crest of the embankment represent lower acceleration measurements compared to A1. Measured acceleration values clearly increases with respect to increased force, duration and broader frequency ranges applied and relatedly the highest acceleration values were measured from the experiments where the dynamic input of 1-250Hz 27kN 120s was used (Figure 5.64).

Displacement responses of the Unreinforced Embankment model reveal significant variations across different dynamic motions and sensor locations. For D1, the resultant displacement values, shows a gradual increase with higher forces and longer durations. The Sensor D2 experiences higher displacements compared to D1 indicating more pronounced responses to increased force. Sensor D3 exhibits a notably larger range of displacements particularly under higher forces and longer durations which demonstrates its sensitivity to the

characteristics of the dynamic motion. Sensor D4, which measures the vertical displacements, shows the highest displacement values in response to the applied dynamic motions. The overall trend indicates that displacement increases with both force and duration, with the most substantial displacements recorded at sensors D3 and D4.

Experimental data from GRE shows that, recorded acceleration values are reduced with respect to the distance from the source. A1 gives the highest acceleration measurements that is closest to the MSS. Measured acceleration values from A2, A3 and A4 decreases with respect to height. Accelerometers located at the crest of the embankment represent lower acceleration measurements compared to A1. Similarly, measured acceleration values increases with respect to increased force, duration and broader frequency ranges applied and relatedly the highest acceleration values were measured from the experiments where the dynamic input of 120Hz 27kN 120s was used (Figure 5.82). The reinforcement provided by the geogrid layers appears to help distribute the seismic forces, as indicated by slightly lower crest accelerations compared to the unreinforced embankment, but overall patterns remain similar.

The displacement responses of the Geogrid Reinforced Embankment model show distinct variations across different dynamic motions and sensor locations, with generally lower displacements compared to the Unreinforced Embankment model. The sensor D1 demonstrates the least displacement values among all displacement sensors. Measured displacements increase with higher forces and longer durations. Sensor D2 experiences slightly higher displacements compared to D1. Sensor D3 displays the highest displacement values that reflects its sensitivity to dynamic motions but also demonstrating the stabilizing effect of the geogrid reinforcement. Sensor D4 shows the minor vertical displacement values which is significantly lower compared to the Unreinforced model.

The data obtained from the EPS Geofoam Embankment model from the experimental tests with MSS experiments clearly shows that, recorded acceleration measurements decrease with respect to the distance from the source. Similarly, A1 gives the highest acceleration measurements as it is closest to the dynamic source. Measured acceleration values from the

slope of the embankment (A2, A3 and A4) decreases with respect to height. Accelerometers located at the crest of the embankment represent much lower acceleration measurements compared to A1. Similarly, measured acceleration values increases with respect to increased force, duration and broader frequency ranges applied and relatedly the highest acceleration values were measured from the experiments where the dynamic input of 120Hz 27kN 120s was used (Figure 5.99). The EPS geofoam embankment appears to help absorb and distribute the seismic forces effectively, leading to slightly lower accelerations at the crest compared to the unreinforced and geogrid reinforced embankments.

The displacement responses of the EPS Geofoam Embankment model show distinct patterns across different dynamic motions and sensor locations, with generally the lowest displacements compared to both the Unreinforced and Geogrid Reinforced embankments. For sensor D1, the displacement remains consistently low showing minimal variation with changes in force and duration. Sensor D2 exhibits higher displacements with respect to increased height and reflecting a moderate increase with higher forces but still well-controlled due to the EPS Geofoam's damping properties. Sensor D3 shows minor variations under different motions due to the increased distance from source (MSS). Sensor D4 represents the lowest recorded displacements which highlights the effective performance of the EPS Geofoam in minimizing deformation.

6.2.1. Effects of Geogrid Reinforcement on Seismic Response of Embankment Models

Comparison of the transmitted accelerations on the slope (A3) and at crest (A11) of the embankment models under proposed input motions are given (perpendicular to the road direction) in this section to discuss the effects of geogrid reinforcement on seismic response of embankment models.

Comparison of the transmitted accelerations on slope from A3 under 1-100Hz 15kN 30s, and 1-100Hz 27kN 30s for the perpendicular to the road direction is given in Figure 6.13.

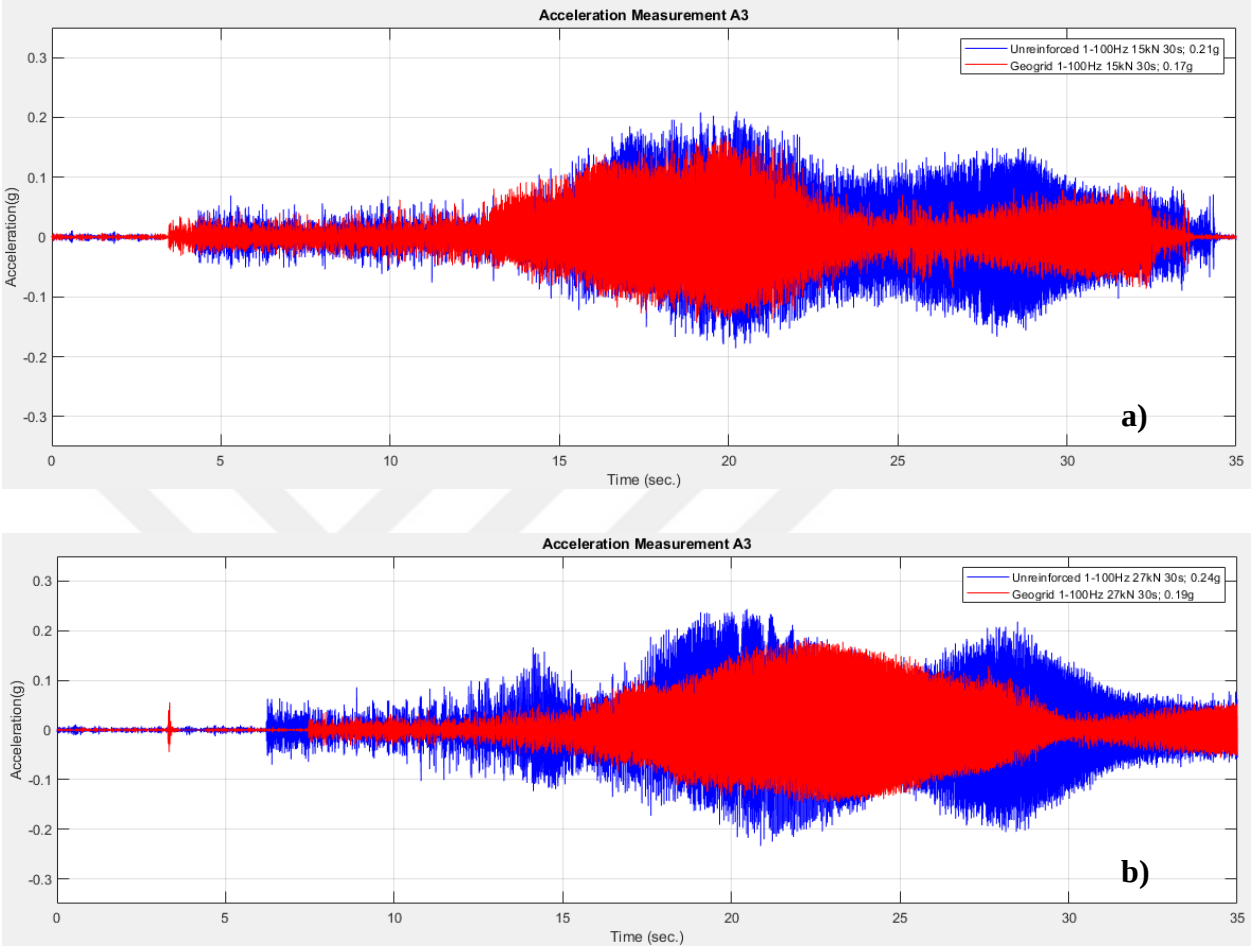

Figure 6.13. Comparison of the transmitted accelerations on slope from A3, a) 1-100Hz 15kN 30s, b) 1-100Hz 27kN 30s.

As represented in Figure 6.13a, transmitted accelerations measured on the slope of the GRE are 19% less compared to URE when subjected to 1-100Hz 15kN 30s. Similarly, slope accelerations are 21% less under 1-100Hz 27kN 30s (Figure 6.13b). Increased force level increased the efficiency of the geogrid material.

Comparison of the transmitted accelerations on slope from A3 under 1-250Hz 15kN 30s, and 1-250Hz 27kN 30s is given in Figure 6.14.

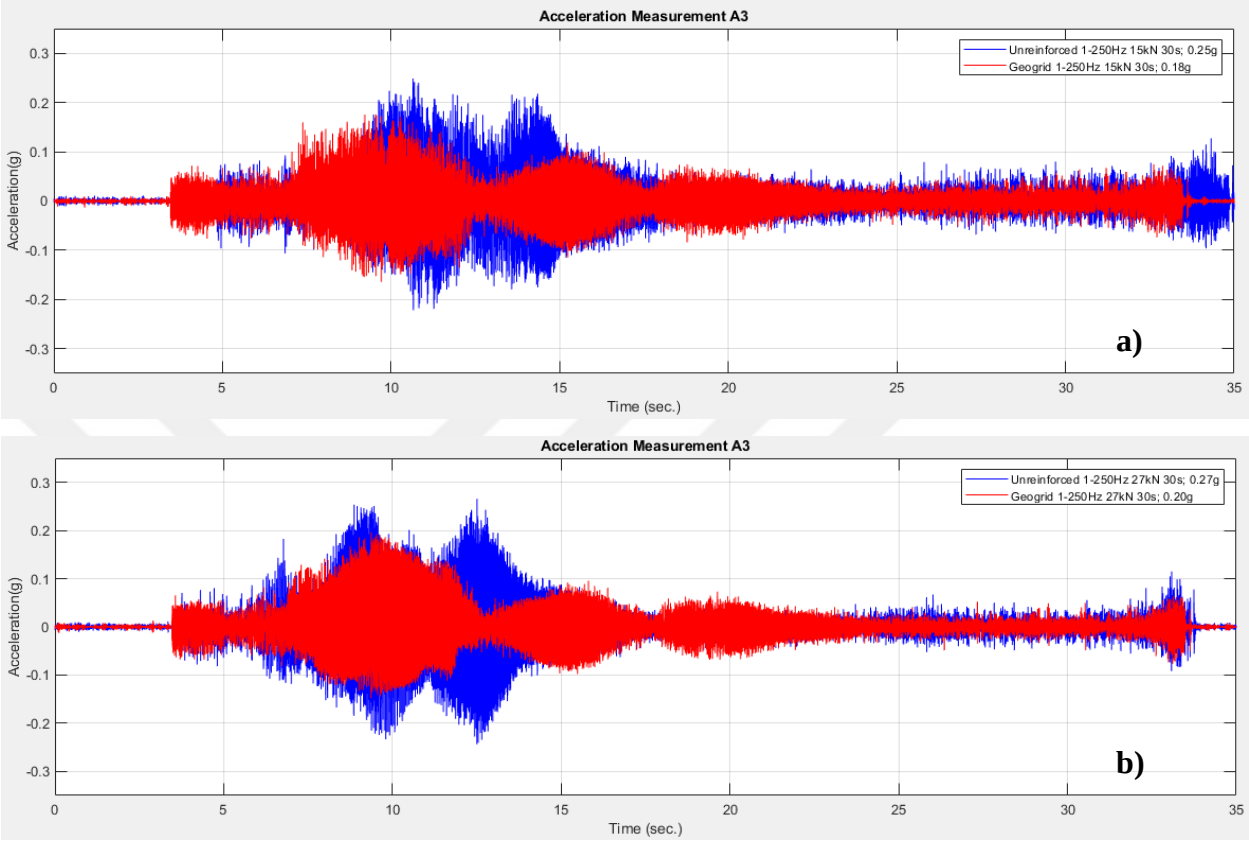

Figure 6.14. Comparison of the transmitted accelerations on slope from A3, a) 1-250Hz 15kN 30s, b) 1-250Hz 27kN 30s.

As represented in Figure 6.14a, transmitted accelerations measured on the slope of the GRE are 28% less compared to URE when subjected to 1-250Hz 15kN 30s. Similarly, slope accelerations are 26% less under 1-250Hz 27kN 30s (Figure 6.14b). Increased frequency range from 100Hz to 250Hz significantly increased the efficiency of the geogrid material (Compared to Figure 6.13).

Comparison of the transmitted accelerations on slope from A3 1-250Hz 27kN 120s is given in Figure 6.15.

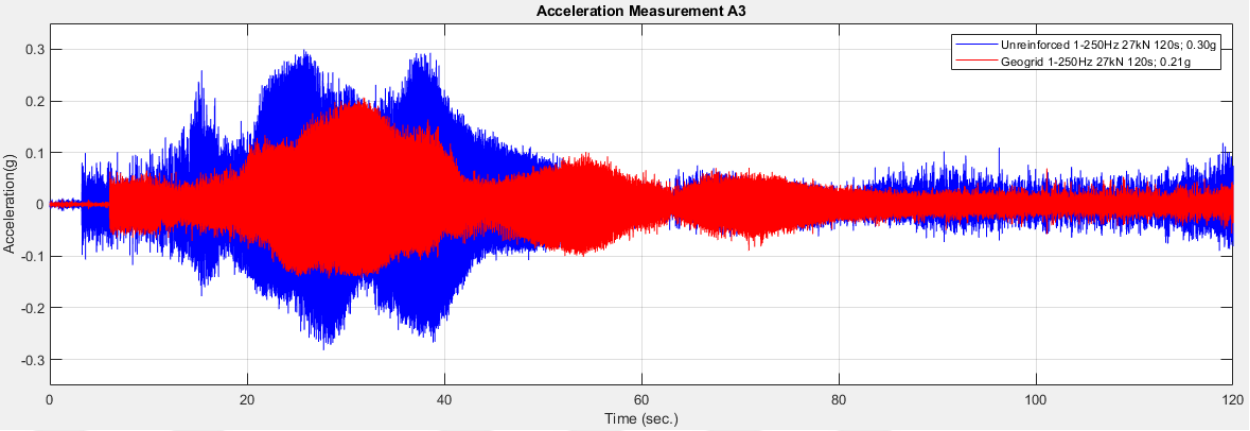

Figure 6.15. Comparison of the transmitted accelerations on slope from A3 under 1-250Hz 27kN 120s.

As represented in Figure 6.15, transmitted accelerations measured on the slope of the GRE are 30% less compared to URE when subjected to 1-250Hz 27kN 120s. Increased duration of the dynamic motion from 30s to 120s increased the efficiency of the geogrid material (Compared to Figure 6.14).

Comparison of the crest transmitted accelerations from A11 under 1-100Hz 15kN 30s, and 1-100Hz 27kN 30s is given in Figure 6.16.

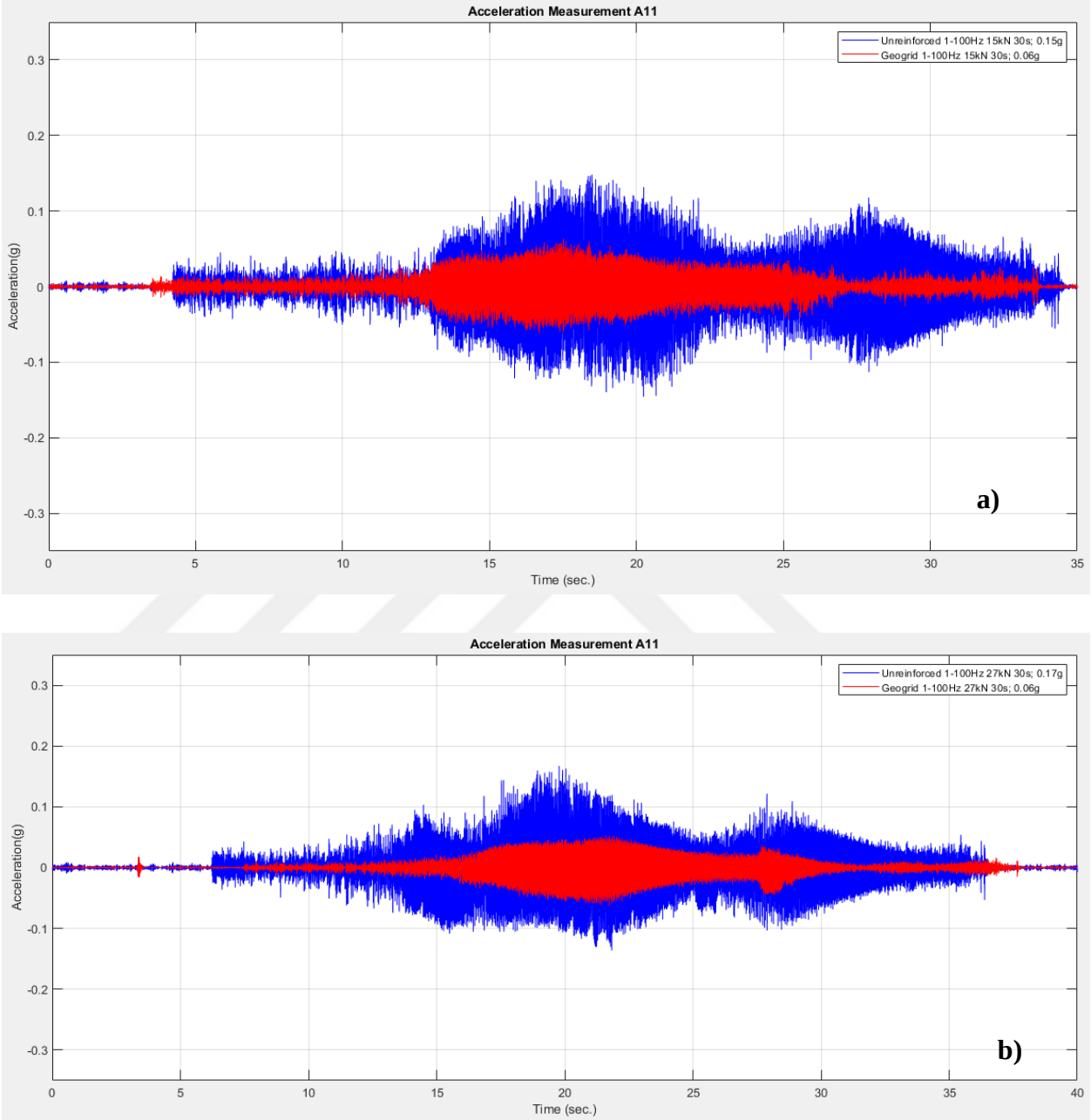

Figure 6.16. Comparison of the transmitted accelerations at crest (A11), a) 1-100Hz 15kN 30s, b) 1-100Hz 27kN 30s.

Comparison of the seismic performances of URE and GRE in terms of transmitted accelerations represent that effect of geogrid reinforcement is dependent on the input dynamic motion. As represented in Figure 6.16a, crest accelerations are up to 60% less under 1-100Hz

15kN 30s. Under the effect of the input dynamic motion of 1-100Hz 27kN 30s, crest accelerations are up to 64.7% (A11) less in the Geogrid Reinforced Model (Figure 6.16b). Increased force level increased the efficiency of the geogrid material (Figure 6.16).

Comparison of the transmitted accelerations at crest (A11) under 1-250Hz 15kN 30s, and 1-250Hz 27kN 30s of motion is given in Figure 6.17.

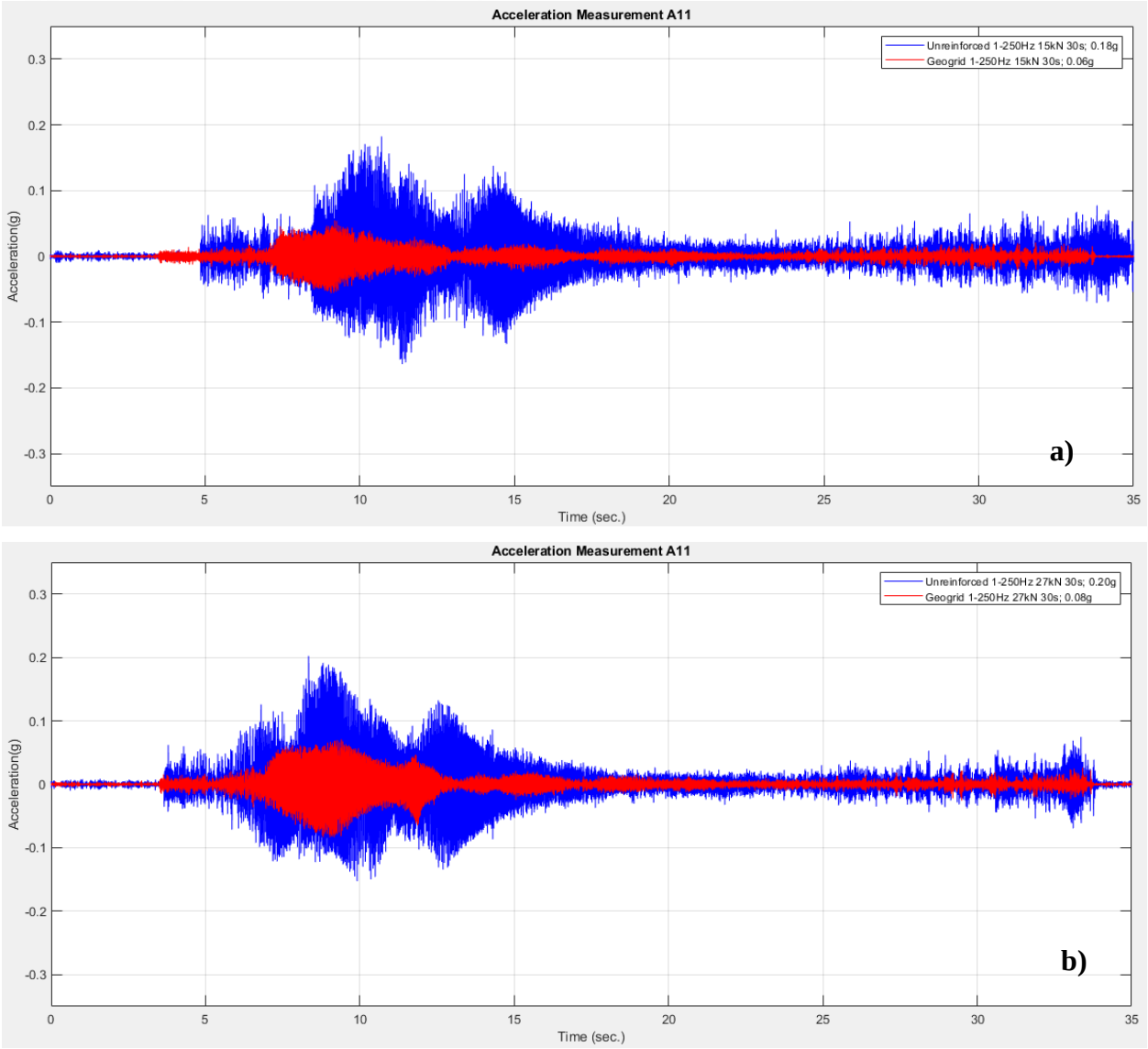

Figure 6.17. Comparison of the transmitted accelerations at crest (A11), a) 1-250Hz 15kN 30s, b) 1-250Hz 27kN 30s.

Reduction ratios of the acceleration measurements tend to increase with respect to increased force, duration and broader frequency ranges applied. Comparison of the seismic performance of URE and GRE under 1-250Hz 15kN 30s shows that measured accelerations are 66.7% less at the slope of the Geogrid Reinforced Embankment model when compared to the Unreinforced Model (Figure 6.17a). Similarly, crest accelerations are up to 60% less (A11) under 1-250Hz 27kN 30s (Figure 6.17b).

Comparison of the transmitted accelerations at crest (A11) under 1-250Hz 27kN 120s, is given in Figure 6.18.

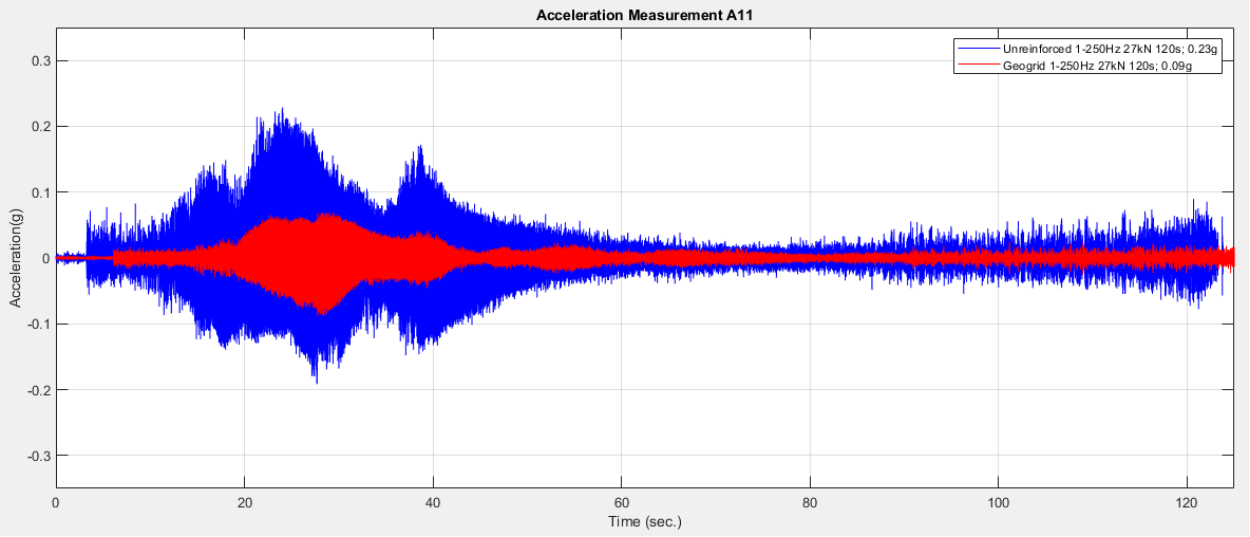

Figure 6.18. Comparison of the transmitted accelerations at crest (A11) under 1-250Hz 27kN 120s.

When the defined input dynamic motion of 1-250Hz 27kN 120s is considered, crest accelerations are successfully reduced by 68.8% in GRE compared to the URE (Figure 6.18). Obtained results from Figure 6.13 to Figure 6.18 reveal that the effect of geogrid reinforcement is highly dependent on the input dynamic motion and reduction ratios of the acceleration measurements increases with respect to increased force, duration and broader frequency ranges

applied. Thus, the the effect of geogrid reinforcement is observed the best under the input motion of 1-250Hz 27kN 120s.

Comparison of the spectral accelerations on the slope (A3) and at crest (A11) of the embankment models under proposed input motions are given in this section to discuss the effects of geogrid reinforcement on seismic response of embankment models. Comparison of response spectra obtained from slope of the models (A3) under all input motions are represented in Figure 6.19.

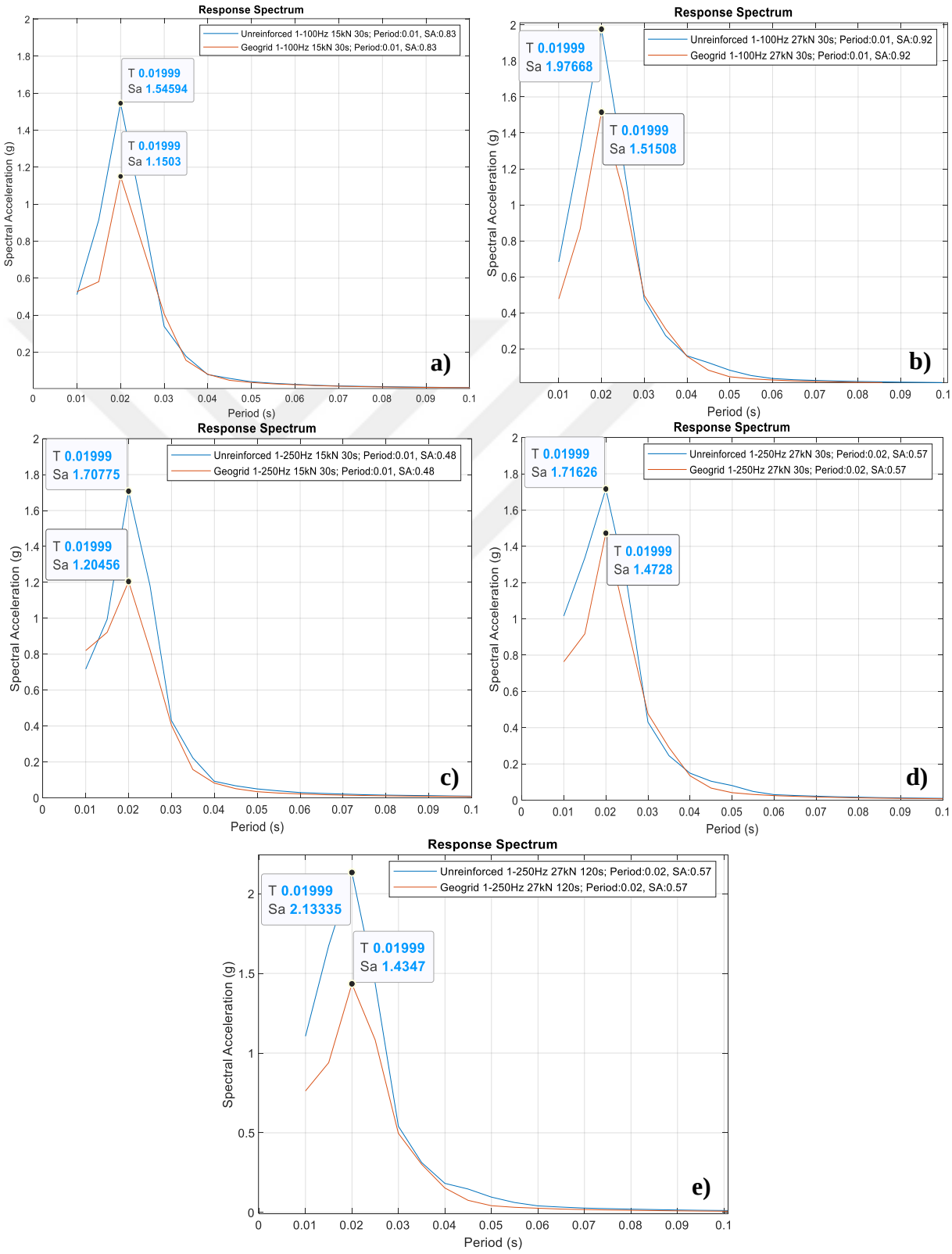

Figure 6.19. Comparison of Response Spectra from slope (A3), a) 1-100Hz 15kN 30s, b) 1-100Hz 27kN 30s, c) 1-250Hz 15kN 30s, d) 1-250Hz 27kN 30s, e) 1-250Hz 27kN 120s.

Given response spectra in Figure 6.19 show that, spectral accelerations on the slope of the GRE are reduced due to the geogrid reinforcement during the performed seismic response tests. As represented in Figure 6.19, Sa reductions range from 15% (d) to 33 % (e). Sa reductions are usually higher when the Geogrid Reinforced Model is subjected to increased force, duration and broader frequency ranges. For instance, Sa reduction ratio increased from 26% to 30% when the frequency range of the dynamic motion was increased from 1-100Hz to 1-250Hz. The structural periods are obtained as 0.02s for all cases (Figure 6.19). Similar results with the same pattern were obtained from other sensors (Section 5.2.10.1 compared to Section 5.2.10.2).

Comparison of response spectra obtained from crest of the embankments (A11) under all input motions are represented in Figure 6.20.

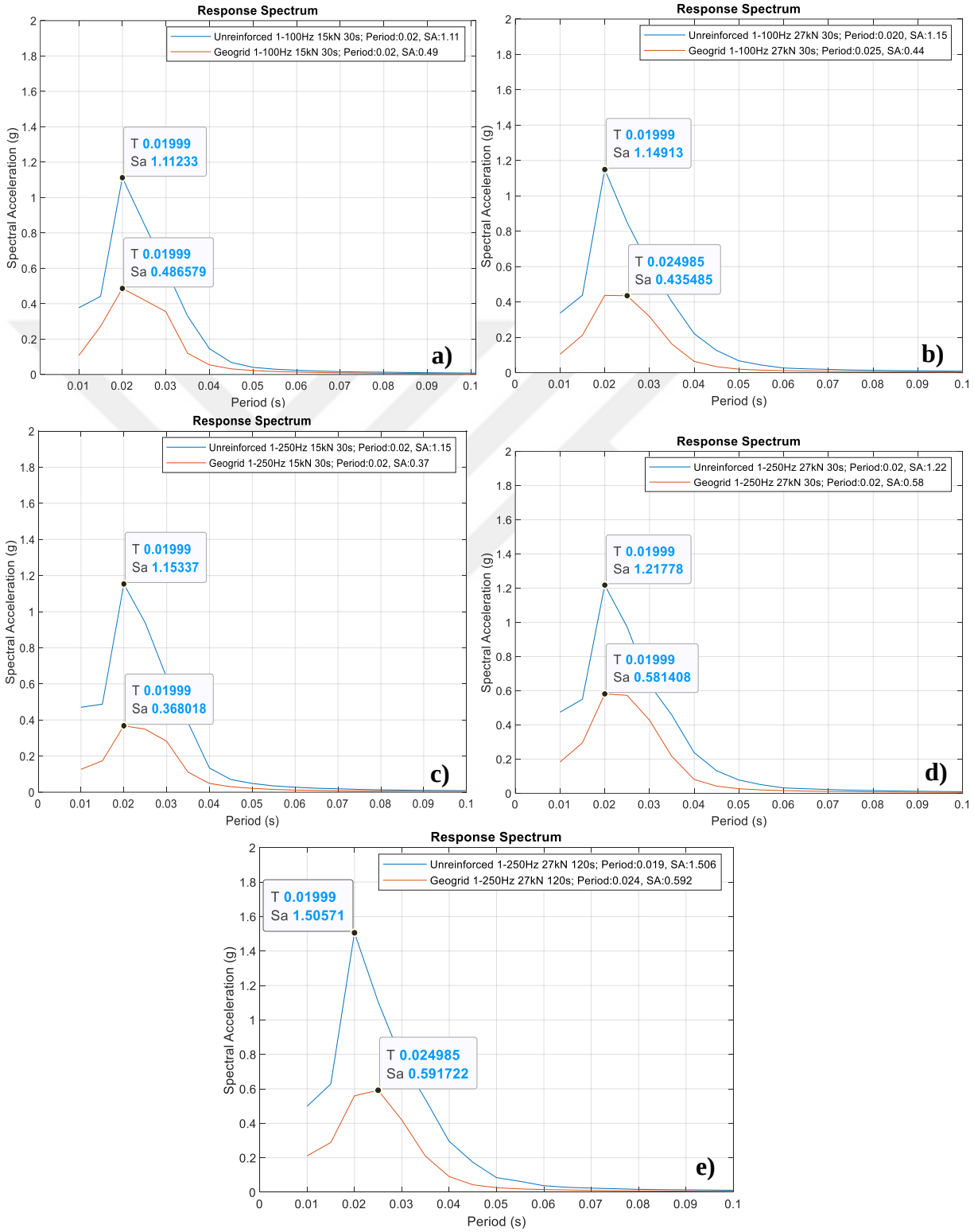

Figure 6.20. Comparison of Response Spectra from crest (A11), a) 1-100Hz 15kN 30s, b) 1-100Hz 27kN 30s, c) 1-250Hz 15kN 30s, d) 1-250Hz 27kN 30s, e) 1-250Hz 27kN 120s.

Spectral Accelerations are successfully decreased with the help of the geogrid reinforcement during the performed seismic response tests. As represented in Figure 6.20, Sa reductions range from 56.3% (a) to 72 % (e). Sa reductions are usually higher when the Geogrid Reinforced Model is subjected to increased force, duration and broader frequency ranges. Relatedly, the structural periods are in the range of 0.015s to 0.019s for the Unreinforced Embankment Model and due to the additional tensile strength provided, the structural periods shift up to 0.035s in the Geogrid Reinforced Embankment Model. Similar results with the same pattern were obtained from other sensors (Section 5.2.10.1 compared to Section 5.2.10.2).

Comparison of horizontal displacement responses obtained from D2, which is located at the mid-height of the embankment, for all input motions are given Figure 7.21, where as the comparison of vertical displacement responses obtained from D4, which is located at crest, are given Figure 6.22.

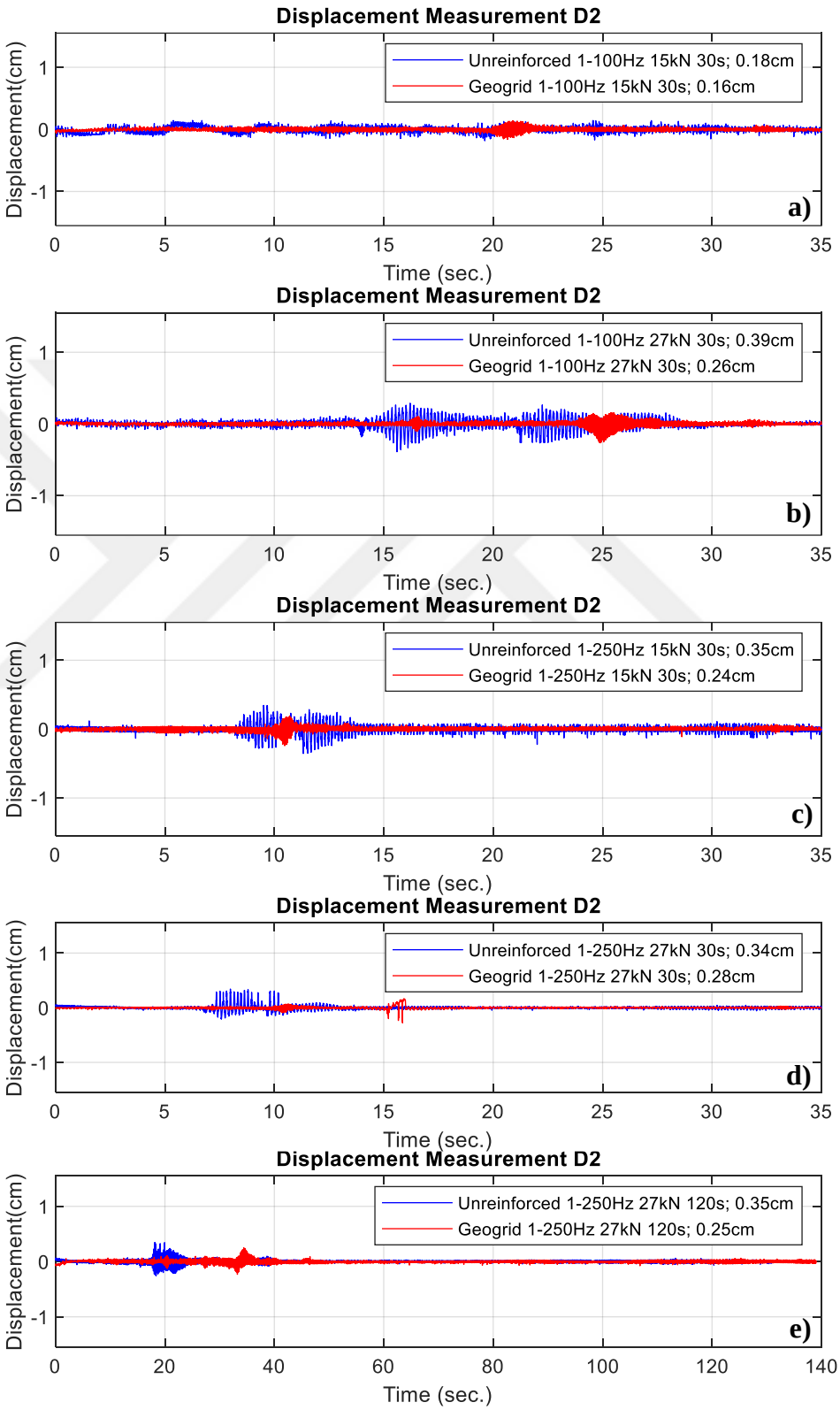

Figure 6.21. Comparison of Horizontal Displacement Responses from slope (D2), a) 1-100Hz 15kN 30s, b) 1-100Hz 27kN 30s, c) 1-250Hz 15kN 30s, d) 1-250Hz 27kN 30s, e) 1-250Hz 27kN 120s.

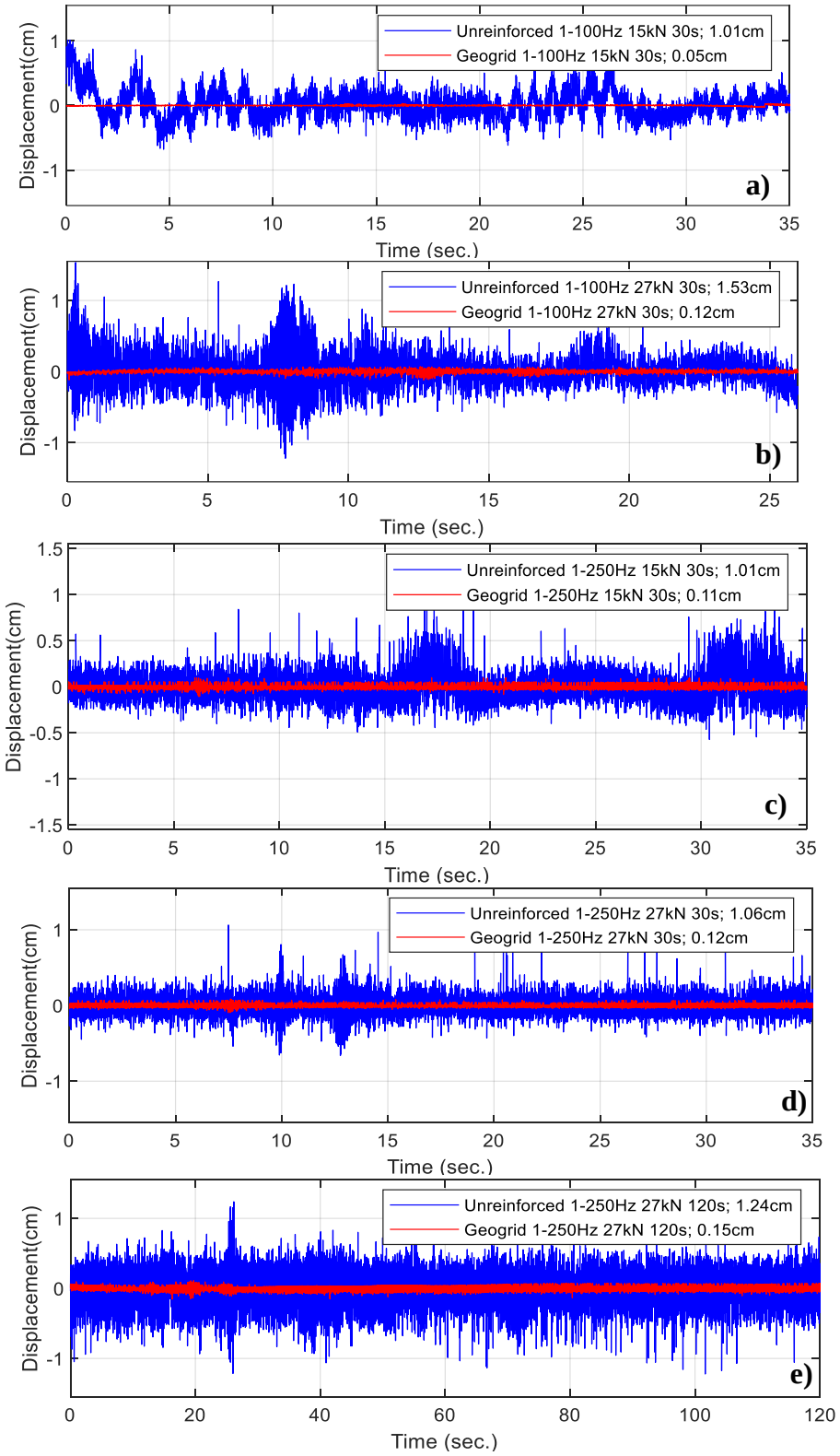

Figure 6.22. Comparison of Vertical Displacement Responses from crest (D4), a) 1-100Hz 15kN 30s, b) 1-100Hz 27kN 30s, c) 1-250Hz 15kN 30s, d) 1-250Hz 27kN 30s, e) 1-250Hz 27kN 120s.

The comparison of the displacement responses between the URE and GRE models demonstrate significant reductions in displacement when the two layers of geogrid reinforcement is applied to the highway embankment model. For displacement sensor D1, which measures the horizontal displacement at toe, the reductions range from 28.57% to 40.00%, indicating consistent improvement across various dynamic motions and forces (Section 5.2.10.1 compared to Section 5.2.10.2). Displacement sensor D2, which measures the horizontal displacement at mid-height, shows reductions ranging from 11.11% to 33.33%, reflecting substantial stabilization, particularly at higher forces (Figure 6.21). Displacement values obtained from D3, which measures the horizontal displacement at crest are reduced in the range of 47.22% to 84.52% (Section 5.2.10.1 compared to Section 5.2.10.2). Reduction ratios increase with respect to increased force and duration. Finally, sensor D4 exhibits the highest reductions, from 88.41% to 95.05%, emphasizing critical improvements in the embankment's response to dynamic forces (Figure 6.22). Geogrids reduce displacements on embankments under dynamic loads by reinforcing the soil and enhancing stability. They distribute dynamic loads along the embankement, while increasing tensile strength and shear resistance through soil interlocking effect. By confining soil particles, geogrids limit their movement, improve slope stability, and enhance the embankment’s ability to absorb and dissipate energy from dynamic forces. These combined effects reduce overall displacements and makes the embankment more resistant to dynamic forces.

6.2.2. Effect of EPS Geofoam on Seismic Response of Highway Embankment Models

Comparison of the transmitted accelerations on the slope (A3) and at crest (A11) of the URE and EGE under proposed input motions are given in this section to discuss the effects of EPS geofoam fill on seismic response of embankment models. Comparison of the transmitted accelerations on slope from A3 under 1-100Hz 15kN 30s and 1-100Hz 27kN 30s (perpendicular to the road direction) is given in Figure 6.23.

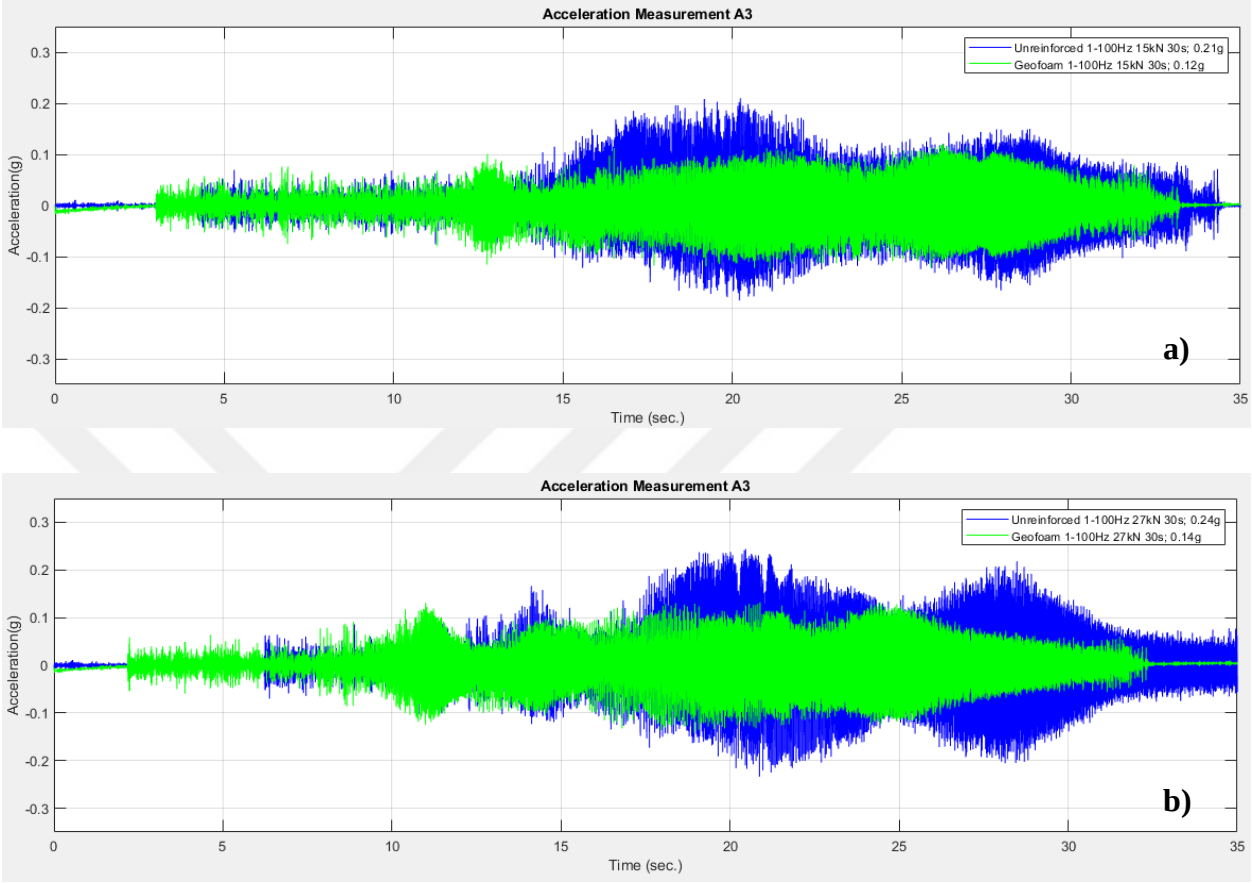

Figure 6.23. Comparison of the transmitted accelerations at slope (A3), a) 1-100Hz 15kN 30s, b) 1-100Hz 27kN 30s.

As represented in Figure 6.23a, transmitted accelerations measured on the slope of the EGE are 43% less compared to URE when subjected to 1-100Hz 15kN 30s. Similarly, slope accelerations are 42% less under 1-100Hz 27kN 30s (Figure 6.23b). Acceleration measurements on the slope are lower in EGE compared to URE due to the energy absorption and damping properties of the geofoam material.

Comparison of the transmitted accelerations on slope from A3 under 1-250Hz 15kN 30s, and 1-250Hz 27kN 30s is given in Figure 6.24.

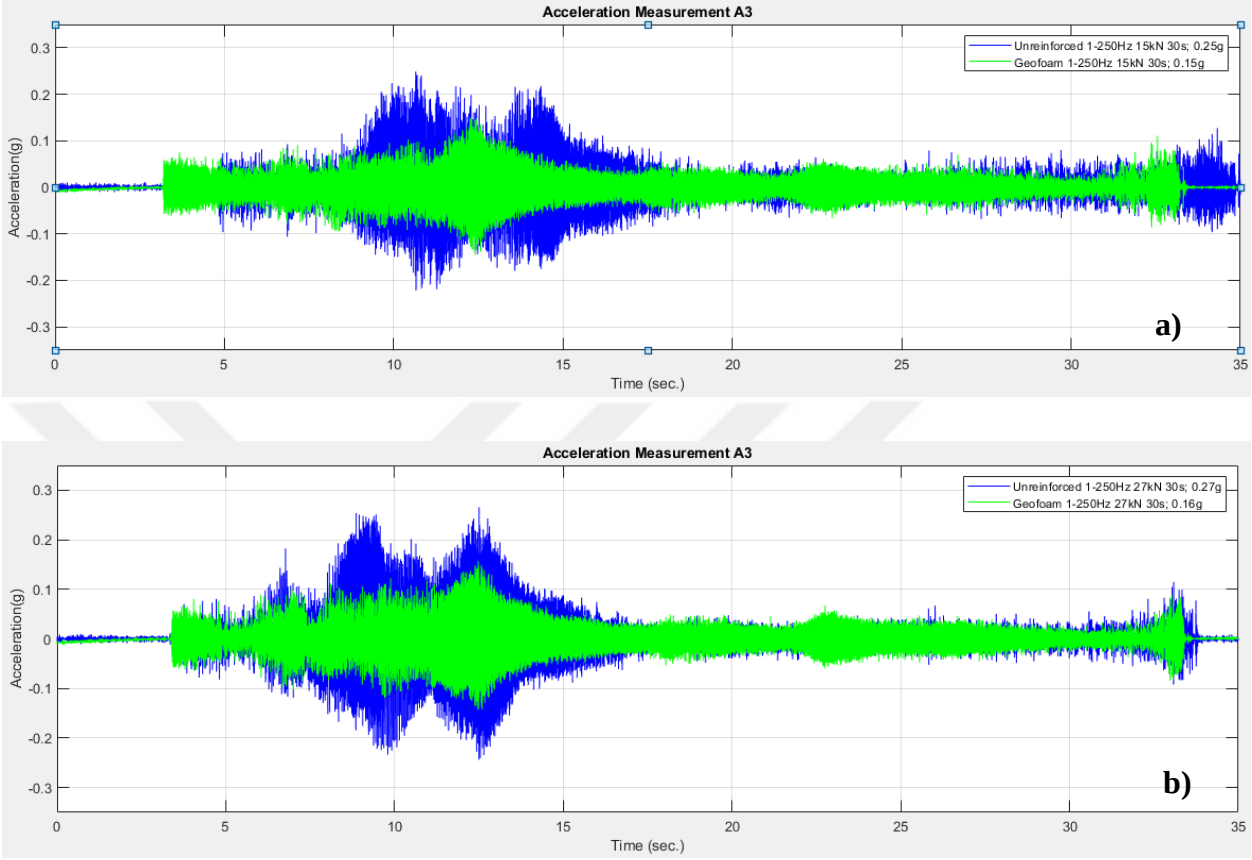

Figure 6.24. Comparison of the transmitted accelerations at slope (A3), a) 1-250Hz 15kN 30s, b) 1-250Hz 27kN 30s.

Given in Figure 6.24a, transmitted accelerations measured on the slope of the EGE are 40% less compared to URE when subjected to 1-250Hz 15kN 30s. Similarly, slope accelerations are 41% less under 1-250Hz 27kN 30s (Figure 6.24b). Transmitted acceleration reductions are consistantly around 40% under given cases (Figure 6.23 and Figure 6.24).

Comparison of the transmitted accelerations on slope from A3 under 1-250Hz 27kN 120s is given in Figure 6.25.

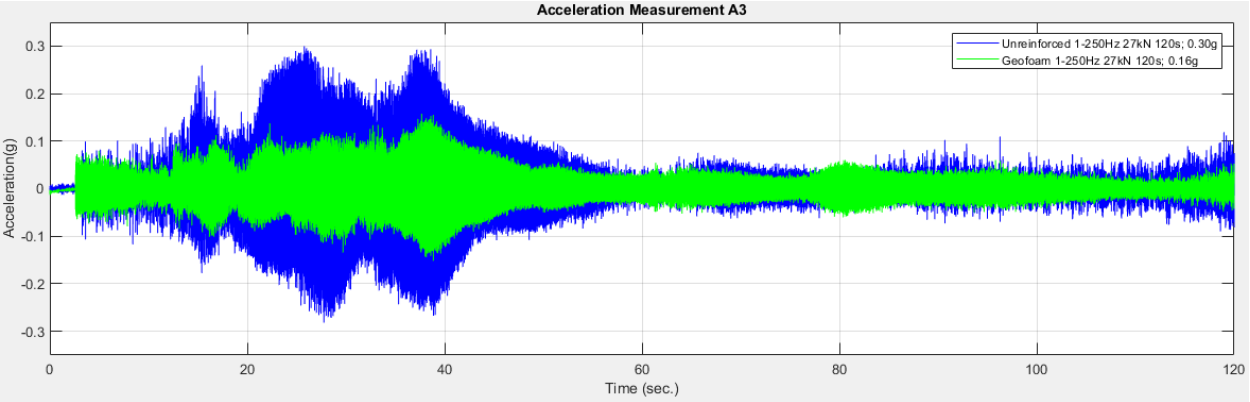

Figure 6.25. Comparison of the transmitted accelerations at slope (A3) under 1-250Hz 27kN 120s.

As represented in Figure 6.25, transmitted accelerations measured on the slope of the EGE are 47% less compared to URE when subjected to 1-250Hz 27kN 120s. Increased duration of the dynamic motion from 30s to 120s increased the efficiency of the EPS geofoam material and the highest reduction ratio in terms of transmitted accelerations was achieved in this case (Figure 6.25).

Comparison of the transmitted accelerations at crest (A11) under 1-100Hz 15kN 30s, and 1-100Hz 27kN 30s of motion is given in Figure 6.26.

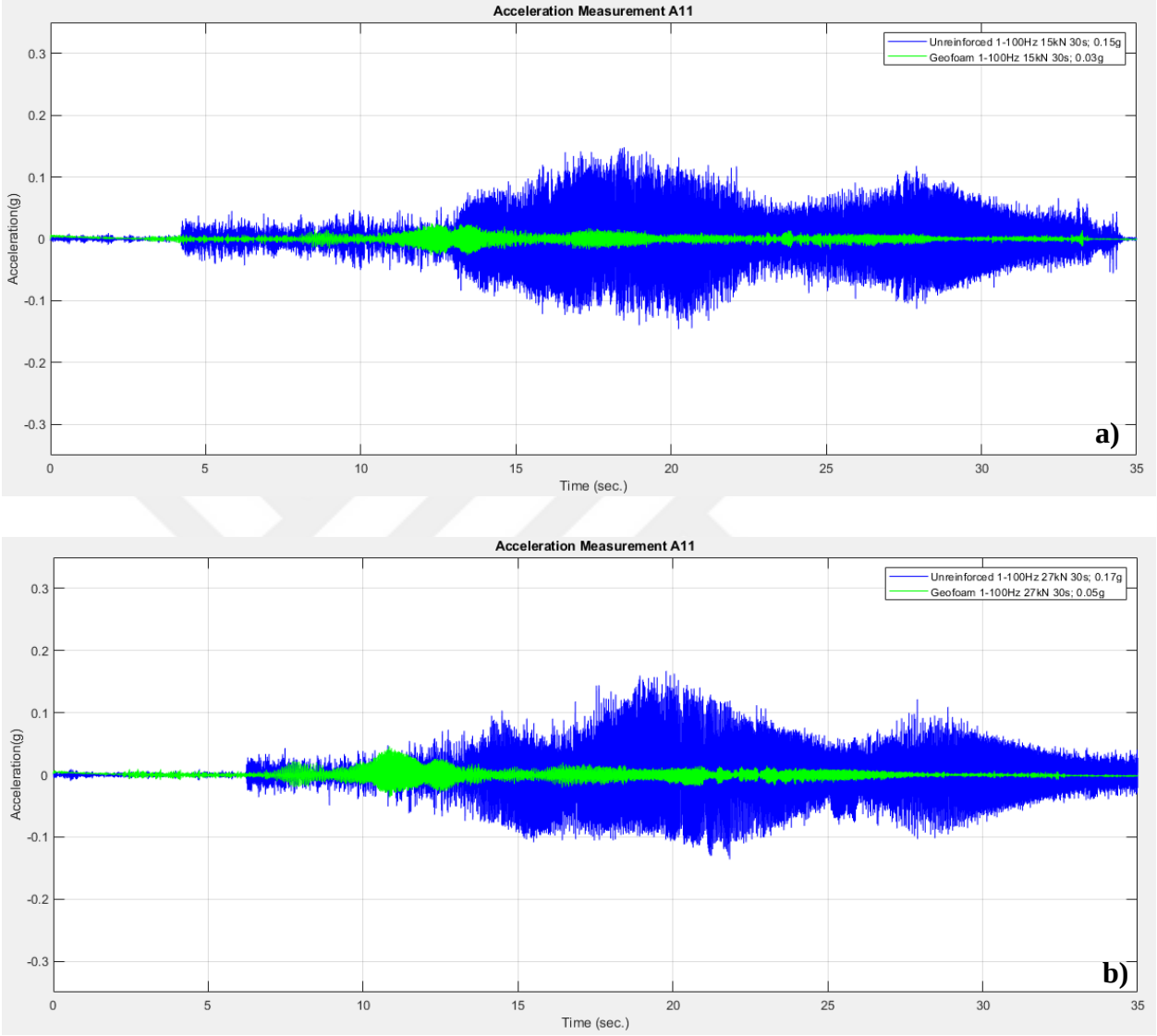

Figure 6.26. Comparison of the transmitted accelerations at crest (A11), a) 1-100Hz 15kN 30s, b) 1-100Hz 27kN 30s.

As represented in Figure 6.26a, crest accelerations are up to 80% less under 1-100Hz 15kN 30s Under the effect of the input dynamic motion of 1-100Hz 27kN 30s, crest accelerations are up to 70.6% less in EGE compared to URE (Figure 6.26b). Reduction ratios increase with respect to increased force levels. Comparison of the transmitted accelerations at crest (A11) under 1-250Hz 15kN 30s, and 1-250Hz 27kN 30s of motion is given in Figure 6.27.

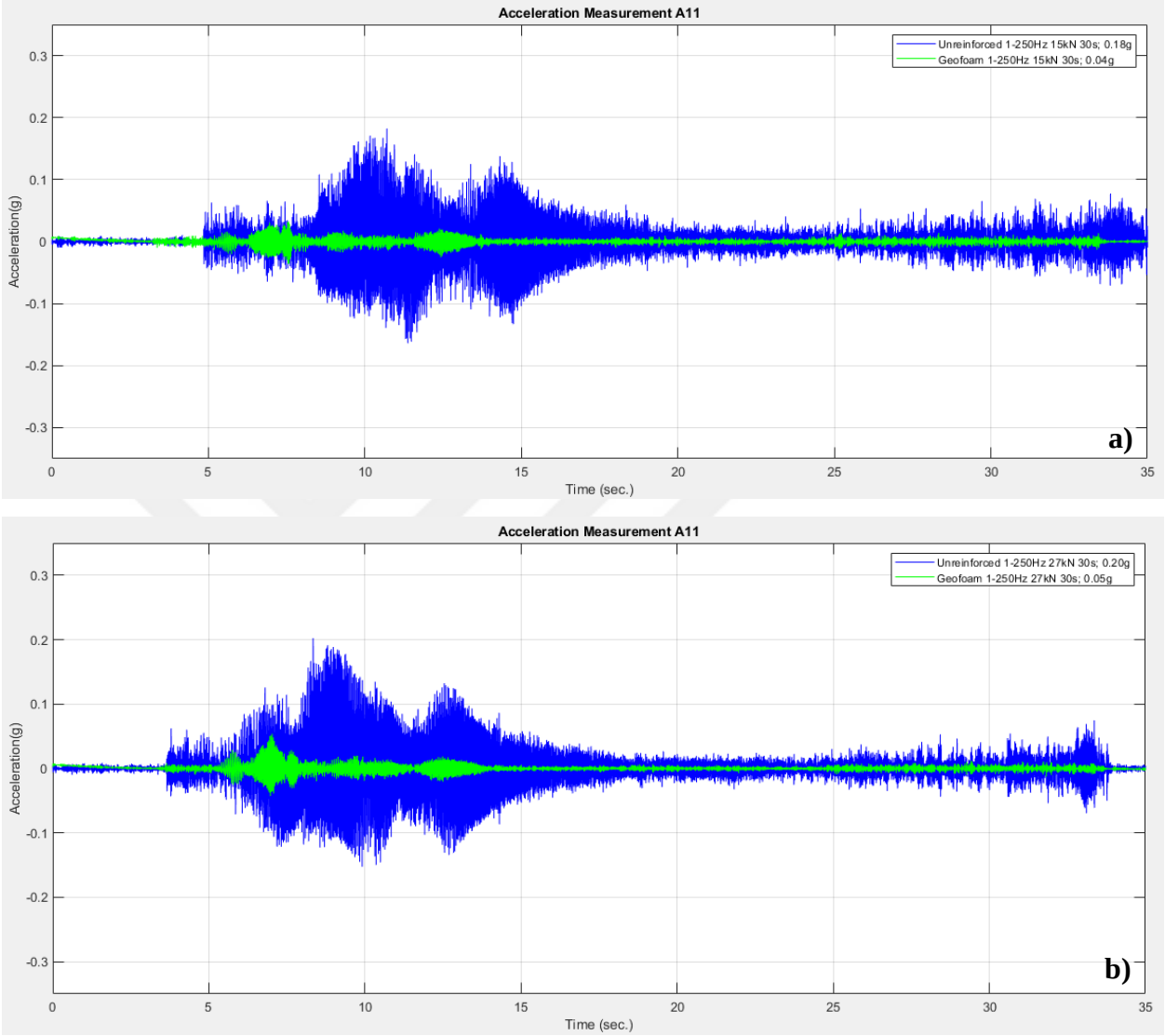

Figure 6.27. Comparison of the transmitted accelerations at crest (A11), a) 1-250Hz 15kN 30s, b) 1-250Hz 27kN 30s.

Comparison of the seismic performance of URE and EGE under 1-250Hz 15kN 30s shows that measured accelerations are up to 77.8% less at the crest of the EPS Geofoam Embankment model when compared to the Unreinforced Model (Figure 6.27a). Transmitted accelerations measured at crest are up to 75% less under mentioned motion (Figure 6.27b). Comparison of the crest level transmitted accelerations from A11 under 1-250Hz 27kN 120s is given in Figure 6.28.

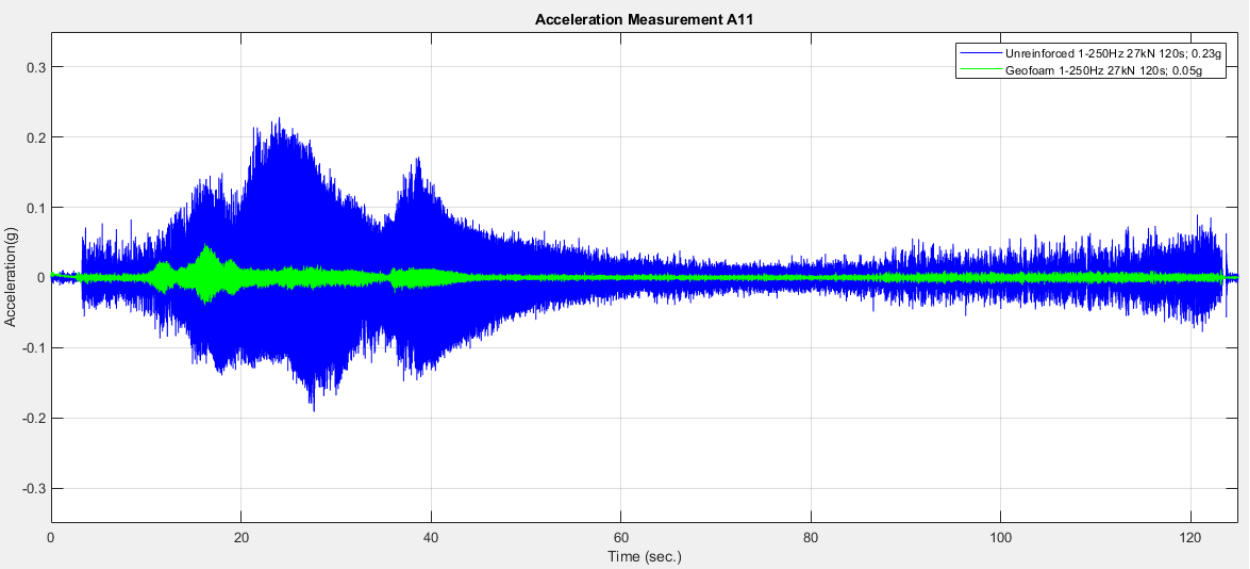

Figure 6.28. Comparison of the transmitted accelerations at crest (A11) under 1-250Hz 27kN 120s.

When the proposed input dynamic motion of 1-250Hz 27kN 120s is considered, crest accelerations are successfully reduced by up to 78.3% in EGE compared to URE. Comparison of the dynamic performances of URE and EGE in terms of transmitted accelerations clearly show that the dynamic performance of lightweight EPS geofoam is highly dependent on the characteristics of the input dynamic motion. Similar to other cases, EGE mostly performs better in terms of dynamic performance when subjected to increased force, duration and broader frequency ranges applied. Damping properties of the EPS geofoam material, that contribute to its effectiveness in reducing vibrations and absorbing seismic energy, successfully reduces the transmitted accelerations under proposed dynamic motions (Athanasopoulos et al., 1999) (Figure 6.23 - Figure 6.28).

Comparison of the spectral accelerations on the slope (A3) and at crest (A11) of the embankment models under proposed input motions are given in this section to discuss the effects of EPS geofoam fill on seismic response of embankment models. Comparison of response spectra obtained from slope of the URE and EGE (A3) under all input motions are represented in Figure 6.29.

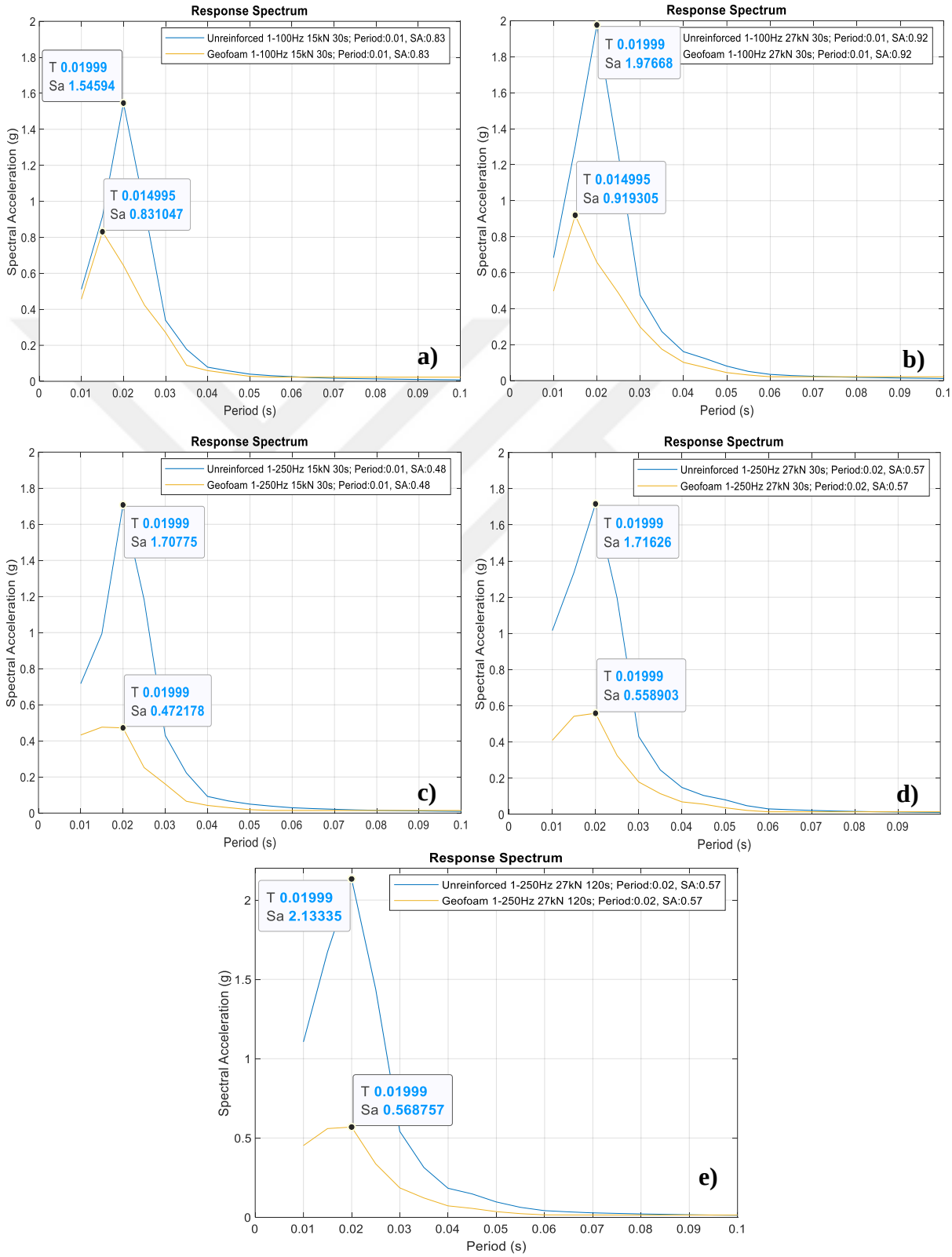

Figure 6.29. Comparison of Response Spectra at slope (A3), a) 1-100Hz 15kN 30s, b) 1-100Hz 27kN 30s, c) 1-250Hz 15kN 30s, d) 1-250Hz 27kN 30s, e) 1-250Hz 27kN 120s.

Given response spectra in Figure 6.29 show that, spectral accelerations on the slope of the EGE are reduced with the help of the damping properties of the EPS geofoam during the performed seismic response tests. As represented in Figure 6.29, Sa reductions range from 54% (b) to 73 % (e). Sa reductions are typically higher when the EGE is subjected to increased force, duration and broader frequency ranges. For instance, Sa reduction ratio increased from 46% (a) to 72% (c) when the frequency range of the dynamic motion was increased from 1-100Hz to 1-250Hz. The structural periods are in the range of 0.015 to 0.02s for all cases (Figure 6.89). EPS geofoam demonstrates a significant reduction in Sa values on embankment slope compared to unreinforced embankment due to its lower density and high energy absorption capacity, which attenuates seismic wave propagation and diminishes the dynamic loads.

Comparison of response spectra obtained from crest of the embankment (A11) under all input motions are represented in Figure 6.30 for URE and EGE.

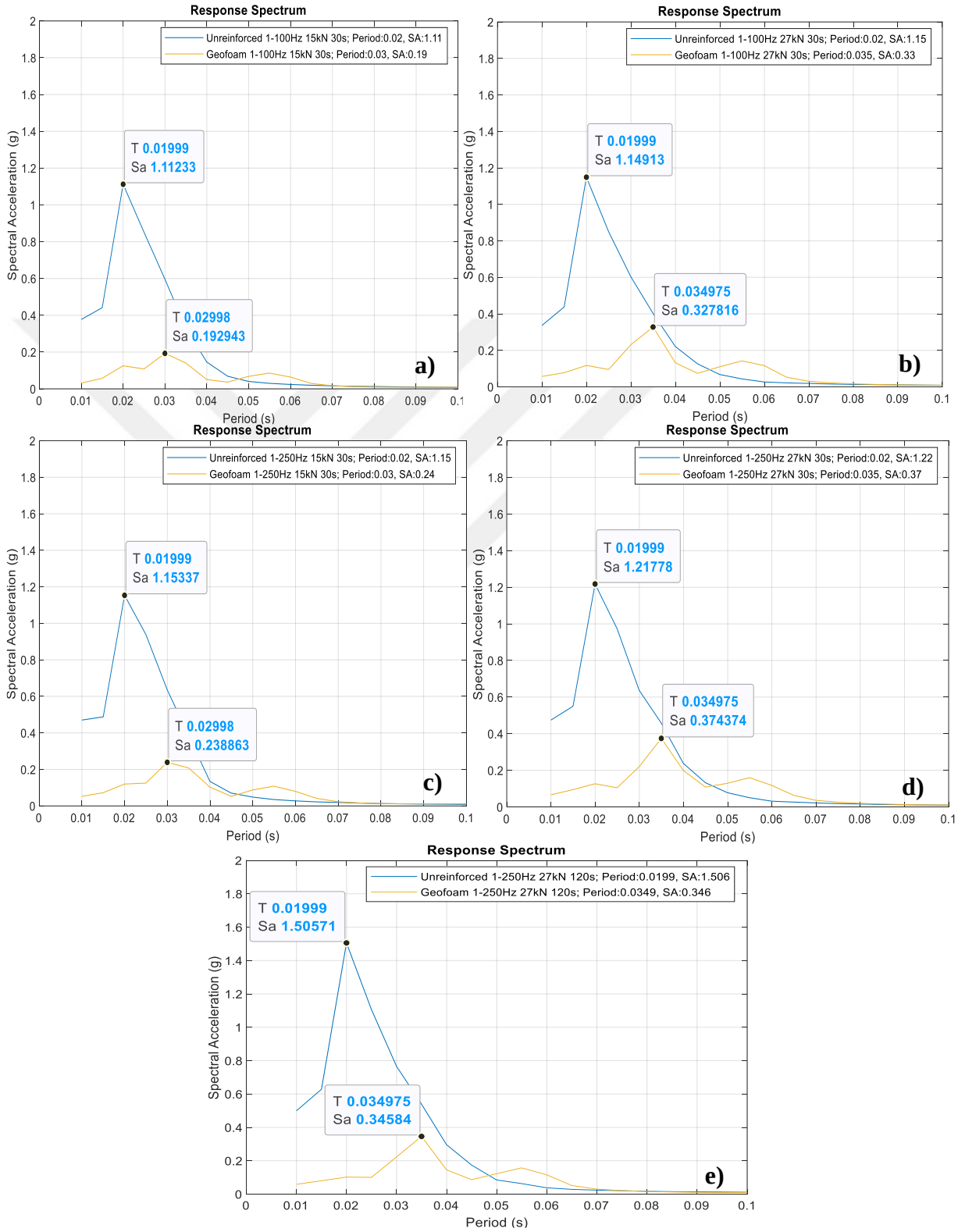

Figure 6.30. Comparison of Response Spectra at crest (A11), a) 1-100Hz 15kN 30s, b) 1-100Hz 27kN 30s, c) 1-250Hz 15kN 30s, d) 1-250Hz 27kN 30s, e) 1-250Hz 27kN 120s.

As represented in Figure 6.30, spectral accelerations values are also effectively decreased with the help of the EPS Geofoam blocks. Sa reductions range from 69.7% (a) to 82.9 % (e). Relatedly, the structural periods are in the range of 0.025s to 0.039s for EGE which clearly reflects the period-shift effect successfully. As previously mentioned, EGE performs much better in terms of dynamic performance when subjected to increased force, duration and broader frequency ranges. This situation is due to the material's lightweight and compressible nature, which allows it to absorb and dissipate energy more effectively compared to URE.

The comparison of the displacement responses between the URE and EGE models demonstrate outstanding reductions in displacement when EPS geofoam fill is used. Comparison of horizontal displacement responses (D2) for all input motions are given Figure 6.31, where as the comparison of vertical displacement responses (D4) are given Figure 6.32.

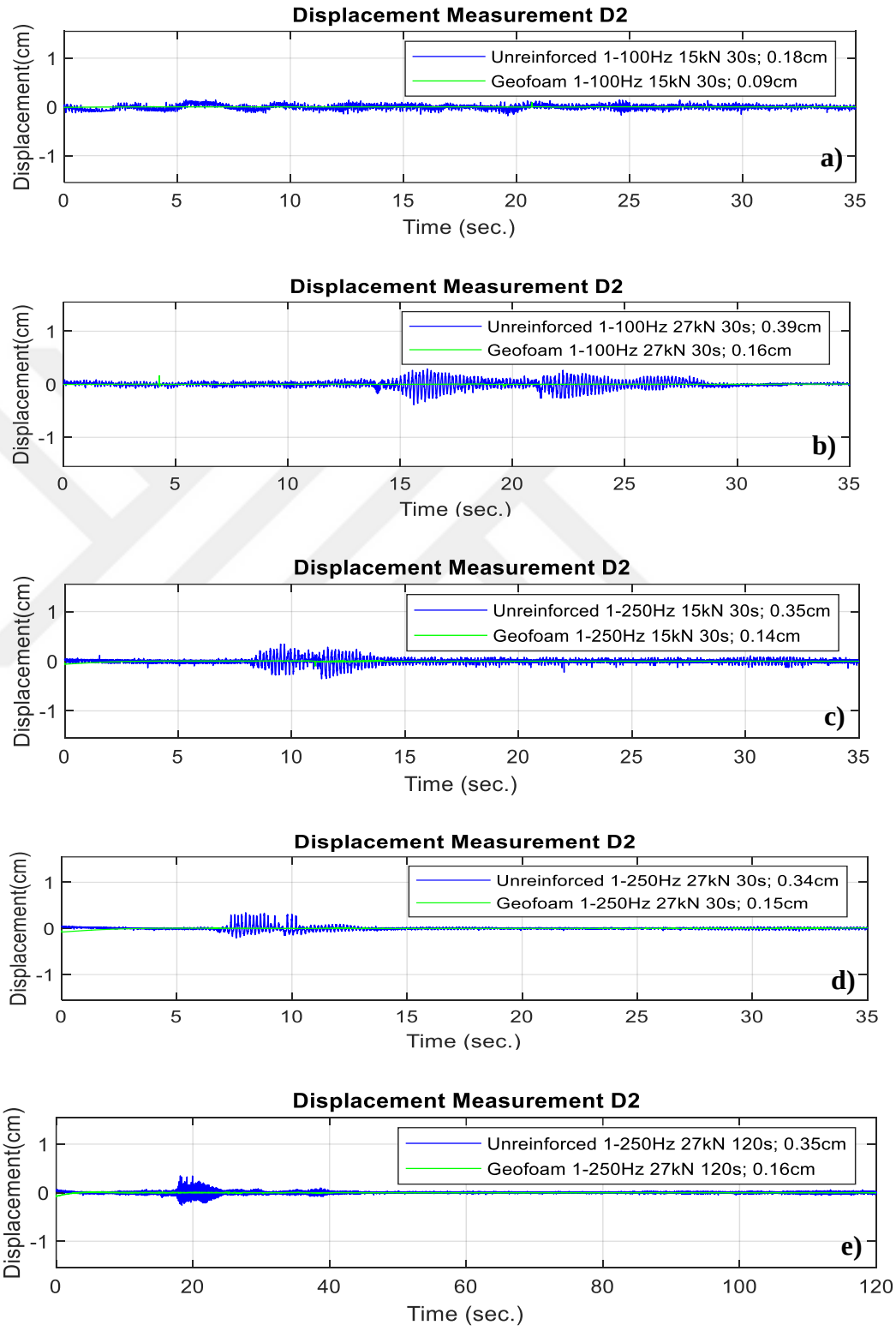

Figure 6.31. Comparison of Horizontal Displacement Responses at slope (D2), a) 1-100Hz 15kN 30s, b) 1-100Hz 27kN 30s, c) 1-250Hz 15kN 30s, d) 1-250Hz 27kN 30s, e) 1-250Hz 27kN 120s.

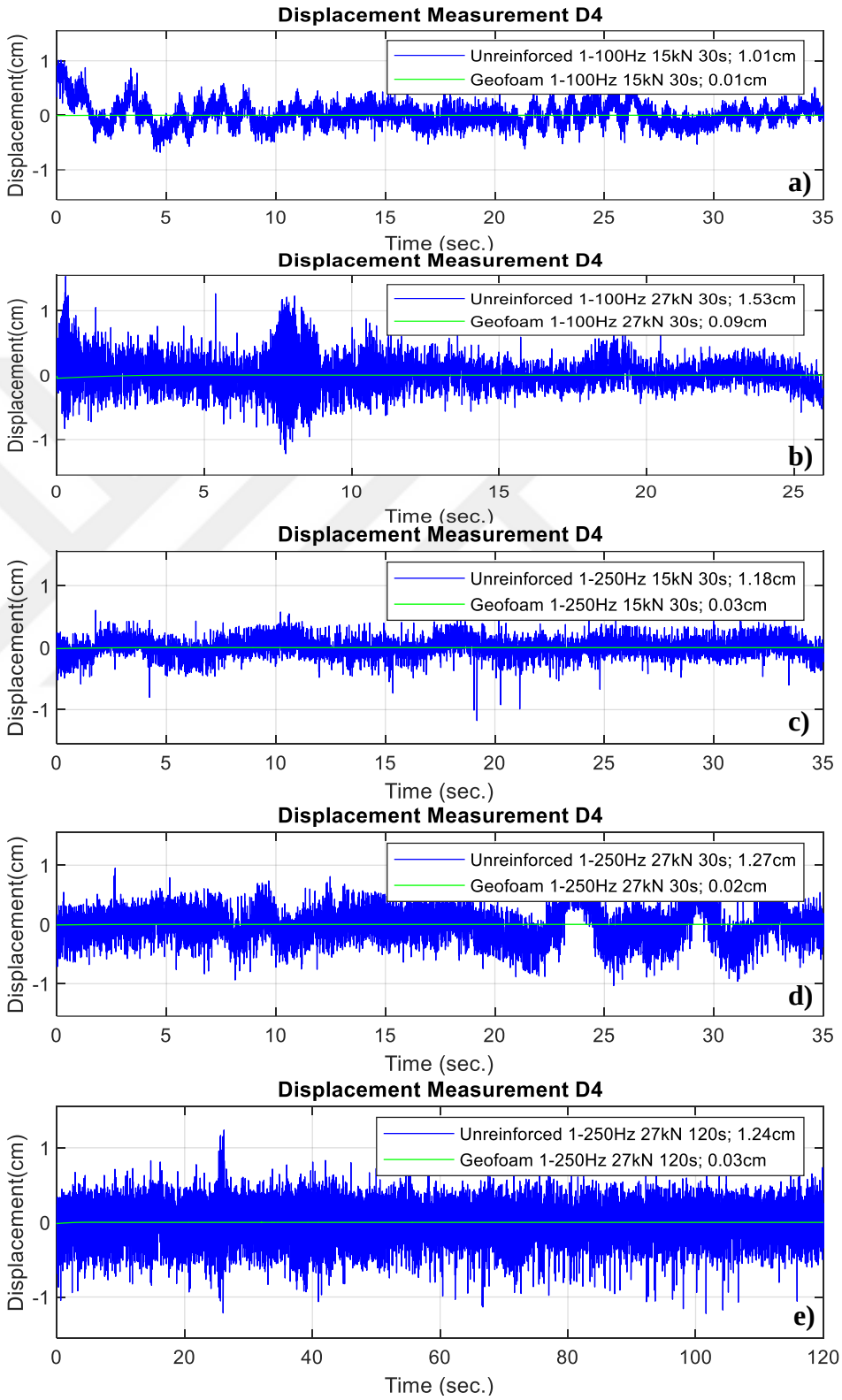

Figure 6.32. Comparison of Vertical Displacement Responses at crest (D4), a) 1-100Hz 15kN 30s, b) 1-100Hz 27kN 30s, c) 1-250Hz 15kN 30s, d) 1-250Hz 27kN 30s, e) 1-250Hz 27kN 120s.

The comparison between the Unreinforced Embankment and EPS Geofoam Embankment models highlights substantial reductions in displacement when EPS Geofoam is used. For displacement sensor D1, the reductions range from 66.67% to 76.92%, indicating significant improvement across various dynamic motions and forces. Displacement sensor D2 shows reductions ranging from 50.00% to 60.00%, reflecting consistent stabilization due to the damping properties of EPS Geofoam (Figure 6.31). Sensor D3 demonstrates the percentage reductions from 83.33% to 95.48%, highlighting the effectiveness of EPS Geofoam in minimizing horizontal displacements under higher dynamic loads. Finally, sensor D4 exhibits the highest reductions, from 97.10% to 99.34% (Figure 7.32), emphasizing critical improvements in the embankment's response in terms of vertical displacements (settlements).

6.2.3. Discussions on Normalized Accelerations and Displacements of All Embankment Models

Evaluation of the experimental results by means of normalized accelerations and displacements for EW direction are given in this section. Normalized accelerations are calculated based on the data from A11. Similarly, normalized displacements are calculated based on the data from D3 (horizontal) and D4 (vertical) for each and every input motion. The variation of normalized accelerations at crest for URE, GRE and EGE for all input motions are given in Figure 6.33.

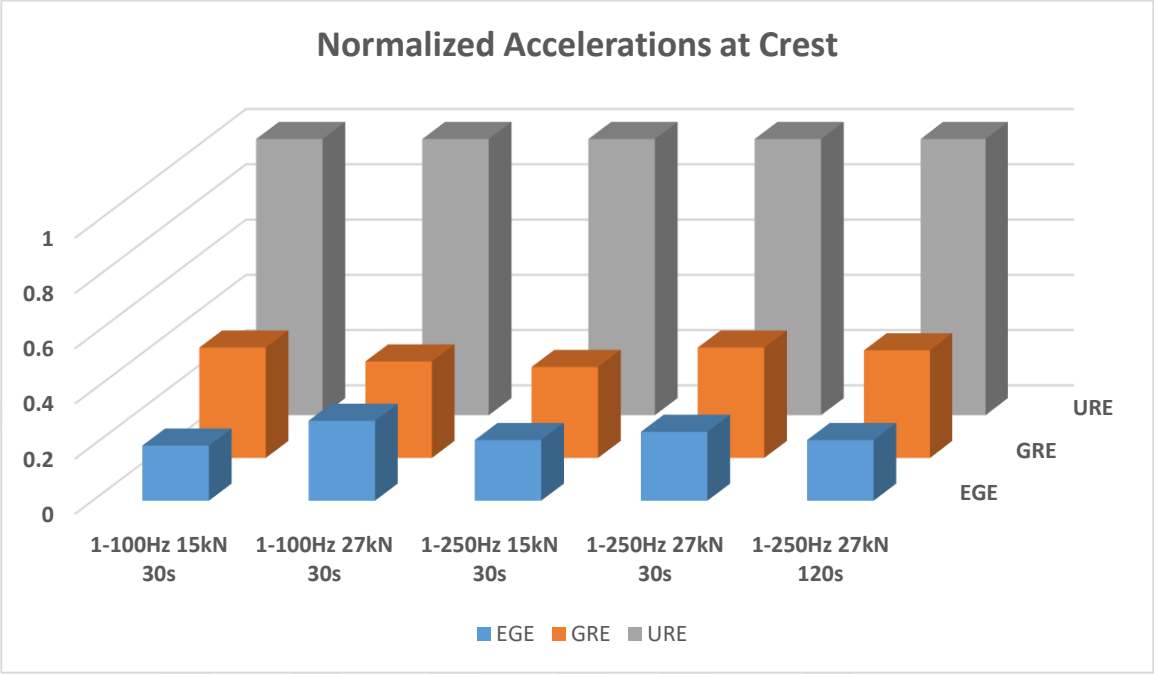

Figure 6.33. Normalized accelerations for URE, GRE and EGE at crest (A11) for all dynamic motions.

Given in Figure 6.33, normalized accelerations at crest in Geogrid and EPS Geofoam Embankment models are 60% and 80% less, respectively for the proposed dynamic motion. When the force level increases to 27kN, normalized accelerations are 65% and 71% less for the Geogrid Reinforced and EPS Geofoam Embankment models, respectively. Under, 1-250Hz 15kN 30s, normalized accelerations are 67% and 78% less for the Geogrid Reinforced and EPS Geofoam Embankment models, respectively. Similarly, when the force level increases to 27kN in the same frequency range, normalized accelerations are 60% and 75% less for GRE and EGE, respectively for the given dynamic motion. Subjected to 1-250Hz 27kN 120s, normalized accelerations are 61% and 78% less for the GRE and EGE, respectively. As can be inferred from the results, normalized accelerations are up to 67% and 80% less in GRE and EGE, respectively when all cases are considered. However, the infuence of input motion characteristics as increased force, frequency range and duration were found to be ambiguous on reduction ratios of normalized accelerations for the given input motions of this study.

The variation of horizontal normalized displacemenets at crest (D3) for URE, GRE and EGE for all input motions are given in Figure 6.34.

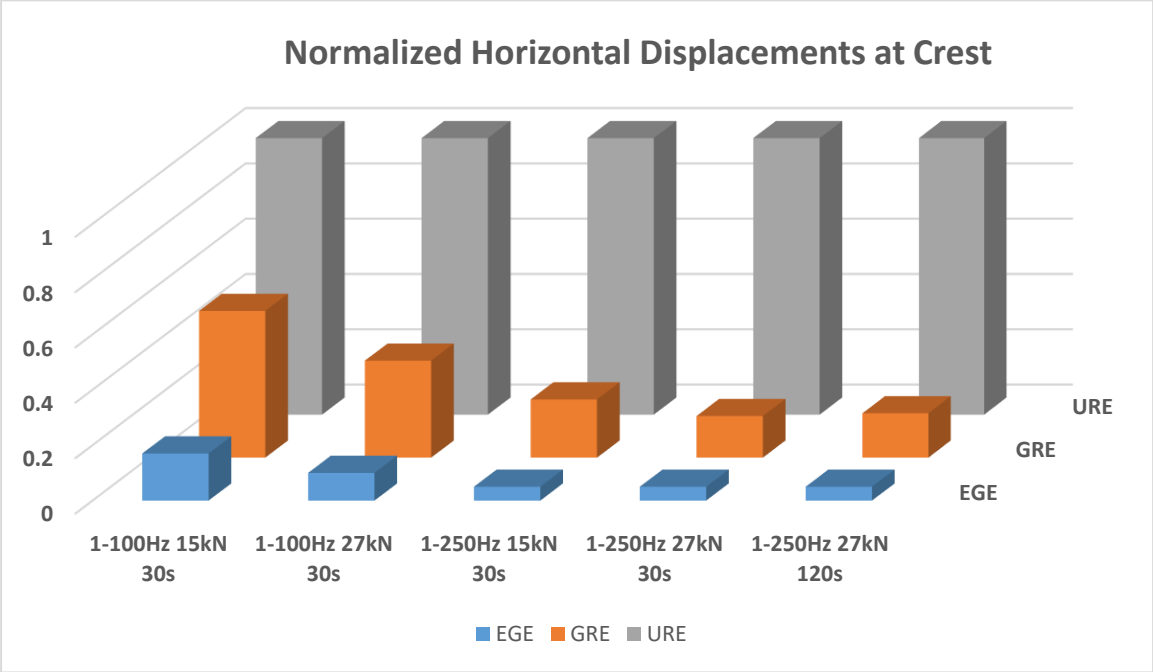

Figure 6.34. Horizontal Normalized Displacements at Crest (D3) for URE, GRE and EGE for all dynamic motions.

Given in Figure 6.34, horizontal normalized displacements at crest in Geogrid and EPS Geofoam Embankment models are 47% and 83% less, respectively for the proposed dynamic motion. When the force level increases to 27kN, normalized displacements are 65% and 90% less for the Geogrid Reinforced and EPS Geofoam Embankment models, respectively. Under, 1-250Hz 15kN 30s, normalized displacements are 69% and 95% less for the Geogrid Reinforced and EPS Geofoam Embankment models, respectively. Similarly, when the force level increases to 27kN in the same frequency range, normalized displacements are 85% and 95% less for GRE and EGE, respectively for the given dynamic motion. Subjected to 1-250Hz 27kN 120s, normalized displacements are 84% and 95% less for the GRE and EGE, respectively. As can be inferred from the results, horizontal normalized displacements are up to 85% and 95% less in GRE and EGE, respectively. Evaluation of the results clearly show that

reduction ratios of horizontal normalized displacements increase with respect to increased force levels, frequency ranges and duration of input motion characteristics in this study due to the light-weight nature and damping properties of the EPS geofoam and provided additional tensile strength and energy dissipation mechanism due to the soil-geogrid interaction for geogrid layers.

The variation of vertical normalized displacements at crest (D4) for URE, GRE and EGE (EW direction) for all input motions are given in Figure 6.35.

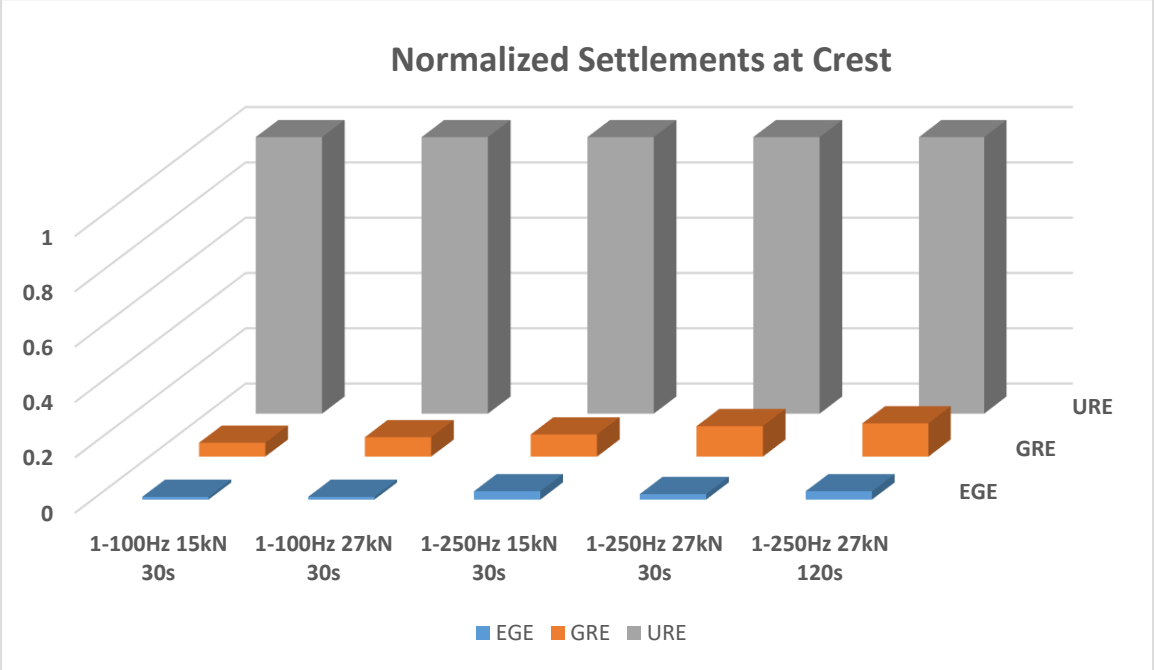

Figure 6.35. Normalized Settlements at crest (D4) for URE, GRE and EGE for all dynamic motions.

Given in Figure 6.35, normalized settlements at crest in Geogrid and EPS Geofoam Embankment models are 95% and 99% less, respectively for the proposed dynamic motion. When the force level increases to 27kN, normalized displacements are 93% and 99% less for the Geogrid Reinforced and EPS Geofoam Embankment models, respectively. Under 1-250Hz 15kN 30s, normalized displacements are 92% and 97% less for the Geogrid Reinforced and

EPS Geofoam Embankment models, respectively. Similarly, when the force level increases to 27kN in the same frequency range, normalized displacements are 89% and 98% less for GRE and EGE, respectively for the given dynamic motion. Subjected to 1-250Hz 27kN 120s, normalized displacements are 88% and 97% less for the GRE and EGE, respectively. As can be inferred from the results, vertical normalized displacements are up to 95% and 99% less in GRE and EGE, respectively. Evaluation of the results show that reduction ratios of normalized displacements are not directly influenced by the input motion characteristics. In other words, the infuence of input motion characteristics as increased force, frequency range and duration were found to be ambiguous on reduction ratios of normalized displacements for the given input motions of this study.

7. SUMMARY AND CONCLUSIONS

Full-scale seismic performance tests of Unreinforced Embankment model, Geogrid Reinforced Embankment model and lightweight EPS Geofoam Embankment model were conducted in field conditions and dynamic motions were applied by the Mobile Seismic Shaker. Five input motions with varying force levels, frequency ranges and durations were used. Also, seismic performance tests of 1/10 scaled Unreinforced, Geogrid Reinforced (T_{ult}: 20kN/m and T_{ult}: 40kN/m) and lightweight EPS Geofoam Highway Embankment models were investigated performing a series of shaking table tests. Summary of the performed experimental studies are summarized in Table 7.1.

Table 7.1. Summary of the performed experimental studies.

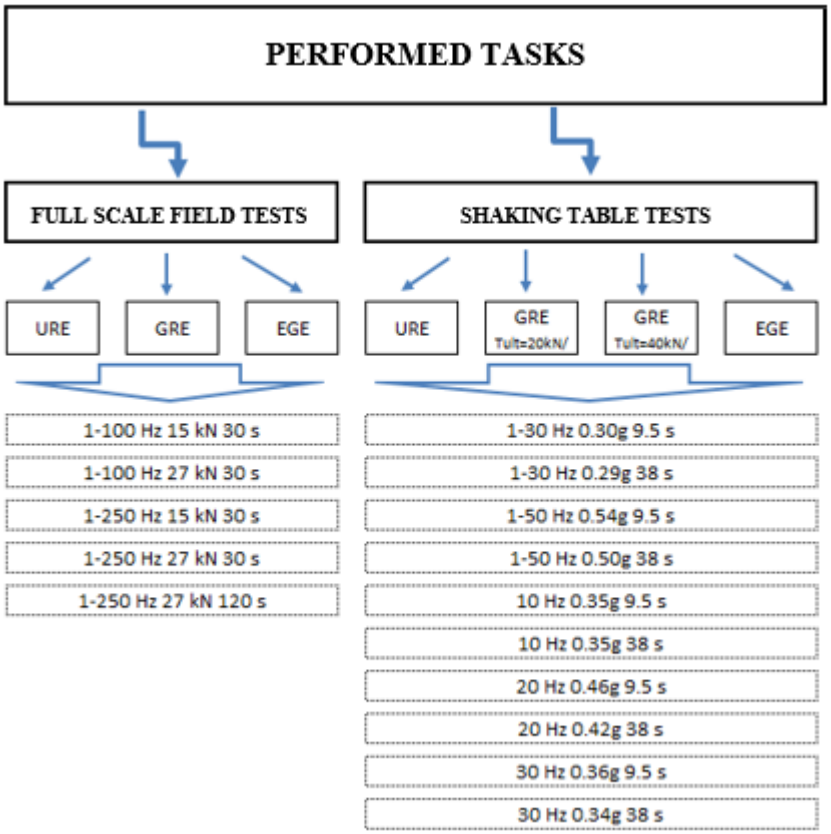

Following conclusions are reached from the scaled shaking table experiments:

- 1/10 scaled shaking table tests were performed with URE, GRE and EGE using 10 different input motions. It is seen that geogrid reinforced embankment model perform much better in terms of dynamic performance when subjected to incremental sine sweep excitations (i.e. 1-50Hz).

- Duration of the dynamic excitation is found to be related with measured displacements. However, no direct influence of duration on dynamic behavior of highway embankment models is found.

- Transmitted accelerations measured at toe (A8) are 24.4% and 39.8% less in geogrid reinforced embankment models with T_{ult}: 20kN/m and T_{ult}: 40kN/m, respectively when compared to the unreinforced case. Transmitted acceleration reduction at toe in EPS geofoam embankment model is limited to 21%. Even though the reduction ratios are similar, geogrid reinforcement successfully reduced the transmitted accelerations at toe with the provided additional tensile strength by the geogrid materials.

- Shaking table test results indicate that horizontal displacements measured from the toe (D11) and the crest (D12) of the geogrid reinforced embankment model are up to 74.6% and 87.2% less, respectively when compared to unreinforced model. Similarly, vertical displacements at crest level (D13) are 83.6% less in comparison with the unreinforced case due to the geogrid-soil interaction. Geogrid reinforcement significantly reduces the displacements on the embankment model.

- SA values are up to 13.3% (A8) and 10.7% (A9) less in geogrid reinforced model in comparison with unreinforced case. Also, effectiveness of geogrid reinforcement in terms of period shift effect is also observed. Structural period at crest level shifts from 0.02s to 0.03s. This is due to the soil-geogrid interaction.

- Related literature suggests that the increasing frequency leads to an increase in secant stiffness of geogrid reinforcement which is directly related with the efficiency of the reinforcement (Bathurst and Cai, 1994). This explains the reason why reduction ratios of total displacements and transmitted accelerations are higher under 1-50Hz incremental motion.

- Transmitted accelerations measured on A8 and A9 are 21% and 29.4% less in EPS geofoam embankment model than unreinforced model case. Damping properties of EPS geofoam caused the reduction of the transmitted accelerations throughout the shaking table experiments.

- Horizontal displacements measured from the toe (D11) and the crest (D12) of the geogrid reinforced embankment model are 71.6% and 75.2% less to that of the unreinforced model. Similarly, vertical displacements at crest level (D13) are 78.3% less.

- Amplification factors (AF) increase due to relative height of the embankment models. AF values are higher in unreinforced model than other two geogrid reinforced models. As the tensile strength of the geogrid increases, the interaction between the soil and geogrid also improves, leading to a decrease in the degree of AF values. In addition, AF values in the foundation soil were found to be lower than 1.

- Up to 34% normalized acceleration reduction is calculated in geogrid reinforced embankment model with T_{ult}: 40kN/m. Crest level normalized accelerations are 29% less in lightweight EPS geofoam embankment model when compared to the unreinforced case.

- Normalized acceleration values are 24% and 40% less in geogrid reinforced embankment models with T_{ult}: 20kN/m and T_{ult}: 40kN/m, respectively in comparison with the unreinforced case. Normalized acceleration reduction ratio for EPS geofoam embankment model is limited to 15%.

- Crest level normalized horizontal displacements are reduced by 86% and %87 in geogrid reinforced embankment models with T_{ult}: 20kN/m and T_{ult}: 40kN/m, respectively. It is seen that geogrid reinforcement layers provide the required additional tensile strength to withstand the induced displacements. The calculated reduction ratio in normalized displacements is found to be 75% in EPS geofoam embankment model.

- Normalized vertical displacements at crest level clearly show the capability of EPS geofoam inclusions in reducing the degree of settlements as calculated normalized displacements are 43% less in comparison with the unimproved case. The reduction of normalized displacements is 29% in both geogrid reinforced embankment models (D13). Geogrid reinforcement in this study is found to be more effective in limiting the horizontal displacements than vertical displacements due to the additional tensile strength, interlocking effect and the soil-geogrid interaction (Koerner, 2005).

- The use of EPS geofoam inclusions effectively reduces overall displacements and transmitted accelerations by taking advantage of its exceptional cushioning properties (super lightweight and high damping).

Following conclusions are reached from the field-scale seismic performance tests with MSS:

- Geogrid Reinforced Embankment model and EPS Geofoam Embankment model perform much better in terms of dynamic performance when subjected to increased force, duration and wider frequency ranges during seismic performance tests with MSS.

- Related literature (Bathurst and Cai, 1994) suggests that the increasing frequency leads to an increase in secant stiffness of geogrid reinforcement which is directly related with the efficiency of the reinforcement. This explains the reason why reduction ratios of total displacements and transmitted accelerations are higher under dynamic motions with broader frequency ranges (1-250Hz).

- Duration of the dynamic excitation is found to be related with measured displacements as expected. Increased duration of the dynamic motion from 30s to 120s increased the efficiency of the geogrid and EPS geofoam material which enhance the dynamic behavior of embankment models.

- Acceleration measurements taken from slopes and the crest of the Geogrid Reinforced Embankment model are up to 30% and 68.8% less, respectively in comparison to the Unreinforced Embankment model.

- Calculated spectral acceleration values are up to 72% less in comparison to the Unreinforced Embankment model under 1-250Hz 15kN 30s.

- Structural periods on Unreinforced Embankment model are generally in the range of 0.015s to 0.019s. However, the effectiveness of the geogrid reinforcement in terms of additional tensile strength and the interlocking effect between aggregates and the geogrid layers, “Period Shift” effect is observed on Geogrid Reinforced Embankment model as the structural periods are in the range of 0.019s to 0.025s under 1-100Hz 27kN 30s and 1-250Hz 27kN 120s of motions.

- Horizontal displacements are up to 88.4% and the vertical displacements are up to 95.1% less on Geogrid Reinforced Embankment model than the Unreinforced Embankment model due to the additional tensile strength of the geogrid materials.

- Up to 67% normalized acceleration reduction is calculated in Geogrid Reinforced Embankment model. Also, normalized horizontal displacements and normalized vertical displacements are 85% and 95% less than the Unreinforced case. Adding the geogrid reinforcement layers provide additional tensile strength to withstand the induced displacements.

- The geogrid reinforcement significantly enhances embankment stability, reducing displacements by noteworthy percentages (up to 95.1%) for the applied dynamic motions, demonstrating its efficacy in decreasing measured displacements under various dynamic motions.

- Acceleration measurements from slopes and the crest of the EPS Geofoam Embankment model are up to 70.6% and 80% less, respectively in comparison to the Unreinforced Embankment model due to the light-weight EPS geofoam material results in lower inertia forces during dynamic loading as stated by Horvath, 1995.

- Calculated spectral acceleration values on EPS Geofoam model are up to 82.7% less in comparison to the Unreinforced Embankment model.

- "Period Shift" effect is also observed on EPS Geofoam Embankment model as the structural periods are generally in the range of 0.025s to 0.039s where the structural periods obtained from Unreinforced Embankment model is in the range of 0.015s to 0.019s. Using EPS geofoam fill might help absorb and dissipate seismic forces affectively.

- EPS Geofoam significantly reduces displacement values under dynamic loading conditions across all sensors, performing so much better than both the Unreinforced and Geogrid Reinforced models. Horizontal slope displacements are up to 97.1%

and the vertical displacements on the crest are up to 99.3% less on EPS Geofoam Embankment model than the Unreinforced Embankment model.

- Calculated normalized accelerations in EPS Geofoam model are up to 80% less than Unreinforced model. Moreover, due to its damping properties, normalized horizontal displacements and normalized vertical displacements are up to 96% and 99% less than the Unreinforced case.

- Overall, EPS Geofoam significantly enhances structural stability, reducing accelerations and displacements by notable percentages (up to 99%) for the applied dynamic motions, demonstrating a very good performance in decreasing displacements under various dynamic motions. This proves the effectiveness of EPS Geofoam in enhancing the embankment stability and resilience of the embankment, making it an excellent solution for applications in earthquake-prone areas.

Obtained experimental results are directly related to the dimensions and material properties of the highway embankment models, the characteristics of the applied dynamic loads and source, and the foundation soil conditions used in this thesis. This is the first intensive study in this field and evaluating the results in comparison with the different improvement techniques will be a guidance for the future studies. Due to limitations, the vehicle load on the model embankments was neglected in the present field studies. Considering the vehicle loads on the embankment models are recommended for the future studies.

.

REFERENCES

1993 AASHTO Guide for Design of Pavement Structures, American Association of State Highway and Transportation Officials, Washington, D.C.

Abdessemed M., S. Kenai, and A. Bali, 2015, "Experimental and numerical analysis of the behavior of an airport pavement reinforced by geogrids", *Construction and Building Materials*, Vol. 94, pp. 547–554.

Abramson, L. W., T. S. Lee, Sharma, S. and G. M. Boyce, *Slope Stability and Stabilization Methods*, John Wiley&Sons, Inc, New York, USA, 2002.

Akay, O., A. T. Özer, G. A. Fox, S.F. Bartlett, and D. Arellano, 2013, "Behavior of Sandy Slopes Remediated by EPS-Block Geofoam under Seepage Flow", *Geotextiles and Geomembranes*, Vol. 37, pp. 81-98.

Arysad, M., I. B. Mochtar, N. E. Mochtar, and Y. F. Arifin, 2020, "Road embankment full-scale investigation on soft soil with geotextile stabilization", *International Journal of GEOMATE*, Vol. 19, No. 71, pp. 145-152.

ASTM D1621-16, Standard Test Method for Compressive Properties of Rigid Cellular Plastics. ASTM International, PA, USA.

ASTM D3999, Standard Test Methods for the Determination of the Modulus and Damping Properties of Soils Using the Cyclic Triaxial Apparatus. ASTM International, PA, USA.

ASTM D422, Standard Test Method for Particle-Size Analysis of Soils. ASTM International, PA, USA.

ASTM D4719-07, StandardTest Methods for Prebored Pressuremeter Testing in Soils. ASTM International, PA, USA.

ASTM D6817/D6817M-17, Standard Specification for Rigid Cellular Polystyrene Geofoam. ASTM International, PA, USA, 2021.

ASTM D7263-21, Standard Test Methods for Laboratory Determination of Density and Unit Weight of Soil Specimens. ASTM International, PA, USA.

ASTM D4439, Standard Terminology for Geosynthetics. ASTM International, PA, USA.

ASTM D4595-11, Standard Test Method for Tensile Properties of Geotextiles by the Wide-Width Method. ASTM International, PA, USA.

Athanasopoulos, G.A., C.P. Nikolopoulou, V.C. Xenaki, and V.D. Stathopoulou, 2007, "Reducing the Seismic Earth Pressure on Retaining Walls by EPS Geofoam Buffers - Numerical Parametric Study", *Proceedings of the Geosynthetics Conference*, Washington, DC.

Athanasopoulos, G.A, P. C. Pelekis, and V. C. Xenaki, 1999, "Dynamic Properties of EPS Geofoam: An Experimental Investigation", *Geosynthetyics International*, Vol. 6, No. 3, pp. 171-194.

Bakir, B. S. and E. Akis, 2005, "Analysis of a highway embankment failure associated with the 1999 Duzce Turkey Earthquake," *Soil Dyn. Earthq. Eng*., Vol. 25, No. 3, pp. 251–260.

Bartlett, S.F., and Z. Amini, 2018, "Design and Evaluation of Seismic Stability of Free-Standing EPS Embankment for Transportation Systems", *5th International Conference*

on the Use of Geofoam Blocks in Construction Applications, May, Kyrenia, Northern Cyprus, 9th – 11th, 2018.

Bathurst, R.J, S. Zarnani, A. Gaskin, 2007, "Shaking table testing of geofoam seismic buffers", *Soil Dynamics and Earthquake Engineering,* Vol. 27, pp. 324–332.

Bathurst, R. J., M. El-Emam and M. M. Mashhour, 2002, "Shaking Table Model Study on the Dynamic Response of Reinforced Soil Walls", *Proceedings of the 7th International Geosynthetics Conference*, Nice, France, 22-27 September 2002. Balkema, Lisse, The Netherlands, Vol. 1, pp. 99-102.

Bay, J., and K. Stokoe II, Development of A Rolling Dynamic Deflectometer for Continous Deflection Testing of Pavements, Project Summary Report 1422-3F, The University of Texas, USA, 1998.

Bergado, D. T., P. V. Long, and B. R. S. Murthy, 2002, "A case study of geotextile-reinforced embankment on soft ground", *Geotextiles and Geomembranes,* Vol. 20, pp. 343-365.

Bertero, S., P. A. Tarazaga, and R. Sarlo, 2022, "In situ seismic testing for experimental modal analysis of civil structures", *Engineering Structures*, Vol. 270.

Boaga, J., I. Barone, G. P. Deidda, G. Cassiani, and C. Strobbia, 2021, "Multi-drive level Vibroseis test to evaluate the non-linear response of soft soils", *Soil Dynamics and Earthquake Engineering*, Vol. 149.

Bosscher, P. J., T. B. Edil, and S. Kuraoka, 1997, " Design of highway embankments using tire chips", *Journal of Geotechnical and Geoenvironmental Engineering,* Vol. 123, No. 4, pp. 295-304.

Çağatay, A., *Investigation of the Effect of Tire Waste Inclusions on the Shear Strength Parameters of Sand*, M.Sc. Thesis, Boğaziçi University, 2008.

Cao, W. Z., J. J. Zheng, J. Zhang, and R. J. Zhang, 2016, "Field test of a geogrid-reinforced and floating pile-supported embankment", *Geosynthetics International*, Vol. 23, No. 5, pp. 348-361.

Chaiyaput, S., D. T. Bergado, and S. Artidteang, 2014, "Measured and simulated results of a Kenaf Limited Life Geosynthetics (LLGs) reinforced test embankment on soft clay", *Geotextiles and Geomembranes*, Vol. 42, pp. 39-47.

Chakraborty, A., and V. A. Sawant, 2024, "Response of embankment on liquefiable soil to sequential ground motions considering mitigation measures", *Soil Dynamics and Earthquake Engineering*, Vol. 176.

Chalaturnyk, R. J., J. D.Scott, D. H. Chan, and E. A. Richards, 1988, "Stresses and deformations in a reinforced slope", *Proceedings of the 3rd Canadian Symposium on Geosynthetics*, Kitchener, Ontario, Canada, pp. 79-89.

Chang, W.J., 2002, *Development of an In-Situ Dynamic Liquefaction Test*, Ph.D. Thesis, The University of Texas at Austin.

Chen, R. P., Y. W. Wang, X. W. Ye, X. C. Bian, and X. P. Dong, 2016, "Tensile force of geogrids embedded in pile-supported reinforced embankment: A full-scale experimental study", *Geotextiles and Geomembranes*, Vol. 44, No. 2, pp. 157-169.

Chen, X., J. Zhang, X. Wang, 2015, "Full-scale field testing on a highway composite pavement dynamic responses", *Transportation Geotechnics*, Vol. 4, pp. 13-27.

Correia, N. S., 2014, *Performance of flexible pavements enhanced using geogrid- reinforced asphalt overlays*, Ph.D. Thesis, University of Sao Paulo, 2014.

Cox, B., 2006, *Development of a Direct Test Method for Dynamically Assessing the Liquefaction Resistance of Soils In Situ*, Ph.D. Thesis, University of Texas at Austin.

Dadashiserej, A., A. Jana, Z. Xu, A. W. Stuedlein, T. M. Evans, K. H. Stokoe, and B. R. Cox, 2023, "Dynamic response of a low plasticity silt deposit: comparison of in-situ and laboratory responses", *Canadian Geotechnical Journal*.

Day, R. W., 2002, *Geotechnical Earthquake Engineering Handbook*, McGRAW-HILL.

Drygala, I. J., J. M. Dulinska, M. A. Polak, 2020, "Seismic Assessment of Footbridges under Spatial Variation of Earthquake Ground Motion (SVEGM): Experimental Testing and Finite Element Analyses", *Sensors*, 20.

Duncan, J. M., S. G. Wright, 2005, *Soil Strenght and Soil Slope Stability*, John Wiley&Sons, Inc, New York, USA.

Edinçliler, A, and Y. S. Toksoy, 2017, "Shake Table Tests to Measure the Dynamic Performance of Geotextile-reinforced Embankment", *Periodica Polytechnica Civil Engineering*, Vol. 6, No. 4, pp. 803-814.

Edinçliler, A. and E. Güler, 1999, "Geotextile-reinforced embankments on soft clays— effects of a foundation soil crust strengthened by lime diffusion," *Geosynthetics International*, Vol. 6, No. 2, pp. 71–91.

Edinçliler, A., and Y. S. Toksoy, 2018, "Investigation of seismic performance of geotextile reinforced embankments by shake table tests and numerical modelling", *11th International Conference on Geosynthetics*, 11ICG, 16-21 September, Seoul, Korea.

Edinçliler, A., and Y. S. Toksoy, 2022, "Effects of Geogrid Reinforcement on the Seismic Performance of Lightweight Embankments", *IOP Conference Series: Material Science and Engineering*, Vol. 1260, pp. 1-11.

Edinçliler, A., 2007, "Using waste tire–soil mixtures for embankment construction", International Workshop on Scrap Tire Derived Geomaterials ''Opportunities and Challenges", *Kanto Branch of Japanese Geotechnical Society*, pp. 319–328.

Edinçliler, A., G. Baykal, and A. Saygılı, 2010, "Influence of different processing techniques on the mechanical properties of used tires in embankment construction", *Waste Management*, Vol. 30, pp. 1073–1080.

Edinçliler, A., and Y. S. Toksoy, 2017, "Physical Model Study of the Seismic Performance of Highway Embankments with and without Geotextile", *Journal of Earthquake and Tsunami*, Vol. 11, No. 2.

Edinçliler, A., and Y. S. Toksoy, 2018, "Effects of improvement techniques on seismic performance of highway embankments.", *16th European conference on earthquake engineering*, 16ECEE, 18–21 June, Thessaloniki, Greece.

El-Emam, M. E. and R. J. Bathurst, 2004, "Experimental design, instrumentation and interpretation of reinforced soil wall response using a shaking table", *Int. J. Phys. Model. Geotecnics*, Vol. 4, pp. 13–32.

El-Emam, M. E. and R. J. Bathurst, 2007, "Influence of reinforcement parameters on the seismic response of reduced-scale reinforced soil retaining walls," *Geotext. Geomemb*, Vol. 25, pp. 33–49.

El-Emam, M. E., and R. J. Bathurst, 2004, "Experimental design, instrumentation and interpretation of reinforced soil wall response using a shaking table", *International Journal of Physical Modelling in Geotecnics*, Vol. 4, pp. 13-32.

Environmental Protection Agency (US), 2002, Secondary Drinking Water Regulations: Guidance for Nuisance Chemicals.

Farrag, S., N. Gucunski, B. Cox, F. Menq, F. Moon, and J. DeVitis, 2019, "Assessing the significance of dynamic soil-structure interaction by using large-amplitude mobile shakers", *Eighth International Conference on Case Histories in Geotechnical Engineering*, pp. 139-150.

Federal Highway Administration (FHWA), 2009, Design and Construction of Mechanically Stabilized Earth Walls and Reinforced Soil Slopes, Publication No. FHWA-NHI-09-083.

Feng, B., Y. I. Basarah, Q. Gu, X. Duan, X. Bian, E. Tutumluer, and H. Huang, 2021, "Advanced full-scale laboratory dynamic load testing of a ballasted high-speed railway track", *Transportation Geotechnics*, Vol. 29.

FHWA NHI-07-092, Geosynthetic Design & Construction Guidelines, U.S. Department of Transportation Federal Highway Administration, Washington, USA,

Foinquinos, R., and J. M. Roesset, 2000, "Elastic layered half-spaces subjected to dynamic surface loads," *Wave Motion in Earthquake Engineering*, pp. 215-246, Southampton, UK.

Forsman, J., T. Dettenborn, P. Skepast, M. Mets, M. Olep, A. Ellman, I. Vallas, I. Tonts, K. Kontson, 2016, "Full scale reinforced road embankment test sections over soft peat layer, Võõbu, Estonia", *Proceedings of the 17th Nordic Geotechnical Meeting Challenges in Nordic Geotechnic*, 25th – 28th of May, Reykjavik, Iceland.

Frary, R., 2002, *Fault Imaging with High-Resolution Seismic Reflection for Earthquake Hazard and Geothermal Resource Assessment in Reno,* Nevada, M.Sc. Thesis, The University of Nevada, USA.

Gade, V.K., and S. M. Dasaka, 2019, "Static and Cyclic Properties of EPS Geofoam. In: Thyagaraj, T. (eds) Ground Improvement Techniques and Geosynthetics", *Lecture Notes in Civil Engineering* , Vol 14. Springer, Singapore.

Gazetas, G., and P. Dakoulas, 1991, "Seismic Analysis and Design of Rockfill Dams: State-of-the-Art, *Soil Dynamics and Earthquake Engineering*", Vol. 11, pp. 27-61.

Graziani, A., E. Pasquini, G. Ferrotti, A. Virgili, and F. Canestrari, 2014, "Structural response of grid-reinforced bituminous pavements", *Materials and Structures*, Vol. 47, pp. 1391-1408.

Han, X., P. Ji, Q. Gu, and G. Mu, 2021, "Model Test Study on Dynamic Response of Expressway Plastic-Reinforced Earth Embankment under Earthquake", *Geofluids*, Vol. 1.

Harris, D. W., N. Snorteland, T. Dolen, and F. Travers, 1999, Shaking Table 2D Models of a Concrete Gravity Dam, Technical Reports, US Department of the Interior Dam Safety Office.

Harris, H. G. and G. M. Sabnis, 1999, *Structural Modeling and Experimental Techniques*, CRC Press, New York.

Hartman, D., M. Ledezma, M. Xiao, and M. Zoghi, 2013, "Shake Table Test of MSE Wall with Tire Derived Aggregerates (TDA) Backfill", *Geo-Congress*, pp. 1168-1177.

Hazarika H., 2001, “Mitigation of Seismic Hazard on Retaining Structures - A Numerical Experiment”, *Proceedings of the 11th International Offshore and Polar Engineering Conference*, Stavanger, Norway, 17-22 June 2001, pp. 459-464.

Hazarika H., and S. Okuzono, 2002, “An Analysis Model for a Hybrid Interactive System Involving Compressible Buffer Material”, *Proceedings of the 12th International Offshore and Polar Engineering Conference,* Kitakyushu, Japan, 26-31 May 2002, pp. 622-629.

Hazarika H., and S. Okuzono, 2004, “Modeling the Behaviour of a Hybrid Interactive System Involving Soil, Structure and EPS Geofoam”, *Soils and Foundations,* Vol. 44, No. 5, pp. 149-162.

Hazarika, H., E. Kohama, and T. Sugano, 2008, “Shaking Table Tests on Waterfront Structures Protected with Tire chips Cushion”, *Journal of Geotechnical and Environmental Engineering,* ASCE, pp.134-11.

Hazarika, H., S. Okuzono, Y. Matsuo, 2003, “Seismic stability enhancement of rigid nonyielding structures”, *Proceedings of the 13th International Offshore and Polar Engineering Conference,* Honolulu, HI, USA, 25–30 May 2003, pp. 1244–1249.

Hryciw, R. D., S. Vitton, and T. G. Thomann, 1990, “Liquefaction and Flow Failure During Seismic Exploration,” *Journal of Geotechnical Engineering,* ASCE, Vol. 116, No. 12, pp. 1881-1899.

Huang, C. C., J. C. Horng, W. J. Chang, J. S. Chiou, and C. H. Chen, 2011, “Dynamic behaviour of reinforced walls - Horizontal displacement response”, *Geotextiles and Geomembranes,* Vol. 29, pp. 257-267.

Huang, J., and J. Han, 2009, "3D coupled mechanical and hydraulic modeling of a geosynthetic-reinforced deep mixed column-supported embankment", *Geotextiles and Geomembranes*, Vol. 27, pp. 272-280.

Huckert, A., L. Briancon, P. Villard, and P. Garcin, 2016, "Load transfer mechanisms in geotextile-reinforced embankments overlying voids: Experimental and analytical approaches", *Geotextiles and Geomembranes*, Vol. 44, No. 3, pp. 442-456.

Humphrey, D. N., 1996, Invertigation of Exothermic Reaction in Tire Shred Fill Located on SR 100 in Ilwaco, Washington, Consulting Report to FHWA, US Department of Transportation.

Iai, S., 1989, "Similitude for shaking table tests on soil-structure fluid models in 1-g gravitational field", *Soils and Foundations*, Vol. 29, No. 1, pp. 105–111.

Iai, S., 1997, "Discussions: One gravity model testing" , *Soils Found*., Vol. 37, No. 1, pp. 137.

Iai, S. and T. Sugano, 1999, "Soil-structure interaction studies through shaking table test" *Earthquake Geotechnical Engineering*, Vol. 3, pp. 927–940.

Karayolları Teknik Şartnamesi, 2013, Karayolları Genel Müdürlüğü, Ankara, Türkiye.

Kavazanjian, E.J., B. Hushmand, G. R. Martin, 1991, "Frictional Base Isolation Using a Layered Soil-Synthetic Liner System", *Proceedings of the Third U.S. Conference on Lifeline Earthquake Engineering*, pp. 1139-1151.

Koerner, R. M., 2005, *Designing with Geosynthetics*, Pearson Education, Inc, Upper Saddle River, NJ, USA.

Kramer, S.L., 1996, *Geotechnical Earthquake Engineering*, Prentice-Hall, New Jersey.

LeBlanc, M.T, 2013, *Field measurement of the linear and nonlinear constrained moduli of granular soil,* Ph.D. Thesis, The University of Texas at Austin, U.S.A.

Lehtonen, V., T. Länsivaara, J. Mansikkamäki, and C. Meehan, 2015, "Full-scale embankment failure test under simulated train loading", *Geotechnique*, Vol. 65, No. 12, pp. 961-974.

Li, P., X. Ling, F. Zhang, Y. Li, and Y. Zhao, 2017, "Field testing and analysis of embankment vibrations induced by heavy haul trains", *Shock and Vibration*.

Likitlersuang, S., K. Kounyou, and G. A. Prasetyaningtiyas, 2020, "Performance of geosynthetic cementitious composite mat and vetiver on soil erosion control", *Journal of Mountain Science*, Vol. 17, No. 6, pp. 1410-1422.

Lin, L.K., L. H. Chen, and R. H. L. Chen, 2010, "Evaluation of geofoam as a geotechnical construction material", *Journal of Materials in Civil Engineering*, Vol. 22, No. 2, pp. 160–170.

Lin, M. L., and K. L. Wang, 2006, "Seismic behavior in a large-scale shaking table test", *Engineering Geology*, Vol. 86, pp. 118-133.

Lin, Y., W. Leng, G. Yang, L. Li, and J. Yang, 2015, "Seismic response of embankment slopes with different reinforcing measures in shaking table tests", *Natural Hazards*, Vol. 76, pp. 791-810.

Ling, H. I., M. H. Wu, D. Leshchinsky, B. Leshchinsky, 2009, "Centrifuge Modelling of Slope Instability", *Journal of Geotechnical and Geoenvironmental Engineering*, Vol. 135, pp. 758-767.

Liu, D., J. Wang, F. Du, 2021, “Research Article Study on the Dynamic Response of Gravel Soil Low Embankment under a Long-Time Dynamic Loading Based on Model Test”, *Advances in Materials Science and Engineering*.

Lo Grasso, A. S., M. Maugeri, and P. Recalcati, 2005, “Seismic Behavior of Geosynthetic Reinforced Slopes with Overload by Shaking Table Tests”, *Slopes and Retaining Structures under Static and Seismic Conditions,* ASCE Geotechnical Special Publication No. 140, CDROM.

Malai, A., and S. Youwai, 2021, “Stiffness of Expanded Polystyrene Foam for Different Stress States”, *International Journal of Geosynthetics and Ground Engineering*, Vol. 7, No. 80.

Mitra, M. V., 1961, “Disturbance produced in an elastic half space by impulsive normal pressure,” *Proc. Camb. Phil. Soc. Math. Phys. Sci*., Vol. 60, pp. 683- 696.

Nakazawa, H., Y. Kawamata, S. Shibuya, S. Kato, K. B. Jeong, J. Baek, and Y. Moriguchi, 2020, “Full-scale experiment of earthquake resistant embankment using flexible container bag” , *Journal of Disaster Research,* Vol. 15, No. 6, pp. 765-781.

NEHRP Recommended Provisions for Seismic Regulations for New Buildings, 1994, FEMA.

Neto, J. A., and D. Rodrigues, 2021, “Instrumented load tests and layered elastic theory analysis of a large-scale EPS block embankment”, *Transportation Geotechnics,* Vol. 26.

Neupane, R., 2015, *Expanded Polystyrene Geofoam embankment for support of railway embankments*, Ph.D. Thesis, The University of Utah, USA.

Nunez, M.A., L. Briancon, and D. Dias, 2013, “Analyses of a pile-supported embankment over soft clay: Full-scale experiment, analytical and numerical approaches”, *Engineering Geology*, Vol. 153, pp. 53-67.

Omer, A. and U. Resat, 2002, “Back-analysis of a seismically induced highway embankment failure during the 1999 Duzce earthquake” ,*Environ. Geol*. Vol. 42, No. 6, pp. 621–631.

Özer, A. T., and E. Akınay, 2019, “First geofoam roadway embankment application in Turkey”, *5th International Conference on Geofoam Blocks in Construction Applications: Proceedings of EPS 2018*, pp. 71-80.

Pelekis, P. C., V. C. Xenaki, and G. A. Athanasopoulos, 2000, “Use of EPS Geofoam for Seismic Isolation of Earth Retaining Structures: Results of an FEM Study”, *Proceedings of the Second European Geosynthetics Conference*, Bologna, Italy, pp. 843-846.

Perez, A., and R. D. Holtz, 2004, “Seismic Response of Reinforced Steep Soil Slopes: Results of Shaking Table Study”, *Geotechnical Engineering for Transportation Projects*, ASCE Geotechnical Special Publication No. 126, pp. 1664-1672.

Pham, T. A., and D. Dias, 2021, “Comparison and evaluation of analytical models for the design of geosynthetic-reinforced and pile-supported embankments”, *Geotextiles and Geomembranes*, Vol. 49, No. 3, pp. 528-549.

Project Development and Design Manual, 2008, FHWA, Washington, USA..

Puppala, A. J., P. Ruttanaporamakul, T. V. Bheemasetti, and A. Shafikhani, 2019, “Laboratory and field investigations on geofoam”, *Journal of Pipeline Systems Engineering and Practice*, Vol. 10, No. 1.

Rajabian, A., H. Ghiassian, and B. V. S. Viswanadham, 2013, “Centrifuge study of anchored geosynthetic slopes”, *Geosynthetics International*, Vol. 20, No.3.

Rezania, M., M. Bagheri, M. M. Nezhad, and N. Sivasithamparam, 2017, "Creep analysis of an earth embankment on soft soil deposit with and without PVD improvement", *Geotextiles and Geomembranes*, Vol. 45, No. 5, pp. 537-547.

Richart, F. E., J. R. Hall, and R. D. Woods, 1970, *Vibration of Soils and Foundations*, Prentice-Hall, Inc., New Jersey.

Roberts, J. N., 2014, *Direct In-Situ Evaluation of Liquefaction Susceptibility*, M.Sc. Thesis, The University of Texas at Austin, TX, USA.

Saevarsdottir, T., and S. Erlingsson, 2015, "Modelling of responses and rutting profile of a flexible pavement structure in a heavy vehicle simulator test", *Road Materials and Pavement Design,* Vol. 16, No. 1, pp. 1-18.

Sahadewa, A., D. Zekkos, R. D. Woods, and K. H. Stokoe, 2015 "Field Testing Method for Evaluating the Small-Strain Shear Modulus and Shear Modulus Nonlinearity of Solid Waste", *Geotechnical Testing Journal*, Vol. 38, No. 4, pp. 427-441.

Sloan, J. A., 2011, *Column-supported embankments: full-scale tests and design recommendations*, Ph.D. Thesis, Virginia Polytechnic Institute and State University, USA.

Srilatha, N.,G. M. Latha, and C. G. Puttappa, 2013, "Effect of frequency on seismic response of reinforced soil slopes in shaking table tests," *Geotext. Geomembr*., Vol. 36, pp. 27–32.

Stark, T. D., D. Arellano, J. S. Horvath, and D. Leshchinsky, Guideline and Recommended Standard for Geofoam Applications in Highway Embankments, 2004, NCHRP Report 529, Washington, USA.

Stokoe II, K., S. Hwang, B. Cox, F. Y. Menq, J. N. Roberts, and K. Park, 2019, "Field studies of the natural and built environments using large mobile shakers", *Earthquake Geotechnical Engineering for Protection and Development of Environment and Constructions*, Proceedings of the 7th International Conference on Earthquake Geotechnical Engineering, Vol. 3, pp. 619-634.

Stokoe, K. H., S. Hwang, J. N. Roberts, F. M. Menq, A. K. Keene, R. C. Lee, and B. B. Redpath, 2017, "Deep Downhole Seismic Testing Using a Hydraulically-Operated, Controlled-Waveform Vibroseis", *16th World Conference on Earthquake Engineering*, 16WCEE.

Stokoe, K. H., J. N. Roberts, S. Hwang, B. R. Cox, and F. Menq, 2016, "Effectiveness of inhibiting liquefaction triggering by shallow ground improvement methods: field shaking trials with T-Rex at one area in Christchurch, New Zealand", *Proc., 24th Geotechnical Conf. of Torino*, Oxfordshire, UK.

Tamate, S., N. Suemasa, and T. Katada, 2012, "Simulation of Precipitation on Centrifuge Models of Slopes", *International Journal of Physical Modelling in Geotechnics*, Vol. 12, pp. 89-101.

Tanchaisawat, T., P. Voottipruex, D. T. Bergado, and S. Hayashi, 2008, "Performance of full scale test embankment with reinforced lightweight geomaterials on soft ground", *Lowland Technology International*, Vol. 10, No. 1, pp. 84-92.

Taylor, C. A., A. R. Dar, and A. J. Crewe, *Shaking Table Modelling of Seismic Geotechnical Problems*, Earthquake Engineering Research Centre, University of Bristol, UK, 2006.

Toksoy, Y. S., 2014, *Investigation of the Seismic Performance of Reinforced Highway Embankments*, M.Sc. Thesis, Boğaziçi University, Istanbul, Turkey.

Toksoy, Y. S., and A. Edinçliler, 2023, "Dynamic Response Analysis of Highway Embankments", *Lecture Notes in Civil Engineering*, Vol. 305, pp. 311-319.

Towhata, I., 2008, *Geotechnical Earthquake Engineering*, Springer, Verlag Berlin Hiedelberg, Germany.

Trandafir, A. C., S. F. Bartlett, and B. N. Lingwall, 2010, "Behavior of EPS geofoam in stress-controlled cyclic uniaxial tests", *Geotextiles and Geomembranes*, Vol. 28, pp. 514-524.

Turan, A., M. H. El Naggar, D. Dundas, 2013, "Investigation of Induced Trench Method Using a Full Scale Test Embankment", *Geotechnical and Geological Engineering*, Vol. 31, No. 2, pp. 557-568.

Turkish Earthquake Code, 2018.

Tutumluer, E., I. I. A. Qamhia, and H. Ozer, 2019, "Field Performance Evaluations of Sustainable Aggregate By-product Applications", *Geotechnics for Transportation Infrastructure*, Lecture Notes in Civil Engineering, Vol. 28, pp. 3-23.

Vega-Meyer, R., and Y. Shao, 2005, "Geogrid-reinforced and pile-supported roadway embankment", *Contemporary Issues in Foundation Engineering*, pp. 1–13.

Viswanadham, B. V. S., and D. König, 2009, "Centrifuge Modelling of Geotextile Reinforced Slopes Subjected to Differential Settlements", *Geotextiles and Geomembranes*, Vol. 27, pp. 77-88.

Wang, J., H. W. Huang, B. Zhang, F. Y. Menq, K. B. Nakshatrala, Y. L. Mo, and K. H. Stokoe, 2022, "Active isolation tests of metamaterial-based barriers and foundation", *Engineering Structures*, Vol. 260.

Wang, J., Q. Li, C. Yang, C. Zhou, 2018, "Dynamic response and damage character of road embankment under strong earthquake", *International Journal of Distributed Sensor Networks*, Vol. 14.

Wang, Z., L. Yao, 2013, "Study on the Performance of Reinforced Embankment on Mountain Slope Using Full-Scale Model Experiments", *Applied Mechanics and Materials*, Vol. 29-294, pp. 987-992.

Wartman, J., R. B. Seed, and J. D. Bray, 2005 "Shaking table modeling of seismically induced deformations in slopes," *J. Geotech. Geoenviron. Eng*, Vol. 131, No. 5, pp. 610–622.

Wood, S., T. Anagnos, P. Arduino, M. O. Eberhard, G. Fenves, T. Finholt, and D. Wilson, 2004, "Using NEES to investigate soil-foundation-structure interaction", *Proc., 13th World Conf. on Earthquake Engineering*, Int. Association for Earthquake Engineering.

Woods, R. D., 1968, "Screening of surface waves in soils", *J Soil Mech Found Div*, Vol. 94, No. 4, pp. 951–979.

Wu, L., G. Jiang, and N. Ju, 2019, "Behavior and numerical evaluation of cement-fly ash-gravel pile-supported embankments over completely decomposed granite soils", *International Journal of Geomechanics*, Vol. 19, No. 6.

Yegian, M., Z. Y. Yee, J. N. Harb, 1995, "Response of geosynthetics under earthquake excitations", *Geosynthetics'95 Conference*, pp. 677-689. Nashville.

Yegian, M. K., A. M. Lahlaf, 1992, "Dynamic interface shear strength properties of geomembranes and geotextiles", *Journal of Geotechnical Engineering*, Vol. 118, No. 5, pp. 760-779.

Yegian, M. K., U. Kadakal, and M. Catan, 1999, "Geosynthetics for earthquake hazard mitigation," *Ind. Fabrics Assoc. Int*., Vol. 1, pp. 87–100.

Yogendrakumar, M., R. J. Bathurst, and W. D. L. Finn, 1991, "Response of reinforced soil slopes to earthquake loadings", *Proceedings of the 6th Canadian Conference on Earthquake Engineering*, Toronto, Ontario, Canada, pp. 445-452.

Yoon, S., M. Prezzi, N. Z. Siddiki, and B. Kim, 2005, "Construction of a Test Embankment Using a Sand-Tire Shred Mixture as Fill Material", *Waste Management*, Vol. 26, pp. 1033-1044.

Zalachoris, G., D. Zekkos, A. Yerro, G. A. Bowers, and K. J. Wissmann, 2023, "3D numerical assessment of rammed aggregate pier performance under dynamic loading in liquefiable soils", *Journal of Geotechnical and Geoenvironmental Engineering*, Vol. 149. No. 3.

Zarnani, S. and R. J. Bathurst, 2005, "Numerical Investigation of Geofoam Seismic Buffers using FLAC", *Proceedings of the North American Geosynthetics Society (NAGS)/GRI19 Conference*, Las Vegas, Nev., pp. 14-16.

Zarnani, S. and R. J. Bathurst, 2006, "Application of EPS Geofoam as a Seismic Buffer: Numerical Study using FLAC", *Proceedings of the 59th Canadian Geotechnical Conference*, Vancouver, B.C.

Zarnani, S. and R. J. Bathurst, 2009, "Numerical Parametric Study of Expanded Polystyrene (EPS) Geofoam Seismic Buffers", *Canadian Geotechnical Journal*, Vol. 46, pp. 318-338.

Zhang, B., H. W. Huang, F. Menq, J. Wang, K. B. Nakshatrala, K. H. Stokoe, and Y. L. Mo, 2022, "Field experimental investigation on broadband vibration mitigation using metamaterial-based barrier-foundation system", *Soil Dynamics and Earthquake Engineering*, Vol. 155.